
“Using the interactions of designed siRNA
and DNA drug carrier systems with human
blood plasma and its components for
controlled drug delivery”

Dissertation zur Erlangung des Grades “Doktor der Naturwissenschaften” im
Promotionsfach Chemie

am Fachbereich Chemie, Pharmazie und Geowissenschaften der
Johannes Gutenberg-Universität Mainz
(D77)

Laura Müller

geb. in Mainz, Deutschland

Mainz, 2016

Dekan:

1. Berichterstatter:

2. Berichterstatter:

Tag der mündlichen Prüfung:

1	ABSTRACT.....	1
2	INTRODUCTION	3
2.1	BLOOD.....	3
2.2	NANOMATERIALS AS DRUG DELIVERY SYSTEMS	5
2.2.1	<i>Liposomes for SIRNA DELIVERY.....</i>	6
2.3	PROTEIN CORONA.....	11
2.3.1	<i>THE STEALTH EFFECT</i>	14
2.4	PROTEIN CORONA ANALYSIS	15
2.4.1	<i>IN SITU ANALYSIS</i>	16
2.4.2	<i>HARD CORONA ANALYSIS</i>	21
2.5	AIM OF THIS WORK	25
3	RESULTS AND DISCUSSION	27
3.1	FRACTIONATION OF HUMAN BLOOD PLASMA	27
3.2	FRACTIONS OF PROTEIN MIXTURES DIFFERENTIALLY AGGREGATE NANOPARTICLES AND INFLUENCE THE CELLULAR UPTAKE	36
3.2.1	<i>THE PARTICLES UNDER INVESTIGATION</i>	37
3.2.2	<i>SOFT PROTEIN CORONA ANALYSIS</i>	38
3.2.3	<i>HARD PROTEIN CORONA ANALYSIS</i>	46
3.2.4	<i>TAILORING THE HARD CORONA.....</i>	48
3.2.5	<i>THE IMPACT OF PROTEIN CONCENTRATION ON PARTICLE AGGREGATION AND STABILIZATION VIA PRE-COATING.....</i>	59
3.2.6	<i>USING PROTEIN MIXTURES AS SURFACTANTS FOR PARTICLE STABILIZATION</i>	67
3.2.7	<i>Summary.....</i>	72
3.3	HUMAN BLOOD PLASMA VERSUS SERUM.....	74
3.4	EVALUATION OF NANOPARTICLE STABILITY IN HUMAN BLOOD SERUM BY DYNAMIC LIGHT SCATTERING: THE IMPACT OF PERSONALIZED HUMAN BLOOD SERUM COMPOSITION	79
3.4.1	<i>ANALYSIS OF INDIVIDUAL AND POOLED HUMAN BLOOD SERUM.....</i>	80
3.4.2	<i>STABILITY EVALUATION OF NANOPARTICLES IN HUMAN BLOOD SERUM BY DYNAMIC LIGHT SCATTERING</i>	83
3.4.3	<i>TAKING ADVANTAGE OF THE INFLUENCE OF PERSONALIZED SERUM ON PARTICLES STABILITY</i> <i>85</i>	
3.4.4	<i>HEAT INACTIVATION OF HUMAN BLOOD SERUM</i>	90
3.4.5	<i>DILUTION AS A TOOL FOR PRE-COATING OF NANOPARTICLES.....</i>	97
3.4.6	<i>Summary.....</i>	100
3.5	THE TRANSFER OF A PROTEIN CORONA	101
3.5.1	<i>THE STEALTH NANOCARRIER</i>	101

3.5.2	CORONA TRANSFER.....	106
3.6	EVALUATION OF DIFFERENT <i>IN VIVO</i> MODELS FOR BIOMEDICAL APPLICATION	111
3.6.1	CHARACTERIZATION OF DIFFERENT BLOOD PLASMA SOURCES	111
3.6.2	INVESTIGATION OF PROTEIN-PARTICLE INTERACTIONS	116
3.7	FROM THE MODEL SYSTEM TOWARDS LIPOSOMES FOR BIOMEDICAL APPLICATION.....	124
3.7.1	EVALUATION OF MULTIFUNCTIONAL LIPOSOMES IN HUMAN BLOOD SERUM BY DYNAMIC LIGHT SCATTERING	124
3.7.2	MULTICOMPONENT LIPOSOMES FOR siRNA DELIVERY TO THE LIVER	131
4	SUMMARY AND OUTLOOK.....	147
5	EXPERIMENTAL SECTION.....	149
5.1	LIST OF EQUIPMENT	149
5.2	METHODS.....	151
5.2.1	<i>Fractionation of human blood plasma</i>	<i>151</i>
5.2.2	<i>Fractions of protein mixture differentially aggregate nanoparticles and influence the cellular uptake</i>	<i>154</i>
5.2.3	<i>Human Blood Plasma versus Serum.....</i>	<i>159</i>
5.2.4	<i>Evaluation of NP stability in human blood serum</i>	<i>159</i>
5.2.5	<i>The transfer of a protein corona</i>	<i>161</i>
5.2.6	<i>Evaluation of different in vivo models.....</i>	<i>162</i>
5.2.7	<i>Evaluation of multifunctional liposomes in human blood serum by dynamic light scattering.....</i>	<i>163</i>
5.2.8	<i>Multicomponent liposomes for siRNA delivery to the liver</i>	<i>163</i>
6	REFERENCES	173
7	APPENDIX.....	183
7.1	ABBREVIATIONS	183
7.2	SUPPLEMENTARY INFORMATION	185
7.2.1	<i>LC-MS DATA FOR BLOOD PLASMA FRACTIONATION</i>	<i>185</i>
7.2.2	<i>OVERVIEW OF SOFT CORONA ANALYSIS CHAPTER 6.2.1</i>	<i>196</i>
7.2.3	<i>OVERVIEW OF HARD PROTEIN CORONA ANALYSIS CHAPTER 6.3.1.....</i>	<i>197</i>
7.2.4	<i>CHARACTERIZATION OF INDIVIDUAL AND POOLED HUMAN SERUM</i>	<i>202</i>
8	ZUSAMMENFASSUNG	203

LIST OF FIGURES

Figure 1. The human plasma proteome. ⁸	4
Figure 2. Passive ¹⁸ (1) versus active (2) targeting. The defect architecture of tumor tissue allows the penetration with nutrients and macromolecules. By conjugating antibodies to macromolecules, the accumulation can be increased by specific antibody-receptor interactions on the surface of tumor cells. Figure 2 (1) Reprinted from <i>Advanced Drug Delivery Reviews</i> , Volume 65, Issue 1, Hirashi Maeda, Hideaki Nakamura, Jun Fang, "The EPR effect for macromolecular drug delivery to solid tumors: Improvement of tumor uptake, lowering of systemic toxicity, and distinct tumor imaging <i>in vivo</i> ", Pages 71-79, Copyright © (2012), with permission from Elsevier Elsevier.....	6
Figure 3. a) Schematic structure of left) phosphoglycerides and right) sphingophospholipids with the polar head (orange) and the apolar tail (blue); b) schematic 3D structure of self-assembled lipids with A) micelle, B) bilayer and C) vesicle; c) PEG modification of liposomes with high density (left) and low density (right). reprinted from <i>Biochemical and Biophysical Research Communications</i> , Volume 468, Issue 3, Laura K. Müller, Katharina Landfester, "Natural liposomes and synthetic polymeric structures for biomedical applications", Pages 411-418, Copyright © (2015), with permission from Elsevier.....	8
Figure 4. Chemical versus biological identity of a nanomaterial after intravenous injection. ⁸⁶ Adapted from "Walkey, C. D.; Chan, W. C. Understanding and controlling the interaction of nanomaterials with proteins in a physiological environment. <i>Chem. Soc. Rev.</i> 2012, 41, 2780-2799." with permission of The Royal Society of Chemistry.....	12
Figure 5. Protein adsorption on stealth-materials (right) is reduced in comparison to non-modified NPs (left).	15
Figure 6. Soft vs. hard corona obtained by the removal of free proteins using for instance centrifugation or magnetic separation.	16
Figure 7. Chromatogram of IgG separation via Protein A column and the corresponding protein amount in the fractions according to a BCA Assay.....	28
Figure 8. A) Protein patterns obtained by SDS-PAGE of plasma and the protein fractions obtained by Protein A affinity chromatography with FT1 = flow through Protein A column. B) LC-MS analysis of the respective protein fractions (LC-MS measurements performed by Dr. Susanne Schöttler).....	29
Figure 9. Chemical structure of Cibacron Blue.	29
Figure 10. Chromatogram of HSA separation via AffiGel-Blue column and the corresponding protein amount in the fractions according to a BCA Assay.....	30
Figure 11. A) Protein patterns obtained by SDS-PAGE of plasma and the protein fractions obtained by series connection of Protein A affinity chromatography and AffiGel Blue affinity chromatography with FT1 = flow through Protein A column and FT2 = FT1 with subsequent HSA removal. B) LC-MS analysis of the respective protein fractions with FT = flow through AffiGel Blue column. (LC-MS measurements performed by Dr. Susanne Schöttler)	31
Figure 12. A) Angular dependency of the inverse hydrodynamic radii of the different protein fractions. B) ACF of $F_{\text{Plasma-w/o-HSA-IgG}}$ with the distribution of the 3 different size fractions at $\Theta = 30^\circ$	33
Figure 13. Chromatogram of DEAE anion exchange chromatography.....	34

Figure 14. LC-MS analysis of elution fraction 1 – 4 (LC-MS performed by Dr. Susanne Schöttler, AK Landfester, Max Planck Institute for Polymer Research, Mainz, 2015) and SDS-PAGE of the respective protein fractions.....	35
Figure 15. SDS-PAGE of series connection of Protein A column, AffiGel Blue column and DEAE column with FT1-3 = flow through after each column and E1-4 elution fraction 1-4 of DEAE column.	35
Figure 16. Angular dependency of the inverse hydrodynamic radii of PS, PS-COOH and PS-NH ₂ obtained by DLS.....	37
Figure 17. TEM images and physicochemical characterization of polystyrene nanoparticles with different surface functionalization.....	38
Figure 18. Size increase of respective PS-particles in dependence of the protein amount.....	39
Figure 19. A) ACFs of the different particles in isolated $F_{\text{Plasma-w/o-IgG-HSA}}$ at $\Theta = 60^\circ$ including data points (•) and the forced fit as the sum of the individual components (red) with the corresponding residuals resulting from the difference between data and fit. B) ACFs of the different particles in human plasma at $\Theta = 60^\circ$ including data points (•), forced fit (red) and fit with additional aggregate function (blue) with the corresponding residuals resulting from the difference between data and the two fits.	40
Figure 20. A) Angular dependency of the inverse hydrodynamic radii as well as ACF at $\Theta = 30^\circ$ including data points (O), force fit (red), and fit including aggregate formation (blue) of PS in IgG and running buffer as medium. B) Angular dependency of the inverse hydrodynamic radii as well as ACF at $\Theta = 30^\circ$ including data points (O), force fit (red) and fit including aggregate formation (blue) of PS in IgG and PBS buffer as medium.	44
Figure 21. A) Angular dependency of the inverse hydrodynamic radii as well as ACF at $\Theta = 30^\circ$ including data points (O), force fit (red), and fit including aggregate formation (blue) of PS in HSA and running buffer as medium. B) Angular dependency of the inverse hydrodynamic radii as well as ACF at $\Theta = 30^\circ$ including data points (O), force fit (red) and fit including aggregate formation (blue) of PS in HSA and PBS buffer as medium.	45
Figure 22. A) CD spectrum of IgG in PBS and running buffer at 37 °C with $c = 1 \text{ g/L}$. B) CD spectrum of HSA in PBS and running buffer at 37 °C with $c = 1 \text{ g/L}$	46
Figure 23. A) SDS-PAGE of protein coronas that were formed upon incubation of the different PS-particles in concentrated human blood plasma. B) Hard corona analysis by protein quantification and ζ -potential measurement.	47
Figure 24. Plasma composition in comparison to the hard corona composition of each particle analyzed via LC-MS (LC-MS measurements performed by Johanna Simon).....	48
Figure 25. A) Angular dependency of the inverse hydrodynamic radius of PS-COOH (•) and centrifuged PS-COOH (•). B) Angular dependency of the inverse hydrodynamic of PS (•), PS after incubation in human plasma and one centrifugation step (•), two (•), three (•), and four centrifugation steps (•).	50
Figure 26. Flow cytometry analysis of RAW 264.7 cells incubated with uncoated or pre-coated nanoparticles for 2 h in DMEM without additional proteins. Nanoparticles were pre-incubated with individual proteins (A) or different protein fractions (B), separated from unbound proteins via centrifugation and added to the cells with a nanoparticle concentration of 75 $\mu\text{g/mL}$. Relative median fluorescence	

intensity (rMFI) values are shown as mean \pm SD of triplicates. The red line serves as a reference for cellular uptake of uncoated nanoparticles (rMFI = 1). A student's t-test was performed to demonstrate the difference in uptake behavior of uncoated and pre-coated nanoparticles (indicated by p values < 0.01* or p < 0.001**) (all cell experiments were performed by Johanna Simon).	51
Figure 27. cLSM images of RAW264.7 cells after incubation with pre-coated nanoparticles for 2h in DMEM without additional proteins. Exemplary shown for PS pre-coated with HSA (A); PS-COOH pre-coated with IgG (B); PS-NH ₂ pre-coated with IgG (C). Scale bars = 10 μ m.....	52
Figure 28. Flow cytometry analysis of RAW 264.7 cells incubated with nanoparticles pre-coated with varying amounts of Ig depleted plasma for 2 h in DMEM without additional proteins. Different pre-coating ratios between the amount of proteins (in mg) and the defined surface of nanoparticles ($5 \cdot 10^{-3} \text{ m}^2$) were chosen. The pre-coated nanoparticles were isolated via centrifugation and added to the cells with a nanoparticle concentration of 75 μ g/mL. Relative median fluorescence intensity (rMFI) values are shown as mean \pm SD of triplicates. The red line serves as a reference for cellular uptake of uncoated nanoparticles (rMFI = 1). A student's t-test was performed to demonstrate the difference in uptake behavior of uncoated and pre-coated nanoparticles (indicated by p values < 0.01* or p < 0.001**) (all cell experiments were performed by Johanna Simon).	53
Figure 29. Pre-coating of nanoparticles ($R_n(\text{cp})$) with distinct low abundant protein fractions stabilizes nanoparticles against aggregation in human plasma. A) DLS analysis demonstrates aggregation formation ($R_n(\text{agg})$) of PS particles ($R_n(\text{p})$) in human plasma. ACF of PS particles in human plasma at $\Theta = 30^\circ$ is shown. B) Pre-coating of PS particles with $F_{\text{Plasma-w/o-IgG-HSA}}$ prevents the formation of aggregates. ACFs of the PS particles in isolated $F_{\text{Plasma-w/o-IgG-HSA}}$ at $\Theta = 30^\circ$ is illustrated.....	55
Figure 30. A+B) Angular dependency of the inverse hydrodynamic radii as well as ACF at $\Theta = 30^\circ$ including data points (\bullet), force fit (red), and fit including aggregate formation (blue) of naked as well as coated PS particles in concentrated human plasma (comparable to <i>in vivo</i> conditions).	57
Figure 31. Protein patterns of formed hard coronas with single (S) as well as double incubation with subsequent plasma incubation (D) of PS particles in A) IgG, B) HSA, C) $F_{\text{Plasma-w/o-IgG}}$, and D) $F_{\text{Plasma-w/o-IgG-HSA}}$	58
Figure 32. Autocorrelation function at $\Theta = 60^\circ$ of PS-COOH in $F_{\text{Plasma-w/o-IgG}}$ including data points (\bullet), force fit (red) and fit with aggregate formation (blue). From A to D, the protein amount per surface area was increased by a factor of 16.....	61
Figure 33. Size increase of PS-COOH in $F_{\text{Plasma-w/o-IgG}}$ with increasing amount of proteins per given surface area of nanomaterial. The intensity contribution at $\Theta = 30^\circ$ to the overall scattered light of aggregates is illustrated in green, the one of particles in red.....	62
Figure 34. ACF at $\Theta = 30^\circ$ including data points, force fit and fit with aggregation in concentrated human plasma of A) PS-COOH, B) PS-COOH coated with 1 mg $F_{\text{Plasma-w/o-IgG}}$, C) PS-COOH coated with 2 mg $F_{\text{Plasma-w/o-IgG}}$, D) PS-COOH coated with 3 mg $F_{\text{Plasma-w/o-IgG}}$, E) PS-COOH coated with 4 mg $F_{\text{Plasma-w/o-IgG}}$. F) Observed aggregated sizes in concentrated human plasma of samples A – E.	65
Figure 35. Surface tension of a solution of $F_{\text{Plasma-w/o-IgG}}$ in water in dependence to the protein concentration.	68

Figure 36. Chemical structure of V59 (left) and V70 (right).....	69
Figure 37. TEM images as well as DLS results of polystyrene with $F_{\text{Plasma-w/o-IgG}}$ as stabilizer.....	70
Figure 38. Angular dependency of the inverse hydrodynamic radii as well as ACF at $\Theta = 30^\circ$ including data points (O), force fit (red) and fit including aggregate formation (blue) of protein stabilized particle in human blood plasma.....	70
Figure 39. A) CellTiter-Glo Assay of PS with proteins as surfactant. B) CellTiter-Glo Assay of Lutensol stabilized PS-particles (data in B provided by Johanna Simon).....	71
Figure 40. SDS-PAGE of A) PS stabilized with $F_{\text{Plasma-w/o-IgG}}$, B) plasma, and C) $F_{\text{Plasma-w/o-IgG}}$	72
Figure 41. Angular dependency of the inverse hydrodynamic radii of A) PS-NH ₂ and B) the different protein sources.....	75
Figure 42. Size increase of PS-NH ₂ in the respective protein sources ($\Theta = 30^\circ$).	75
Figure 43. ACF at $\Theta = 30^\circ$ of PS-NH ₂ including data points (O), force fit (red) and fit regarding aggregate formation (blue) in A) serum, B) citrate plasma, C) heparin plasma, D) FBS + heparin, and E) FBS. D) Aggregate sizes and intensity contribution at $\Theta = 30^\circ$ determined by DLS.....	76
Figure 44. Structure of A) Heparin- and B) Citrate-anion.	77
Figure 45. A) Autocorrelation function of serum pool at scattering angle 30° with the distribution of the three different size fractions. B) Fluctuation of the three different size fractions between different probands.	80
Figure 46. ACF at $\Theta = 30^\circ$ for serum P4 (red), P5 (blue) and pooled human serum (green).....	81
Figure 47. ACF of PS-COOH in pooled human serum (left) and in serum P4 (right) at $\Theta = 30^\circ$ including data points (•), force fit (red) and fit including aggregate formation (blue) of protein stabilized particle in human blood plasma.....	84
Figure 48. Protein patterns of the protein coronas formed on the different functionalized PS particles upon incubation in the different protein sources.	85
Figure 49. ACF of a respective coated particle in pooled human serum at $\Theta = 30^\circ$ including data points (•) and force fit (red) with A) PS coated in P4, B) PS-COOH coated in P4, C) PS-NH ₂ coated in P2 and D) PS-NH ₂ coated in P7.....	86
Figure 50. Angular dependency of the inverse hydrodynamic radius of the particles itself (red), the corresponding aggregates (blue) formed in pooled human serum (black) in comparison with the ones of the coated particles (magenta).....	87
Figure 51. Angular dependency of the inverse hydrodynamic radii as well as the z-averaged value obtained in native human serum pool (A) and heat inactivated human serum pool (B).	91
Figure 52. ACF at $\Theta = 30^\circ$ of native human serum (black) and heat inactivated human serum (red).	91
Figure 53. SDS-PAGE of the different polystyrene particles' protein coronas formed upon incubation in native human serum pool (A) as well as in heat inactivated human serum pool (B) (SDS-PAGE performed by Johanna Simon).	92
Figure 54. Fluorescence at 350 nm determined by nanoDSF of fibrinogen (A), HSA (B), IgG (C) and clusterin (C) in PBS (clusterin was measured by Julius Müller, PhD student, AK Landfester, MPIP).	94

Figure 55. Size increase of the polystyrene particles in native or heat inactivated human serum pool obtained by DLS in comparison with the size increase in native human serum pool after coating with inactive human serum pool.	96
Figure 56. A) Size increase of PS-COOH in concentrated as well as diluted human serum obtained by DLS together with the scattering intensity of particle or rather aggregate at $\Theta = 30^\circ$. B) Size increase of PS-NH ₂ in concentrated as well as diluted human serum obtained by DLS together with the scattering intensity of particle or rather aggregate at $\Theta = 30^\circ$	98
Figure 57. ACF at $\Theta = 30^\circ$ of A) PS-COOH in serum pool as concentrated mixture, B) PS-COOH in serum pool as diluted mixture 1:2, C) PS-COOH in serum pool as diluted mixture 1:5, D) PS-NH ₂ in serum pool as concentrated mixture and E) PS-NH ₂ in serum pool as diluted mixture 1:2 obtained by dynamic light scattering. D) Summary of determined aggregate radii and the corresponding size increase.	99
Figure 58. Illustration of protein corona transfer.	101
Figure 59. A) Angular dependency of the inverse hydrodynamic radius of PS-PEG ₅₀₀₀ obtained by DLS. B) ACF at $\Theta = 30^\circ$ of PS-PEG ₅₀₀₀ in concentrated human plasma including data points and force fit.	103
Figure 60. A) SDS-PAGE of human plasma with subsequent silver staining (1); the protein corona formed on PS-PEG ₅₀₀₀ after incubation in human plasma with (2) and without (3) SDS; the protein corona formed on the second use of PS-PEG ₅₀₀₀ after incubation in human plasma with (4) and without (5) SDS and the protein corona formed on the third use of PS-PEG ₅₀₀₀ after incubation in human plasma with (6) and without (7) SDS. B) Zeta potential of uncoated PS-PEG ₅₀₀₀ as well as of the coated ones after first and third use.	105
Figure 61. A) Fluorescence at 350 nm determined by nanoDSF of “stealth” proteins, B) Fluorescence at 330 nm determined by nanoDSF, and C) the 350/330 nm ratio determined by nanoDSF.	106
Figure 62. A) SDS-PAGE of human plasma (1), the protein corona of PS-NH ₂ formed in human plasma (2), the protein corona of PS-NH ₂ formed in the “stealth” proteins (3) and the “stealth” proteins (4). B) Zeta potential of uncoated PS-NH ₂ as well as of coated PS-NH ₂ with “stealth” proteins.	108
Figure 63. A) ACF at $\Theta = 30^\circ$ of PS-NH ₂ in concentrated human plasma including data points (O), force fit (red) and fit with aggregate formation (blue) with the angular dependency of their inverse hydrodynamic radii. B) ACF at $\Theta = 30^\circ$ of coated PS-NH ₂ in concentrated human plasma with the angular dependency of the obtained inverse hydrodynamic radii.	109
Figure 64. Flow cytometry analysis of RAW 264.7 cells incubated with nanoparticles 2 h in DMEM without additional proteins. The pre-coated nanoparticles were isolated via centrifugation and added to the cells with a nanoparticle concentration of 20 $\mu\text{g}/\text{mL}$. Relative median fluorescence intensity (rMFI) values are shown as mean \pm SD of triplicates (cell experiments were performed by Johanna Simon).	110
Figure 65. A) Fluctuation of the different size fractions for the different plasma sources B) The corresponding ACF at $\Theta = 30^\circ$. C) Obtained values for the different size fractions from DLS.	112
Figure 66. SDS-PAGE of human, rabbit, sheep and mouse plasma.	113
Figure 67. A) Observed size increases in % of the different PS-particles after exposure to human, mouse, rabbit and sheep plasma. B) Zeta potential of uncoated PS-particles as well as coated particles in the different plasma sources under investigation.	117

Figure 68. A) SDS-PAGE of the protein coronas formed on PS, PS-COOH and PS-NH ₂ during incubation in human or mouse plasma. B) SDS-PAGE of the protein coronas formed on the respective particles during incubation in sheep or rabbit plasma.	118
Figure 69. Schematic structure of BNF-Starch and BNF-Dextran.....	119
Figure 70. ACF at $\Theta = 30^\circ$ for BNF-DEX in human, mouse, sheep and rabbit plasma.	120
Figure 71. ACF at $\Theta = 30^\circ$ for BNF-HES in human, mouse, sheep and rabbit plasma.	121
Figure 72. A) SDS-PAGE of protein coronas formed on BNF-HES and –DEX during incubation in human, mouse, sheep and rabbit plasma (performed by Johanna Simon). B) Zeta potential of uncoated as well as coated particles in the different plasma sources under investigation.....	122
Figure 73. Molecular structures of the cholesterol-based amphiphilic lipid analogues. Reprinted (adapted) with permission from (<i>“Evaluation of Multifunctional Liposomes in Human Blood Serum by Light Scattering”</i> Mohr et al., Langmuir 2014, 30, 14954-14962). Copyright © 2014, American Chemical Society.	125
Figure 74. Cartoon of PEGylated liposomes. Reprinted (adapted) with permission from (<i>“Evaluation of Multifunctional Liposomes in Human Blood Serum by Light Scattering”</i> Mohr et al., Langmuir 2014, 30, 14954-14962). Copyright © 2014, American Chemical Society.	126
Figure 75. Cryo-Tem images of three different liposomes. Reprinted (adapted) with permission from (<i>“Evaluation of Multifunctional Liposomes in Human Blood Serum by Light Scattering”</i> Mohr et al., Langmuir 2014, 30, 14954-14962). Copyright © 2014, American Chemical Society (performed by Kristiane Rusitzka, Biology Department, Johannes Gutenberg University, Mainz).	128
Figure 76. Liposomes containing Ch-PEG ₄₄ in human serum: A) L10-PEG, B) L15-PEG, C) L20-PEG and D) L30-PEG. ACF at $\Theta = 30^\circ$ including data points, force fit (red) and aggregate fit (blue). Reprinted (adapted) with permission from (<i>“Evaluation of Multifunctional Liposomes in Human Blood Serum by Light Scattering”</i> Mohr et al., Langmuir 2014, 30, 14954-14962). Copyright © 2014, American Chemical Society (measurements performed by Dr. Kristin Mohr, Max Planck Institute for Polymer Research, Mainz).	129
Figure 77. Liposomes containing Ch-PEG ₃₃ -hbPG ₂₃ in human serum: A) L10-hbPG, B) L15-hbPG, C) L20-hbPG and D) L30-hbPG. ACF at $\Theta = 30^\circ$ including data points, force fit (red) and aggregate fit (blue). Reprinted (adapted) with permission from (<i>“Evaluation of Multifunctional Liposomes in Human Blood Serum by Light Scattering”</i> Mohr et al., Langmuir 2014, 30, 14954-14962). Copyright © 2014, American Chemical Society.	130
Figure 78. Chemical structure of surfactant TF.	131
Figure 79. A) ¹ H NMR of surfactant TF in CD3OD. B) HPLC of dye, cationic lipid TF and TF-dye conjugate; MN-HD8-column 125/4/5µml, T=20°C, 10 min: 5/95-100/0 (THF/water+0.1%TFA) (performed by Beate Müller, AK Landfester, MPIP).	132
Figure 80. Cryo-TEM images of A) L-1:1:1 loaded with siRNA and B) unloaded L-1:1:4-hbPG (performed by Dr. Max Bernhard).	133
Figure 81. Angular dependency of the inverse hydrodynamic radius (A) and Guinier-plots (B) of liposomes.	134

Figure 82. Autocorrelation functions of the different liposomal systems in human serum at 30° and the respective aggregate size with its impact on the scattering intensity. Red lines: Force fit with the pure component correlation, blue lines: Fit with an additional aggregate term. Residues of the respective fits are shown in the lower part of the graphs.....	136
Figure 83. A) Angular dependency of the inverse hydrodynamic radius of siRNA loaded liposomes. B) Guinier-plots of siRNA-loaded liposomes.	137
Figure 84. Zeta potential of L-1:1:1 in comparison to the zeta potential of L-1:1:1 loaded with different types of siRNA.....	138
Figure 85. Comparison of two different work-up procedures for L-1:1:1.	138
Figure 86. Correlation functions (recorded 30° scattering angle) of liposomes and siRNA loaded liposomes in 50% human plasma. A) liposome consisting of DSPC, Chol and lipid TF, B) liposome in A loaded with siRNA (N/P = 34), C) liposome consisting of Chol, DSPC, TF and <i>hb</i> -PG, D) liposome in C loaded with siRNA (N/P = 34). Red lines: Force fit with the pure component correlation function, blue lines: Fit with an additional aggregate ter. Residues of the respective fits are shown in the lower part of the graphs.	139
Figure 87. a) Viability of MHS macrophages in response to increasing amounts of L-1:1:4 lipoplex loaded with scrambled siRNA normalized to PBS; incubation time 24 h (n = 3); MEAN ± SD; b) In vitro knockdown by L-1:1:4 (NP) loaded with anti-CD68 siRNA after 24 h. scsiRNA, negative control; * p < 0.05 (n = 3); MEAN ± SD (measurements performed by Leonard Kaps, Medical department of the Johannes Gutenberg University, Mainz).	140
Figure 88. Top) <i>In vivo</i> knockdown outline. Mice received two retroorbital injections of 1 or 2 anti-CD68 siRNA encapsulated in L-1:1:4 or L-1:1:4- <i>hb</i> PG; in vivo imaging period indicated above timeline. Bottom) In vivo images system (IVIS) pictures of mice injected with 1 mg/kg or 2 mg/kg antiCD68 siRNA loaded in L-1:1:4 lipoplexes (left) or L-1:1:4- <i>hb</i> PG <i>hb</i> PG stabilized lipoplexe (right) labeled with CW800 near infrared dye at 0, 1, 3, 24 and 48h (measurements performed by Leonard Kaps).	142
Figure 89. <i>Ex vivo</i> organ quantification of L-1:1:4 lipoplex (blue) and L-1:1:4- <i>hb</i> PG (red) labeled with near infrared dye 48 h after the second injection, *** p < 0.001; MEAN ± SD (measurements performed by Leonard Kaps).	143
Figure 90. IVIS pictures of ex vivo organs from mice that were injected with 1 mg/kg or 2 mg/kg antiCD68 siRNA loaded in L-1:1:4 or L-1:1:4- <i>hb</i> PG respectively labeled with near infrared dye 48h after injection (measurements performed by Leonard Kaps).	144
Figure 91. <i>In vivo</i> liver resident macrophage uptake of L-1:1:4 lipoplex (blue) and L-1:1:4- <i>hb</i> PG lipoplex (red) labeled with NIR dye 48 h after the second injection; MEAN ± SD (measurements performed by Leonard Kaps).	145
Figure 92. <i>In vivo</i> knockdown of the macrophage specific gene CD68 in the liver of mice that were injected twice with 1 mg/kg or 2 mg/kg anti-CD68 siRNA loaded into L-1:1:4 (blue) or L-1:1:4- <i>hb</i> PG lipoplexe (red). **p<0.01 for anti-CD68 siRNA vs negative controls; MEAN ± SD (measurements performed by Leonard Kaps).	145
Figure 93. Synthesis of surfactant TF according to [153].	164

LIST OF TABLES

Table 1. ρ -ratios and their corresponding geometry for macromolecules. ¹¹³	19
Table 2. Obtained protein fractions ($c = 1$ g/L) with their hydrodynamic radius and composition according to LC-MS.	32
Table 3. Size changes of the uncoated nanoparticles after direct exposure to human plasma or the obtained protein fractions was measured by DLS. Size increase of nanoparticles incubated in the respective protein fraction is calculated based on the size value for the uncoated nanoparticles measured in PBS (Reference value Figure 15).	42
Table 4. Size changes of the uncoated nanoparticles after direct exposure to human plasma or the obtained protein fractions was measured by DLS. Size increase of nanoparticles incubated in the respective protein fraction is calculated based on the size value for the uncoated nanoparticles measured in PBS (Reference value Figure 15).	43
Table 5. Physicochemical parameters of nanoparticles pre-coated with different protein fractions or individual proteins.	49
Table 6. Size changes of pre-coated particles after direct exposure to human plasma. Intensity fractions of the aggregate $I(30^\circ)$ are exemplified for a scattering angle of 30° . Size increase is calculated based on the values for uncoated nanoparticles (see Figure 17) or pre-coated nanoparticles in PBS (see Table 5).	54
Table 7. Physicochemical parameters of coated PS-COOH particles in $F_{\text{Plasma-w/o-IgG}}$	64
Table 8. Top 20 identified proteins in the protein corona formed on PS-COOH particles after incubation in concentrated human plasma (1), IgG-depleted plasma (2), and IgG-depleted plasma with subsequent incubation in concentrated human plasma (3) determined via LC-MS (LC-MS measurements were performed by Johanna Simon).	67
Table 9. Top 20 identified proteins in individual sera P2-P9 as well as serum pool determined via LC-MS (LC-MS measurements were performed by Johanna Simon).	82
Table 10. Stability evaluation of the different polystyrene particles in the respective sera or serum pool (in red).	83
Table 11. TOP 20 identified proteins of the protein coronas (values in %) formed on PS-COOH particles after incubation with pooled human serum, individual serum P4 and double incubation obtained by LC-MS in duplicates A and B (LC-MS measurements performed by Johanna Simon).	88
Table 12. TOP 20 identified proteins of the protein coronas (values in %) formed on PS-NH ₂ nanoparticles after incubation with pooled human serum, individual serum P7 and double incubation obtained by LC-MS in duplicates A and B (LC-MS measurements performed by Johanna Simon).	89
Table 13. TOP 20 identified proteins of the protein coronas (values in %) formed on PS-NH ₂ nanoparticles after incubation with native pooled human serum (A) and heat inactivated human serum (B) obtained by LC-MS (LC-MS measurements performed by Johanna Simon).	93
Table 14. Zeta potential of the different polystyrene particles without incubation and after incubation in native or heat inactivated pooled human serum.	95
Table 15. Physicochemical characterization of PS-NH ₂ (top) and purified PS-PEG ₅₀₀₀ (bottom).	102

Table 16. Top 20 identified proteins of the protein corona formed on PS-PEG ₅₀₀₀ upon incubation in human plasma (LC-MS measurement was performed by Johanna Simon).	104
Table 17. Top 20 identified proteins in human and mouse plasma (LC-MS measurement was performed by Johanna Simon).....	114
Table 18. Top 20 identified proteins in rabbit and sheep plasma (LC-MS measurement was performed by Johanna Simon).....	115
Table 19. Aggregate sizes formed in the different blood plasma sources obtained by DLS.	120
Table 20. Different molar ratios used for the preparation of sterically stabilized liposomes with L = liposomes. Reprinted (adapted) with permission from (" <i>Evaluation of Multifunctional Liposomes in Human Blood Serum by Light Scattering</i> " Mohr et al., Langmuir 2014, 30, 14954-14962). Copyright © 2014, American Chemical Society.....	126
Table 21. Summary of the z-averaged hydrodynamic radii of all investigated liposomes. Reprinted (adapted) with permission from (" <i>Evaluation of Multifunctional Liposomes in Human Blood Serum by Light Scattering</i> " Mohr et al., Langmuir 2014, 30, 14954-14962). Copyright © 2014, American Chemical Society.....	127
Table 22. Composition of investigated liposomes.....	132
Table 23. Zeta potential, DLS- and SLS-results of liposomes.	134
Table 24. Zeta potential, DLS -, SLS results and encapsulated amount of siRNA of loaded liposomes.	137

1 ABSTRACT

The development of nanomaterials for biomedical application has become of great interest in the last decades. Especially in cancer therapy, the encapsulation of drugs in a carrier provides many advantages over administering active ingredients only. The nanomaterials are designed to guide the anti-cancer drug specifically to the tumor tissue. This way, the cytotoxic side effects that occur during chemotherapy can be reduced. In addition, the active compound itself can be protected from degradation.

But still, the application of nanomaterials in cancer treatment is limited due to some drawbacks in understanding and foreseeing the physiological responses a nanocarrier induces upon administration. So far, nanocarriers are usually applied intravenously. This means, that the carrier system immediately comes into contact with the human blood and the therein dissolved proteins. This results in the rapid formation of a protein corona on the nanomaterial's surface that alters its chemical and physical properties in a significant manner.

In this study, the influence of single proteins as well as protein mixtures on the physicochemical properties of polystyrene particles as a model system is investigated. The single proteins as well as protein mixtures that are exempted from the most abundant proteins albumin and immunoglobulin G were obtained from the fractionation of human blood plasma. Incubation of the respective particles in defined protein fractions was used to form predetermined protein coronas that were further investigated in regards of stabilizing or destabilizing effects on a particle under *in vivo* conditions using dynamic light scattering. In addition, the effect of a given protein corona on cellular uptake by macrophages was monitored. This way, the possibility of stabilizing particles against aggregation via pre-coating was introduced.

The concept of pre-coating nanomaterials for tailoring their stability against aggregation was broadened in order to overcome the difficulties that occur because of a fluctuation in the blood serum proteome composition among different individuals.

Next, the focus was put on the transferability of different *in vivo* animal models to humans. It turned out, that the stability of polystyrene as well as dextran- and starch-coated particles against aggregation strongly depends on the protein source.

After screening the mentioned factors that influence the protein corona formation by the use of polystyrene particles as a model system, liposomes for siRNA delivery to the liver have been investigated and optimized regarding their stability against aggregation.

In summary, the closer look that is taken on the different factors that influence the physicochemical properties of a nanomaterial after exposure to human blood offers several opportunities of *pre-in vivo* screening methods for novel nanomaterials. In addition, it introduces possible ways of how the interactions between nanomaterials and proteins can be used for stabilization against aggregation.

2 INTRODUCTION

In the last decades, designing nanomaterials for biomedical applications has become of great interest.¹ These systems are designed for specific targeting of for example tumor cells and by this reduce cytotoxic side-effects.² So far, most drug delivery systems are given parenterally, meaning intramuscular or intravenously.² In consequence, nanomaterials come into contact with biological media like cytosol or blood and interact with present proteins and cells.

2.1 BLOOD

Blood, also “liquid tissue”, has the main task of ensuring the functionality of different body-tissues by transporting oxygen and nutrients. It consists of 45% cellular components and 55% blood plasma. The cellular fraction contains erythrocytes for oxygen transport, leucocytes for immune defense and thrombocytes as part of blood coagulation. The liquid blood fraction, plasma, contains numerous proteins.^{3,4} In order to recover plasma from blood, an anti-coagulant has to be added in order to prevent the blood from clotting. As anti-coagulants ethylene diamine tetra acetic acid (EDTA), heparin, or citrate come into operation.⁵ The cellular fraction can afterwards be removed via centrifugation. The effectiveness of EDTA and citrate is based on complexation of ions that are needed for enzymes as part of the coagulation process. Heparin on the other hand activates anti-thrombin and by this inhibits the coagulation cascade. When the blood is allowed to clot prior to centrifugation, human blood serum is obtained as liquid fraction.⁵ In consequence, proteins that are part of the coagulation process are removed during centrifugation.

The overall concentration of proteins in human blood plasma is about 60-80 g/L. The two most abundant proteins, namely human serum albumin (HSA) and immunoglobulin G (IgG) count about ~75% of the overall protein amount. The composition of the human plasma proteome is illustrated in Figure 1. Albumin, which belongs to the class of globular proteins, is the highest abundant plasma protein with 60%.⁶ Its molecular weight is

66 kDa and the structure is predominantly alpha-helical.⁷ The main function of albumin is the maintenance of the colloid-osmotic pressure.

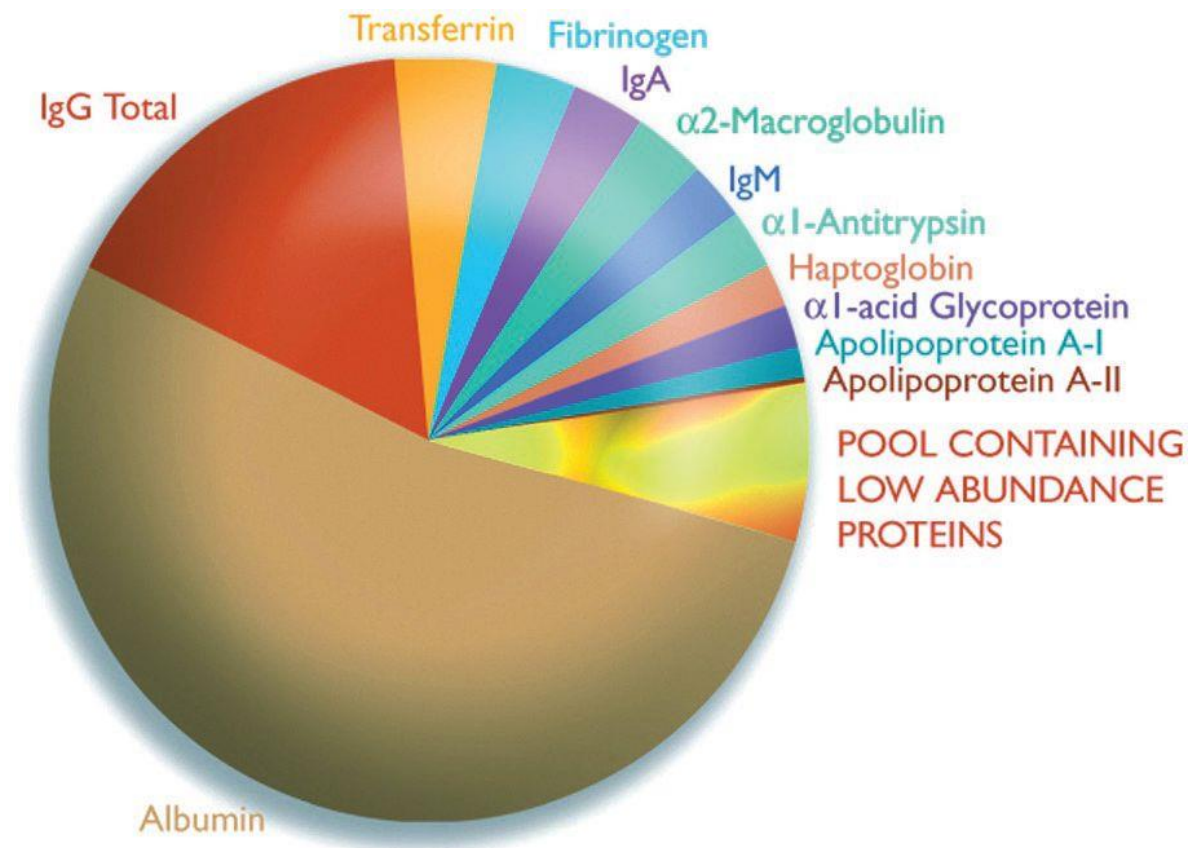


Figure 1. The human plasma proteome.⁸

IgG makes up about 16% of the overall plasma proteome. It is like albumin a globular protein⁹ with a molecular weight of 150 kDa⁶ that belongs to the class of anti-bodies. In general, anti-bodies are built up of two heavy and two light chains. Immunoglobulins comprise five classes (IgG, IgA, IgM, IgD, IgE). They are distinguished by their type of heavy chain. IgG can bind to a specific antigen and by this mark material that is foreign to the body. With this, the protein plays an important role in the activation of the immune system.

α2-Macroglobulin, haptoglobin and α1-antitrypsin belong to the protein class of the acute phase. These proteins are synthesized in an increased manner upon injury.¹⁰

Fibrinogen, which also plays an important role in the hemostatic process, is part of the coagulation process of blood.¹¹ Clotting occurs, when the protein is converted to fibrin by thrombin.¹²

Apolipoprotein A-I and A-II belong to the class of lipoproteins. Lipoproteins are aggregates that are build-up of proteins, lipids and cholesterol. Their main function is the transport of lipids. According to their density, lipoproteins can be divided in chylomicrons, high density lipoprotein (HDL), intermediate density lipoproteins (IDL), low density lipoprotein (LDL), and very low density lipoprotein (VLDL).¹³

2.2 NANOMATERIALS AS DRUG DELIVERY SYSTEMS

Nanoparticles (NPs) for biomedical applications are a very promising and exciting research field. Especially when it comes to cancer treatment, the idea of incorporating drugs into nano-sized drug carriers is very attractive, since the so far used chemotherapeutics cause several cytotoxic side-effects. On the one hand, the encapsulation of drugs offers the opportunity of targeting to the desired cells and by this increasing the mentioned specificity. On the other hand, the loading of drugs into nanomaterials protects the drug itself from degradation.

In general, two mechanisms for guiding a nanoparticle to the desired body tissue are possible. The first one relies on the so-called enhanced permeability and retention (EPR) effect.^{14, 15} The basis of this passive mechanism is a defect of architecture in most tumor blood vessels.¹⁶ This results in an enhanced permeability for oxygen and nutrients, but in addition offers the possibility of transporting macromolecules into the tumor tissue with subsequent accumulation. The second possible guiding strategy is a form of active targeting. Targeting moieties such as antibodies are conjugated to the drug delivery systems in order to increase the effectiveness.¹⁷

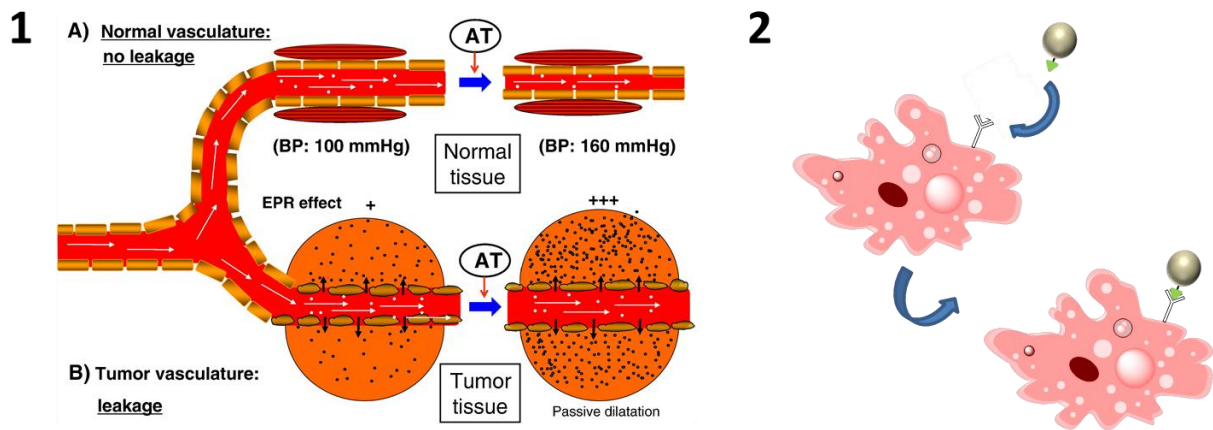


Figure 2. Passive¹⁸ (1) versus active (2) targeting. The defect architecture of tumor tissue allows the penetration with nutrients and macromolecules. By conjugating antibodies to macromolecules, the accumulation can be increased by specific antibody-receptor interactions on the surface of tumor cells. Figure 2 (1) Reprinted from *Advanced Drug Delivery Reviews*, Volume 65, Issue 1, Hirashi Maeda, Hideaki Nakamura, Jun Fang, “The EPR effect for macromolecular drug delivery to solid tumors: Improvement of tumor uptake, lowering of systemic toxicity, and distinct tumor imaging *in vivo*”, Pages 71-79, Copyright © (2012), with permission from Elsevier Elsevier.

A variety of nano-particular systems are investigated for cancer therapy. They include polymeric nanoparticles,¹⁹ liposomes,^{20, 21} metallic core nanoparticles,^{22, 23} dendrimers,²⁴ polymeric micelles,²⁵⁻²⁷ and viral nanoparticles.²⁸ Each system bears several advantages but also limitations. Liposomes are a very prominent strategy to incorporate siRNA for delivery and are therefore discussed in detail within this introduction.²²

2.2.1 LIPOSOMES FOR SIRNA DELIVERY

This chapter has already been published and is reprinted from *Biochemical and Biophysical Research Communications*, Volume 468, Issue 3, Laura K. Müller, Katharina Landfester, “Natural liposomes and synthetic polymeric structures for biomedical applications”, Pages 411-418, Copyright © (2015), with permission from Elsevier.²⁹

Since the discovery of RNA interference (RNAi) as novel therapeutic strategy for gene silencing by Fire *et al.* in 1998³⁰ and Elbashir *et al.* in 2001,^{31, 32} the development of suitable carrier systems for (synthetic) siRNA targeted towards specific disease relevant

genes became of great interest. Despite their high efficiency for siRNA delivery, viral vectors are limited in application due to possible inflammatory and immunogenic responses.³³ Therefore, the design of novel non-viral delivery strategies is a rapidly growing field. Among them, the direct chemical modification of siRNA³⁴ as well as loading the cargo into carrier systems such as nanoparticles have been widely studied. Polymeric nanoparticles consisting of biodegradable or biocompatible polymers like chitosan have been successfully used for the delivery of siRNA into the lungs of mice in order to silence GAPDH or EGFP.^{35, 36} Another approach for the development of non-viral siRNA delivery vectors is inspired by naturally occurring structures such as eukaryotic membranes. Systems based on self-assembled structures out of amphiphilic molecules are the most prominent and well-studied siRNA carriers.³⁷

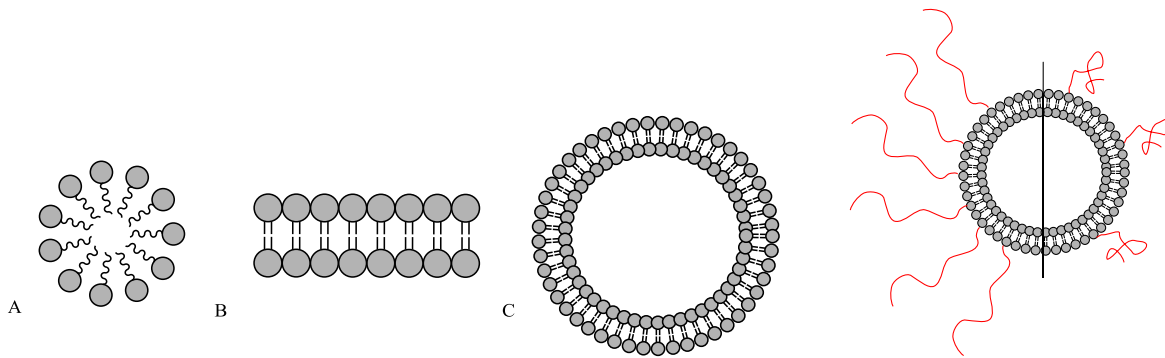
An important example for such amphiphilic molecules are natural occurring lipids.³⁸ Up to a certain concentration, these lipids are soluble on a molecular level in water, but above a critical concentration aggregates are formed.³⁹ In order to minimize the repelling interactions with water the hydrophobic tails cluster together while the hydrophilic heads repel each other due to sterical and electrostatic hindrance. This way, three dimensional assembled structures like micelles, bilayers, or vesicles are formed (Figure 3b).⁴⁰

If composed of (phospho-)lipids (Figure 3a), the latter ones are also usually called liposomes⁴¹⁻⁴³ and can be both single-component systems and multi-component systems, which means that other molecules like for example cholesterol are also incorporated. This is also the case for the natural cell membrane, where cholesterol plays an important role for the membranes viscosity according to the fluid mosaic model from Singer and Nicholson.⁴⁴

a)



b)



c)

Figure 3. a) Schematic structure of left) phosphoglycerides and right) sphingophospholipids with the polar head (orange) and the apolar tail (blue); b) schematic 3D structure of self-assembled lipids with A) micelle, B) bilayer and C) vesicle; c) PEG modification of liposomes with high density (left) and low density (right). reprinted from *Biochemical and Biophysical Research Communications*, Volume 468, Issue 3, Laura K. Müller, Katharina Landfester, “Natural liposomes and synthetic polymeric structures for biomedical applications”, Pages 411-418, Copyright © (2015), with permission from Elsevier.

Due to their structure shown in Figure 3b, liposomes allow the encapsulation of a high variety of drugs such as hydrophilic (inside the core), hydrophobic (in the hydrophobic part of the membrane) as well as amphiphilic molecules (as part of the membrane). The loading of siRNA cargo into “man-made” liposomes is a very prominent strategy²² due to the biocompatibility of the constituents and the simple preparation by only mixing the different components. “Lipoplexes”, which are formed due to electrostatic interactions between positively charged lipids and the negatively charged siRNA,²⁰ were identified to enhance the efficiency of siRNA delivery in contrast to using naked siRNA.⁴⁵ Numerous studies on cationic lipidic vectors have been reported,⁴⁶ among them 1-oleoyl-2-[6-[(7-nitro-2-1,3-benzoxadiazol-4-yl)amino]hexanoyl]-3-trimethylammonium propane

(DOTAP)⁴⁷ or N-[1-(2, 3-dioleoyloxy)propyl]-N,N,N-trimethylammonium chloride (DOTMA).⁴⁸ A major drawback of using cationic lipids is the potential undesired interaction with negatively charged serum proteins as well as possible inflammation response.⁴⁹⁻⁵¹ The addition of cholesterol or other neutral lipids such as distearoyl phosphatidylcholine (DSPC)⁵² to lipoplexes in order to form multi-component liposomes is a successful method to overcome the above mentioned problems.^{53, 54} In addition, cholesterol offers the opportunity of simple modification strategies with for example ligands. Another approach to circumvent the described drawbacks is the surface modification of liposomes with poly(ethylene glycol) (PEG) (see Figure 2c).⁵⁵ The conformation of PEG on a liposomes' surface is dependent on many factors such as density of the grafted polymer mirroring the available space the polymer chains can capture.⁵⁶ In case of low grafting density, each PEG chain has enough space to be in coiled-structures, but when the grafting density is increased, the chains are forced to elongate due to the steric hindrance between two chains. In the presence of this highly biocompatible polymer, reduced aggregation as well as prolonged blood circulation time of liposomes was obtained.⁵⁷⁻⁵⁹ The so-called "stealth-liposomes"⁶⁰ already found their way into clinical use.^{61, 62} The most prominent and commercially available among them is DoxilTM, which is a liposomal formulation with doxorubicin (DOX) as drug for anticancer treatment.^{63, 64} Doxorubicin belongs to the group of anthracyclines that have an antineoplastic effect but also cause several side effects like for example cardiotoxicity.⁶⁵ Encapsulation of DOX in liposomes was found to reduce the drug accumulation in heart and to increase its localization in tumor cells.⁶⁶ The latter feature was contributed mainly to the prolonged half-life in blood circulation of the PEGylated liposomal system.^{66, 67}

According to the fact, that neutral lipids and PEG-modified ones are limited in electrostatic interactions with siRNA, the formulation of more complex systems needs a little more effort than just mixing the components. Among the several approaches, the lipid film method is the most prominent one in order to synthesize highly PEGylated liposomes.³⁷ In principle, a dried thin lipid film with all liposomal components is dissolved with a concentrated siRNA solution.⁶⁸ Downsizing and size-control can further be done by sonication⁶⁹⁻⁷¹ or by extrusion through a polycarbonate membrane with defined pore sizes.⁷²

The synthesis of lipids often requires multiple steps and several purification methods.⁷³ Therefore Langer and Anderson developed a new class of “lipidoids”⁷⁴ which are lipid-like materials, that can be synthesized rapidly. A combinatorial library was provided and the new components screened in animal models regarding efficiency and safety for siRNA delivery. By this, a formulation was identified that allows low-dose gene silencing in the liver of mice.⁵² According to Langer and Anderson, the advantage of low-dose gene-silencing would be the reduced amount of carrier material injected intravenously or the possibility of multiple gene-silencing with only one intravenous administration within the tolerability of the carrier materials. It was shown, that simultaneous silencing of five hepatocellular gene targets in C57BL/6 mice is possible. The fact, that low-dose gene-silencing could also be achieved in non-human primates (*Cynomolgus* monkeys), paves the way for safe and effective siRNA delivery.⁵² In recent studies, the lipid-like materials were advanced to co-deliver siRNA and pDNA for the combined application of gene silencing and expression.⁷⁵ 1,3,5-Triazine-2,4,6-trione (TNT) lipid derivatives were identified, that encapsulated more than 99% of siRNA as well as pDNA. Injection of luciferase pDNA and Tie2 siRNA in C57BL/6 mice resulted in simultaneous gene expression and silencing. This could be of great interest for future treatment of diseases that are related to the disordered function of several genes.

An approach towards understanding and ranking the efficiency of lipid-based siRNA delivery systems was made by Zhang *et al.*, who developed an *in vitro* assay that is based on the delivery pathway liposomal systems are believed to undergo after intravenous injection⁷⁶ including distribution, cell uptake ending in endosomes and siRNA release. The different stages *in vivo* were mimicked by for example incubating the lipidic systems with anionic liposomes mirroring endosomal escape and the amount of released siRNA was quantified. It turned out that with increasing amount of anionic liposome add-on to the cationic liposomes under investigation, the siRNA release was increased drastically at pH=6 (mimicking endosomal environment), whereas the siRNA release only slightly increased at pH=7.5.⁷⁶ 16 liposomal systems were investigated with the introduced *in vitro* assay regarding the siRNA release. The percentage of siRNA release out of the different liposomal systems after incubation in rat serum correlated nicely with the effectiveness of the respective system regarding the *in vivo* knockdown of ApoB at mRNA level in Sprague-

Dawley female rats, offering the possibility of identifying promising systems prior to *in vivo* evaluation.

The interaction of cationic liposomes for siRNA delivery with anionic liposomes at physiological pH points towards a well-known problem of liposomal drug delivery in general. The composition of the lipid shell varies due to interactions and exchange with other lipids. This phenomenon is originated in the highly dynamic equilibrium between lipids in solution and lipids incorporated in the designed liposomes as well as the high similarity of the designed liposomes to naturally occurring systems like for example LDL and HDL also containing for instance cholesterol.

Effort towards solving this and enhancing the stability of the described delivery systems was taken by Aigner and coworkers, who combined liposomal systems with polymers in order to design “lipopolyplexes” for DNA or siRNA delivery.⁷⁷

2.3 PROTEIN CORONA

Many approaches have been made towards the use of nanoparticles for biomedical applications. The synthetic identity of a nanomaterial designed in the lab plays an important role when it comes to the cellular uptake of the system. Lerch *et al.* investigated the correlation between the size of NPs and the effectiveness of overcoming the cell membrane barrier.⁷⁸ But also the material's shape⁷⁹ as well as surface charge⁸⁰ influence the cellular uptake.

As already mentioned, most drug delivery systems are applied intravenously. This means that they come into contact with blood and its components in the first place. As soon as a nanoparticle enters the blood stream it is rapidly covered with surrounding proteins that adsorb onto the material's surface. This protein layer is called protein corona and it has become more and more clear that it defines the biological identity of a given material significantly.⁸¹⁻⁸⁵

The transformation of a nanomaterial's chemical identity into its biological identity is illustrated in Figure 4.

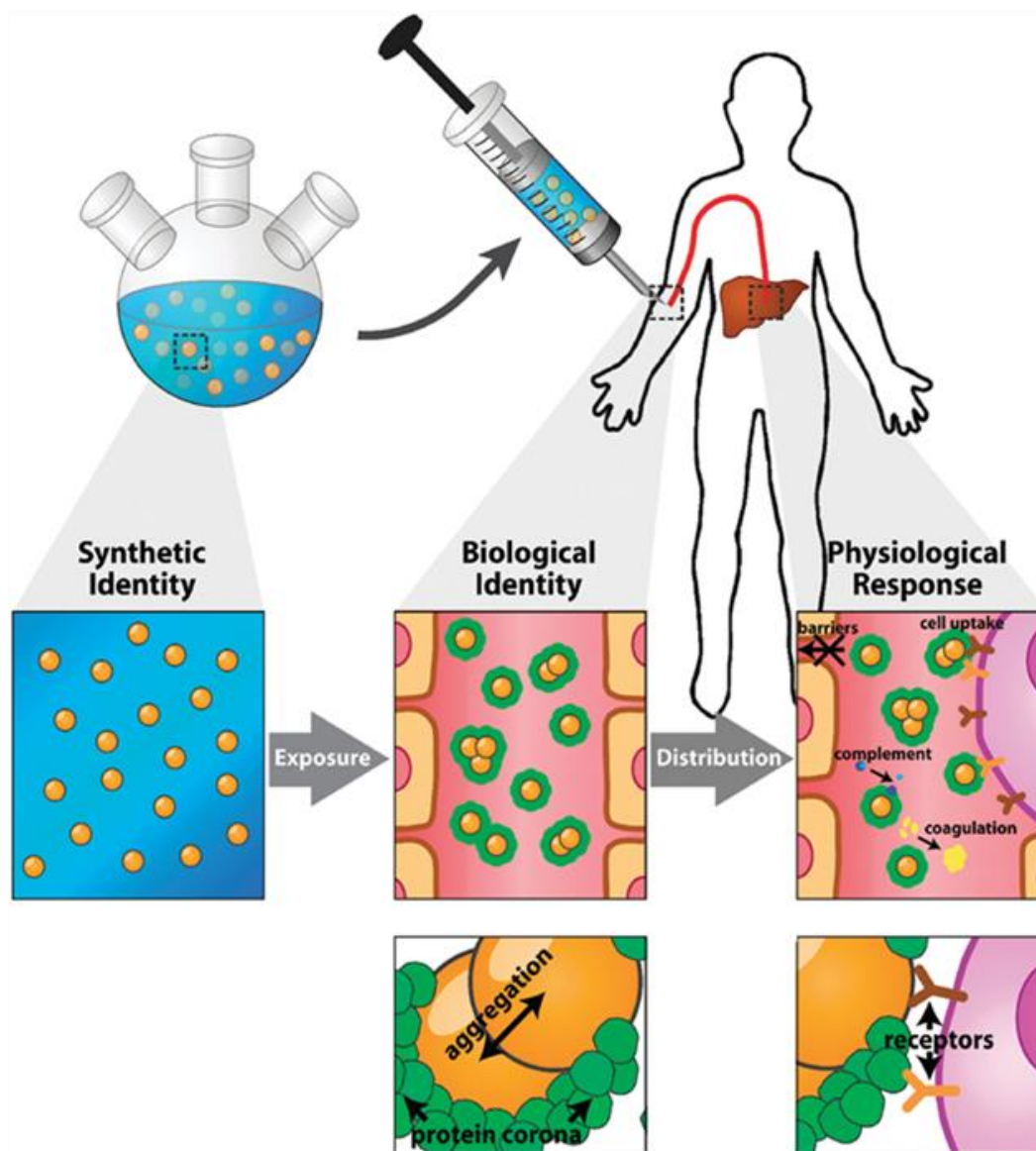


Figure 4. Chemical versus biological identity of a nanomaterial after intravenous injection.⁸⁶ Adapted from “Walkey, C. D.; Chan, W. C. Understanding and controlling the interaction of nanomaterials with proteins in a physiological environment. *Chem. Soc. Rev.* 2012, 41, 2780-2799.” with permission of The Royal Society of Chemistry.

The protein corona can be divided up into two parts, the so-called “hard” and “soft” corona.⁸⁷ Both differ in the binding strength of proteins and thus their exchange times between the adsorbed and dissolved state.⁸⁸ High abundance proteins adsorb onto a nanomaterial’s surface rapidly due to their availability. But it is already known that those proteins are more and more replaced by proteins with a higher affinity. This effect is known in literature as Vroman effect, who studied the subsequent replacement of fibrinogen by other proteins on flat surfaces.^{89, 90}

The change from flat surfaces towards curved surfaces as in the case for nanoparticles leads also to changes in protein interactions.⁹¹ Cedervall *et al.* investigated the adsorption of HSA on *N*-isopropylacrylamide:*N*-*tert*-butylacrylamide copolymer nanoparticles with different sizes representing different surface curvatures.⁹² It turned out, that the equilibrium association constant of HSA is independent of the nanoparticles' size, but the amount of protein that is needed to reach saturation differs in relation to the particle size and with this the surface curvature. The more hydrophobic surface is available for protein interactions, the number of bound protein molecules increases.

As a nanomaterial is body-foreign material, macrophages as part of the immune system play a critical role in the blood circulation time of the carrier system. Proteins within a nanomaterial's protein corona that enhance the uptake of the reticuloendothelial system are referred to as "opsonins".^{93,94} One example for opsonins is IgG. Lunov *et al.* showed, that IgG-adsorption onto polystyrene particles (PS) initiates phagocytosis by human macrophages.⁹⁵ HSA and apolipoproteins on the other hand are often referred to as dysopsonins, that enhance the circulation time of a nano carrier.⁹⁶

The type of interactions between nanoparticles and proteins can be electrostatic as well as hydrophobic. Roser *et al.* investigated the interactions of surface-modified albumin spheres with human serum in regards of phagocytosis and bio-distribution.⁹⁷ With this a direct correlation of surface charge and protein adsorption was shown. But more and more it became clear, that the main driving forces for protein adsorption are hydrophobic interactions. In general, hydrophobic particles show increased protein coverage compared to hydrophilic particles.^{98,99}

It is already known, that the adsorption of proteins on a nanomaterials surfaces can induce conformational changes.¹⁰⁰ With this, their enzymatic activity can be lost¹⁰¹ or binding sites for other proteins can be hidden. Norde *et al.* monitored the structural changes of bovine serum albumin (BSA) between the adsorbed and dissolved state.¹⁰² Structural changes of the protein during adsorption on hydrophilic silica particles haven been found to be reversible, meaning it regained its native structure when dissolved again. On the other hand, the adsorption of BSA onto hydrophobic polystyrene nanoparticles has been found to be irreversible leading to changes in the secondary structure of the respective protein.

The proteins present in biological fluids are in consequence of enzymatic or chemical reactions glycosylated in high amounts. This means, that carbohydrates are covalently attached to them. Recently, Wan *et al.* analyzed the role of glycans present in a protein corona on nanoparticle-cell interactions.¹⁰³ The removal of carbohydrates from a given protein corona was found to increase cell membrane adhesion as well as cell uptake of SiO₂ NPs.

As already mentioned, particle size and surface charge influence a nanomaterial's body-distribution and cellular uptake. The adsorption of proteins leads to an increase in size and a coverage of initial particle surface charge. Thus it is obvious, that the protein composition on a NP strongly influences its body-distribution. Taken this together with the concept of opsonization, many efforts have been made towards surface modification of nanomaterials in order to reduce protein adsorption.

2.3.1 THE STEALTH EFFECT

The surface modification with protein repellent substances is a wide-spread method in order to decrease the degree of opsonization and to increase the time in blood-circulation of nanoparticles. As opsonization and adsorption of proteins is increased on hydrophobic nanomaterials, hydrophilic molecules have been used for modification. The most prominent example is poly (ethylene glycol) (PEG). By PEGylation, a nanomaterial is masked against rapid immunological responses.¹⁰⁴ The resulting materials are therefore also termed "stealth" materials.¹⁰⁵ The modification can be done either by covalently attaching PEG or also by adsorption of polymer chains onto the nanomaterial's surface.¹⁰⁶ As already described for liposomes, the degree or surface density of PEG has consequences on its 3D structure and with this also on protein corona formation.¹⁰⁴ With increasing density of PEG chains, the protein adsorption was found to be reduced but not completely prevented.

Schöttler *et al.* recently showed, that the presence of distinct proteins within the protein corona of stealth materials is even required and necessary in order to prevent un-specific cellular uptake of nanomaterials.¹⁰⁷ Clusterin, which is also termed apolipoprotein J, was

identified to play a major role in the stealth effect. PEGylated stealth particles were found to be taken up by macrophages in similar range as non-PEGylated particles when no proteins were present. Only in the presence of plasma, the unwanted uptake of stealth materials could be completely inhibited, while the non-PEGylated control-particles showed no significant change in cellular uptake behavior. This opens new possibilities when it comes to surface modification of nanomaterials. Not only the attachment of polymers, but also the modification with specific proteins could be promising candidates in order to make “stealth” materials.

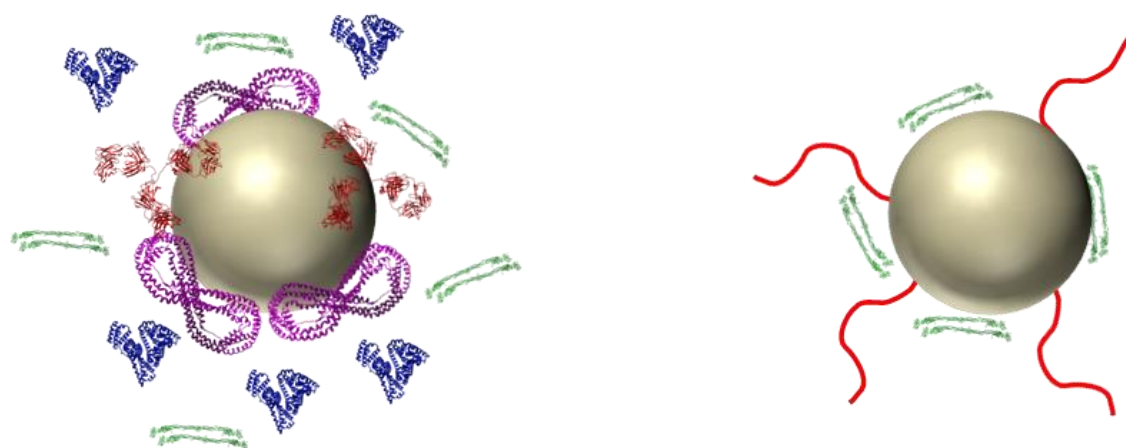


Figure 5. Protein adsorption on stealth-materials (right) is reduced in comparison to non-modified NPs (left).

2.4 PROTEIN CORONA ANALYSIS

Due to the fact that the protein corona can be divided up into the soft and the hard corona, which differ in the binding strength of present proteins, the analysis of protein-particle interactions strongly depends on prior sample preparation.¹⁰⁸

In general, the protein corona formation is usually carried out by introducing a certain surface area of nanomaterial into a respective protein source like human blood plasma or serum. After incubation, some methods like isothermal titration calorimetry (ITC), dynamic light scattering (DLS) or asymmetric flow – field flow fractionation (AF-FFF) are suitable methods to analyze the soft corona as no washing steps are needed prior to

analysis. On the other hand, methods like liquid chromatography-mass spectrometry (LC-MS), SDS polyacrylamide gel electrophoresis (SDS-PAGE) or protein quantification within the corona require the removal of unbound proteins. This can either be done by centrifugation of the particle protein mixture or by separation via a magnetic field. The latter one is limited to magnetic particles. Depending on the binding strength of proteins within the corona, the shear forces applied for separation of unbound proteins lead also to a removal of weakly bound proteins of the soft corona and with this to an altering of corona composition. This is illustrated in Figure 6.

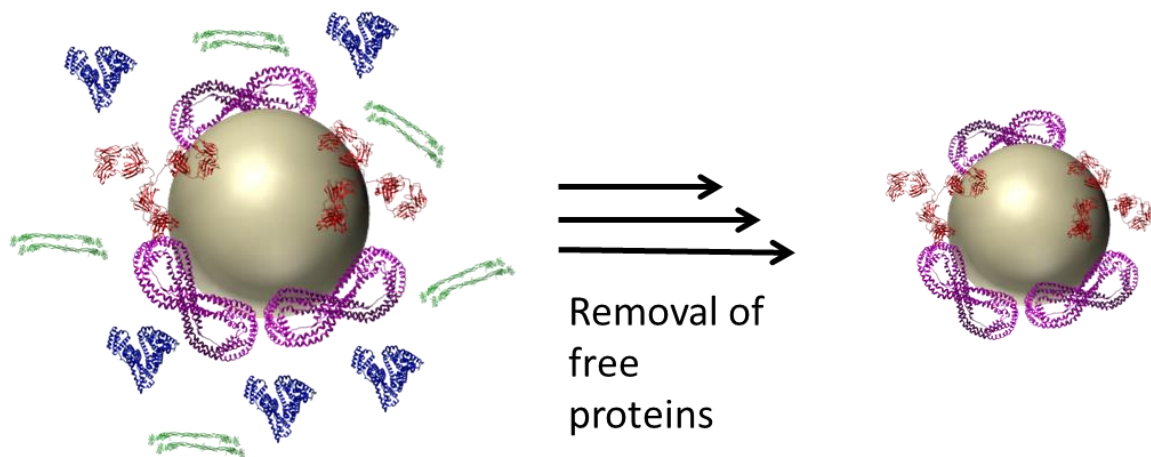


Figure 6. Soft vs. hard corona obtained by the removal of free proteins using for instance centrifugation or magnetic separation.

2.4.1 *IN SITU* ANALYSIS

2.4.1.1 ISOTHERMAL TITRATION CALORIMETRY

Isothermal titration calorimetry is a technique that monitors heat changes that occur during adsorption of proteins on a nanomaterials surface.^{109, 110} In principle, two measurement cells are isolated by a mantle in order to keep the temperature constant. One cell, the measurement cell, is equipped with one component like the nanomaterial under investigation, while the second cell serves as reference cell. The temperature of both cells is kept constant during the whole measurement. When a second component under investigation like a protein solution is added stepwise in the measurement cell, a

temperature change occurs in case there is some interaction between both components. This temperature change can be detected and adjusted. ITC is a method that therefore allows to determine binding thermodynamics between proteins and nanomaterials.

2.4.1.2 FIELD FLOW FRACTIONATION

Asymmetric flow – field flow fractionation (AF-FFF) is a chromatography like technique. This method is suitable for the separation and size determination of polymers and colloids in solution. In principle, a laminar flow is applied between two parallel plates in a thin channel. This leads to a parabolic flow profile. Is now a cross flow applied that acts perpendicular to this flow, particles or molecules introduced into the channel are pushed against the so called accumulation wall. This leads to a higher local concentration of particles at the wall and thus induces diffusion of particles in the opposite direction. According to their diffusion coefficients, particles with different sizes are located with different distances from the accumulation wall and can therefore be separated.

Tsai *et al.* used AF-FFF together with complementary techniques in order to investigate the adsorption and conformation of bovine serum albumin (BSA) on gold nanoparticles (AuNP). Here, the method was applied in order to fractionate possible agglomerates after BSA and AuNP conjugation. The size-determination of every fraction could be correlated with results obtained from dynamic light scattering.¹¹¹

2.4.1.3 DYNAMIC LIGHT SCATTERING

As dynamic light scattering (DLS) is an often used method within this work, it will be described in more detail.

Dynamic light scattering in general is a method that determines the size of a given species by using the diffusion of molecules in solution. At each scattering angle during the measurement a given scattering volume is under investigation. Due to the already mentioned diffusion of molecules, they diffuse in and out of the observation volume. This

leads to a fluctuation in scattering intensity over time, which is the detected measurand. An auto-correlator converts the signal into an autocorrelation function (ACF) of scattering intensity:

$$g_2(q, t) = \frac{\langle I(q, t)I(q, t+\tau) \rangle}{\langle I(q, t)^2 \rangle} \quad (1)$$

$I(q, t)$ is the time dependent scattering intensity that gets multiplied with the scattering intensity $I(q, t+\tau)$ that is shifted by the time τ . With the Siegert equation,¹¹² that gives the relation between equation (1) and the experimentally measurable field autocorrelation function $g_1(q, t)$, equation (2) is valid for a given scattering vector q :

$$g_1(t) = \sqrt{\frac{g_2(t) - A}{A}} \quad (2)$$

In equation (2) A describes the experimentally determined baseline. For monodisperse particles, the autocorrelation function $g_2(q, t)$ can be described as a simple exponential decay:

$$g_2(q, t) = A \times e^{(-q^2 D t)} \quad (3)$$

The diffusion coefficient D is related to the inverse correlation time Γ :

$$\Gamma = \frac{1}{\tau} = q^2 D \quad (4)$$

For disperse samples, an averaged diffusion coefficient is determined, that is dependent on the scattering angle q . Therefore, the true value has to be calculated by extrapolating $q \rightarrow 0$. With the use of the Stokes-Einstein equation, the z-averaged hydrodynamic radius R_h can be obtained from the extrapolated diffusion coefficient D_z :

$$\left\langle \frac{1}{R_h} \right\rangle_z^{-1} = \frac{kT}{6\pi\eta D_z} \quad (5)$$

When the temperature T and the solvent's viscosity η are known, the hydrodynamic radius can be obtained. The ratio of radius of gyration obtained from static light scattering

and the hydrodynamic radius obtained from dynamic light scattering gives information about the geometry of the system under investigation:

$$\rho = \frac{\sqrt{\langle R_g^2 \rangle_z}}{\langle \frac{1}{R_h} \rangle_z^{-1}} \quad (6)$$

Table 1 sums up the geometry for different ρ -ratios.

Table 1. ρ -ratios and their corresponding geometry for macromolecules.¹¹³

ρ -ratio	geometry
0.778	Homogeneous sphere
1.00	Monodisperse vesicle
1.50	Monodisperse Gaussian coil, Θ condition
1.78	Monodisperse Gaussian coil in good solvent
1.73	Polydisperse Gaussian coil, Θ condition
2.05	Polydisperse Gaussian coil in good solvent
>2	Rigid rod

2.4.1.3.1 LIGHT SCATTERING OF MULTICOMPONENT SYSTEMS

In this work, the software HDRC was used for the evaluation of dynamic light scattering data obtained from multicomponent analysis. The software from Oliver Nirschl¹ uses the

¹ Oliver Nirschl, Diploma Student of Professor Dr. Manfred Schmidt, Mainz, 2007

simplex algorithm (downhill-simplex) in order to describe non-linear functions that depend on several parameters.

HDRC was used in this work in order to evaluate light scattering data from a mixture that contains two components, namely nanoparticles and proteins in form of serum/plasma. Data were evaluated by applying the method according to Rausch *et al.*¹¹⁴ Briefly, the autocorrelation function of the particles under investigation can be described by a sum of two exponentials (7) whereas the autocorrelation function (ACF) in the case of human plasma/serum can be perfectly fitted by a sum of three exponentials (8) with the amplitude a_i , the Brownian diffusion coefficient D_i and the decay times $t_i=1/(q^2D_i)$:

$$g_{1,np}(t) = a_{1,np} * \exp\left(-\frac{t}{\tau_{1,np}}\right) + a_{2,np} * \exp\left(-\frac{t}{\tau_{2,np}}\right) \quad (7)$$

$$g_{1,p}(t) = a_{1,p} * \exp\left(-\frac{t}{\tau_{1,p}}\right) + a_{2,p} * \exp\left(-\frac{t}{\tau_{2,p}}\right) + a_{3,p} * \exp\left(-\frac{t}{\tau_{3,p}}\right) \quad (8)$$

If the ACF of human plasma or the protein mixture (8) and the one of the respective particle (1) are known, the mixture of both can be studied. If no aggregation occurs, both components in the resulting mixture co-exist and the corresponding ACF can be described as the sum of the two individual ACFs with known parameters for the two mixture-components (9) named as force fit:

$$g_{1,m}(t) = f_p g_{1,p}(t) + f_{np} g_{1,np}(t) \quad (9)$$

f_p represents the intensity contribution of plasma/protein mixture while f_{np} describes the one of the nanoparticle. If the interactions of plasma proteins with particles result in larger sizes, the resulting mixture can no longer be described as a co-existence of the individual compounds and an additional term to describe the ACF (10) is needed with the intensity contribution f_{agg} of the newly formed species within the mixture under investigation and the unknown relaxation $t_{1,agg}$ (11):

$$g_{1,m}(t) = f_p g_{1,p}(t) + f_{np} g_{1,np}(t) + f_{agg} g_{1,agg}(t) \quad (10)$$

$$g_{1,agg} = a_{1,agg} * \exp\left(-\frac{t}{\tau_{1,agg}}\right) \quad (11)$$

The above described method was first introduced by Rausch *et al.* in 2010.¹¹⁴ In 2014, a work was presented, that correlates the results obtained from dynamic light scattering with the *in vivo* body distribution of polystyrene nanoparticles in mice.¹¹⁵ Nanoparticles that formed aggregates accumulated in the liver of mice, while stable particles with no significant size increase were distributed over the whole mice body due to their blood circulation.

2.4.1.4 FLUORESCENT CORRELATION SPECTROSCOPY

Fluorescent correlation spectroscopy (FCS)¹¹⁶ is in principal very similar to DLS, but in contrast the intensity fluctuation of a fluorescence signal is detected. Röcker *et al.* used this technique in order to analyze the adsorption of HSA on small polymer-coated nanoparticles.¹¹⁷ The limitation of this method is obvious. While with dynamic light scattering every species within a mixture can be detected, FCS only observes fluorescence labelled species.

2.4.2 HARD CORONA ANALYSIS

The methods described in the following have the requirement of removing unbound proteins and can therefore not be performed *in situ*. Thus, only the hard corona with strongly bound proteins is under investigation.

For analysis, the proteins have to be detached from the particle surface via add-on of anionic detergents like sodium dodecyl sulfate (SDS), urea or thiourea.

The amount of proteins present in a nanomaterial's hard corona can be determined afterwards by using assays that are based on calorimetric quantification like the BCA protein assay. The assay is based on the protein quantification with bichinonic acid (BCA) and is a combination of biuret reaction and complexation of copper (I) ions with BCA.¹¹⁸ The BCA complex has an adsorption maximum at 562 nm and can therefore be used for protein quantification as its amount is directly proportional to a present protein amount.

2.4.2.1 SDS POLYACRYLAMIDE GEL ELECTROPHORESIS

A first idea of the composition of a protein corona under investigation can be obtained by using SDS polyacrylamide gel electrophoresis (SDS-PAGE). The method is based on the separation of proteins according to their molecular weight when an electrical field is applied. To ensure the separation of proteins only according to their molecular weight, other factors that may interfere have to be reduced. Therefore, the tertiary structure of proteins is destroyed prior to analyzing them via gel-electrophoresis. This is done by the adding of SDS¹¹⁹ and a reducing agent for the reduction of disulphide bonds. In addition, SDS guarantees the coverage of protein charges resulting in a negative charge that is directly proportional to the peptide chain length. The denaturated proteins are deposited onto a polyacrylamide gel. When voltage is applied, the proteins migrate through the gel in the direction of the anode according to their negative charge. The gel acts like a filter allowing small molecules to diffuse faster than big molecules.

After the successful separation of proteins, the protein pattern that has been formed on the gel can be visualized by different staining procedures. The most common ones are the silver staining and the staining with Commassie brilliant blue.

The drawback of the described method is the limited resolution. Proteins with similar molecular weights co-migrate through the gel and can therefore not be separated. That makes it very difficult to identify single proteins. Nevertheless it is a suitable method for the comparison of different protein patterns.

In order to increase the separating capacity, the SDS-gel electrophoresis can be done in two dimensions¹²⁰ or extended to western blotting. But the most powerful tool to identify proteins within a certain corona so far is the combination of liquid chromatography with mass spectrometry.

2.4.2.2 LIQUID CHROMATOGRAPHY-MASS SPECTROMETRY

As already said, this method is a combination of liquid chromatography (LC) and mass spectrometry (MS). Prior to analysis, the proteins need to be digested into smaller

fragments. This can be done by adding the protein trypsin.¹²¹ The peptide-mixture can afterwards be separated in a first step by liquid chromatography. This chromatography method is based on the dissolving of analytes in a liquid phase. The liquid phase afterwards passes a stationary phase that can either be hydrophilic or hydrophobic (reversed phase). The separation principle is based on the adjustment of an equilibrium in interactions of the analytes with both mobile and stationary phase. The analytes are therefore separated according to their hydrophobic or rather hydrophilic character. After a first separation, the analytes, in this case peptide fractions, can be transferred into a mass-spectrometer for further separation. Mass spectrometry is a powerful tool in order to separate analytes according to their mass to charge ratio. This indicates that the analytes have to be ionized prior to separation. For proteins, the electro-spray ionization (ESI) is a widely used method, as it is a suitable tool to ionize macromolecules. In principle, a solution of analytes passes a capillary, on whose end an electric field is applied. Ions within the analyte solution are attracted by the counter-electrode. A so-called Taylor-cone forms at the end of the capillary in which ions repel each other. Due to the repulsion, an aerosol of ions in solvent is formed. While the solvent evaporates, the droplets are scaled down, which again leads to repulsion between single ions within one droplet. This leads to a decay into smaller droplets. At the end of the cascade, single ions are obtained in the gas phase that can afterwards be analyzed according to their mass to charge ratio. There are different types of analyzers like a time of flight (TOF) analyzer or a quadrupole. The first one accelerates ions by an electric field of known strength. This acceleration results in the same kinetic energy for ions with the same charge. The velocity of the ions depend on the mass-to-charge ratio, meaning that the time a particle needs to reach the detector gives the mass to charge ratio of the ion when the experimental parameters like distance are known. Quadrupoles consists of four rod-electrodes that are ordered parallel, while each opposing rod pair is connected together electrically. In addition, a superimposed high frequency alternating current voltage is applied, leading ions to travel down the quadrupole between the rods. Only ions with a specific mass to charge ratio can reach the detector, as the trajectory of every other m/z -ratio is unstable and thus the ions collide with the electrodes. By varying the potentials of the electrodes and the superimposed high frequency alternating current voltage, the ions are consecutively guided through the quadrupole according to their mass to charge ratio. The combination of three quadrupoles in series allows the detection of MS/MS spectra, which means, that ions, that are

separated in a first quadrupole can be fragmented further on and again be separated according to their mass to charge ratio with the third quadrupole. The second quadrupoles serves for the fragmentation. When the third quadrupole is replaced by a TOF analyzer, the system is called Q-TOF and is part of the setup that was used to perform LC-MS measurements shown in this work.

The detected mass to charge ratios can be compared to a database that allows the identification of distinct proteins or protein fragments.

Tenzer *et al.* used label-free quantitative LC-MS in order to obtain time-resolved profiles of corona formation on silica and polystyrene nanoparticles.¹²² Nanoparticle-specific coronas were found to form rapidly, that change only in the amount of adsorbed protein but not in the protein composition.

LC-MS also allowed the already mentioned determination of distinct proteins, that play a critical role in the stealth effect.¹⁰⁷

2.4.2.3 ZETA-POTENTIAL

The zeta potential or electric potential of a diffusing particle in solution mirrors the surface charge of the respective particle under investigation and can thus also provide information about possible protein adsorption.

When charged particles are in solution, ions with the opposite charge present in the suspension medium attach at the particles' surface. Further ions arrange loosely around the first ion layer and form a diffuse layer. When an electrical field is applied, the particles will move according to their charge. Ions in the diffuse layer are sheared off building up a potential that is called zeta potential ζ . Under similar conditions, the zeta potential can be used as measurand for a particle's surface potential. 1 mM potassium chloride solution is usually used as suspension medium. When an electrical field is applied, ions in suspension diffuse according to their charge, while the diffusion speed is depending on the particle size. The so-called electrophoretic mobility can be transferred into the zeta potential by using the Smoluchowsky¹²³ equation:

$$u_E = 4\pi\varepsilon_0 \times \frac{D\zeta}{4\pi\eta} = \frac{\varepsilon\zeta}{\eta} \quad (12)$$

Here u_E stands for the electrophoretic mobility, η for the viscosity, ε for the dielectric constant and D for the diffusion coefficient.

As the majority of the plasma proteins is negatively charged, the adsorption of proteins onto a nanomaterial's surface results in a change of the zeta potential to negative values even if the particle itself is positively charged.¹²⁴ For example Baier *et al.* monitored the BSA adsorption on differentially charged polystyrene nanoparticles via zeta potential measurements.¹²⁵

2.5 AIM OF THIS WORK

The aim of this work is to get a better understanding of nanoparticle protein interactions and how these interactions can be useful for further biomedical applications. Therefore single proteins as well as low abundant protein mixture were obtained by the fractionation of human plasma. Their influence on nanoparticle stability and effect on cellular uptake was investigated. By the combination of dynamic light scattering under *in vivo* conditions and the protein identification via LC-MS, single proteins could be identified, that play a role in protein corona formation and stabilization of respective particles under investigation against aggregation. Critical steps in the evaluation of novel nanomaterials for biomedical application like the universal validation of protein corona studies when examining single probands as well as the transfer from *in vivo* animal models to humans were investigated.

In general, protein particle interactions are very complex and depend on many factors. Therefore studies are often based on phenomenological observations while a physicochemical description remains difficult. In this work, the analysis of protein induced aggregation of nanoparticles using dynamic light scattering is also based on phenomenological studies. The process of observed aggregation can involve nanoparticle bridging, the adsorption of proteins and protein-protein aggregates on the nanomaterial's surface. By combining dynamic light scattering with fluorescent correlation spectroscopy,

one basic approach towards understanding the processes involved in protein induced aggregation of nanoparticles was made.

3 RESULTS AND DISCUSSION

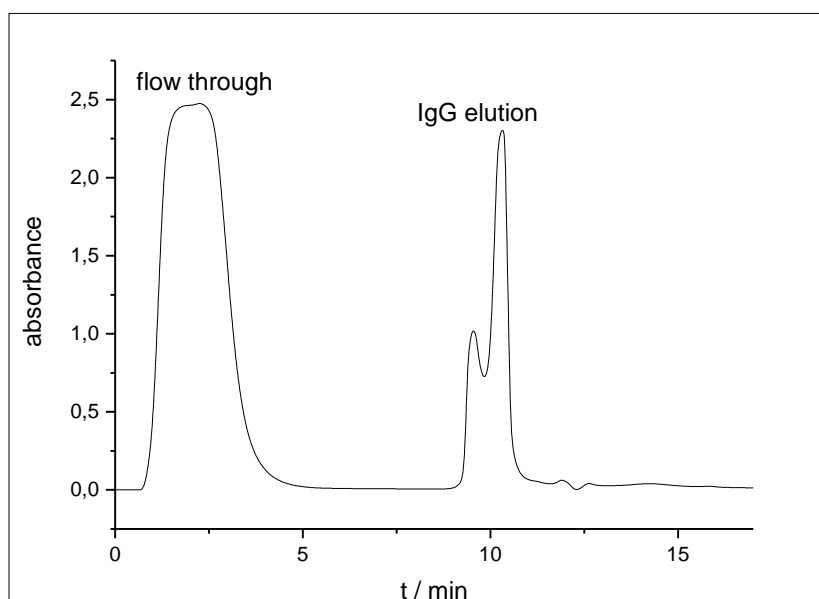
The results part of this work is divided up into seven parts. After presenting the different protein mixtures that were obtained by fractionation of human plasma, the interactions of the respective protein fractions with polystyrene particles as model system were investigated. Afterwards, a short overview of the impact of different protein sources like human blood serum or plasma on pre-*in vivo* studies is given. In the fourth and fifth chapter, the difference in blood serum composition of individual probands as well as the protein composition of the corona of stealth materials were utilized for particle stabilization against aggregation. In chapter six, the transferability of different *in vivo* models on humans is discussed. In the last section, the model system of polystyrene particles is changed towards the investigation of multifunctional liposomes for biomedical applications.

3.1 FRACTIONATION OF HUMAN BLOOD PLASMA

As already described in the introduction, human serum albumin and IgG are very abundant in human plasma. Thus, these proteins adsorb onto an introduced nanomaterial's surface in the first place. But over time, the proteins are replaced by proteins with higher affinities. The interactions of low abundant proteins with nanoparticles are therefore of great interest in order to get a better understanding of protein corona formation and particle stability under physiological conditions. Plasma fractionation is a widely used process to enrich specific components from human plasma like IgG and was utilized in this work in order to deplete human blood plasma from the two most abundant proteins. Highly complex protein mixtures with various low abundant proteins were created and could be used for the investigation of particle-protein interactions. As already defined in the introduction, the human blood proteome can be either obtained as plasma or serum, depending on the preparation method. In contrast to serum, plasma contains also the proteins that are part of the coagulation process. As the low abundant proteins play a major role in this study, human blood plasma stabilized with citrate (and not serum) was chosen for the fractionation. A detailed study on the different protein sources for pre-*in vivo* studies will be given in chapter 3.3.

In this work, three different columns were used for the isolation of single proteins as well as various low abundant protein mixtures in order to investigate their influence on protein nanomaterial interactions. Two of them are based on affinity chromatography and were used for most questions discussed in further chapters. The third one is predicated on anion-exchange chromatography.

For the separation of IgG a ToyoSreen AF-rProtein A HC-650F column was used. The column consists of a resin with immobilized Protein A that binds to the heavy chain of IgG. This way IgG, similar proteins and IgG-bound proteins are retained, while the other ones flow through the column. By the addition of citric acid, the interactions of IgG and Protein A are disrupted and IgG can be eluted from the column. Figure 7 shows the chromatogram of the IgG separation from human plasma. According to protein quantification via BCA Assay, 93% of the total amount of injected proteins could be recovered. 15% of the total eluted amount consists of IgG.



sample	Concentration g/L	Amount / mg	Amount / %
injection	22	11	100
Flow Through	5.7	8.6	78
IgG	1.7	1.7	15

Figure 7. Chromatogram of IgG separation via Protein A column and the corresponding protein amount in the fractions according to a BCA Assay.

The efficiency of IgG removal was investigated via LC-MS and SDS-PAGE. Figure 8 shows the according results.

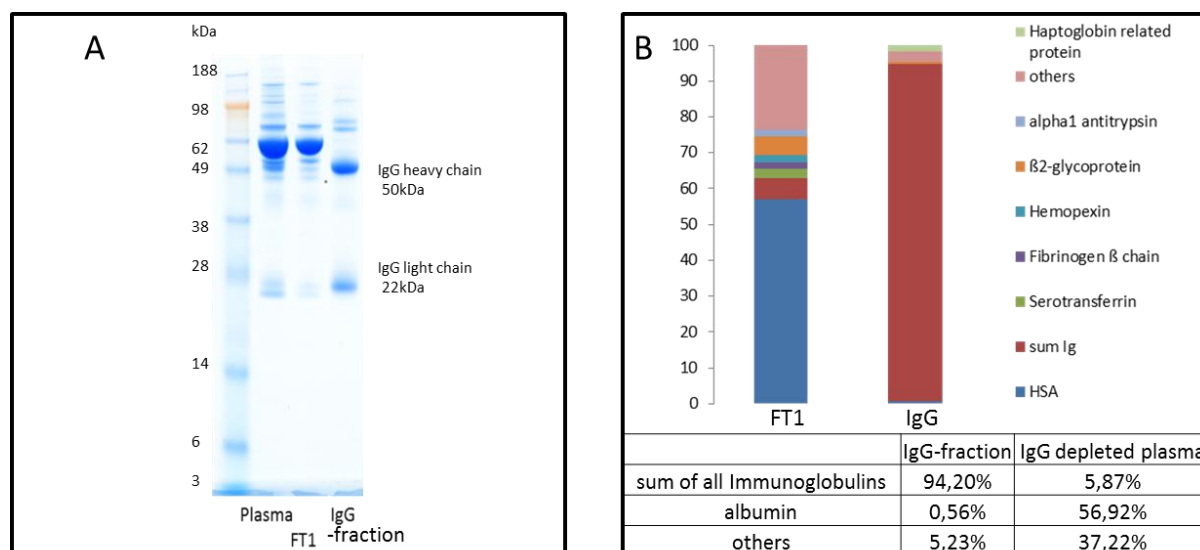


Figure 8. A) Protein patterns obtained by SDS-PAGE of plasma and the protein fractions obtained by Protein A affinity chromatography with FT1 = flow through Protein A column. B) LC-MS analysis of the respective protein fractions (LC-MS measurements performed by Dr. Susanne Schöttler).

LC-MS data confirmed that an IgG protein fraction was obtained, that consists of more than 94% immunoglobulins. The remaining plasma protein mixture contained only about 6% IgG showing a good separating capacity of the Protein A column. A comprehensive list of the LC-MS data will be presented in the supplementary information.

By applying a ToyoScreen AF-Blue HC-650M column, human serum albumin (HSA) could be isolated. The column's resin exhibits covalently attached Cibacron Blue F3GA dye on its surface as shown in Figure 9.

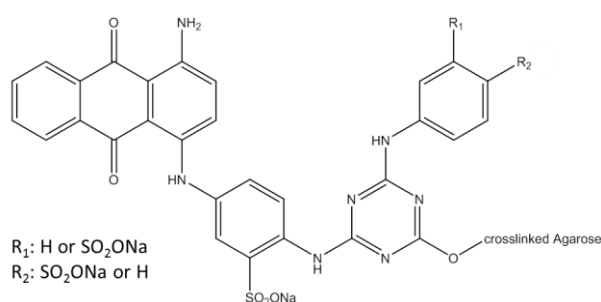
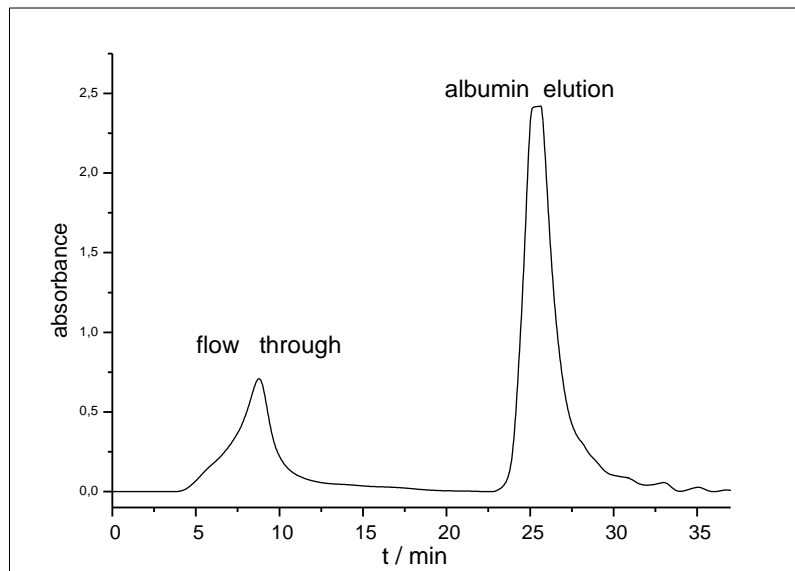


Figure 9. Chemical structure of Cibacron Blue.

HSA has a strong binding affinity to the dye that is caused by hydrophobic and electrostatic interactions. Therefore, high concentrations of salt are required to detach the protein.¹²⁶ This was done by the addition of 2 M sodium chloride solution. Figure 10 shows the chromatogram of HSA separation.



sample	Concentration g/L	Amount / mg	Amount / %
injection	5.7	5.7	
Flow Through	0.6	1.3	9.9*
HSA	1.8	3.6	56*

*calculated from the total protein amount in plasma, not from the injection.

Figure 10. Chromatogram of HSA separation via AffiGel-Blue column and the corresponding protein amount in the fractions according to a BCA Assay.

Again, the efficiency of HSA-removal was monitored by applying SDS-PAGE and LC-MS. Figure 11 shows the results. The flow through protein fraction contained only 4% of HSA. When looking at the corresponding albumin elution fraction it turned out that it consists of immunoglobulins and albumin in comparable amounts. This phenomenon is already well-known in literature, describing that Cibacron Blue F3GA also has a strong affinity to IgG and other plasma components.^{126, 127}

In order to increase the purity of isolated HSA both chromatography techniques were combined, meaning that IgG and HSA removal columns were connected in series (step by step). This way, the amount of Albumin could be increased up to 84%. A detailed overview of LC-MS data is provided in the supplementary information. According to protein quantification via a BCA assay, the total HSA amount recovered by the series connection was 56% of the total protein amount which is in good agreement with literature values (HSA amount in plasma ~60%).⁶

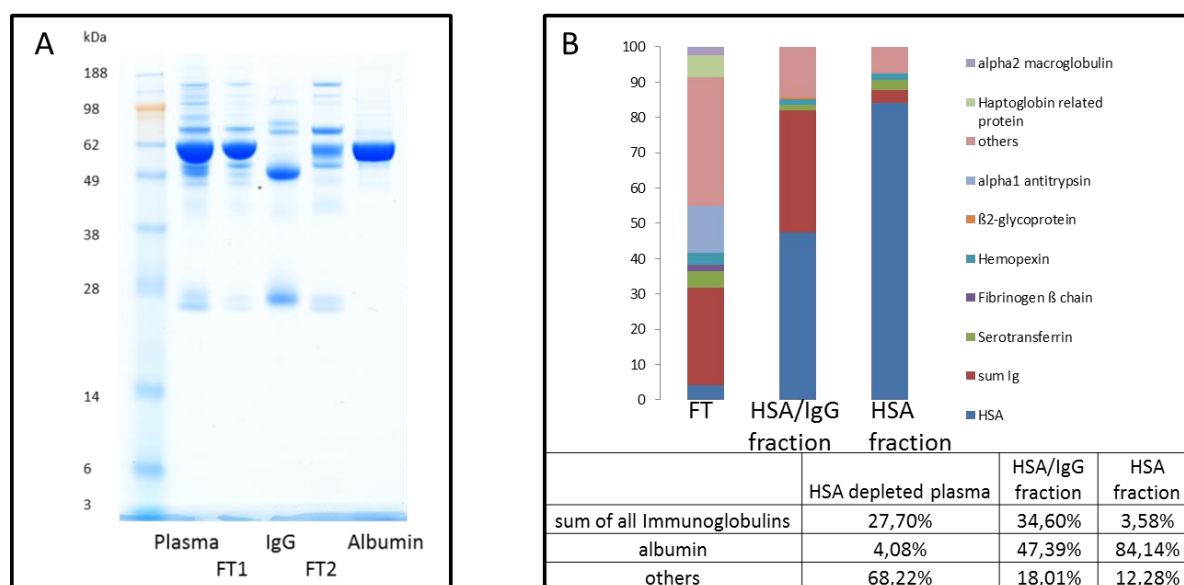


Figure 11. A) Protein patterns obtained by SDS-PAGE of plasma and the protein fractions obtained by series connection of Protein A affinity chromatography and AffiGel Blue affinity chromatography with FT1 = flow through Protein A column and FT2 = FT1 with subsequent HSA removal. B) LC-MS analysis of the respective protein fractions with FT = flow through AffiGel Blue column. (LC-MS measurements performed by Dr. Susanne Schöttler)

The resulting protein fractions were further on characterized with dynamic light scattering (DLS) in order to determine their hydrodynamic radius $\langle 1/R_h \rangle_z^{-1}$. In order to simplify the description and to distinguish them from commercially available proteins, the enriched fractions of isolated proteins/protein mixtures are named as F_{Protein} , whereas the plasma fractions depleted from certain proteins are denominated as $F_{\text{Plasma-w/o-Protein}}$. Table 2 summarizes the DLS results.

Table 2. Obtained protein fractions ($c = 1$ g/L) with their hydrodynamic radius and composition according to LC-MS.

Fraction	Protein	Hydrodynamic radius
F_{IgG}	94.2% Ig 0.56% HSA 5.24% others	$\langle 1/R_h \rangle_z^{-1} = 6.8$ nm
F_{HSA}	84.14% HSA 3.58% Ig 12.28% others	$\langle 1/R_h \rangle_z^{-1} = 3.1$ nm
$F_{HSA/IgG}$	47.39% HSA 34.6% Ig 18.01% others	$\langle 1/R_h \rangle_z^{-1} = 3.7$ nm
$F_{Plasma-w/o-IgG}$	56.92% HSA 5.87% Ig 1.85% Fibrinogen 35.36% others	$\langle 1/R_h \rangle_z^{-1} = 7.6$ nm
$F_{Plasma-w/o-HSA}$	4.08% HSA 27.7% Ig 4.51% Serotransferin 13.38% alpha1-antitrypsin 0.33 others	$\langle 1/R_h \rangle_z^{-1} = 7.6$ nm
$F_{Plasma-w/o-IgG-HSA}^*$	15.4% Haptoglobulin 14.7% α -1-antitrypsin 12.3% Serotransferrin 7.9% α -2-macroglobulin	$\langle 1/R_h \rangle_z^{-1} = 7.9$ nm

* $c = 0.6$ g/L

For IgG a hydrodynamic radius of $\langle 1/R_h \rangle_z^{-1} = 6.8$ nm was found, whereas for albumin a value of $\langle 1/R_h \rangle_z^{-1} = 3.1$ nm was found. Both values are in good agreement with the literature.¹²⁸ For example, Rausch *et al.* reported a z-averaged hydrodynamic radius for albumin ($c = 0.62$ g/L in DPBS) of $\langle 1/R_h \rangle_z^{-1} = 3.6$ nm.¹²⁹ As $F_{HSA/IgG}$ presents a mixture of both proteins it is obvious that the detected hydrodynamic radius has to be within the range of the already mentioned radii with a measured value of $\langle 1/R_h \rangle_z^{-1} = 3.7$ nm. Figure 12.A shows the corresponding angular dependency of the inverse hydrodynamic radii of each protein fraction. In general, the detected values are very small. This effect can be traced back to the low protein concentration compared to concentrated plasma. When plasma is diluted 1:60, the z-averaged hydrodynamic radius decreases from $\langle 1/R_h \rangle_z^{-1} = 19$ nm to $\langle 1/R_h \rangle_z^{-1} = 11$ nm. Also for the individual size fractions R_{h1} , R_{h2} , and R_{h3} trends can be observed. While the smallest size fraction remains constant in the range of ~ 3 nm, the values for R_{h2} and R_{h3} are halved upon dilution. Another indication that the small values are only based on dilution and not on removal of bigger protein species during fractionation is shown in Figure 12.B. Figure 12.B shows the autocorrelation function of

$F_{\text{Plasma-w/o-IgG-HAS}}$ and the intensity contribution of the different observed size fractions at a scattering angle of $\Theta = 30^\circ$. Three fractions were detected. Among them, the biggest protein fraction with a radius of $R_{h3} = 82$ nm was present.

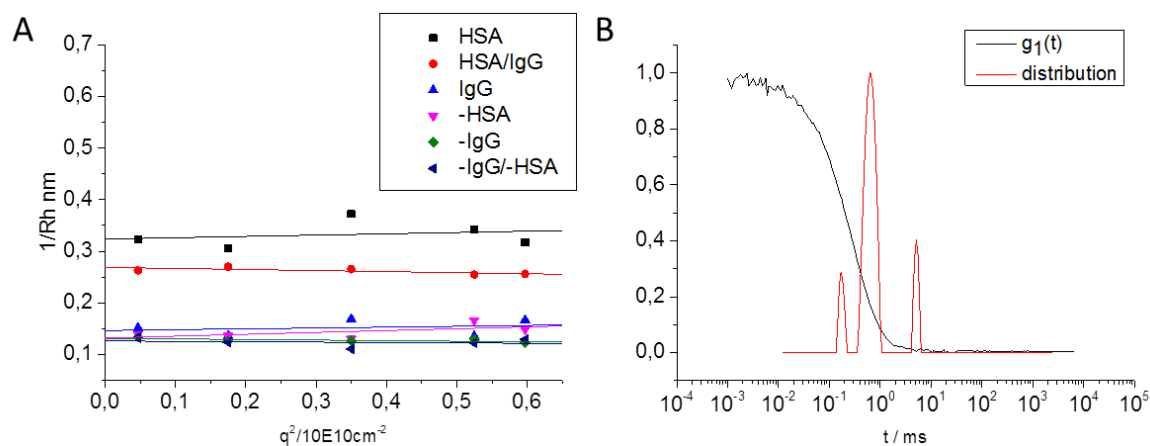


Figure 12. A) Angular dependency of the inverse hydrodynamic radii of the different protein fractions. B) ACF of $F_{\text{Plasma-w/o-HSA-IgG}}$ with the distribution of the 3 different size fractions at $\Theta = 30^\circ$.

As mentioned in the beginning of this chapter a third type of column was used to perform human blood plasma fractionation, namely ToyoScreen DEAE-650M. This column consists of an immobilized methacrylate matrix with di-ethyl amino groups on its surface that are positively charged. The mostly negatively charged plasma proteins bind to that resin and can be successively eluted by increasing the ionic strength of the running buffer. Again, sodium chloride with different concentrations between 0.155-1 M was used. Figure 13 shows the resulting chromatogram of anion exchange chromatography.

To make sure, that nearly all proteins bind to the resin, the initial flow through was reinjected two times. Protein quantification confirmed that nearly no remaining protein could be detected in the flow through afterwards. The four elution fractions were analyzed by LC-MS and SDS-PAGE. The results are shown in Figure 14.

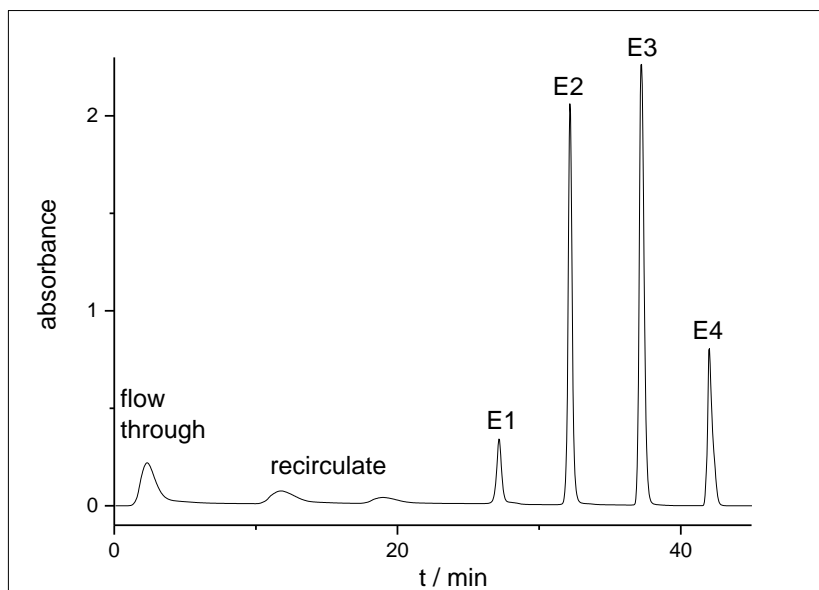


Figure 13. Chromatogram of DEAE anion exchange chromatography.

What comes first into mind when looking at both, LC-MS data as well as SDS-PAGE (see Figure 13), is the absence of HSA (in yellow) in elution fraction 1. All other fractions contain the high abundance protein. This underlines the already mentioned fact that a high ionic strength is needed to overcome the strong binding affinity of the HSA.

As a next step, all three columns were connected in series, meaning sequential removal of IgG and HSA followed by anion exchange chromatography resulting in very low protein concentrations in each fraction. The success of the overall series connection was monitored by using SDS-PAGE shown in Figure 15. The SDS-PAGE shows the good enrichment of single proteins in the elution of IgG and albumin, as well as the corresponding change in relative band intensities in the separation of E1-E4.

In conclusion, by applying Protein A and AffiGel-Blue affinity chromatography it was possible to enrich the single proteins F_{IgG} and F_{HSA} with good purity. In addition, the three low abundant protein mixtures $F_{\text{Plasma-w/o-IgG}}$, $F_{\text{Plasma-w/o-HSA}}$ and $F_{\text{Plasma-w/o-IgG-HSA}}$ could be obtained. As a second tool for fractionation, DEAE anion exchange chromatography was used to obtain four elution fractions E1-4. Those protein fractions were used for further investigations on protein-nanoparticle interactions.

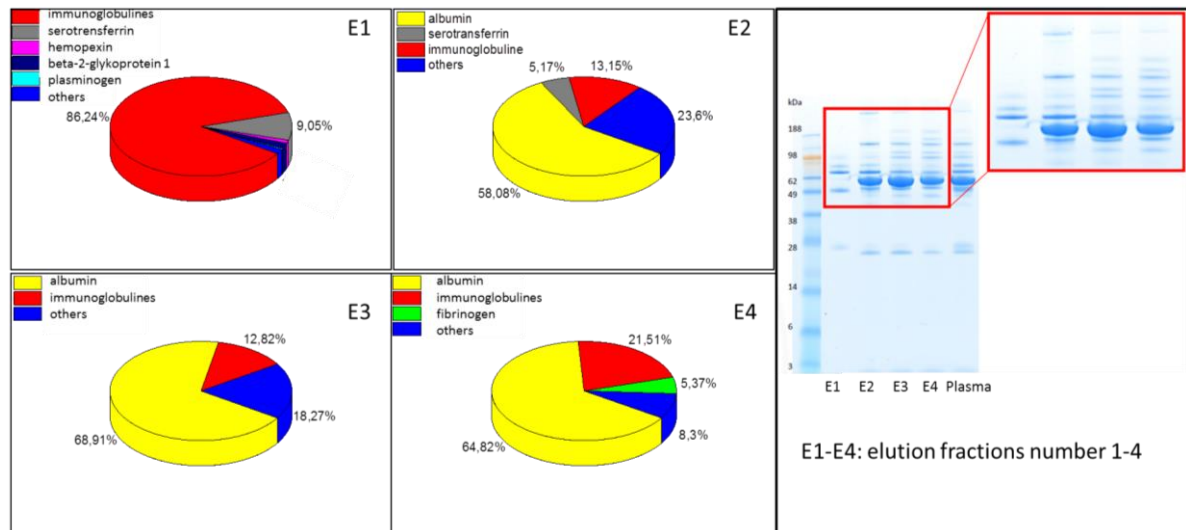


Figure 14. LC-MS analysis of elution fraction 1 – 4 (LC-MS performed by Dr. Susanne Schöttler, AK Landfester, Max Planck Institute for Polymer Research, Mainz, 2015) and SDS-PAGE of the respective protein fractions.

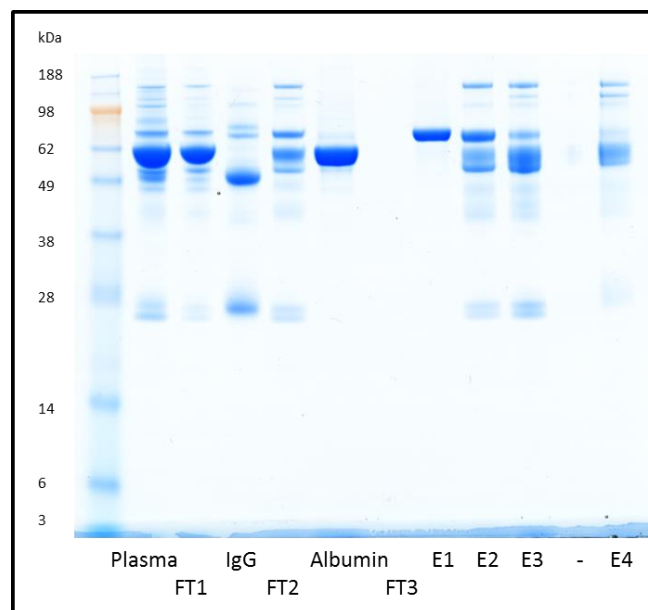


Figure 15. SDS-PAGE of series connection of Protein A column, AffiGel Blue column and DEAE column with FT1-3 = flow through after each column and E1-4 elution fraction 1-4 of DEAE column.

3.2 FRACTIONS OF PROTEIN MIXTURES DIFFERENTIALLY AGGREGATE NANOPARTICLES AND INFLUENCE THE CELLULAR UPTAKE

The formation of a protein corona on a nanomaterial's surface is a highly complex process that is influenced by various factors such as size, shape and charge of the nanomaterial. In addition, the protein source itself, namely blood plasma, is very complex and contains thousands of different proteins. Especially the influence of the low abundant proteins on particle stability and corona formation is of great interest, since the high abundant proteins are partly replaced by them over time upon blood exposure on the surface of nanomaterials. By depletion of HSA and IgG, various low abundant protein mixtures could be obtained and their composition could be determined precisely by using LC-MS as shown in the previous chapter. By introducing nanoparticles into the defined protein mixtures, a monitoring of the effects on particle stability and of the changes in physicochemical parameters was possible. This way, the overall process of nanomaterial-plasma interactions could be fragmented into low abundant and high abundant protein interactions with a nanomaterial. A closer look and deeper understanding of the processes involved in the protein corona formation could be addressed by this means. As already known in the literature¹²⁴ and described in the introduction, the coating of nanoparticles in single commercially available proteins can alter the nanomaterial's properties. With respect to their influence on the particle stability, the protein fractions here could be used for that approach as well. As benefit, the fractionation of human plasma into protein fractions could possibly be performed from the patient's own plasma and used as pre-coating of the nanocarriers *ex vivo*. The overall procedure therefore qualified as pre-*in vivo* screening method for nanomaterials designed for biomedical applications and the directed adjustment of carrier properties.

The different obtained protein fractions were used to investigate the stability of polystyrene nanoparticles against aggregation using DLS. The protein fractions were further applied to form a predetermined protein corona on differently functionalized polystyrene nanoparticles (PS). DLS was also used to investigate the stability of the protein-coated nanoparticles when re-introduced into human plasma. In addition, the influence of the artificially created protein corona on cellular uptake of nanomaterials was studied. Cell experiments were carried out by Johanna Simon (Max Planck Institute for

Polymer Research, Mainz). LC-MS measurements were done either by Johanna Simon or Dr. Susanne Schöttler.

3.2.1 THE PARTICLES UNDER INVESTIGATION

Three differently functionalized polystyrene particles were synthesized via direct miniemulsion copolymerization as already described in literature,¹²⁵ namely without surface modification (PS) and with amino (PS-NH₂) or carboxy-functionalization (PS-COOH). For stabilization of the different particle dispersions Lutensol AT50 was used as a non-ionic surfactant. Figure 16 shows the angular dependency of the inverse hydrodynamic radii of the three particles under investigation obtained by DLS and Figure 17 summarizes the physicochemical parameters of the different particles regarding hydrodynamic radius (R_h) determined by DLS, charge obtained by ζ -potential measurements and number of surface groups per NP quantified by particle charge titration.

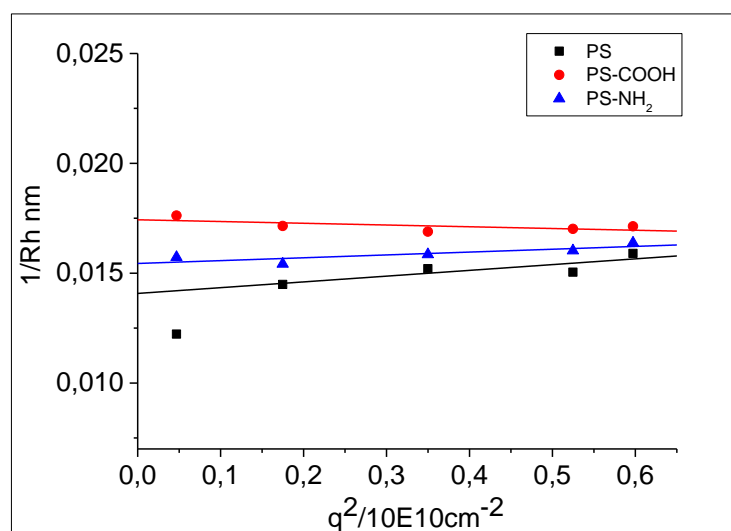


Figure 16. Angular dependency of the inverse hydrodynamic radii of PS, PS-COOH and PS-NH₂ obtained by DLS.

The 1 mM KCl solution used for zeta potential determination has an approximately neutral pH. Under these conditions, the carboxy-groups of PS-COOH are deprotonated resulting in the detected negative charge, while the amine groups in PS-NH₂ are extensively protonated and thus positively charged.

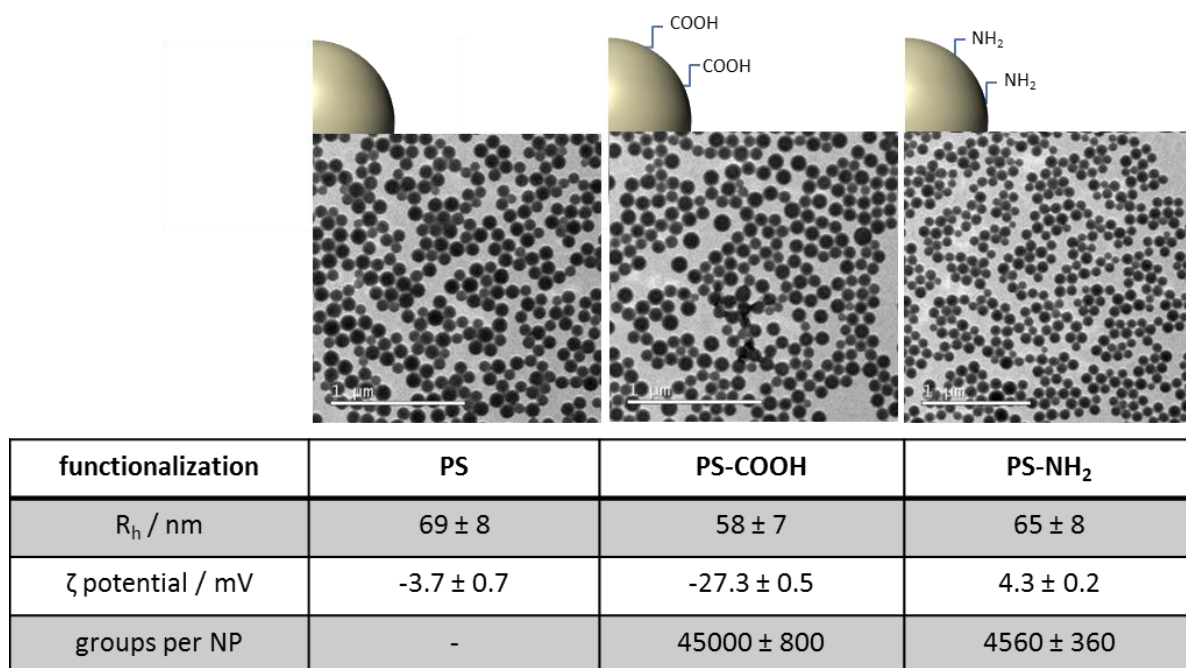


Figure 17. TEM images and physicochemical characterization of polystyrene nanoparticles with different surface functionalization.

3.2.2 SOFT PROTEIN CORONA ANALYSIS

With DLS it was possible to directly monitor the size increase of nanoparticles in the respective protein fractions/full plasma. The data were evaluated by applying the method according to Rausch *et al.*¹¹⁴ that was already described in the introduction. It has to be noted that the additional size formed in the respective mixture can be either caused by nanoparticle bridging, the adsorption of proteins or protein-protein aggregates on the nanomaterial's surface.

Prior to experiments with the different protein fractions, the effect of the protein amount in relation to a given surface area of NPs on the aggregation behavior of the different polystyrene particles was monitored using different dilutions of the plasma. The surface area of particles introduced into a given volume of plasma/dilution was kept constant at

$5 \times 10^{-4} \text{ m}^2$ resulting in different ratios of surface area per mg protein. The results are summarized in Figure 18.

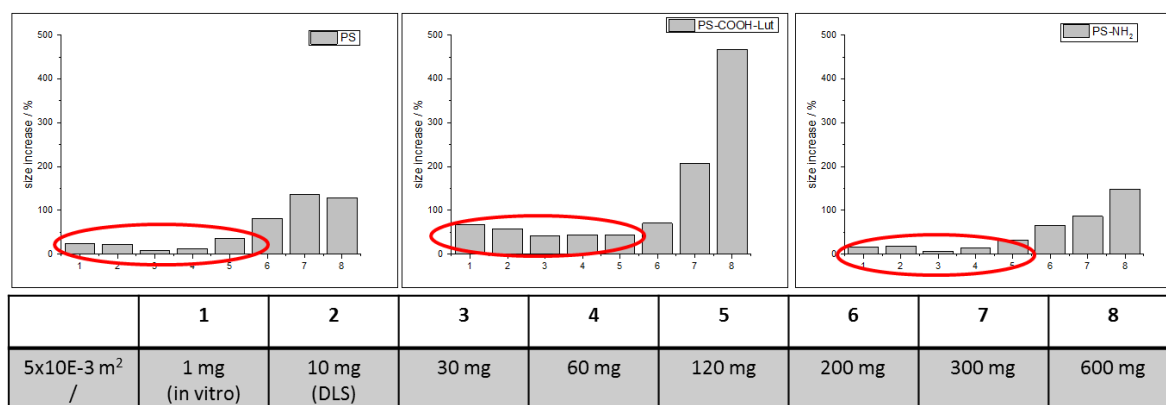


Figure 18. Size increase of respective PS-particles in dependence of the protein amount.

The aggregation behavior in the range between 0.1 and 12 mg plasma proteins in relation to the given surface area was comparable. Only for very high amounts and thus concentrations of proteins, the size increased dramatically. In order to be able to compare with low abundant proteins a low amount of proteins (1 mg) for the given surface area was chosen for all experiments with the isolated protein fractions. Similar particles have already been under investigation in a likewise approach by Mohr *et al.*, who investigated the aggregation behavior in concentrated human serum and diluted human serum by a factor of ten. But in contrast to the work presented here, the amount of particles was also reduced by a factor of ten.¹¹⁵ Therefore and because of the use of serum instead of plasma, trends can be compared, but not the absolute results of the DLS measurements. For the study presented here, human plasma was the protein source of choice because of the great importance of the low abundant proteins (see also page 27). Mohr *et al.* determined the size increase of non-functionalized PS and PS-NH₂ particles to be independent of the protein concentration, while the aggregate formation of PS-COOH particles was strongly dependent on the surrounding serum concentration.¹¹⁵ The results presented here show a similar trend. While the size increase of PS and PS-NH₂ particles was found to be moderate with increasing protein concentration, the size of PS-COOH particles increased significant with increasing protein concentration.

In Figure 19 the autocorrelation functions (ACFs) of a mixture of the respective PS-particle and $F_{\text{Plasma-w/o-IgG-HSA}}$ (A) or concentrated human plasma (B) are shown exemplarily, where $g_1(t)$ is the field correlation function and res the residuum between the fits and data. Measurements were performed at 37 °C for better *in vivo* mimicking. The force fit (indicated by the red line, Figure 19.A) could perfectly describe the ACF of the mixture of nanoparticles and $F_{\text{Plasma-w/o-IgG-HSA}}$. In contrast, an additional aggregate fraction (indicated by the blue line, Figure 19.B) was observed for the particles and plasma. Smaller scattering angles like e.g. 30° or 60° are more sensitive for the detection of a small amount of formed bigger species within a mixture under investigation compared to bigger scattering angles. Therefore, these angles give the best information about aggregation. 30° measurements are the most sensitive ones and the corresponding intensity contribution (I%) and ACFs are therefore shown in this work with favor. But 30° measurements are also most prone to artefacts. Thus, 60° data are sometimes shown instead of 30° ACFs.

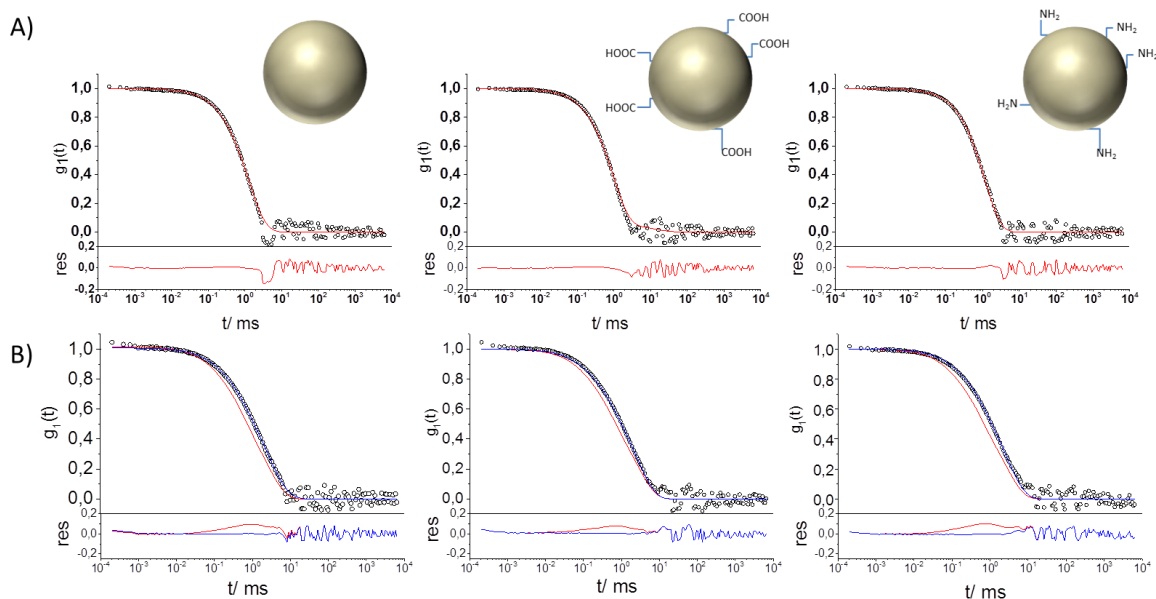


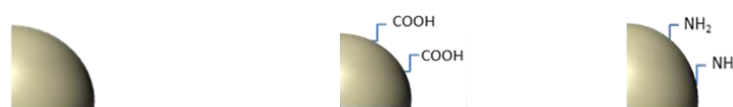
Figure 19. A) ACFs of the different particles in isolated $F_{\text{Plasma-w/o-IgG-HSA}}$ at $\Theta = 60^\circ$ including data points (\bullet) and the forced fit as the sum of the individual components (red) with the corresponding residuals resulting from the difference between data and fit. B) ACFs of the different particles in human plasma at $\Theta = 60^\circ$ including data points (\bullet), forced fit (red) and fit with additional aggregate function (blue) with the corresponding residuals resulting from the difference between data and the two fits.

Table 3 gives an overview of the DLS results of all uncoated particles after direct exposure to the different protein fractions obtained by affinity chromatography. In addition, measurements were also performed in human plasma and commercially available proteins in buffer. IgG was purchased from privigen[®] as solution for infusion with a purity 98%. The hydrodynamic radius in running buffer was determined to be $\langle 1/R_h \rangle_z^{-1} = 5.5$ nm, which is in good agreement with the value for F_{IgG} ($\langle 1/R_h \rangle_z^{-1} = 6.8$ nm). The small deviation can be related to the small amount of other ingredients like e.g. L-prolin. Human serum albumin was purchased from sigma as lyophilized powder with a purity of >99%. With DLS the radius in the running buffer was determined to be of $\langle 1/R_h \rangle_z^{-1} = 5.7$ nm. Small aggregates were observed that explain the slightly bigger value compared to F_{HSA} (of $\langle 1/R_h \rangle_z^{-1} = 3.1$ nm). Human plasma was used undiluted in order to be as close as possible to *in vivo* conditions.

First of all, it was noted that all uncoated particles aggregated in human plasma. A size increase with values between $R_h(\text{Agg}) = 174$ nm and $R_h(\text{Agg}) = 292$ nm was measured.

Next, it was found that the non-functionalized polystyrene particle changes its size in nearly every protein fraction. In contrast, the amino-functionalized particle remained stable except in the presence of IgG. This is significant considering that the hard corona formed around these two nanoparticles in human plasma is very similar as shown in Figure 20. Therefore the relevant protein probably is part of the soft corona which can so far only be studied with DLS. The absence of a detected size increase does therefore also not mean that there is no corona present. It just cannot be detected due to the sensitivity of the methods. It is only possible to detect additional sizes in the plasma / particle mixture if the intensity fractions (i. e. amplitudes) of the newly formed complexes surpass the detection limit for DLS. In detail, intensity fractions between 3% (for sizes outside the size range of the original components) and 20% (for sizes in the size range of the original components) of newly formed particles are necessary to be detected by the described fitting procedure.

Table 3. Size changes of the uncoated nanoparticles after direct exposure to human plasma or the obtained protein fractions was measured by DLS. Size increase of nanoparticles incubated in the respective protein fraction is calculated based on the size value for the uncoated nanoparticles measured in PBS (Reference value Figure 15).



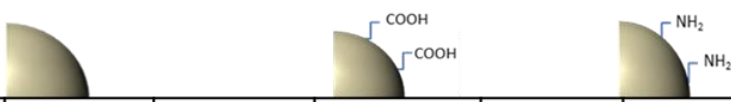
Exposed to	R_h /nm	Size increase	R_h /nm	Size increase	R_h /nm	Size increase
Human Plasma*	292 ± 35	323%	174 ± 21	200%	195 ± 23	200%
F _{Plasma-w/o-IgG-HSA}	61 ± 7	0%	54 ± 6	0%	96 ± 12	48%
F _{Plasma-w/o-IgG}	146 ± 18	112%	84 ± 10	45%	70 ± 8	0%
F _{Plasma-w/o-HSA}	137 ± 16	99%	58 ± 7	0%	102 ± 12	57%
F _{IgG}	224 ± 27	225%	96 ± 12	66%	207 ± 25	219%
F _{HSA}	122 ± 15	77%	62 ± 7	0%	72 ± 9	0%
F _{IgG/HSA}	480 ± 58	596%	91 ± 11	57%	138 ± 17	112%
IgG (commercial)	195 ± 23	183%	642 ± 77	1007%	335 ± 40	415%
HSA (commercial)	170 ± 20	146%	64 ± 8	0%	81 ± 10	25%

*Concentrated human plasma for *in vivo* mimicking.

For completeness, the same procedure was done for the different protein fractions obtained via anion exchange chromatography. Table 4 summarizes the results.

Whereas PS-COOH is the only particle that shows no significant size increase in commercially available HSA, it is now the only particle showing a significant increase in elution E1 that is lacking of HSA. This indicates that HSA has some stabilizing effect on PS-COOH when it comes to aggregation. In general, the size increases are moderate in the different elution fractions. The sole exception is the non-functionalized polystyrene particle that shows aggregation behavior in E2 and E3. Both protein fractions are dominated by albumin, which correlates with the observed size increase of PS in F_{HSA} as well as commercially available HSA in buffer.

Table 4. Size changes of the uncoated nanoparticles after direct exposure to human plasma or the obtained protein fractions was measured by DLS. Size increase of nanoparticles incubated in the respective protein fraction is calculated based on the size value for the uncoated nanoparticles measured in PBS (Reference value Figure 15).



Exposed to	R_h /nm	Size increase	R_h /nm	Size increase	R_h /nm	Size increase
E1	68 ± 7	0%	113 ± 15	92%	70 ± 4	0%
E2	80 ± 10	16%	75 ± 12	29%	79 ± 6	22%
E3	182 ± 69	164%	84 ± 4	45%	98 ± 21	51%
E4	170 ± 25	146%	53 ± 5	0%	67 ± 9	0%

In order to monitor the reproducibility or rather the sensitivity of the applied method, the aggregation behavior of the different PS-particles was investigated in a solution of commercially available albumin as well as IgG in two different solutions. On the one hand, the proteins were dissolved in PBS buffer and on the other hand in running buffer as it is the case for the protein fractions obtained from chromatography. Figure 20 exemplarily shows the results for non-functionalized polystyrene after exposure to IgG.

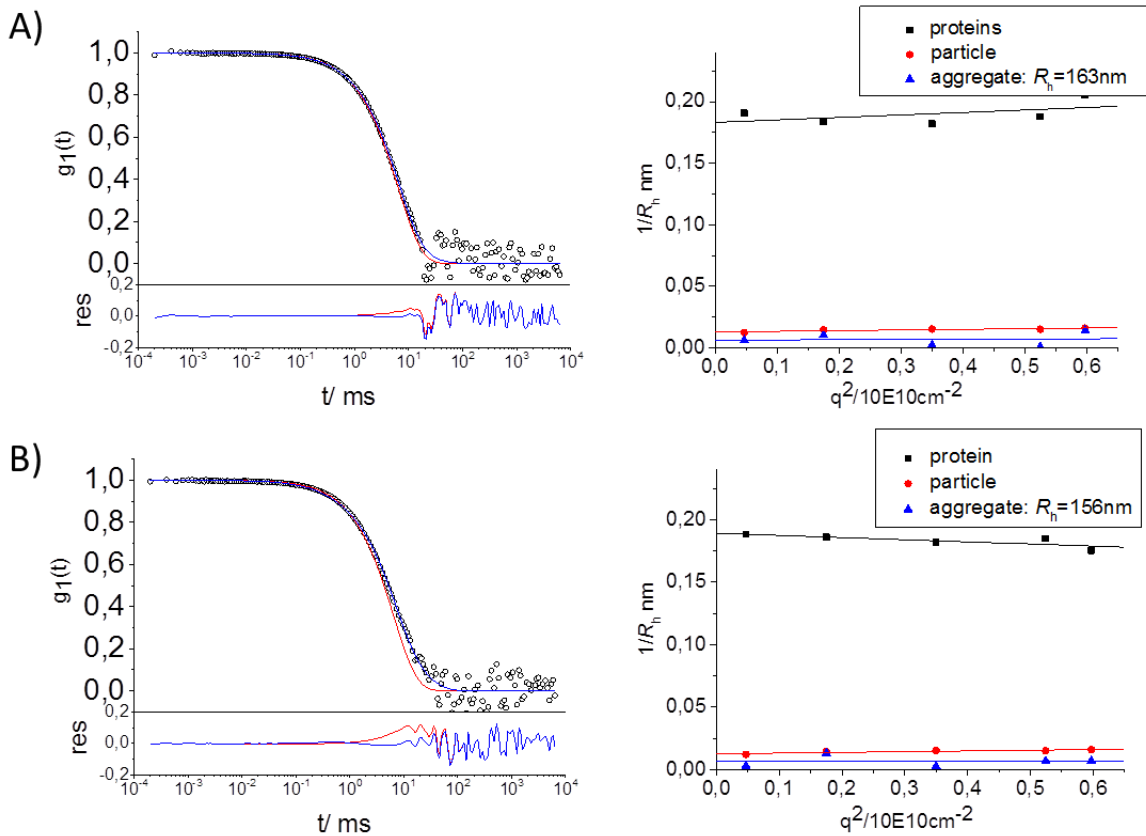


Figure 20. A) Angular dependency of the inverse hydrodynamic radii as well as ACF at $\Theta = 30^\circ$ including data points (O), force fit (red), and fit including aggregate formation (blue) of PS in IgG and running buffer as medium. B) Angular dependency of the inverse hydrodynamic radii as well as ACF at $\Theta = 30^\circ$ including data points (O), force fit (red) and fit including aggregate formation (blue) of PS in IgG and PBS buffer as medium.

Figure 20.A shows the angular dependency of the observed hydrodynamic radii as well as the ACF at a scattering angle of 30° including data points, force fit, and fit including aggregate formation of PS in IgG and running buffer as the medium, whereas Figure 20.B shows the corresponding results for PBS as medium under investigation. In both cases aggregates were formed in the size range between 312 and 326 nm in diameter. For human serum albumin in running buffer and PBS, also comparable results were obtained, while aggregates in the size range between 352 and 374 nm in diameter were detected (Figure 21).

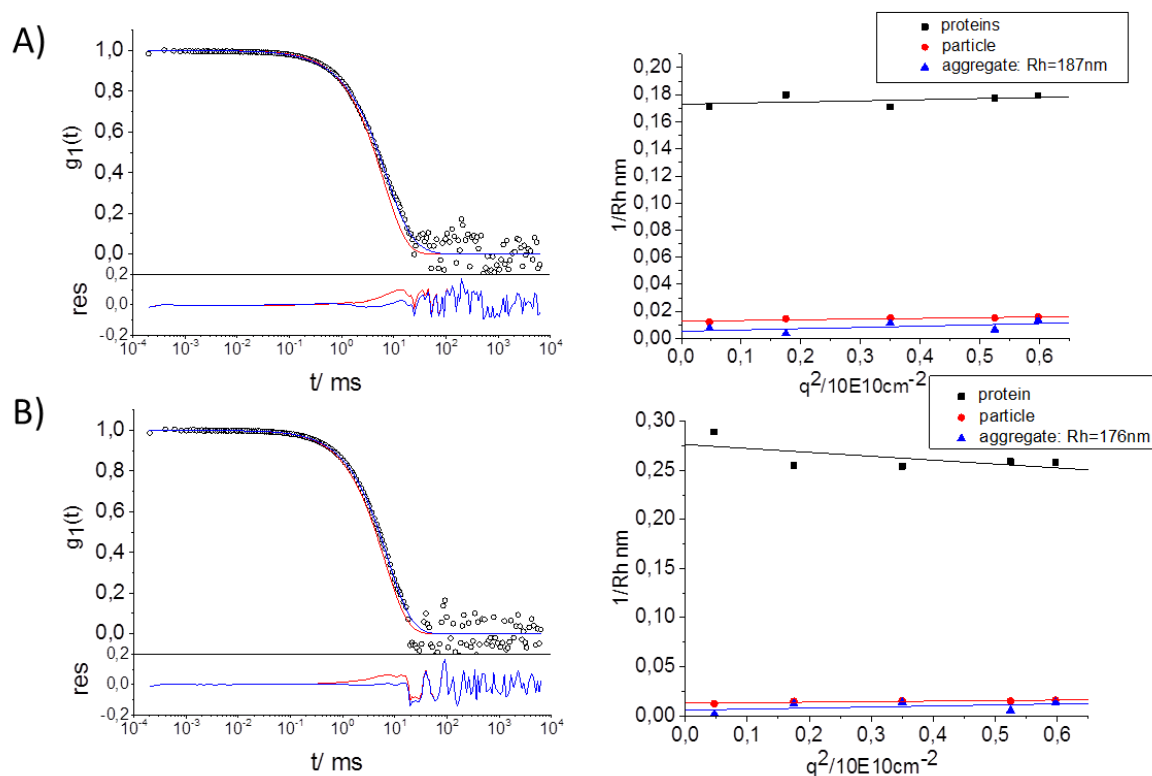


Figure 21. A) Angular dependency of the inverse hydrodynamic radii as well as ACF at $\Theta = 30^\circ$ including data points (O), force fit (red), and fit including aggregate formation (blue) of PS in HSA and running buffer as medium. B) Angular dependency of the inverse hydrodynamic radii as well as ACF at $\Theta = 30^\circ$ including data points (O), force fit (red) and fit including aggregate formation (blue) of PS in HSA and PBS buffer as medium.

Additionally, both proteins were analyzed with circular dichroism (CD) spectroscopy in PBS as well as running buffer. Again, no significant change for the different solutions could be observed. The resulting spectra are shown in Figure 22 and are in good agreement with spectra reported in literature.^{7, 9, 130} Therefore it can be assumed, that both proteins have a similar secondary structure in both buffers under investigation.

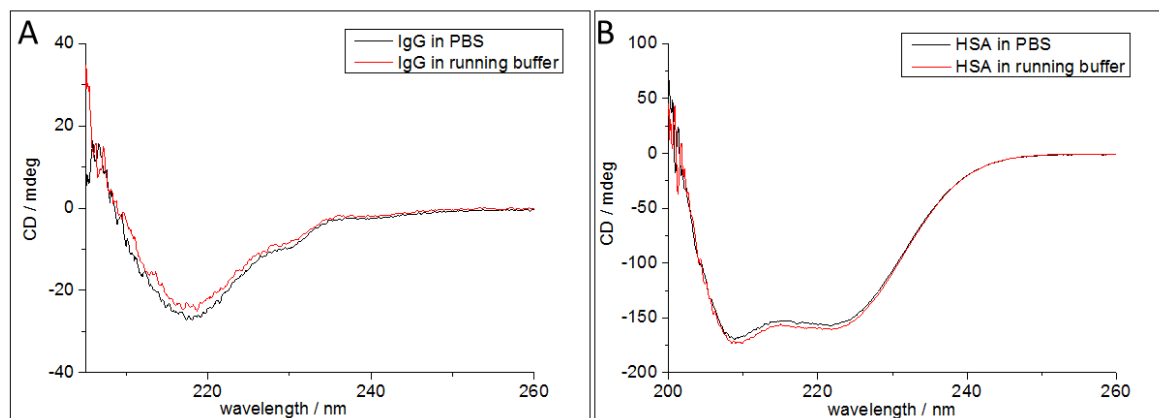


Figure 22. A) CD spectrum of IgG in PBS and running buffer at 37 °C with $c = 1$ g/L. B) CD spectrum of HSA in PBS and running buffer at 37 °C with $c = 1$ g/L.

3.2.3 HARD PROTEIN CORONA ANALYSIS

To study the hard protein corona, the nanoparticles were incubated in human plasma. Particles in complex with proteins were separated from free protein via centrifugation and redispersed in PBS. Zeta potentials, the amount of adsorbed protein, and the hard protein corona pattern were analyzed.

In agreement with results found in literature¹²⁴ the surface charge indicated by the zeta-potential after the incubation in human plasma is the same for all functionalization types in the range between $\zeta = - (32-38)$ mV whereas prior to incubation differences related to the surface functionalization were measured. The change in the detected zeta potentials to negative values in a similar range makes clear, why the different PS particles show similar aggregation behavior in concentrated human plasma independent of their surface functionalization. When the nanomaterial is introduced into plasma, the surface is covered with proteins and the initial surface charge masked by the protein corona. The amount of bound proteins after incubation in human plasma was quantified via a Pierce 660 nm assay. Interestingly, the hard corona of all particles formed after exposure to human plasma contains nearly the same amount of proteins for all particles in the range between ~ 275 and $326 \mu\text{g}$ proteins per 0.05 m^2 particle surface area (Figure 23), but when analyzing the formed hard protein corona profile via SDS-PAGE, the differences between the particles becomes apparent (Figure 23). While the protein pattern of PS and PS-NH₂ are very similar, the one of PS-COOH differs a lot. The same phenomenon was

observed via LC-MS and is shown in Figure 24. A detailed list of data is given in the supplementary information.

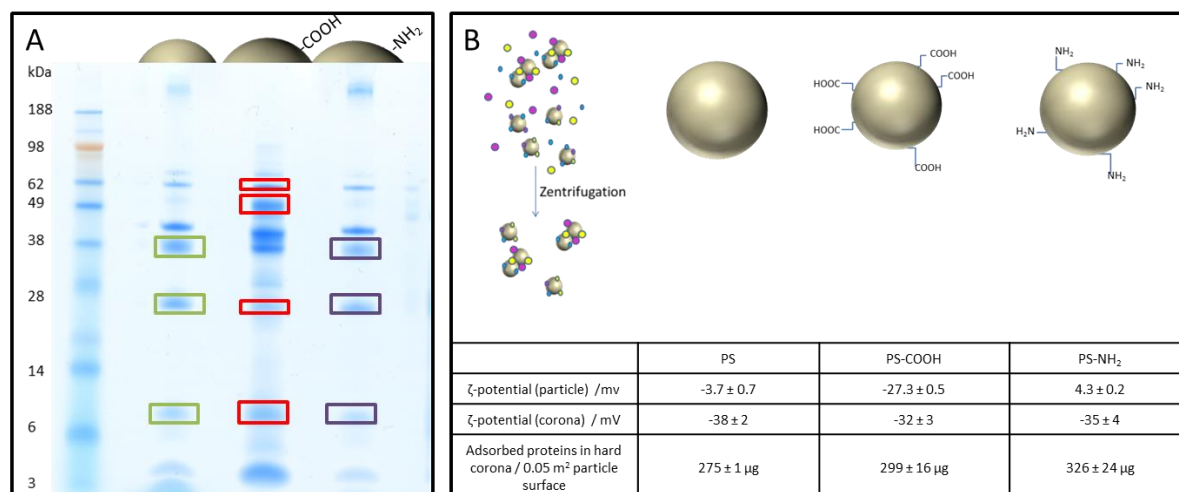


Figure 23. A) SDS-PAGE of protein coronas that were formed upon incubation of the different PS-particles in concentrated human blood plasma. B) Hard corona analysis by protein quantification and ζ-potential measurement.

Based on the LC-MS data, single protein bands in the patterns obtained from SDS-PAGE could be related to specific proteins. For PS and PS-NH₂ nanoparticles, intense bands at ~ 38 kDa belonging to clusterin, ~ 28 kDa corresponding to apolipoprotein A-I, and ~ 9 kDa corresponding to apolipoprotein C3 can be seen in Figure 21. For PS-COOH nanoparticles, the protein bands at ~ 64 kDa and ~ 47 kDa can be related to the alpha and beta chains of fibrinogen. The two bands at lower molecular ranges at ~ 28 kDa and ~ 9 kDa also correspond to the already mentioned proteins apolipoprotein A-I and C3.

LC-MS data confirmed, that the protein coronas formed on PS and PS-NH₂ nanoparticles contain mostly clusterin and apolipoproteins A-I and A-IV, that can be summarized altogether as lipoproteins. PS-COOH particles on the other hand also adsorbed a lot of fibrinogen on its surface upon incubation that is part of the coagulation proteins illustrated in red in Figure 24. These results are again in good agreement with the obtained results from Mohr *et al.* after incubation of the already mentioned related particles in human serum. For PS and PS-NH₂ particles, the reported protein coronas are

also very similar and contain mostly lipoproteins while the profile of PS-COOH particles after serum incubation differs and contains also a high amount of coagulation proteins.¹¹⁵

To sum up, despite somehow similar formed hard coronas on PS and PS-NH₂ the stability of both in the respective protein mixtures differ a lot. This leads to the assumption, that the proteins leading to significant size increases are only present in the soft corona. In addition, the masking of particle surface charge by mostly negative plasma proteins explains the similar aggregation behavior of all particles in concentrated human plasma.

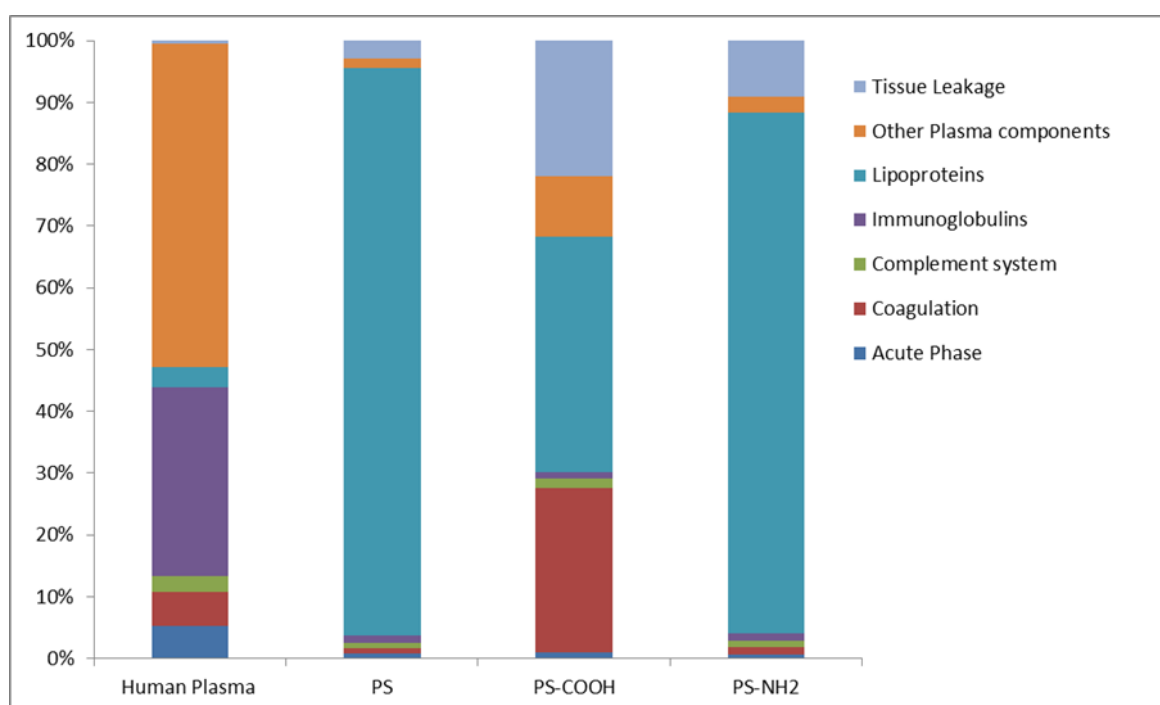


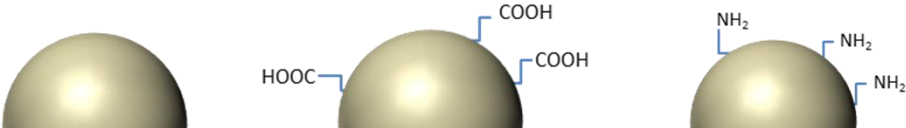
Figure 24. Plasma composition in comparison to the hard corona composition of each particle analyzed via LC-MS (LC-MS measurements performed by Johanna Simon).

3.2.4 TAILORING THE HARD CORONA

The so far discussed polystyrene particles were modified by coating their surface with the obtained protein fractions from affinity chromatography. This way, a predetermined protein corona was created that will further on be related to as the so called “artificial protein corona”. Nanoparticles were incubated with different protein fractions or individual proteins for 1 h at 37 °C (5×10^{-3} m² overall surface area / mg protein).

Afterwards, unbound and weakly bound proteins were removed via centrifugation. The resulting pre-coated nanoparticles were characterized regarding their zeta potential as well as their size (Table 5).

Table 5. Physicochemical parameters of nanoparticles pre-coated with different protein fractions or individual proteins.



Protein fraction	R_h / nm	ζ -potential / mV	R_h / nm	ζ -potential / mV	R_h / nm	ζ -potential / mV
$F_{\text{plasma-w/o-IgG-HSA}}$	89 ± 9	-30.0 ± 1.1	63 ± 6	-33.3 ± 0.9	89 ± 9	-29.6 ± 0.5
$F_{\text{Plasma-w/o-IgG}}$	97 ± 10	-25.2 ± 0.1	75 ± 8	-20.4 ± 0.2	92 ± 9	-27.1 ± 2.8
$F_{\text{Plasma-w/o-HSA}}$	228 ± 23	-24.6 ± 0.4	62 ± 6	-29.7 ± 1.4	202 ± 20	-35.6 ± 0.0
F_{IgG}	110 ± 11	-13.3 ± 0.8	374 ± 37	-10.6 ± 0.1	112 ± 11	-9.87 ± 0.5
F_{HSA}	94 ± 9	-22.8 ± 0.4	60 ± 6	-27.3 ± 1.3	68 ± 7	-16.9 ± 0.8

Table 5 shows the resulting size increase of the different PS particles as well as the zeta potential upon coating with the different protein fractions. While the coating in HSA and the low abundant protein mixtures $F_{\text{Plasma-w/o-IgG-HSA}}$ and $F_{\text{Plasma-w/o-IgG}}$ leads to no significant size increase compared to the values of the uncoated ones (Figure 17), the coating with HSA-depleted plasma and IgG resulted in slight or distinct increases in the particle size. For example, PS-COOH particles formed species with $R_h = 374$ nm after incubation with IgG. The detected size increases can either be caused by protein adsorption only, but also by forming aggregates upon coating. The small size increases can be assumed to be caused by protein adsorption only. In addition, the overall negative zeta potentials indicate, that proteins are present on all nanoparticles after coating. In order to exclude the influence of centrifugation on the particle size after redispersion, PS-COOH was exemplarily centrifuged without prior incubation. It turned out that the radius of PS-COOH remains constant within the error margin of DLS (see also Figure 25.A). In addition, the effect of centrifugation on the particle stability after incubation with proteins (in this case human serum) was investigated using DLS. After one centrifugation step, non-functionalized PS

remained stable mirrored by the slope of the angular dependency of the inverse hydrodynamic radii (see Figure 25.B). A size increase of ~ 20 nm (radius) originated in the formed protein layer was detected. But already after the second centrifugation step, the particles precipitated during the DLS measurement indicated by the negative slope of the angular dependency of the inverse hydrodynamic radii. The redispersion after the fourth centrifugation step was difficult and already formed aggregates / bigger species sedimented. The sample taken for DLS is therefore not representative and explains why the data points are shifted to smaller radii again (but very broad).

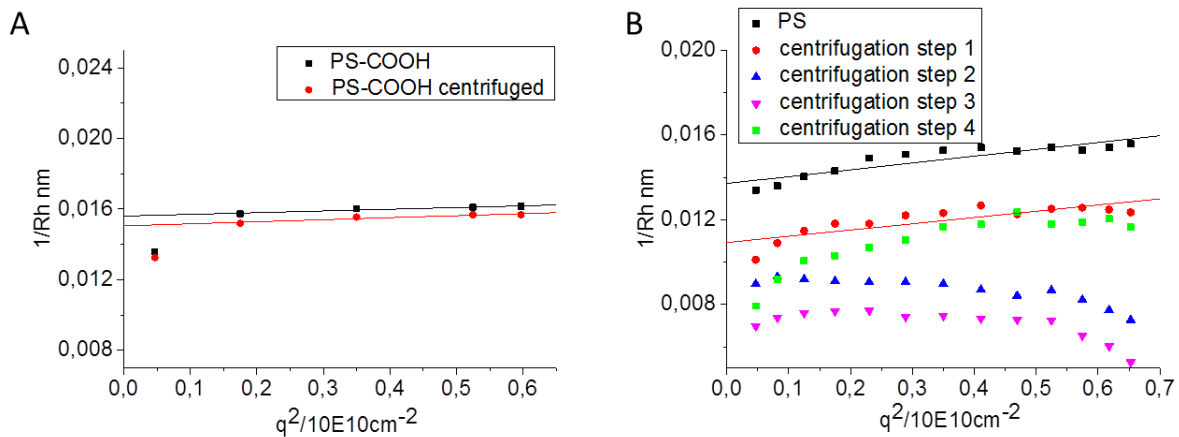


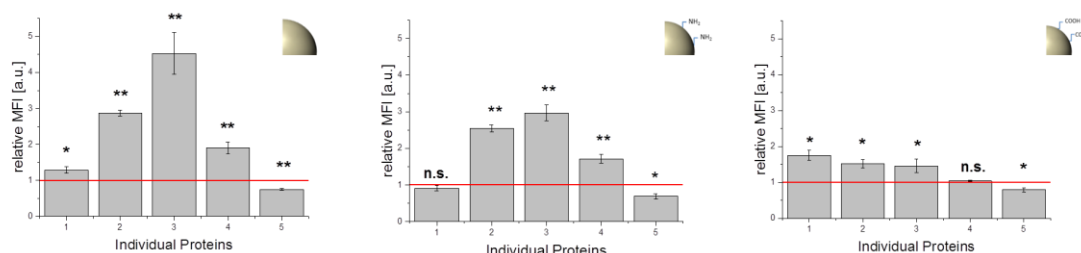
Figure 25. A) Angular dependency of the inverse hydrodynamic radius of PS-COOH (•) and centrifuged PS-COOH (•). B) Angular dependency of the inverse hydrodynamic of PS (•), PS after incubation in human plasma and one centrifugation step (•), two (•), three (•), and four centrifugation steps (•).

According to the above described DLS results, the PS particles in Table 5 were only centrifuged once after incubation in the different protein fractions. Those pre-coated nanoparticles were used to investigate the stability of an “artificial protein corona” under *in vivo* conditions and its impact on cellular uptake.

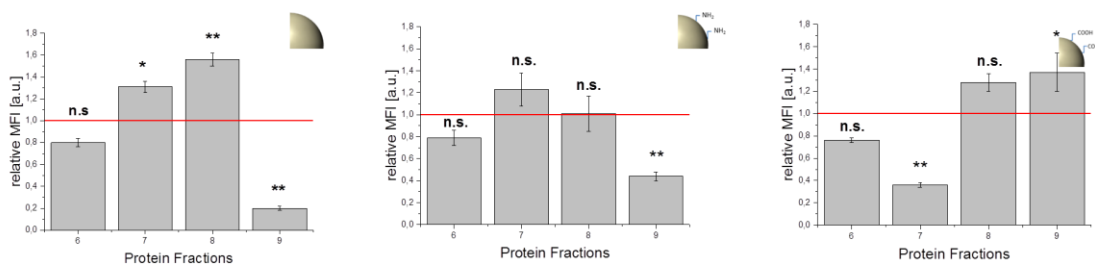
A murine macrophage-like cell line (RAW 264.7) was used to study whether it is possible to specifically trigger cellular uptake by pre-coating of nanoparticles with different protein fractions obtained after plasma fractionation. Flow cytometry analysis gave quantitative information about uptake behavior (Figure 26) and confocal laser scanning microscopy

(cLSM) (Figure 27) was used to visualize the uptake process. To ensure the absence of any additional proteins cellular uptake studies were carried out in medium without plasma or serum proteins. To demonstrate the effect of pre-coating, cellular uptake behavior of the uncoated (“naked”) particles is represented by the red line in Figure 26.

A. Cellular uptake of nanoparticles pre-coated with individual proteins



B. Cellular uptake of nanoparticles pre-coated with different protein fractions



1	2	3	4	5	6	7	8	9
HSA _{com.}	F _{HSA}	F _{HSA/IgG}	F _{IgG}	IgG _{com.}	Human Plasma	F _{Plasma-w/o-IgG}	F _{Plasma-w/o-HSA}	F _{Plasma-w/o-HSA-IgG}

Figure 26. Flow cytometry analysis of RAW 264.7 cells incubated with uncoated or pre-coated nanoparticles for 2 h in DMEM without additional proteins. Nanoparticles were pre-incubated with individual proteins (A) or different protein fractions (B), separated from unbound proteins via centrifugation and added to the cells with a nanoparticle concentration of 75 $\mu\text{g}/\text{mL}$. Relative median fluorescence intensity (rMFI) values are shown as mean \pm SD of triplicates. The red line serves as a reference for cellular uptake of uncoated nanoparticles (rMFI = 1). A student’s t-test was performed to demonstrate the difference in uptake behavior of uncoated and pre-coated nanoparticles (indicated by p values < 0.01* or p < 0.001**) (all cell experiments were performed by Johanna Simon).

In general, non-functionalized and amino-functionalized particles (Figure 26) showed similar uptake trends after pre-incubation. Especially, pre-incubation with F_{HSA} (2) and F_{IgG/HSA} (3) caused strongly enhanced cellular uptake (p < 0.001**) in comparison to uncoated (“naked”) particles. There was no significant size increase observed for PS and PS-NH₂ particles pre-coated with F_{HSA}. As cellular uptake was strongly altered due to pre-

incubation with F_{HSA} , it illustrates that cellular uptake is triggered by protein adsorption. Confocal laser scanning microscopy (Figure 27) confirmed the intracellular localization of the pre-coated nanoparticles. Analog results were obtained for PS-COOH particles pre-coated with F_{HSA} (2) and $F_{\text{IgG/HSA}}$ (3); although this effect was not as significant ($p < 0.01^*$) as for PS and PS-NH₂. In addition, pre-coating with F_{IgG} (4) caused increasing cellular uptake compared to uncoated particles as well. Hence, there was a size increase measured after the particles were pre-incubated with F_{IgG} (R_h values, Table 5). Therefore, it was not possible to clearly demonstrate that cellular uptake is triggered by the adsorption of IgG or if uptake behavior is altered due to the size increase. Macrophages take up nanoparticles by several mechanisms.^{131, 132} One of the most interesting uptake mechanism is called phagocytosis that also enables the uptake of bigger species.

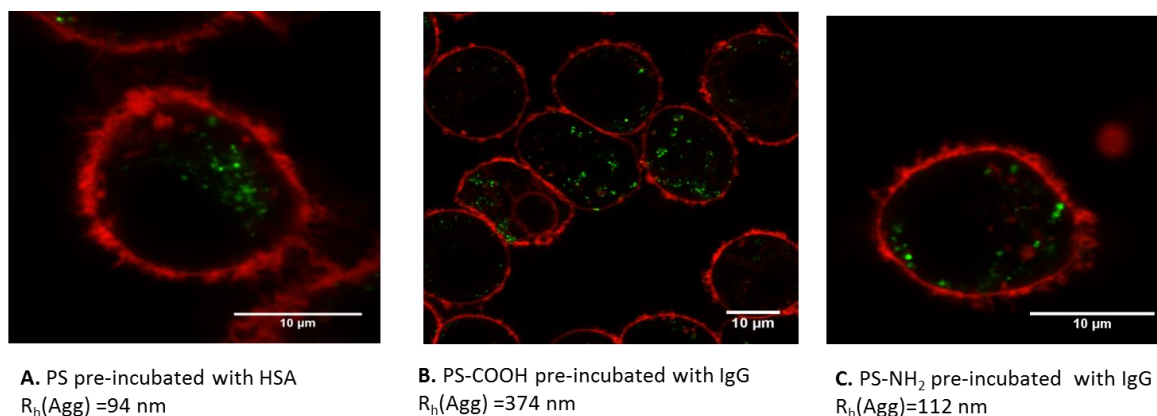


Figure 27. cLSM images of RAW264.7 cells after incubation with pre-coated nanoparticles for 2h in DMEM without additional proteins. Exemplary shown for PS pre-coated with HSA (A); PS-COOH pre-coated with IgG (B); PS-NH₂ pre-coated with IgG (C). Scale bars = 10 μm .

Going further, the influence of pre-coating with various low-abundant protein fractions (Figure 26.B) was studied. Here it was found, that pre-coating with some protein fractions resulted in significantly decreased cellular uptake ($p < 0.001^{**}$) compared to uncoated nanoparticles. This effect was caused by the low abundant protein fraction $F_{\text{Plasma-w/o-HSA-IgG}}$ for PS and PS-NH₂ particles. In contrast, pre-coating of PS-COOH with $F_{\text{Plasma-w/o-HSA-IgG}}$ revealed no significant influence on uptake behavior. Interestingly, pre-coating of PS-COOH with $F_{\text{Plasma-w/o-IgG}}$ caused strongly reduced uptake compared to uncoated particles.

Importantly, there was only a slight change (Table 5) observed of PS/PS-NH₂ pre-coated with F_{Plasma-w/o-HSA-IgG} and PS-COOH pre-incubated with F_{Plasma-w/o-IgG}. This highlights that cellular uptake is strongly influenced by adsorption of the less abundant plasma proteins on the nanoparticles' surface.¹²⁴

In addition, it was analyzed, whether the pre-coating ratio between nanoparticles and proteins had an effect on cellular uptake behavior. As exemplary shown in Figure 28, PS-COOH nanoparticles were pre-coated with varying amounts of IgG depleted plasma.

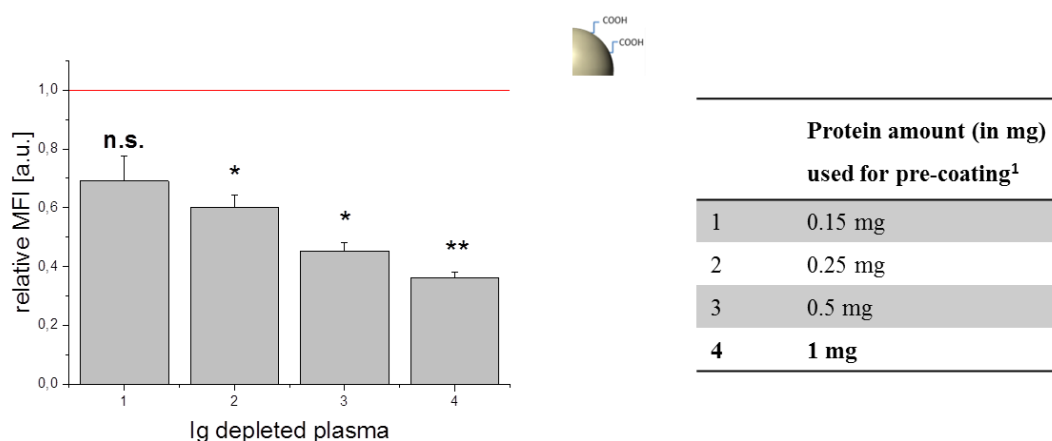


Figure 28. Flow cytometry analysis of RAW 264.7 cells incubated with nanoparticles pre-coated with varying amounts of Ig depleted plasma for 2 h in DMEM without additional proteins. Different pre-coating ratios between the amount of proteins (in mg) and the defined surface of nanoparticles ($5 \cdot 10^{-3} \text{ m}^2$) were chosen. The pre-coated nanoparticles were isolated via centrifugation and added to the cells with a nanoparticle concentration of $75 \mu\text{g/mL}$. Relative median fluorescence intensity (rMFI) values are shown as mean \pm SD of triplicates. The red line serves as a reference for cellular uptake of uncoated nanoparticles (rMFI = 1). A student's t-test was performed to demonstrate the difference in uptake behavior of uncoated and pre-coated nanoparticles (indicated by p values $< 0.01^*$ or $< 0.001^{**}$) (all cell experiments were performed by Johanna Simon).

A strong correlation between the amount of proteins used for pre-coating and cellular uptake was found (Figure 28). Going down to a pre-coating ratio of $150 \mu\text{g}$ proteins per of $5 \cdot 10^{-3} \text{ m}^2$ NP surface area (1), there was no significant difference between the uptake behavior of coated and uncoated NP. Clearly, the strongest influence on uptake behavior

was found for nanoparticles pre-coated with the chosen ratio of $5 \times 10^{-3} \text{ m}^2$ overall surface area per mg protein (described in material/methods and shown in Figure 26).

Altogether, these results demonstrate the great potential to trigger and control uptake behavior via pre-coating of nanoparticles with specific proteins or protein fractions. It was shown, that the uptake behavior is critically altered due to pre-coating of nanoparticles with distinct protein fractions. Proteins were identified (e.g. HSA) which caused a significant increase in uptake. More interestingly, on the other side it was possible to demonstrate that uptake is significantly decreased if particles are pre-coated with certain low abundant protein fractions.

In order to investigate the stability of the artificial preformed protein corona under physiological conditions, pre-coated nanoparticles were exposed to human plasma and size changes monitored with DLS. The results are summarized in Table 6.

Table 6. Size changes of pre-coated particles after direct exposure to human plasma. Intensity fractions of the aggregate $I(30^\circ)$ are exemplified for a scattering angle of 30° . Size increase is calculated based on the values for uncoated nanoparticles (see Figure 17) or pre-coated nanoparticles in PBS (see Table 5).



Protein pre-coating	$R_h(\text{Agg})$ /nm	Size increase	$I(30^\circ)$ /%	$R_h(\text{Agg})$ /nm	Size increase	$I(30^\circ)$ /%	$R_h(\text{Agg})$ /nm	Size increase	$I(30^\circ)$ /%
none ¹	292 nm	323 %	26	174 nm	200 %	25	195 nm	200 %	40
$F_{\text{plasma-w/o-IgG-HSA}}^2$	no aggregation (89 nm particle)			168 nm	166 %	43	no aggregation (89 nm particle)		
$F_{\text{plasma-w/o-HSA}}^2$	538 nm	136 %	53	110 nm	77 %	11	435 nm	115 %	63
$F_{\text{plasma-w/o-IgG}}^2$	314 nm	223 %	30	256 nm	241 %	70	203 nm	121 %	50
F_{IgG}^2	232 nm	111 %	67	no aggregation (374 nm particle)			no aggregation (112 nm particle)		
F_{HSA}^2	135 nm	44 %	75	154 nm	157 %	54	290 nm	326 %	22

¹compared to values in Figure 17; ²compared to values in Table 5

Table 6 shows the detected hydrodynamic radii of formed aggregates upon exposure of PS particles to concentrated human plasma. In order for better comparability, these values were transferred into a corresponding size increase compared to the initial “naked” or

coated particles. In addition, the intensity contribution of the newly formed species on the overall scattered light at a scattering angle $\Theta = 30^\circ$ is shown. This value is proportional to concentration \times molecular weight of the formed aggregates.

The amino-functionalized as well as the non-functionalized particle could be stabilized against aggregation via a pre-coating with $F_{\text{Plasma-w/o-IgG-HSA}}$ (Table 6). This is of great interest as the original particles formed aggregates in human plasma in the size range of $R_h(\text{Agg})\text{PS} = 292 \text{ nm}$ and $R_h(\text{Agg})\text{PS-NH}_2 = 195 \text{ nm}$. In contrast, the pre-coating of PS-COOH with $F_{\text{Plasma-w/o-IgG-HSA}}$ leads to the formation of aggregates in a size range of $R_h(\text{Agg})\text{PS-COOH} = 168 \text{ nm}$ (Table 6).

The principal method to stabilize nanoparticles against aggregation in human plasma via pre-coating with an artificial protein corona is illustrated in Figure 29. Furthermore, the ACFs of the uncoated as well as the pre-coated PS particles in human plasma are shown exemplary.

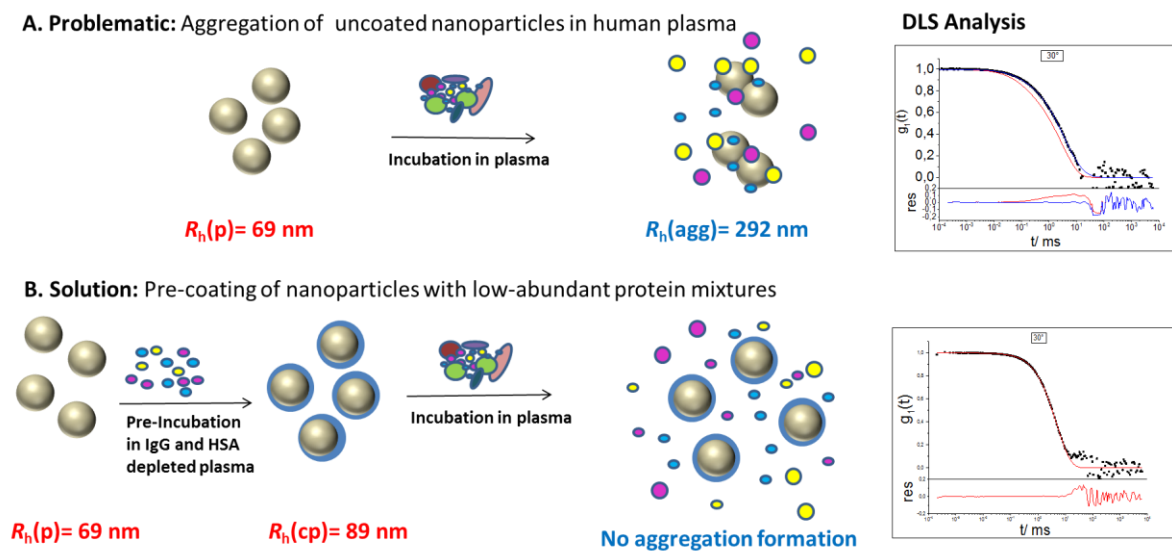
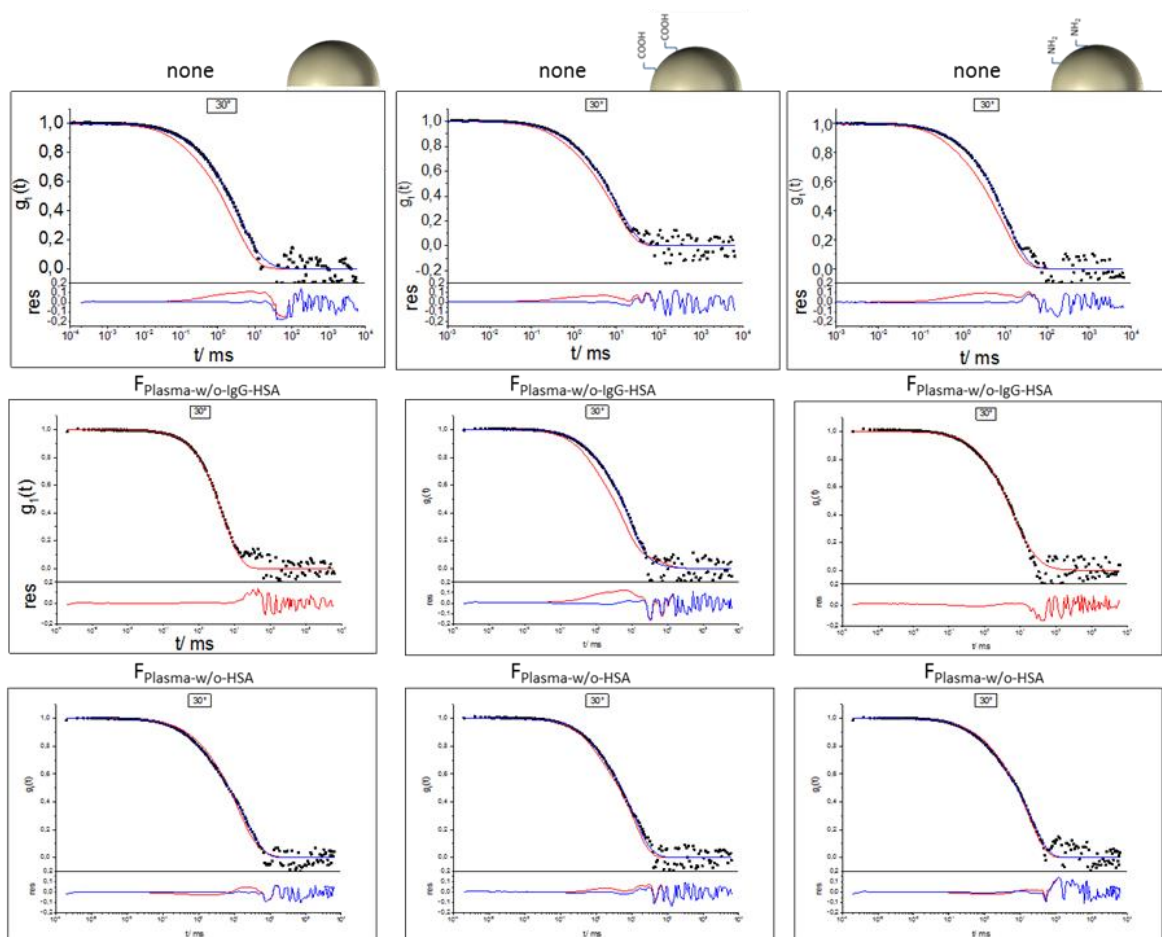


Figure 29. Pre-coating of nanoparticles ($R_h(\text{cp})$) with distinct low abundant protein fractions stabilizes nanoparticles against aggregation in human plasma. A) DLS analysis demonstrates aggregation formation ($R_h(\text{agg})$) of PS particles ($R_h(p)$) in human plasma. ACF of PS particles in human plasma at $\Theta = 30^\circ$ is shown. B) Pre-coating of PS particles with $F_{\text{Plasma-w/o-IgG-HSA}}$ prevents the formation of aggregates. ACFs of the PS particles in isolated $F_{\text{Plasma-w/o-IgG-HSA}}$ at $\Theta = 30^\circ$ is illustrated.

Most intriguingly, PS-COOH and PS-NH₂ pre-coated with IgG remained stable after exposure to human plasma. However, those particles showed a size increase after pre-coating (values see Table 5) in contrast to PS and PS-NH₂ particles pre-coated with F_{Plasma}-w/o-IgG-HSA (values see Table 5).

In order for completeness and better illustration, all ACFs of naked as well as coated particles under *in vivo* conditions are shown in Figure 30. If no additional size could be detected in regards to all scattering angles, no additional force fit was applied.

A)



B)

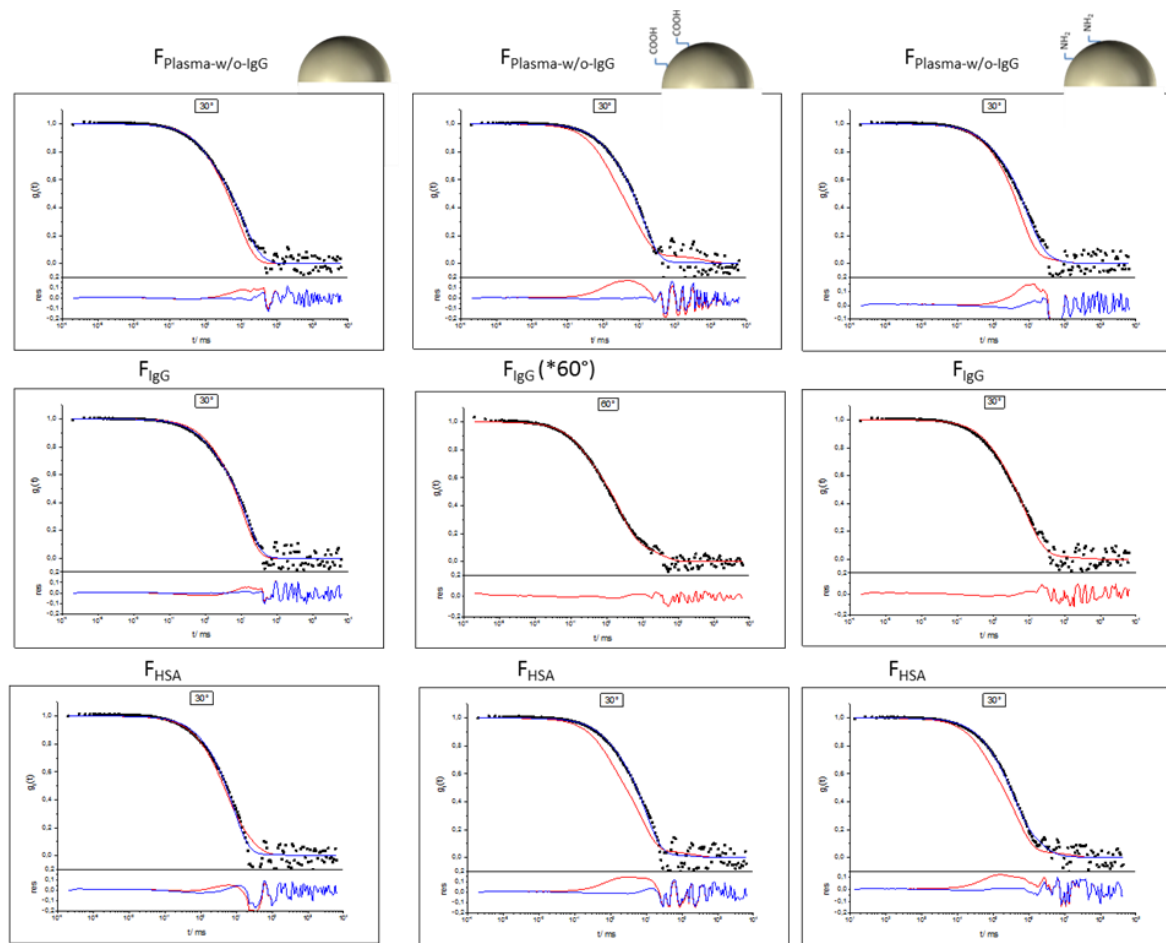


Figure 30. A+B) Angular dependency of the inverse hydrodynamic radii as well as ACF at $\theta = 30^\circ$ including data points (\bullet), force fit (red), and fit including aggregate formation (blue) of naked as well as coated PS particles in concentrated human plasma (comparable to *in vivo* conditions).

In order to get a better understanding of the obtained DLS results SDS-PAGE was used to analyze the protein patterns of the different PS particles after incubation in the different protein fractions as well as after subsequent incubation in human plasma. Both incubations were carried out for 1 h at 37°C . In Figure 31, the protein patterns are shown. “S” describes the single incubation of PS particles in the respective protein fraction, whereas “D” describes the incubation in a protein fraction with subsequent incubation in human plasma.

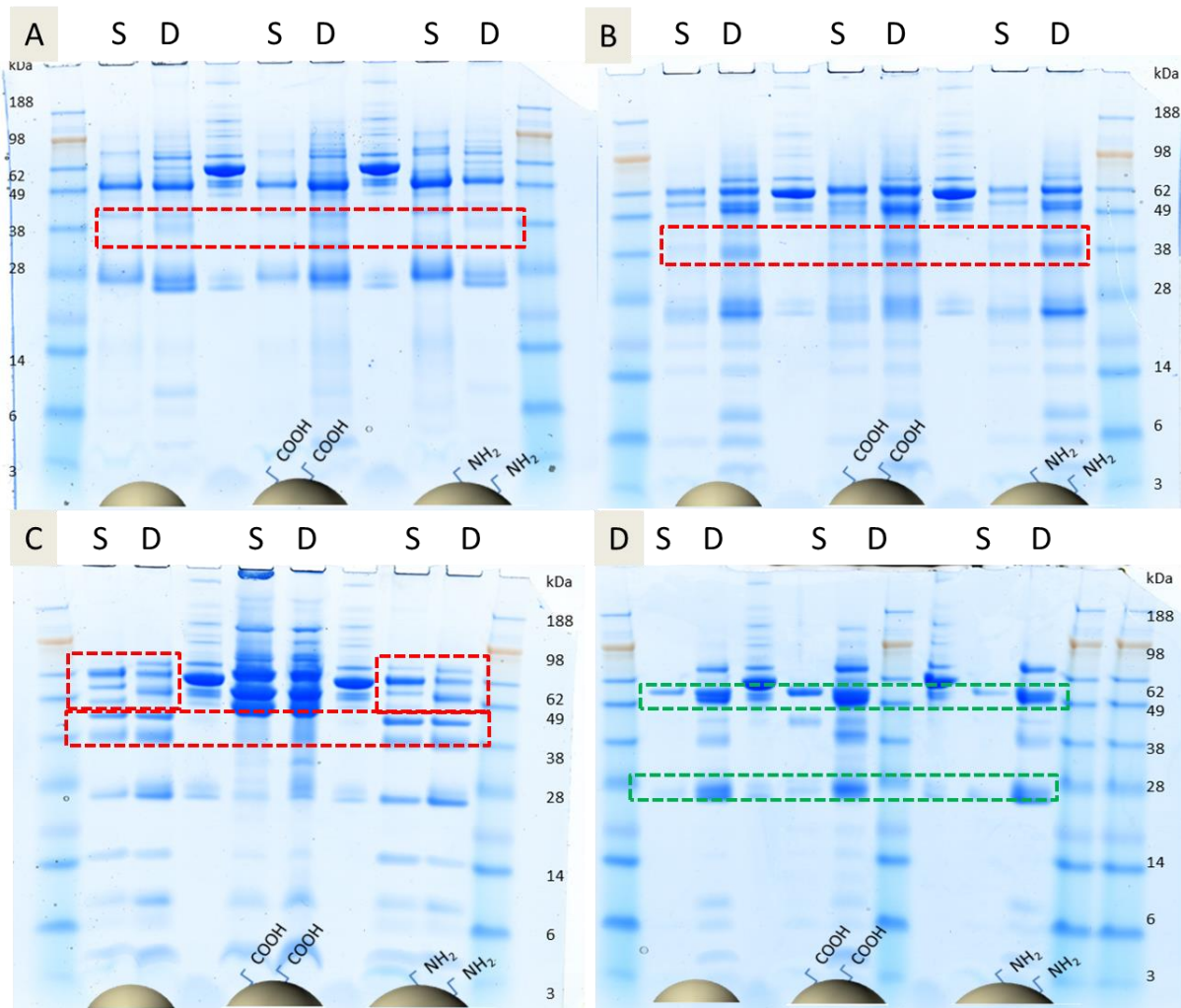


Figure 31. Protein patterns of formed hard coronas with single (S) as well as double incubation with subsequent plasma incubation (D) of PS particles in A) IgG, B) HSA, C) $F_{\text{Plasma-w/o-IgG}}$, and D) $F_{\text{Plasma-w/o-IgG-HSA}}$.

As already shown in Figure 23.A, the protein patterns of the three different polystyrene particles show very intense bands in the range between ~ 35 - 45 kDa after incubation in human plasma. Figure 31.A shows single incubation in F_{IgG} as well as double incubation in F_{IgG} and human plasma. The results of the single incubation show, that the protein corona pattern varies with the pool of proteins present in the incubation medium. For the double incubation, the patterns look very similar to the corresponding patterns of the IgG-coated particles. Significant is the absence or very weak presence of proteins in the range between ~ 35 - 45 kDa (marked in red) that are the most abundant ones for single incubation in human plasma. This shows that the once formed protein corona is stable even after re-introduction in human plasma. For the single incubation of PS particles in

HSA (Figure 31.B) the protein patterns also show the absence or very weak presence of protein bands at the already described molecular weight range. Nevertheless, after subsequent incubation in human plasma, a protein band at ~ 28 kDa becomes visible for all particles. Figure 31.C shows the protein patterns for single and double incubation with IgG depleted plasma. Despite looking very similar for the single as well as double incubation in the first place, differences in the protein patterns could be observed for PS and PS-NH₂ in the higher molecular range between ~ 62 and 98 kDa. As requested also for the incubation in HSA, this shows, that the protein corona formation continues during the double incubation. This could be an explanation for the detected aggregate formation of the coated particles that were observed with DLS upon exposure to human plasma. Figure 31.D shows the protein patterns after single as well as double incubation of the three PS particles. The most intense protein bands at ~ 28 kDa and ~ 50 kDa for the single incubation remain the most intense bands also after subsequent incubation in human plasma. Despite the appearance of additional protein bands, this indicates, that the protein corona formed upon single incubation is somehow solid. Again, a correlation to the stabilization of coated PS and PS-NH₂ in concentrated human plasma can be drawn.

Taken together, these results show that an artificially created protein corona can enable the stabilization of nanoparticles against aggregation in human plasma and moreover, offers the possibility to specifically trigger cellular uptake behavior. Once formed, an artificially created protein corona remains stable in particular cases when re-introduced in human plasma.

3.2.5 THE IMPACT OF PROTEIN CONCENTRATION ON PARTICLE AGGREGATION AND STABILIZATION VIA PRE-COATING

When inspecting Table 3 (see chapter 3.2.4), the three differently functionalized polystyrene nanoparticles change their size in some protein fractions only very slightly. As already pointed out, aggregate formation can in general involve nanoparticle bridging, the adsorption of proteins or protein-protein aggregates on the nanomaterial's surface. This chapter addresses the question which processes are involved when DLS detects small size increases of the particles. It is possible that the small size increases can be related solely

to the formation of a protein corona around the nanomaterials. Another explanation could also be a small percentage of bridged nanoparticles due to incomplete protein coverage on the particles' surfaces. So far, the processes cannot be distinguished with DLS.

In order to get a better understanding, the aggregation of PS-COOH in $F_{\text{Plasma-w/o-IgG}}$ was chosen for further investigations. For the conditions discussed in the previous chapter, a size increase of PS-COOH particles in the respective protein fraction of 45% was detected. Theoretically, 1 mg protein for the discussed particle surface area of $5 \times 10^{-4} \text{ m}^2$ would be enough to cover the entire particle surface area. $F_{\text{Plasma-w/o-IgG}}$ contains mostly HSA. As approximation, an overall molecular weight of $\sim 70 \text{ kDa}$ can therefore be assumed. This means that in 1 mg overall protein amount a number n of 8.6×10^{12} single proteins is present. As human serum albumin belongs to the group of globular proteins (see also introduction part of this work), the overall surface area of proteins can be estimated with the following equation:

$$\text{surface area proteins} = n \times O \quad (13)$$

$$O = 4\pi r^2 \quad (14)$$

Here, n describes the number of proteins and O the surface area of one globular protein. With DLS, a radius r of $\langle 1/R_h \rangle_z^{-1} = 7.6 \text{ nm}$ for $F_{\text{Plasma-w/o-IgG}}$ was determined (see also Table 2, chapter 3.1). Using equation (14) for the surface area of a sphere, a surface area of 726 nm^2 for one protein can be calculated. When applying equation 13, this leads to an overall protein surface area of 60 cm^2 , a value that is 12.5 times bigger than the particle surface area of 5 cm^2 . Nevertheless, $F_{\text{Plasma-w/o-IgG}}$ still represents a mixture of proteins with different affinities to PS-COOH. It is possible that only distinct proteins adsorb onto the nanomaterial's surface and the coverage is not complete. In order to investigate this, the amount of present proteins during incubation of PS-COOH was varied and the influence on particle size investigated via DLS. Figure 32 shows the ACFs including data points, force fit and fit considering aggregate formation of each sample at $\Theta = 60^\circ$.

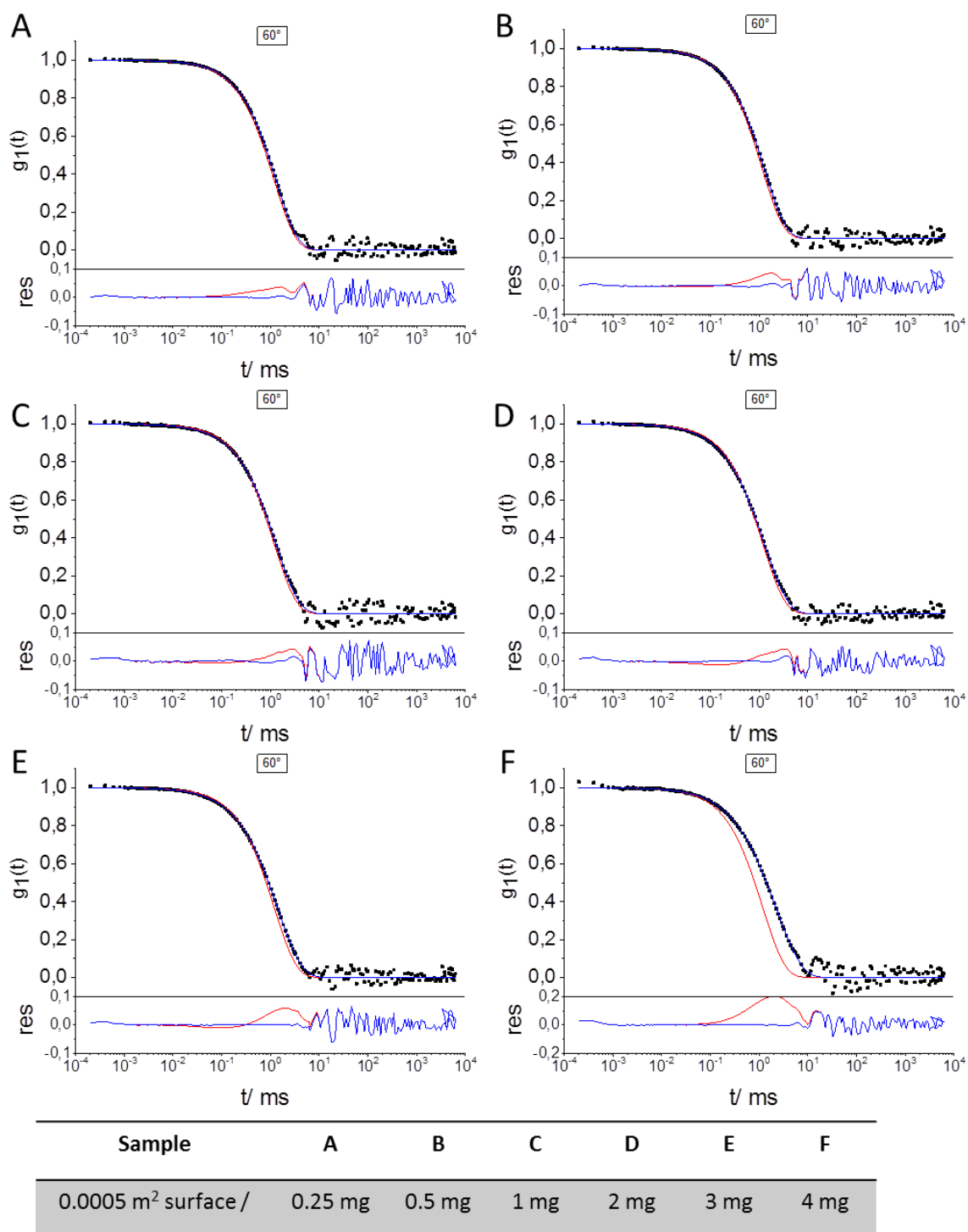


Figure 32. Autocorrelation function at $\Theta = 60^\circ$ of PS-COOH in $F_{\text{Plasma-w/o-IgG}}$ including data points (\bullet), force fit (red) and fit with aggregate formation (blue). From A to D, the protein amount per surface area was increased by a factor of 16.

Figure 33 shows the respective size increase of formed aggregates in each sample together with the intensity contribution (%) at $\Theta = 30^\circ$ of aggregate (green) and particle (red).

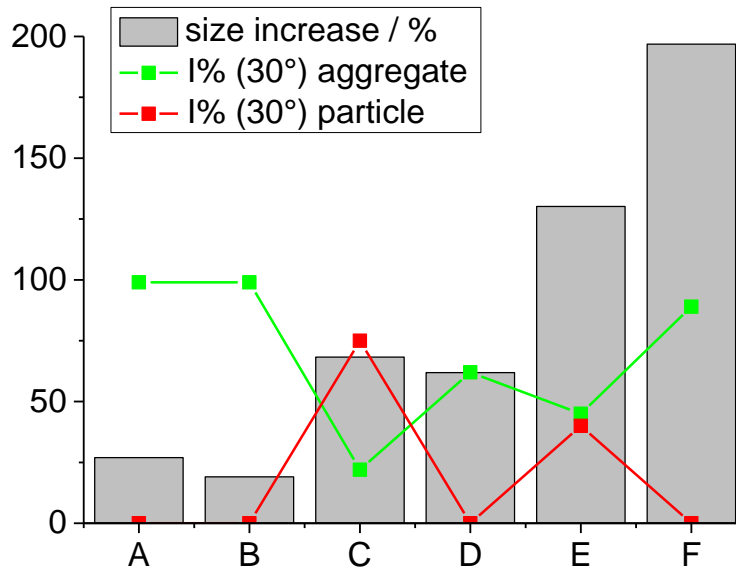


Figure 33. Size increase of PS-COOH in $F_{\text{Plasma-w/o-IgG}}$ with increasing amount of proteins per given surface area of nanomaterial. The intensity contribution at $\Theta = 30^\circ$ to the overall scattered light of aggregates is illustrated in green, the one of particles in red.

In general, the size of formed aggregates increased with increasing amount of present proteins during incubation. For very low protein concentrations (see Figure 32 and 33 A + B) a size increase of 24 – 27% was observed. This corresponds to 12 – 17 nm particle increase in radius and is in good agreement with the observed size increase of PS-COOH in concentrated human serum after one centrifugation step representing the formed hard corona under saturated conditions (see Figure 25, size increase ~ 20 nm in radius). In addition, the particle in original size was not detectable anymore within the mixture, the formed small “aggregates” contributed 99% to the overall scattered light at $\Theta = 30^\circ$.

When the amount of proteins was increased to 1 mg (sample C) or 2 mg (sample D) per given surface area, the PS-COOH particles increased $\sim 60\%$ in radius. For 1 mg, the particles predominated the scattered light at $\Theta = 30^\circ$ with a contribution of 1% = 75%, while for 2 mg the aggregates predominated with 1% = 62%. This indicates that with increasing amount of proteins, the degree of aggregation increases. In addition, the overall size increase contradicts the assumption of incomplete surface coverage leading to bridged nanoparticles for the determined size increase of PS-COOH in $F_{\text{Plasma-w/o-IgG}}$ that was observed and discussed in the previous chapter 3.2.4.

The presumption that bridged nanoparticles are not the origin for the observed small size increases becomes even more likely when looking at sample E and F in Figure 32 and 33. These samples represent the highest amount of proteins during incubation of PS-COOH particles in $F_{\text{Plasma-w/o-IgG}}$. The observed size-increase amounts 127 – 194% and again, the aggregates predominated the scattered light for very high protein concentrations (sample F). All in all, the DLS results suggest that at very low concentration the proteins adsorb onto the nanomaterial's surface and tend to induce protein-protein aggregation on the nanoparticles that also involve the accumulation of particles when the protein amount is increased.

In order to tighten these suggestions, chosen samples have also been investigated with FCS performed by Jennifer Schultze (PhD student in the group of Dr. Kaloian Koynov, AK Butt, Max-Planck-Institute for Polymer Research, Mainz). In contrast to DLS, FCS only detects fluorescent species within the sample under investigation, namely the particles. An averaged size can be detected and in addition, the determined fluorescent brightness (in counts per fluorescent object) implies information about possible aggregate formation containing multiple particles. In general, FCS measurements of the PS particles under investigation included difficulties. The concentration used for DLS measurements is very low in comparison to the ones than are usually used for FCS measurements (magnitude of 10). Moreover, the particles are very hydrophobic and tended to adsorb onto the partially hydrophobic (due to surface modification) bottom glass slide of the used FCS measurement chambers (Nunc® Lab-Tek). Therefore, only trends can be observed and discussed. For PS-COOH particles in buffer, a hydrodynamic radius of $R_h \sim 60$ nm was determined by FCS, which is in good agreement with the size determined by DLS. The fluorescent brightness was in the range of 66 kHz for the used excitation laser intensity. When $5 \times 10^{-4} \text{ m}^2$ surface area of PS-COOH particles were incubated in 1 mg $F_{\text{Plasma-w/o-IgG}}$ protein solution (sample C), the averaged hydrodynamic radius increased to $R_h \sim 80$ nm. Simultaneously, the fluorescent brightness increased to 440 kHz. This means that the small size increase that was also detected in DLS includes the formation of aggregates containing more than one particle. When the amount of proteins during incubation was quadruplicated (sample F), the averaged detected size using FCS was in the range of $R_h \sim 110$ nm and the fluorescent brightness at 250 kHz. The trend for increasing size with increasing protein amount during incubation correlates again with the DLS measurements.

In addition, the formed aggregates contained once more multiple PS-COOH particles which became apparent in the fluorescent brightness. The sample C was measured 1 h later than sample F which could be one possible explanation for the higher brightness. Still, the trend of increasing the fluorescent object's brightness after incubation in $F_{\text{Plasma-w/o-IgG}}$ is valid.

Altogether the results presented in this chapter lead to the assumption that aggregate formation includes the formation of species containing multiple particles. As the aggregate size and degree of aggregation increase with increasing protein amount during incubation, the process is supposed to involve protein-protein aggregation on the nanomaterial's surface that lead to the accumulation of particles.

Another experimental setup that sheds light on the question whether the PS-COOH surface area of $5 \times 10^{-4} \text{ m}^2$ is covered completely when incubated in 1 mg $F_{\text{Plasma-w/o-IgG}}$ is the pre-coating procedure (see also chapter 3.2.4) with subsequent introduction of coated particles into concentrated human plasma. The amount of proteins per given surface area during incubation was therefore doubled, tripled and quadruplicated. Afterwards, the physicochemical parameters like size and zeta potential as well as the stability of coated particles against aggregation was monitored using DLS. The size of the coated particles determined via DLS and the zeta potential are summed up in Table 7.

Table 7. Physicochemical parameters of coated PS-COOH particles in $F_{\text{Plasma-w/o-IgG}}$.

pre-coating of $5 \times 10^{-4} \text{ m}^2$ surface area in	none	1 mg	2 mg	3 mg	4 mg
$\langle 1/R_h \rangle_z^{-1} / \text{nm}$	63	90	87	90	92
zeta potential / mv	$- 27.5 \pm 0.5$	$- 25.9 \pm 0.5$	$- 27.6 \pm 0.2$	$- 26.8 \pm 1.1$	$- 23.1 \pm 1.2$

The size of the coated particles determined by DLS was found to be independent of the protein amount used for the coating procedure in the range of $\langle 1/R_h \rangle_z^{-1} = 87 - 92 \text{ nm}$. Also for the zeta potential no significant trend for varying protein amount was observed.

The coated as well as non-coated particles in Table 7 were introduced into concentrated human plasma and their stability against aggregation monitored using DLS.

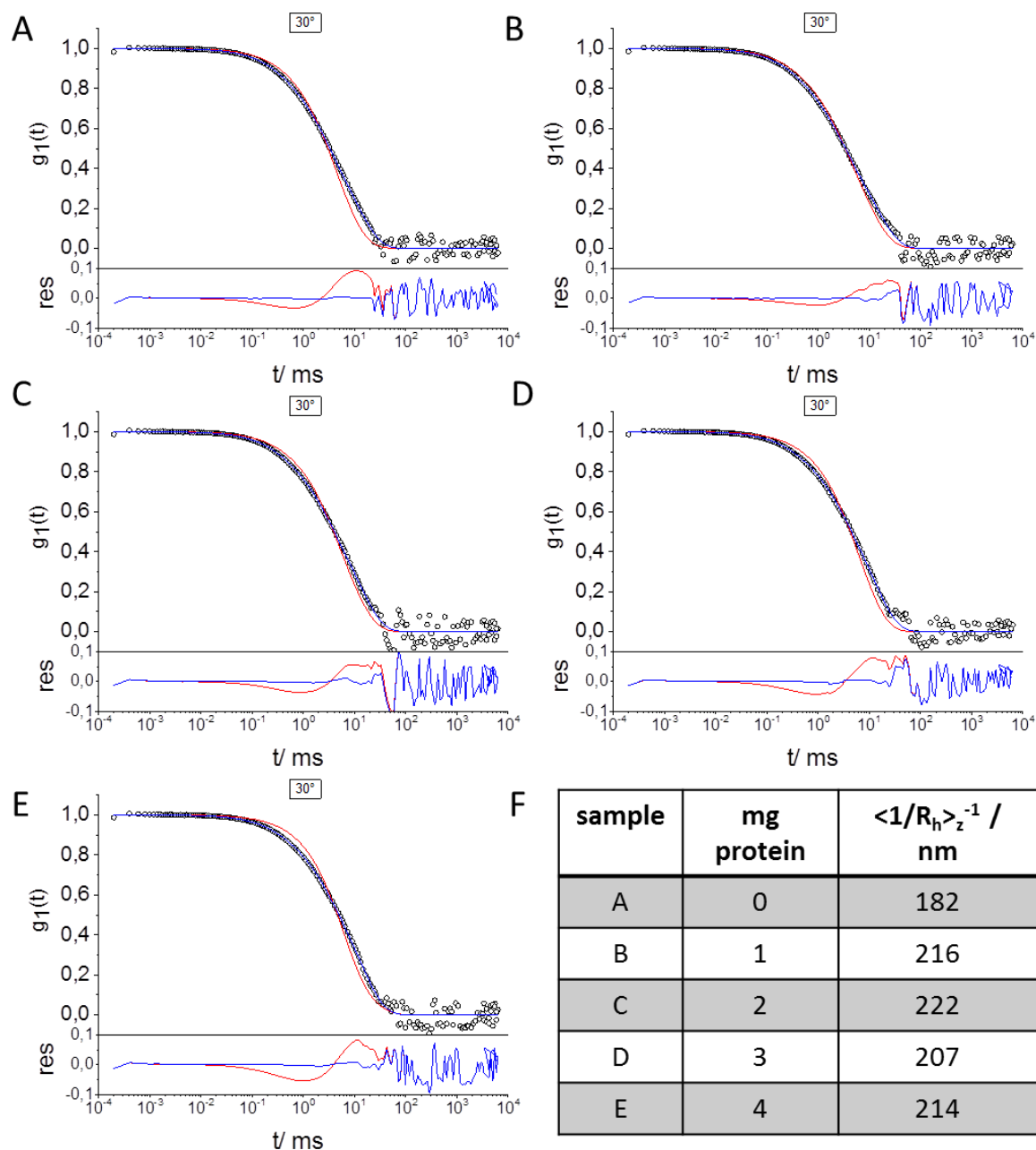


Figure 34. ACF at $\Theta = 30^\circ$ including data points, force fit and fit with aggregation in concentrated human plasma of A) PS-COOH, B) PS-COOH coated with 1 mg $F_{\text{Plasma-w/o-IgG}}$, C) PS-COOH coated with 2 mg $F_{\text{Plasma-w/o-IgG}}$, D) PS-COOH coated with 3 mg $F_{\text{Plasma-w/o-IgG}}$, E) PS-COOH coated with 4 mg $F_{\text{Plasma-w/o-IgG}}$. F) Observed aggregated sizes in concentrated human plasma of samples A – E.

Figure 34 shows the ACF of “naked” as well as coated PS-COOH with $F_{\text{Plasma-w/o-IgG}}$ in concentrated human plasma at $\Theta = 30^\circ$. In general, all coated particles formed aggregates in the size range of $\langle 1/R_h \rangle_z^{-1} (\text{agg}) = 207 - 222 \text{ nm}$. The observed size increase was therefore independent of the protein amount used for the pre-coating procedure. The observed results are in good agreement with the already discussed results of chapter 3.2.4 with obtained aggregates in the range of $\langle 1/R_h \rangle_z^{-1} = 256 \text{ nm}$ for coated PS-COOH particles with $1 \text{ mg } F_{\text{Plasma-w/o-IgG}}$ (see also Table 6). This underlines the previous discussed assumption that the coverage of PS-COOH particles in $F_{\text{Plasma-w/o-IgG}}$ is complete even for the chosen and in comparison low protein amount of $1 \text{ mg} / 5 \times 10^{-4} \text{ m}^2$ particle surface area.

To make sure that the entire particle surface area is covered, LC-MS measurements were performed. $0.5 \text{ mg } F_{\text{Plasma-w/o-IgG}}$ were used for the incubation of $5 \times 10^{-4} \text{ m}^2$ overall surface area of PS-COOH particles. The coated particles were afterwards incubated in concentrated human plasma and the protein corona profile determined after single and double incubation via LC-MS. Table 8 presents the top 20 identified proteins of the protein coronas formed on PS-COOH particles after incubation in concentrated human plasma (1), IgG-depleted plasma (2), and IgG-depleted plasma with subsequent incubation in concentrated human plasma (3). Especially the three highest abundant proteins after incubation in IgG-depleted plasma, namely fibrinogen gamma chain, fibrinogen beta chain, and fibrinogen alpha chain remain the most abundant proteins present in the particles' protein corona even when reintroduced in concentrated human plasma. For single incubation in concentrated human plasma the most abundant protein within the particle's hard corona was vitronectin. In addition to the enrichment of fibrinogen, the amount of apolipoprotein A-I is significantly reduced for single and double incubation (see sample 2 and 3 in Table 8).

Altogether, the presented results confirm that the chosen ratio for the pre-coating procedure introduced in the previous chapter is sufficient for complete surface coverage. The elevation of protein amount did not lead to a change in particle stability against protein induced aggregation.

Table 8. Top 20 identified proteins in the protein corona formed on PS-COOH particles after incubation in concentrated human plasma (1), IgG-depleted plasma (2), and IgG-depleted plasma with subsequent incubation in concentrated human plasma (3) determined via LC-MS (LC-MS measurements were performed by Johanna Simon).

	1	2	3
Fibrinogen gamma chain	2.19	32.59	20.71
Fibrinogen beta chain	1.44	22.84	14.93
Fibrinogen alpha chain	2.05	18.21	11.8
Clusterin	12.5	3.45	6.83
Ig mu chain C region	0.8	1.74	1.36
Beta-2-glycoprotein 1	7.63	1.6	2.81
Serum albumin	3.14	1.6	1.41
Vitronectin	33.38	1.47	19.16
Transthyretin	0.53	1.36	1.18
Apolipoprotein E	4.96	0.8	2.58
Apolipoprotein A-I	12.96	0.67	1.7
Ig kappa chain C region	2.02	0.5	0.95
Inter-alpha-trypsin inhibitor heavy chain H4	2.8	0.25	1.4
Ig gamma-1 chain C region	0.77	0.2	0.43
Ig lambda-2 chain C regions	0.53	0.14	0.36
Complement C1q subcomponent subunit B	0.55	0.13	0.11
Ig gamma-3 chain C region	0.6	0.12	0.2
Complement factor H-related protein 1	0.52	0.1	0.3
Complement C1q subcomponent subunit C	0.66	0.06	0.16
Lipopolysaccharide-binding protein	0.71	0.02	0.2

3.2.6 USING PROTEIN MIXTURES AS SURFACTANTS FOR PARTICLE STABILIZATION

Going one step further, the question arose whether it is possible to use the obtained protein fractions for stabilization of particles from the beginning, meaning as amphiphilic stabilizer (“surfactant”) during synthesis. $F_{\text{Plasma-w/o-IgG}}$ was chosen as the most suitable protein mixture as it is the protein mixture with the highest concentration of proteins after removal of one high abundance protein. The critical aggregation or micelle concentration (CMC) determination of the respective protein solution is shown in Figure 35.

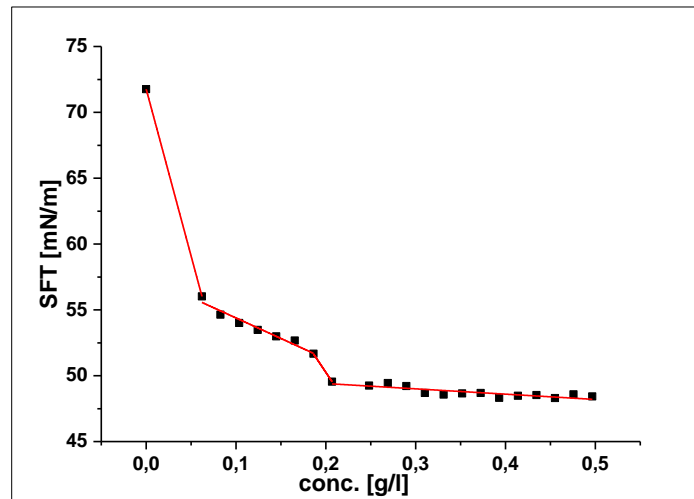


Figure 35. Surface tension of a solution of $F_{\text{Plasma-w/o-IgG}}$ in water in dependence to the protein concentration.

As $F_{\text{Plasma-w/o-IgG}}$ represents a mixture of proteins, no distinct CMC or critical aggregation concentration could be determined. Moreover, the trend of surface tension at the air/water interface shown in Figure 29 shows approximately two plateaus. This indicates that micelle (or aggregate) formation takes place subsequent when reaching a CMC of a protein component in the still very complex mixture. In addition, the values for amphiphile (“surfactant”) concentration are very low compared to conventional ones such as sodium dodecyl sulfate (SDS). SDS has a CMC in water of 8.2 mM. As IgG depleted plasma contains mostly albumin a molecular weight of the protein mixture can be assumed in the range of 70 kDa. 0.2 g/L of proteins would therefore correspond to a 0.003 mM solution. This would correlate to a reduction of amphiphile amount with a factor of 2500 compared to SDS. As the surface tension in emulsion is much bigger than for the air/water interface only and the surfactant under investigation very complex, an amount of 1 g/L for the polymerization of styrene was chosen (~4 w%).

Polystyrene was synthesized via direct mini-emulsion using either V59 or V70 as initiator. V59 was chosen because it is the standard initiator of the so far discussed particles. V70 was chosen in addition, because it has a lower half-life decomposition temperature than V59 (67 °C), in fact 30 °C, which is lower than the denaturation temperature of proteins.

Both structures are shown in Figure 36. The exact sample composition will be given in the experimental part.

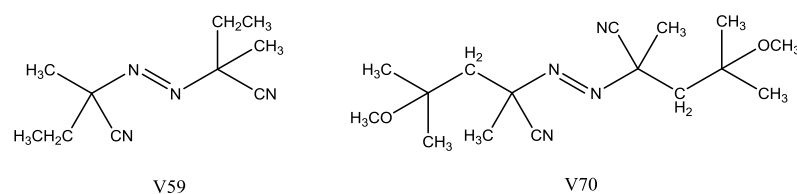


Figure 36. Chemical structure of V59 (left) and V70 (right).

After sonication and stirring over night at 30 °C or rather 67 °C, the sample with V70 at 30 °C did not lead to particle formation which is probable due to an inefficient radical formation or capture of the formed radicals by presence of the proteins amino groups.¹³³ However, for the sample with V59 as initiator particles with a diameter of 230 nm could be obtained. The corresponding DLS results as well as TEM images are shown in Figure 37. The molar ratio of monomer:surfactant was calculated to $\sim 13700:1$. This is compared to the lutensol stabilized particles discussed in this chapter very high (M:S = 290:1) and underlines again the low protein amount needed for stabilization compared to low molecular surfactants (see page 68) and also polymeric surfactants as lutensol.

DLS measurements were repeated after four months in order to investigate the stability of the respective dispersion. No size change could be detected meaning that the dispersion remained stable.

When looking at the TEM images in Figure 37, the particles seem to be smaller than the values determined by DLS. The latter method is very sensitive towards bigger species within the mixture and could therefore lead to bigger values. By TEM imaging, an average radius in the range between 75 and 100 nm was observed.

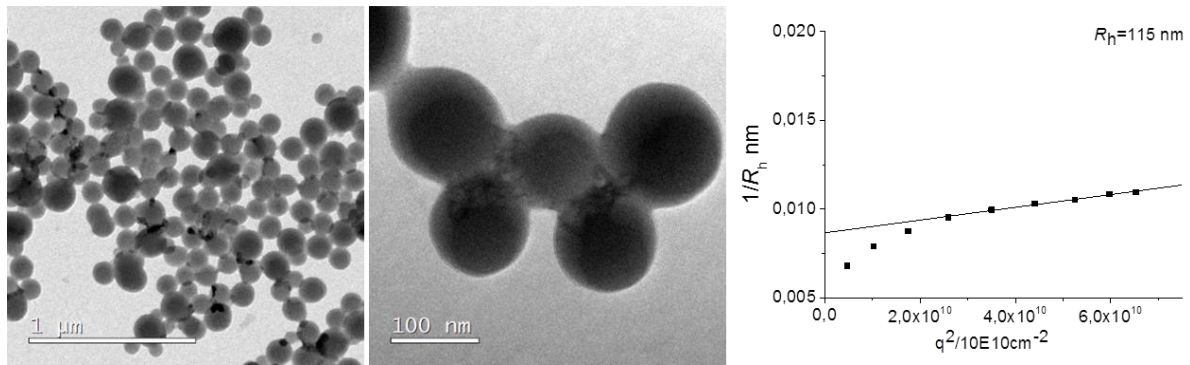


Figure 37. TEM images as well as DLS results of polystyrene with $F_{\text{Plasma-w/o-IgG}}$ as stabilizer.

For the evaluation of stability against aggregation, the particle was introduced into concentrated human plasma. Figure 38.A shows the ACF at 30° , Figure 38.B the angular dependency of the observed hydrodynamic radii.

In the presence of concentrated human plasma aggregates were formed, that are about 1.9 times bigger than the original particles. The intensity contribution of formed aggregates at $\Theta = 30^\circ$ was determined to 41%. This is comparable to the behavior of the three different Lutensol stabilized polystyrene particles in plasma as discussed in chapter 3.2.2. But in contrast, no additional chemical surfactant is needed.

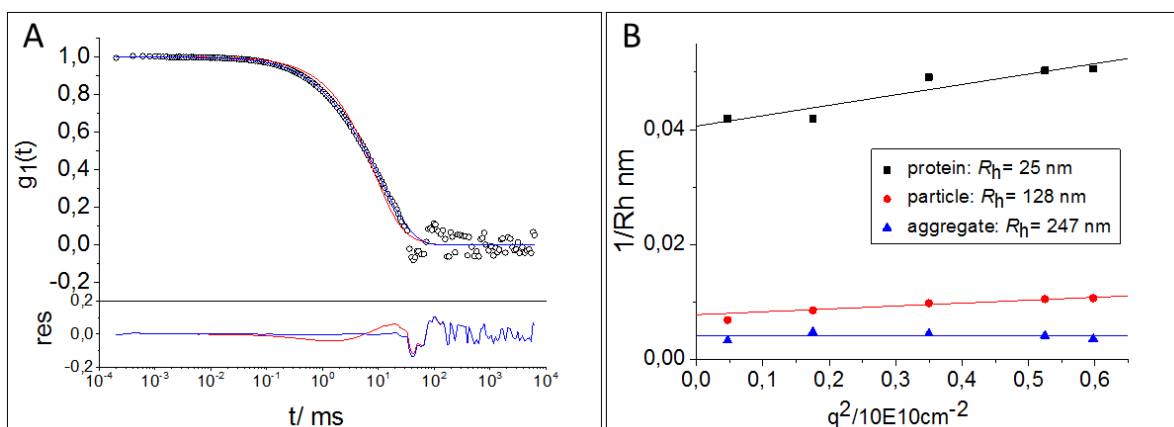


Figure 38. Angular dependency of the inverse hydrodynamic radii as well as ACF at $\Theta = 30^\circ$ including data points (O), force fit (red) and fit including aggregate formation (blue) of protein stabilized particle in human blood plasma.

The protein stabilized particles were investigated via CellTiter-Glo Assay regarding their cytotoxicity (Figure 39). For a concentration of 75 $\mu\text{g}/\text{mL}$, protein stabilized particles reduced the metabolic activity of the RAW 264.7 cells in an acceptable range of only $\sim 10\%$. This would be important for *in vitro* experiments that are typically performed under these conditions. Even when the amount of particles was doubled, the majority of cells kept their metabolic activity. Lutensol stabilized particles showed almost no effect on the metabolic activity of the cells.

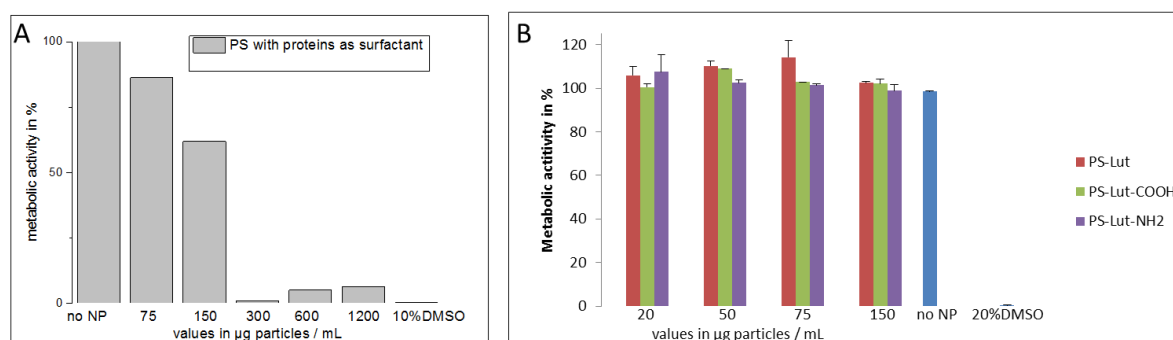


Figure 39. A) CellTiter-Glo Assay of PS with proteins as surfactant. B) CellTiter-Glo Assay of Lutensol stabilized PS-particles (data in B provided by Johanna Simon).

SDS-PAGE was used to analyze the protein pattern of the particle itself and compared to the one of IgG-depleted plasma as discussed previously. The patterns are shown in Figure 40. The most abundant protein on the polystyrene particle is albumin that is also most abundant in $F_{\text{Plasma-w/o-IgG}}$. But in contrast to the mixture itself, a second protein of ~ 98 kDa is enriched on the nanomaterial's surface. As already shown in Figure 31.C, the protein corona patterns of PS, PS-NH₂ and PS-COOH stabilized with Lutensol also show more than one intense protein band after incubation in $F_{\text{Plasma-w/o-IgG}}$. Only PS-COOH shows protein bands in the higher molecular range and there is only a very weak band at ~ 98 kDa. On the one hand this shows again that the most abundant proteins present in a mixture like albumin are not necessarily most abundant in a particle's protein corona or have the highest affinity to it. As Lutensol AT50 is a nonionic surfactant with the molecular formula $\text{C}_{(16-18)}\text{O}(\text{CH}_2\text{CH}_2\text{O})_{50}\text{H}$ and contains a PEG chain of about 50 monomers, it plays a strong role in the protein adsorption. As shown in the literature, PEGylated polystyrene particles

adsorb a lot of clusterin on their surface.¹⁰⁷ A corresponding protein band at 38 kDa can be observed for non-functionalized PS in IgG depleted plasma as shown in Figure 31 as well.

In conclusion, it is possible to stabilize PS particles with IgG depleted plasma without the need of an additional low molecular weight surfactant. The effect on the metabolic activity of cells is suitable for *in vitro* experiments while the aggregation behavior in concentrated human plasma is similar to the previously discussed Lutensol stabilized polystyrene particles. As a benefit, the impact of Lutensol on protein adsorption can be excluded.

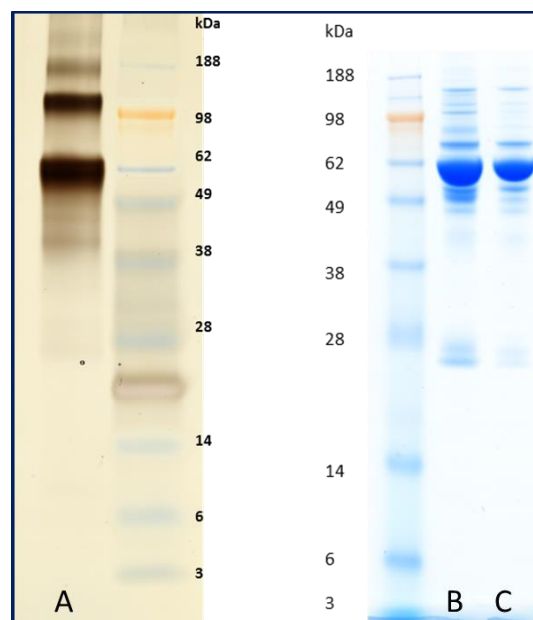


Figure 40. SDS-PAGE of A) PS stabilized with $F_{\text{Plasma-w/o-IgG}}$, B) plasma, and C) $F_{\text{Plasma-w/o-IgG}}$.

3.2.7 SUMMARY

In this chapter, the very complex overall process of nanomaterial-plasma interactions was fragmented in low abundance protein and high abundance protein interaction. Single proteins or mixtures could be identified, that play a major role in particle stability against aggregation. With respect to that, polystyrene particles were coated with protein fractions

and decorated with a predetermined “artificial” protein corona. Their effect on cellular uptake in macrophages as well as stabilization against aggregation in concentrated human plasma was demonstrated. The protein fraction $F_{\text{Plasma-w/o-IgG}}$ could be also used for the stabilization of particles as “surfactant” during synthesis.

Altogether this shows that the interactions between plasma proteins and nanomaterials designed for biomedicine can not only limit their application, but can in fact be used as tool for the adjustment and fine tuning of the nanocarrier’s physicochemical properties. The stability of predetermined hard coronas upon exposure to concentrated human blood plasma opens the possibility of defining not only the chemical identity of nanomaterials in the laboratory, but moreover also the biological identity to a certain extend.

3.3 HUMAN BLOOD PLASMA VERSUS SERUM

When looking in the literature, many different protein sources are used for pre-*in vivo* studies on nanomaterials. Fetal bovine serum (FBS) is found as cell culture media supplement and commercially available. In 1975, Honn, Singley and Chavin already pointed out, that a high variability of serum could be observed depending on charge and supplier.¹³⁴ But also human serum or plasma comes into operation for pre-*in vivo* studies. Dawson and coworkers used human plasma to evaluate the differences in protein corona formation on silica and polystyrene nanoparticles depending on the protein concentration during incubation.⁸⁷ In contrast, Walkey *et al.* used human serum in order to investigate the impact of size and surface chemistry on protein adsorption onto gold nanoparticles.¹³⁵

As already pointed out in the introduction part of this work, human blood serum and human blood plasma can be both obtained after blood withdrawal from probands. But they differ in their protein composition depending on the preparation method. For the recovery of plasma from blood, an anti-coagulant has to be added in order to prevent the blood from clotting. The cellular fraction of blood can afterwards be removed via centrifugation. When the blood is allowed to clot prior to centrifugation, human blood serum is obtained that lacks of proteins that are part of the coagulation process. The situation becomes even more complex, as different anti-coagulants can be used for plasma stabilization. Pozzi *et al.*¹³⁶ and Monopoli *et al.*⁸⁷ both used EDTA stabilized human plasma for protein corona studies, whereas Winzen *et al.* used heparin stabilized plasma for the same.¹⁰⁸ The effectiveness of EDTA is based on the complexation of ions that are needed for enzymes as part of the coagulation process. Heparin on the other hand activates anti-thrombin and by this inhibits the coagulation cascade. Very recently, Schöttler *et al.* showed that the protein source as well as the added anti-coagulant affect nanoparticle protein corona and cellular uptake.¹³⁷

In this chapter, the influence of protein source and anti-coagulant on particle aggregation is discussed. CTMA-Cl stabilized polystyrene particles with amino groups on the surface that are already published^{107, 137} were introduced in human blood serum, citrate stabilized plasma, heparin plasma, FBS, and FBS with additional heparin. The aggregation behavior was monitored using DLS. Figure 41, 42, and 43 show the corresponding results.

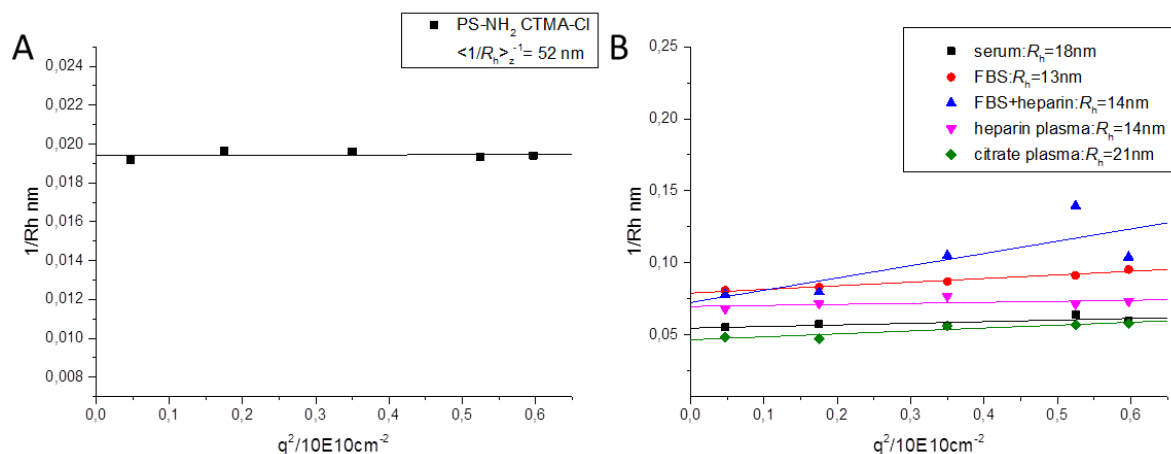


Figure 41. Angular dependency of the inverse hydrodynamic radii of A) PS-NH₂ and B) the different protein sources.

Arising from Figure 41.B the z-averaged inverse hydrodynamic radii of the protein sources differ a lot. While human serum and citrate stabilized plasma show values between $\langle 1/R_h \rangle_z^{-1} = 18$ nm (serum) and $\langle 1/R_h \rangle_z^{-1} = 21$ nm (citrate plasma), the sizes of the other three protein sources were determined to be in a smaller range of $\langle 1/R_h \rangle_z^{-1} = 13$ -14 nm. The influence of the different protein sources on particle stability against aggregation is shown in Figure 42 and 43.

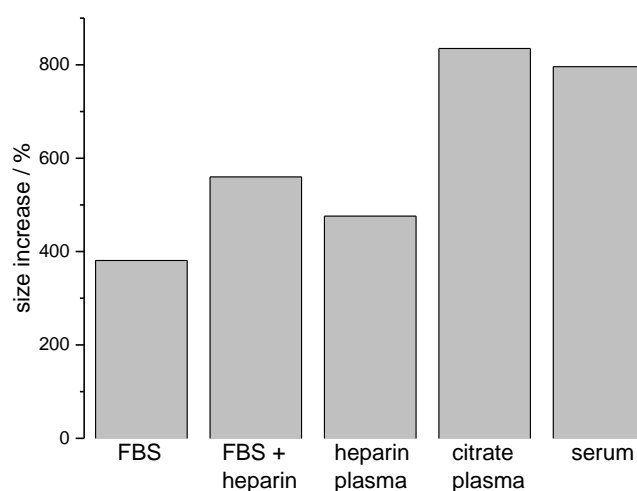


Figure 42. Size increase of PS-NH₂ in the respective protein sources ($\Theta = 30^\circ$).

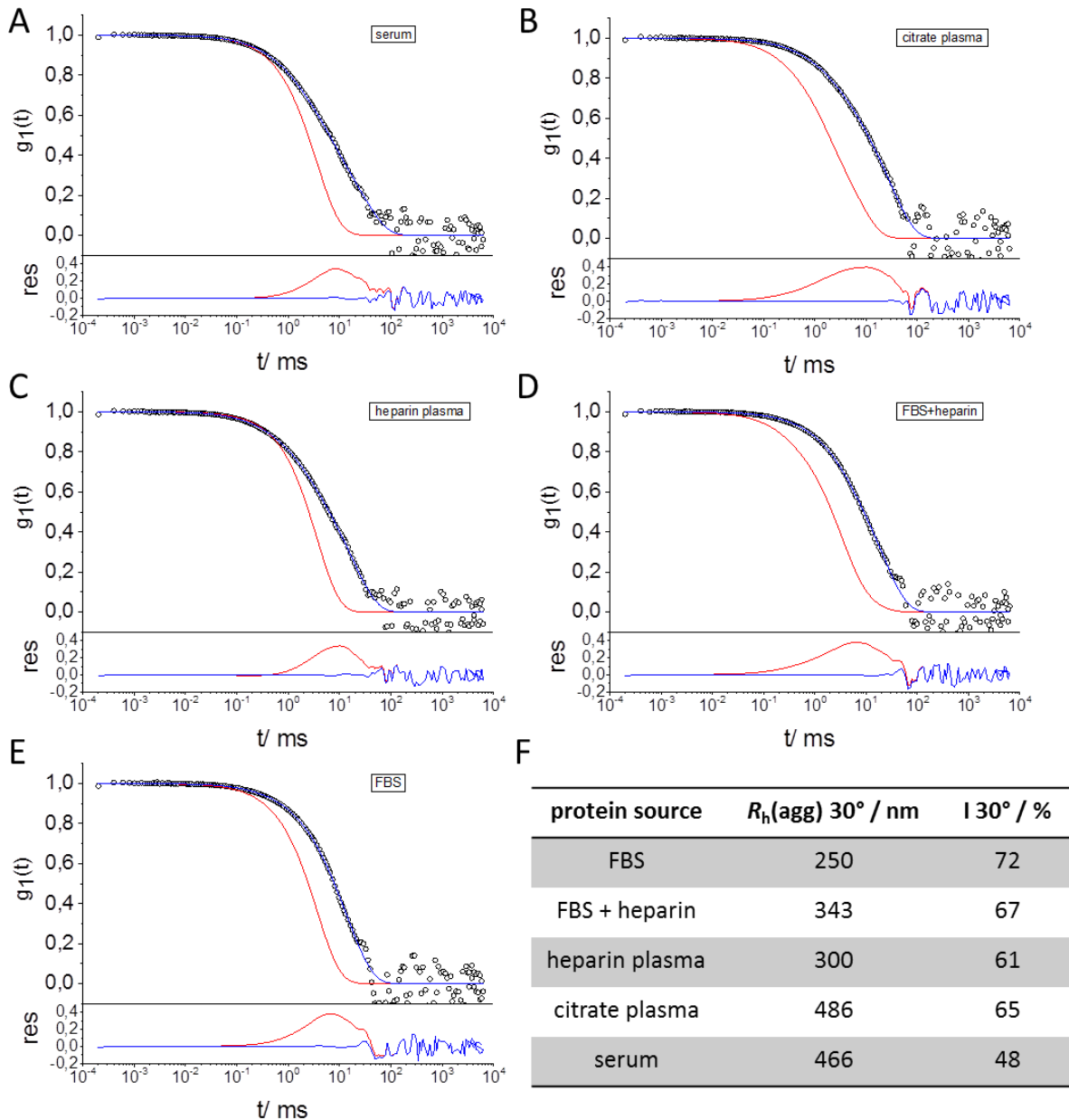


Figure 43. ACF at $\Theta = 30^\circ$ of PS-NH₂ including data points (O), force fit (red) and fit regarding aggregate formation (blue) in A) serum, B) citrate plasma, C) heparin plasma, D) FBS + heparin, and E) FBS. D) Aggregate sizes and intensity contribution at $\Theta = 30^\circ$ determined by DLS.

First of all, all protein sources induce significant aggregate formation when PS-NH₂ is introduced into a respective solution. When the amino-functionalized PS particle was introduced into FBS, aggregates were detected with a radius of $R_h = 250$ nm at $\Theta = 30^\circ$ that corresponds to a size increase of $\sim 380\%$ compared to the initial particle. When heparin was added to FBS prior to the incubation with particles, particle aggregates were

formed that are about 200 nm bigger in diameter than compared to the aggregate formation of PS-NH₂ in FBS solely. This means that the anti-coagulant heparin has a significant influence on particle-protein interactions.

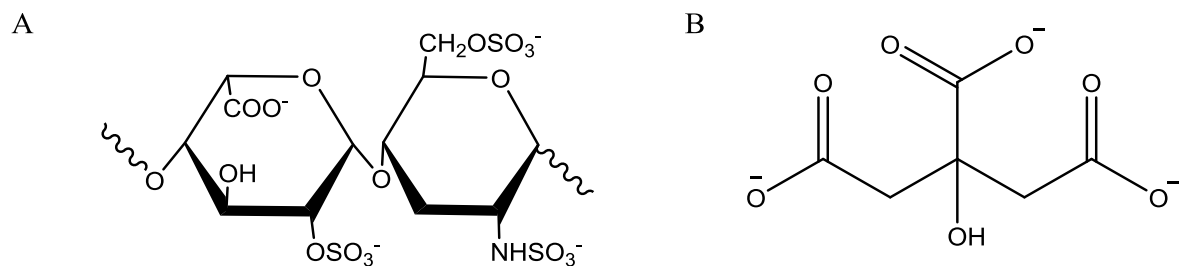


Figure 44. Structure of A) Heparin- and B) Citrate-anion.

As shown in Figure 44.A, heparin is a polyanion with a disaccharide as repeating unit. It activates antithrombin and by this inhibits the coagulation cascade. Due to the high negative charge density in heparin it is supposed to strongly interact with a nanomaterial's surface. The adsorption of heparin on the latter one could lead to interactions with mostly negative plasma proteins resulting in aggregation.

Next, the formed aggregates in human serum or rather citrate stabilized plasma were determined to be in the range between $R_h (\Theta = 30^\circ) = 466$ nm and $R_h (\Theta = 30^\circ) = 486$ nm which is much bigger than the formed aggregates in all other protein sources. On the one hand, these results indicate that human serum and human citrate plasma induce aggregation with size increases that are in a comparable range. On the other hand, the difference between heparin stabilized plasma and citrate stabilized plasma again points out that the choice of anti-coagulant plays a major role for the outcome of *pre-in vivo* experiments. In contrast to heparin, citrate is a threefold negatively charged anion (see Figure 44.B) that complexes ions that are needed for enzymes as part of the coagulation process. Citrate as anion may have an influence on the diffuse Stern layer around the nanoparticles that possibly leads to aggregation.

The impact of the protein source and anti-coagulant on protein corona formation and cellular uptake of PS-NH₂ has already been investigated and published by Schöttler *et al.*¹³⁷ For RAW264.7 macrophages that were already discussed in the previous chapter 3.2, a strong dependence of uptake-behavior and protein source used for incubation was observed. While the incubation of PS-NH₂ in FBS or heparin plasma led to a strong uptake in RAW264.7 macrophages, there was only a very weak uptake detectable after incubation in citrate plasma or human serum. The anti-coagulant therefore also plays a critical role in the outcome of *in vitro* studies. Additionally, the cell experiments strengthen the assumption that citrate plasma and serum lead to comparable results under the mentioned conditions.¹³⁷

Altogether, protein source as well as anti-coagulant play a critical role in protein-particle interactions and therefore influence the outcome of pre-*in vivo* experiments. As the effectiveness of heparin as anticoagulant is based on interactions with proteins, citrate was chosen as anti-coagulant for plasma experiments that complexes ions needed for the coagulation cascade. DLS together with cellular uptake studies from Schöttler *et al.*¹³⁷ indicate that protein induced aggregation of nanoparticles as well as uptake in RAW264.7 macrophages after incubation in serum or rather citrate plasma do not differ in a significant manner.

3.4 EVALUATION OF NANOPARTICLE STABILITY IN HUMAN BLOOD SERUM BY DYNAMIC LIGHT SCATTERING: THE IMPACT OF PERSONALIZED HUMAN BLOOD SERUM COMPOSITION

In the previous chapter, the influence of distinct protein fractions obtained from human blood plasma on particle stability against aggregation as well as protein corona formation was investigated. From literature it is already known that the human blood plasma composition is related to the genetic background or geographical origin of healthy individuals.¹³⁸ As the stability of polystyrene particles has been demonstrated to be strongly dependant on the proteins present during incubation, their stability and interactions with proteins were assumed to be in addition strongly dependent on the composition of individual human blood proteomes. The following chapter addresses the questions of how big the differences of blood composition are between diverse probands and how this can influence the stability of nanocarriers against aggregation. After analysis of six individual sera and one serum pool, the stability of PS particles in the respective protein solution was investigated using dynamic light scattering. In addition, protein corona formation was analyzed using LC-MS. The LC-MS measurements were performed by Johanna Simon. By combining DLS and LC-MS data, a correlation between particle stability under *in vivo* conditions and protein corona composition was evaluated. The already described coating of nanoparticles in order to stabilize them was applied to overcome the limitations arising from personalized blood serum composition. It will be shown within the next chapter, that a once formed protein corona on a nanomaterial's surface remains stable even when re-introducing it into another serum source. This could also be of great interest for nanomaterials that are designed to treat special diseases, meaning that the protein composition of target subject differs from the one of healthy individuals.^{138, 139}

Human blood serum was used for the investigations in this case as the highest number of individual probands was available. This way, the best statistical representation could be obtained. In addition, the influence of anti-coagulant mentioned in chapter 3.3 could be excluded.

3.4.1 ANALYSIS OF INDIVIDUAL AND POOLED HUMAN BLOOD SERUM

As already described in the introduction, the ACF of human serum determined by dynamic light scattering can be described by the sum of three exponentials. Each of them represents one size fraction of serum proteins. Figure 45.A exemplarily shows the ACF of a serum pool from nine different blood donators.

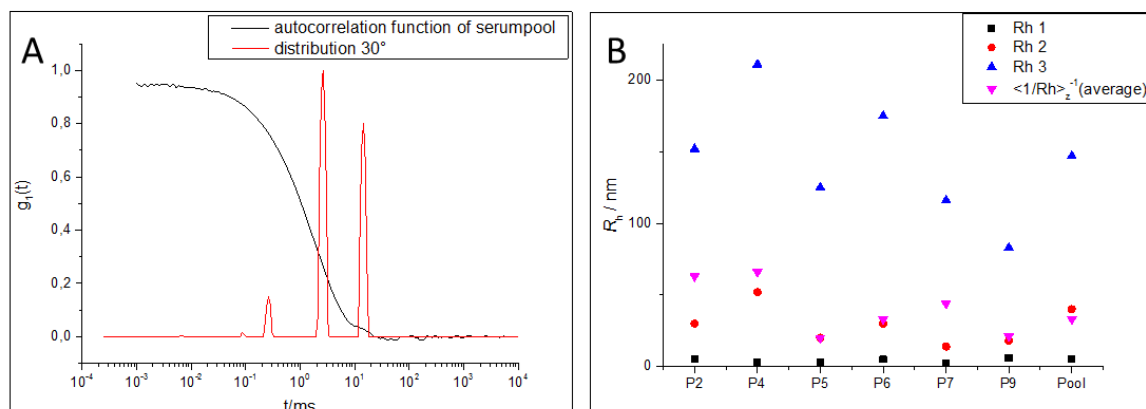


Figure 45. A) Autocorrelation function of serum pool at scattering angle 30° with the distribution of the three different size fractions. B) Fluctuation of the three different size fractions between different probands.

The first size fraction represents smaller proteins such as human serum albumin or IgG. The intermediate fraction comprises slightly bigger proteins like IgM or LDL. The third size fraction is the biggest one and represents mostly lipoproteins, for example big chylomicrons. Depending on the serum composition and the concentration of individual proteins, the hydrodynamic radii of each size fraction can vary. Addressing this question, dynamic light scattering was used to investigate 6 individual sera and one pool regarding their size distribution. Figure 45.B shows the result. For the first size fraction, hydrodynamic radii in the range between $R_{h,1} = 3-6$ nm were detected. For the second one, bigger differences between the sera under investigations were measured. For example, the second protein fraction of P7 was determined to be $R_{h,2} = 14$ nm, while the one of P4 was much bigger with $R_{h,2} = 52$ nm. The biggest size fraction showed values between $R_{h,3} = 83-211$ nm. The variation in sizes of each protein group in consequence leads to a fluctuation of the z-averaged hydrodynamic radii. This fluctuation becomes also

apparent in Figure 46 showing exemplarily the ACFs at $\Theta = 30^\circ$ for individual sera P4 and P5 and the one of pooled human serum.

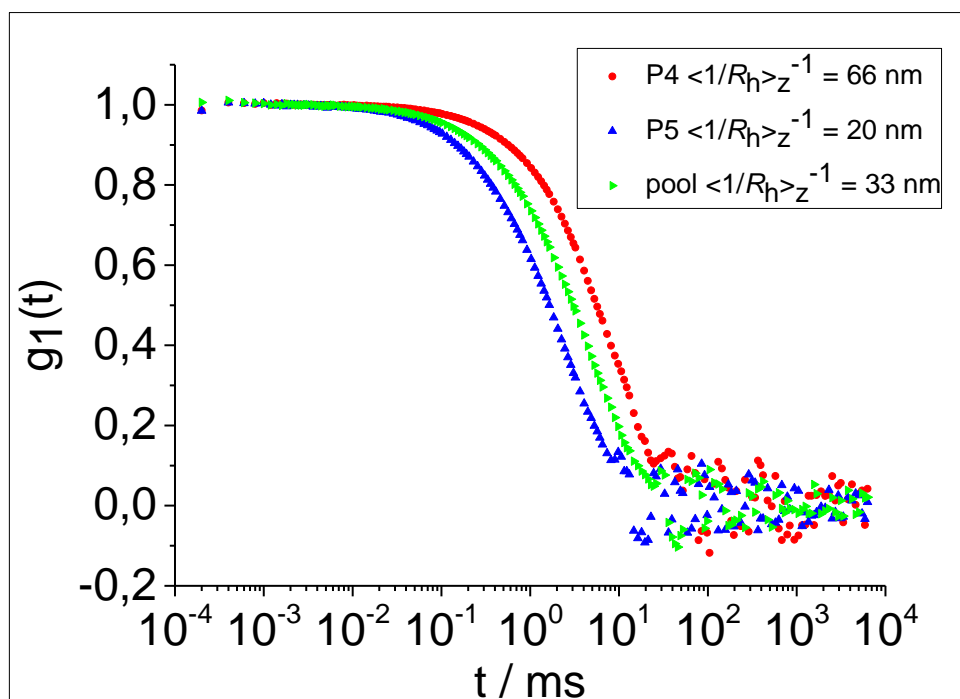


Figure 46. ACF at $\Theta = 30^\circ$ for serum P4 (red), P5 (blue) and pooled human serum (green).

In addition to dynamic light scattering, the different protein sources were analyzed with LC-MS. Table 9 shows the top 20 identified proteins of each serum and the serum pool in percent. The captions of individual sera as proband P2, P4 etc. were adapted as initially defined after receiving them from the blood transfusion center of the medical department of the Johannes Gutenberg University, Mainz. All of them are part of the serum pool consisting of 9 probands. The individual sera of proband 1, 3 and 8 were not part of this work due to a lack in availability.

The amount of the most abundant protein, human serum albumin, differs a lot depending on the protein source. For example, P9 contains only 35% HSA, while the pooled human serum consists of more than 50% of the respective protein. For all other proteins, the fluctuation is not that strong due to their lower abundance in human blood serum. But still big differences between the different probands can be observed. For instance serum

P4 contains only 0.07% of Inter-alpha-trypsin inhibitor heavy chain, while serum P2 contains a 24-fold amount of it.

These results show that there is a strong dependency of the blood donator on serum protein composition. Due to the results discussed in chapter 3.2 it can be assumed that nanoparticles introduced into each protein source show different responses in regards of aggregate or protein corona formation. This would in consequence limit the applicability of nanocarriers designed for biomedical applications for a very diverse group of receivers. In addition, it also limits the transferability of *in vitro* and *in vivo* experiments to the actual situation in clinical studies

Table 9. Top 20 identified proteins in individual sera P2-P9 as well as serum pool determined via LC-MS (LC-MS measurements were performed by Johanna Simon).

Identified Proteins (TOP 20) in %	2	4	5	6	7	9	Serumpool
Serum albumin	42,91	46,43	48,19	45,64	37,11	35,01	53,28
Ig gamma-1 chain C region	13,5	10,64	9,57	15,04	14,66	13,93	7,87
Ig kappa chain C region	9,05	9,01	5,72	8,92	8,99	11,09	9,85
Ig gamma-2 chain C region	1,58	2,87	1,44	4,01	3,94	5,1	2,58
Serotransferrin	2,93	2,75	4,15	3,99	3,97	3,46	2,61
Ig lambda-2 chain C regions	2,21	2,77	1,76	2,64	2,49	2,83	1,72
Alpha-1-antitrypsin	1,06	1,39	1,95	2,18	2,23	2,38	1,74
Haptoglobin	1,29	1,63	1,64	1,7	1,68	0,99	2,03
Inter-alpha-trypsin inhibitor heavy chain H1	1,68	0,07	1,34	1,17	1,13	0,93	0,2
Ig alpha-1 chain C region	1,09	2,21	0,68	1,53	1,54	1,28	1,46
Complement factor B	1,37	1,07	1,04	0,62	0,62	1,05	0,15
Hemopexin	1,03	1,04	1,16	1,34	1,32	1,31	1,43
Immunoglobulin lambda-like polypeptide 5	1,01	1,22	0,75	1,2	1,12	1,25	0,88
Beta-2-glycoprotein 1	1,31	0,32	1,01	1,18	1,18	0,66	0,23
Alpha-1-acid glycoprotein 2	0,9	0,73	0,81	0,28	0,27	0,66	0,23
Alpha-2-macroglobulin	1,07	0,84	0,96	0,91	0,92	1,09	0,87
Ig gamma-4 chain C region	1,4	0,82	0,14	0,9	0,91	0,56	0,06
Complement C3	0,63	0,71	0,91	0,69	0,69	0,68	1,31
Ig mu chain C region	0,58	0,49	1,59	0,74	0,75	0,73	0,87
Apolipoprotein A-I	0,74	1,03	1,07	1,33	1,31	1,15	1,88
Apolipoprotein B-100	0,59	0,65	0,71	0,52	0,51	0,54	0,2

3.4.2 STABILITY EVALUATION OF NANOPARTICLES IN HUMAN BLOOD SERUM BY DYNAMIC LIGHT SCATTERING

In the next step, the influence of blood serum composition on particle stability against aggregation was investigated via DLS. As in previous studies, non-functionalized as well as amino- and carboxy-functionalized polystyrene particles were used as a model system.

First, it has to be noted, that all three particles show aggregation in the pooled human serum (see Table 10). The size of the formed aggregates were determined to be in a range between $R_h = 150 - 250$ nm. This is still very small and in comparison to the initial particles corresponds to a size increase of 100% (for PS) to 200% (for PS-NH₂), meaning that no bigger agglomerates were formed. Nevertheless, individual sera could be determined that caused no size increase of the respective particle. For example PS-COOH showed aggregate formation in pooled human serum resulting in aggregates that were about 2.6 times bigger than the particles itself, while PS-COOH showed no change of size in serum P4. The corresponding ACFs including data points, force fit and fit regarding aggregate formation are shown in Figure 47 exemplarily. Similar results were found for PS and PS-NH₂ nanoparticles.

Table 10. Stability evaluation of the different polystyrene particles in the respective sera or serum pool (in red).

PS ($R_h = 93$ nm)		PS-COOH ($R_h = 58$ nm)		PS-NH ₂ ($R_h = 83$ nm)		Serum
$R_h(\text{Aggregate})/\text{nm}$	I%(30°)	$R_h(\text{Aggregate})/\text{nm}$	I%(30°)	$R_h(\text{Aggregate})/\text{nm}$	I%(30°)	
No Aggregation		161	54	No Aggregation		P2
183	36	No Aggregation		329	27	P4
526	33	529	69	157	41	P5
229	38	169	37	138	41	P6
135	83	163	45	No Aggregation		P7
256	10	146	51	221	27	P9
186	46	151	14	253	39	Pool

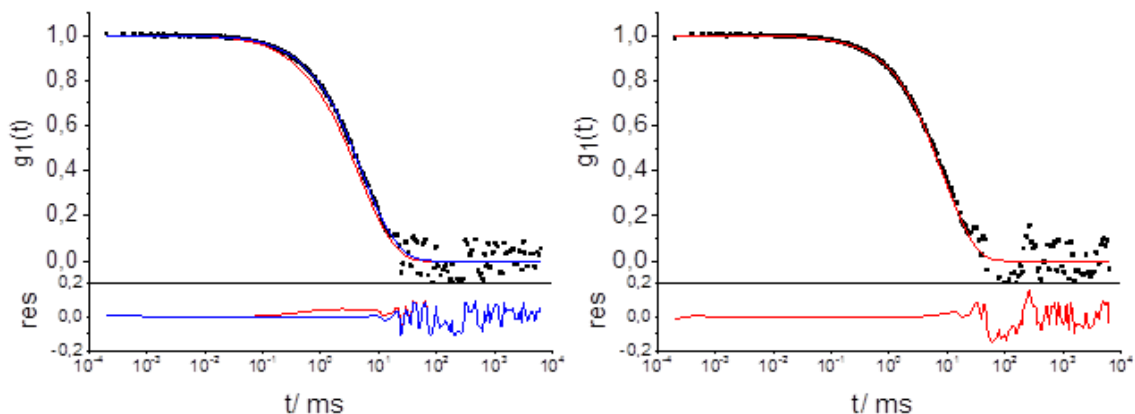


Figure 47. ACF of PS-COOH in pooled human serum (left) and in serum P4 (right) at $\Theta = 30^\circ$ including data points (\bullet), force fit (red) and fit including aggregate formation (blue) of protein stabilized particle in human blood plasma.

These results indicate, that the behavior and with this the biodistribution of a nanocarrier designed for biomedical application could possibly be dependent on the proband himself. The relation between particle aggregation determined by DLS and the biodistribution in mice is already known in literature.¹¹⁵

The disparity in particle interactions with the different protein sources was also monitored by applying SDS-PAGE. The corresponding protein patterns are shown in Figure 48. Due to the sensitivity of SDS-PAGE, the protein patterns of the coronas formed on the PS particles upon incubation in the different protein sources in general look very similar. Nevertheless, small differences can be observed. For example, the protein coronas formed on PS as well as PS-NH₂ particles in the pooled human serum show the existence of a protein band between 38 and 49 kDa corresponding to apolipoprotein A-IV (marked in red). The same bands can also be seen very weakly for PS particles in the corresponding protein coronas formed in individual serum P2 and for PS-NH₂ particles in P2, P4 and P6. In the protein patterns of the coronas formed in P7 and P9, these bands are completely absent. Of course, these differences can also occur due to small fluctuations in the applied protein amount onto the gel, but the intensity of the other bands in the protein patterns formed for example after incubation in P7 show, that the differences in protein corona patterns can be related to the differences in the composition of the protein sources.

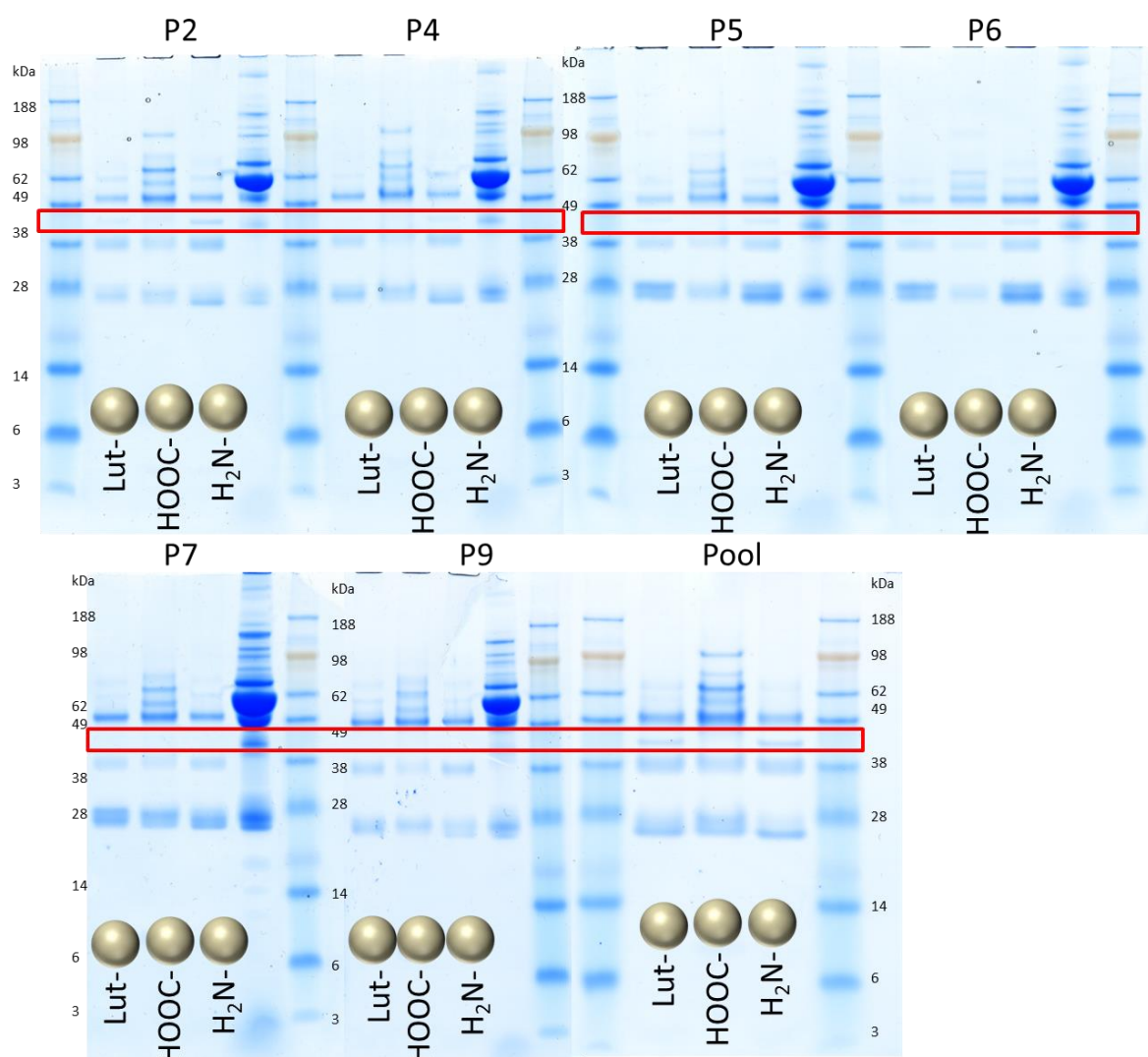


Figure 48. Protein patterns of the protein coronas formed on the different functionalized PS particles upon incubation in the different protein sources.

3.4.3 TAKING ADVANTAGE OF THE INFLUENCE OF PERSONALIZED SERUM ON PARTICLES STABILITY

As was shown in chapter 3.2, the pre-coating of PS-particles with certain protein mixtures can stabilize them against aggregation in human blood plasma. The question was addressed whether this approach could be adapted in order to stabilize particles under investigation and by this overcome the limitations that arise from the fluctuation in personalized human blood serum composition and the corresponding particle-protein interactions. When combining DLS with LC-MS data the impact of single proteins within a given protein corona on particle aggregation can be monitored. Therefore, the three

different Lutensol-stabilized polystyrene particles were incubated in individual sera that were determined to cause no size increase of the respective particle. Afterwards, the coated particles were introduced into the human serum pool and the stability was evaluated using DLS (see Figure 49).

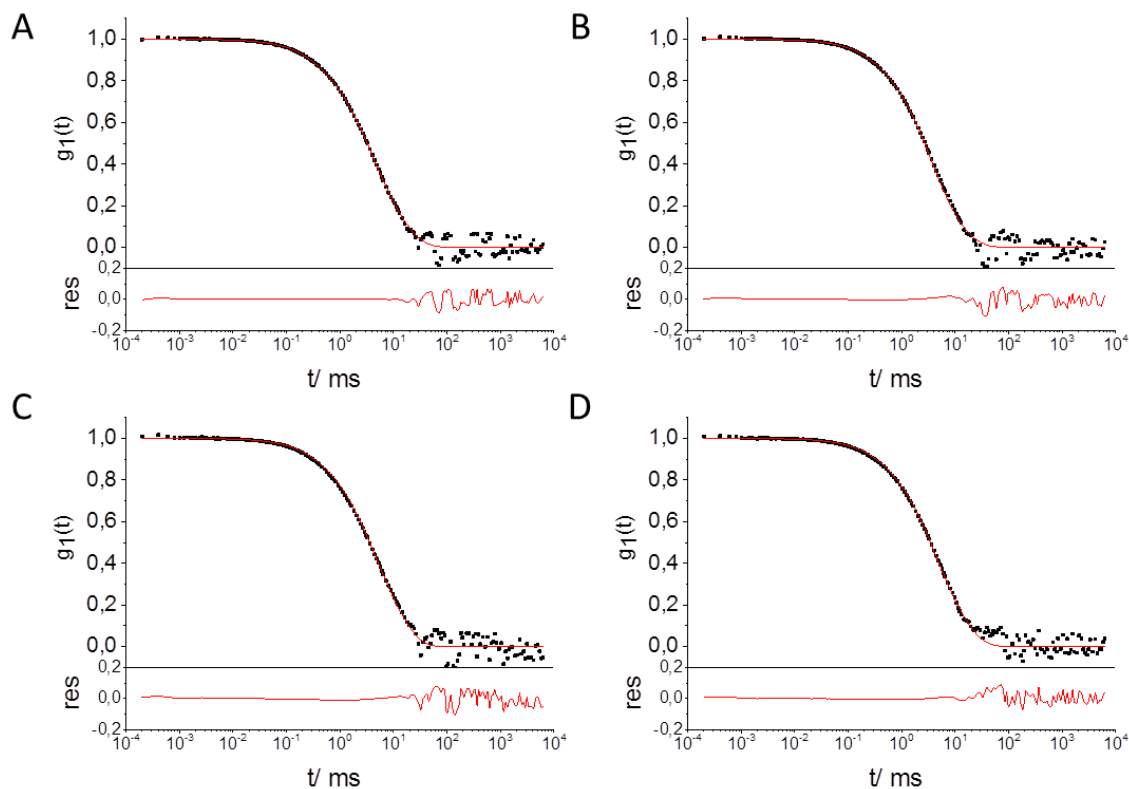


Figure 49. ACF of a respective coated particle in pooled human serum at $\Theta = 30^\circ$ including data points (\bullet) and force fit (red) with A) PS coated in P4, B) PS-COOH coated in P4, C) PS-NH₂ coated in P2 and D) PS-NH₂ coated in P7.

For each particle, no size increase in pooled human serum could be detected after pre-coating in individual sera. Due to the formation of a protein corona, the particles' size itself was increased, but for PS-COOH and PS-NH₂ the resulting size was much smaller compared to the ones of the primary detected aggregates (see Figure 50). This means, that the size increase of the respective PS particles in pooled human serum can be limited and pre-determined by the formation of a protein corona in individual sera that did not lead to a destabilization. This would be of great interest when a given nanomedicine

should be applied to a proband whose serum composition leads to intense aggregation and the formation of big agglomerates.

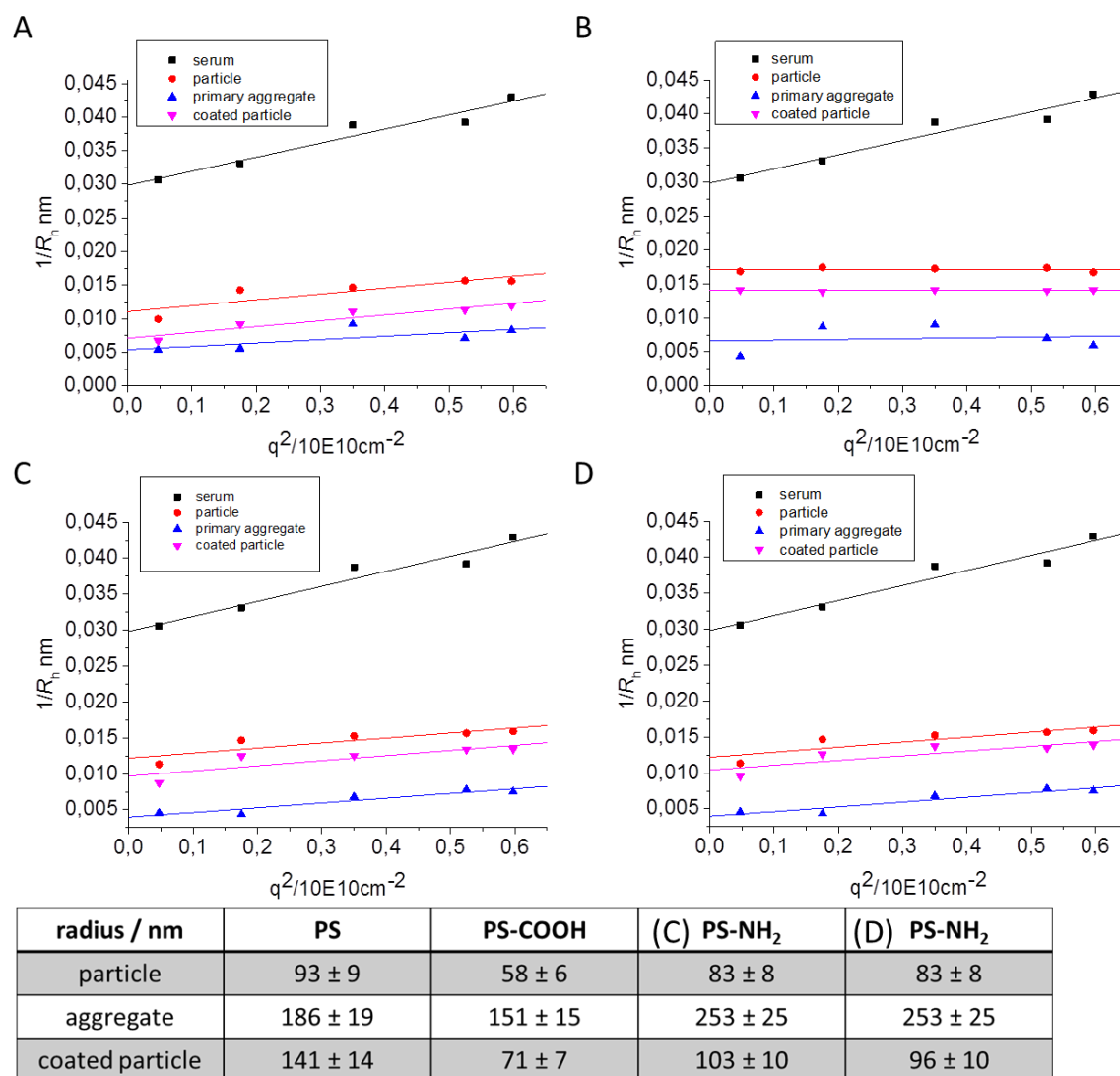


Figure 50. Angular dependency of the inverse hydrodynamic radius of the particles itself (red), the corresponding aggregates (blue) formed in pooled human serum (black) in comparison with the ones of the coated particles (magenta).

It can be summarized, that the pre-coating of a PS-particle in individual serum can stabilize it against aggregation in pooled human serum.

Further, the stability of the pre-formed protein corona after introduction in the human serum pool was investigated via LC-MS for chosen samples. PS-COOH particles pre-coated with serum P4 and PS-NH₂ particles pre-coated with serum P7 have been studied. Table 11 shows the results for PS-COOH particles.

Table 11. TOP 20 identified proteins of the protein coronas (values in %) formed on PS-COOH particles after incubation with pooled human serum, individual serum P4 and double incubation obtained by LC-MS in douplicates A and B (LC-MS measurements performed by Johanna Simon).

KK84 (PS-Lut.-COOH)	Incubation with					
	Serumpool		P4		Pre P4 in Serumpool	
Description	A	B	A	B	A	B
Vitronectin	26,44	25,51	32,31	30,33	28,6	29,4
Clusterin	15,95	15,22	11,22	11,02	7,49	7,52
Prothrombin	7,38	7,02	7,92	7,77	9,18	9,3
Beta-2-glycoprotein	5,73	5,91	4,82	4,95	4,08	4,21
Apolipoprotein A-I	5,45	5,45	5,02	6,42	5,42	6,22
Antithrombin-III	5,14	4,75	5,31	4,9	6,79	6,61
Apolipoprotein E	4,22	4,08	11,49	12,11	10,41	9,96
Serum albumin	3,17	5,06	3,29	2,71	2,74	2,4
Inter-alpha-trypsin inhibitor heavy chain H4	4	4,05	2,67	2,47	2,19	2,34
Heterogeneous nuclear ribonucleoprotein A3	3,16	2,56	1,78	2,27	1,52	1,39
Platelet factor 4	1,44	2,17	0,92	0,93	6,33	5,7
Kininogen-1	1,05	1,05	0,74	0,7	0,54	0,51
Zinc finger protein basonuclin-2	1,02	0,91	0,62	0,66	0,47	0,45
Complement C3	0,83	0,96	0,58	0,58	1	1,04
Complement factor H	0,9	0,87	0,16	0,18	0,22	0,19
Apolipoprotein B-100	0,94	0,78	0,45	0,97	0,53	0,51
Complement C4-B	0,82	0,82	0,49	0,42	0,55	0,55
Ig kappa chain C region	0,78	0,84	0,59	0,61	0,74	0,64
Lipopolysaccharide-binding protein	0,76	0,82	0,45	0,4	0,42	0,48

In general, the protein coronas of PS-COOH formed in serum P4 and pooled human serum are very similar. However, one difference becomes obvious (marked in red, see Table 11). The amount of Apolipoprotein E in the protein corona formed in the serum pool is much smaller than the one in the corona formed in serum P4. When PS-COOH was pre-coated

with the respective protein source, the amount of Apolipoprotein E remains constant, even after re-introduction in the serum pool. Similar results were found for PS-NH₂ particles as Table 12 shows.

Table 12. TOP 20 identified proteins of the protein coronas (values in %) formed on PS-NH₂ nanoparticles after incubation with pooled human serum, individual serum P7 and double incubation obtained by LC-MS in duplicates A and B (LC-MS measurements performed by Johanna Simon).

Description	KK85 (PS-Lut.-NH ₂)		Incubation with					
			Serumpool		P7		Pre P7 in Serumpool	
	A	B	A	B	A	B		
Clusterin	65,05	65,76	47,62	44,76	51,5	49,47		
Apolipoprotein A-I	5,47	6,02	25,67	22,22	18,1	19,26		
Apolipoprotein A-IV	4,23	4,23	1,6	1,71	1,41	1,74		
Serum albumin	4,24	3,99	5,45	9,21	5,75	6,44		
Vitronectin	3,28	3,63	1,19	1,42	1,48	1,41		
Zinc finger protein basonuclin-2	2,46	2,64	1,29	1,84	1,58	1,53		
Apolipoprotein E	1,65	1,66	5,91	4,06	4,07	4,5		
Apolipoprotein C-III	1,56	1,37	1,55	1,7	1,64	1,57		
Prothrombin	1,13	0,83	0,13	0,14	0,23	0,24		
Ig kappa chain C region	1	0,89	0,82	0,93	1,3	1,26		
Apolipoprotein B-100	0,92	0,66	0,69	0,64	0,66	0,76		
Ig gamma-1 chain C region	0,77	0,74	0,82	0,85	1	1,03		
Antithrombin-III	0,62	0,38	0,07	0,09	0,14	0,13		
Ig gamma-2 chain C region	0,53	0,44	0,56	0,54	0,54	0,57		
Ig mu chain C region	0,43	0,41	0,34	0,41	0,66	0,63		
Phospholipid transfer protein	0,41	0,41	0,21	0,24	0,27	0,27		
Ig alpha-1 chain C region	0,37	0,36	0,31	0,33	0,39	0,37		
V-type proton ATPase subunit H	0,31	0,37	0,17	0,27	0,22	0,22		
Complement C1r subcomponent	0,33	0,27	0,26	0,42	0,27	0,3		

This time, four different proteins could be detected whose amount in the protein coronas of PS-NH₂ particles formed in serum P7 and pooled human serum differ namely clusterin, apolipoproteins A-I, A-IV and E (marked in red, see Table 12). Again, the amount of Apolipoprotein E in the protein corona formed in individual serum P7 is bigger compared to the one formed in pooled human serum. This remains constant even after reintroduction in the latter one. A similar phenomenon was found for Apolipoprotein A-I, while the amount of Apolipoprotein A-IV was decreased by the pre-incubation process.

The results presented in Table 11 and 12 show that a once formed protein corona on polystyrene particles in distinct protein sources is stable, when it is re-introduced into another protein source. Together with the previously described dynamic light scattering results it can be assumed that the mentioned proteins play an important role in serum protein induced aggregation or rather stability against aggregation.

3.4.4 HEAT INACTIVATION OF HUMAN BLOOD SERUM

In the last chapter 3.3.3 it was demonstrated, that the incubation of polystyrene particles in sera with individual protein composition can lead to a stable protein corona on the respective particles when they were introduced into pooled human serum that initially induced slight aggregation. This pointed out once again, that the composition of a protein source critically affects the protein adsorption onto a nanomaterial's surface and with this the stability against aggregation. This led to the assumption, that a change in serum preparation with involved changes in protein composition prior to incubation with nanoparticles also effects the interaction with the latter ones. The inactivation of human serum proteins is a widely used method for protein sample preparation in order to denaturate the complement system. For example fetal bovine serum (FBS) that is used *in vitro* is heated up to 56 °C for 30 min prior to cell experimental use. Therefore, the effect of heat inactivation on protein corona formation on PS-particles was investigated. First, the effect of heating serum up to 56 °C for 30 min was monitored by dynamic light scattering. Afterwards, the effect on the particle stability and protein corona formation of polystyrene particles was monitored. The observed changes in regards of stability and protein corona formation were evaluated as additional tool for the stabilization of the particles under investigation when introduced into native pooled human serum. Figure 51 shows the angular dependency of every size fraction and the z-averaged inverse hydrodynamic radius of the native serum pool (Figure 51.A) and the heat-inactivated serum pool (Figure 51.B). The z-averaged values for both are very similar, but the heating has an influence on the distribution of the single protein size fractions.

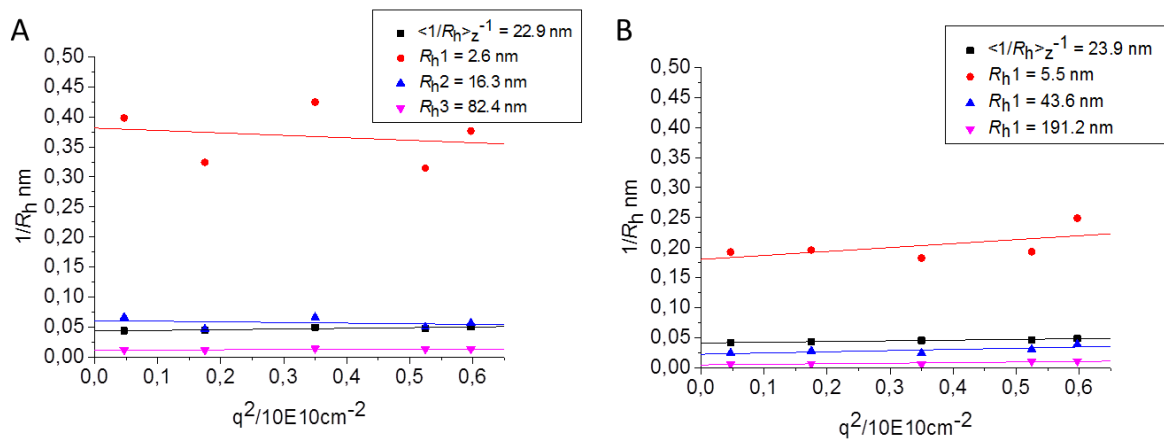


Figure 51. Angular dependency of the inverse hydrodynamic radii as well as the z-averaged value obtained in native human serum pool (A) and heat inactivated human serum pool (B).

The similarity for the z-averaged inverse hydrodynamic radius becomes also apparent when looking at Figure 52. The ACFs at $\Theta = 30^\circ$ of native human serum (black) and heat inactivated human serum (red) are shown and are more or less identical.

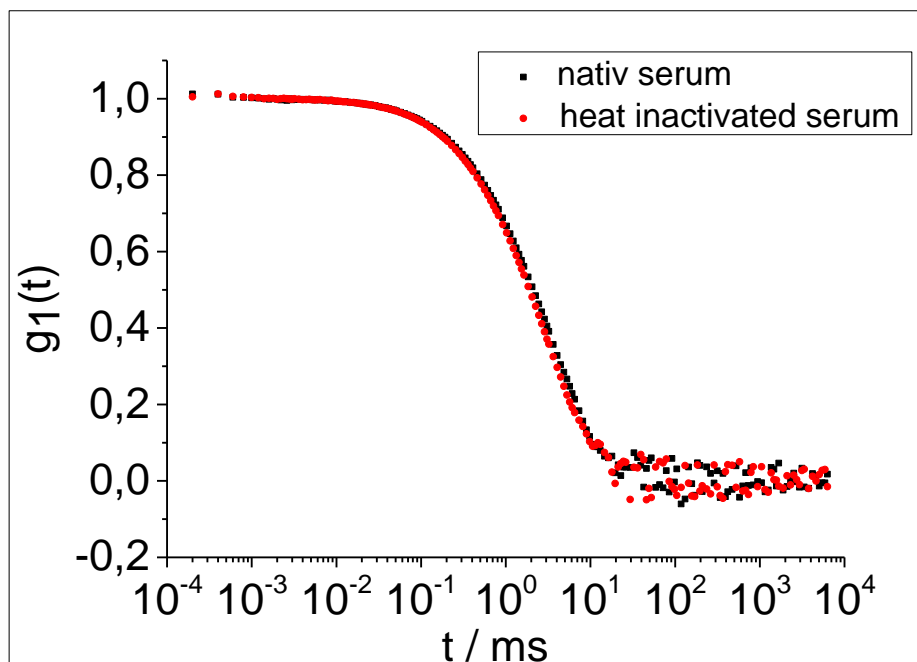


Figure 52. ACF at $\Theta = 30^\circ$ of native human serum (black) and heat inactivated human serum (red).

The previously described polystyrene particles were incubated in the human serum pool as well as in the heat inactivated serum pool in order to investigate the above described effect on protein corona formation on the respective particles. The protein pattern was analyzed using SDS-PAGE (see Figure 53).

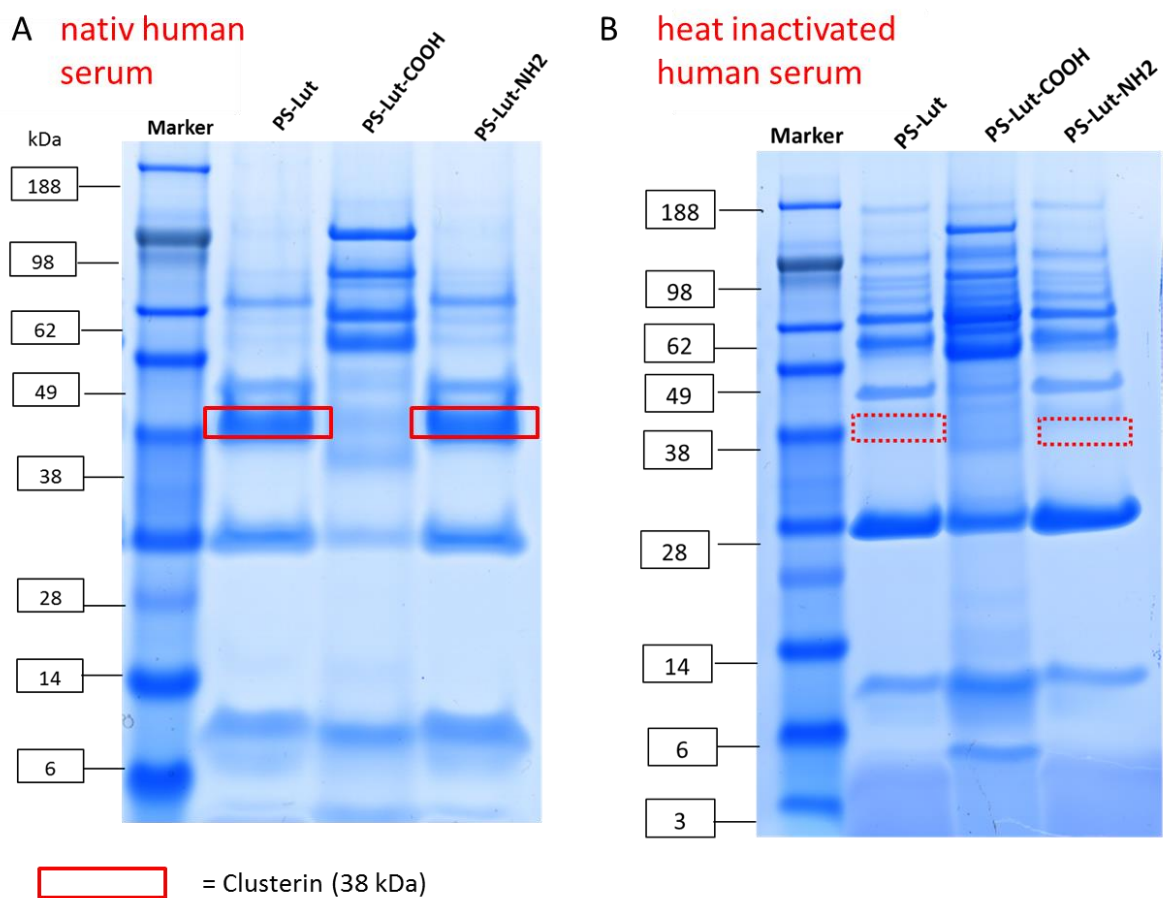


Figure 53. SDS-PAGE of the different polystyrene particles' protein coronas formed upon incubation in native human serum pool (A) as well as in heat inactivated human serum pool (B) (SDS-PAGE performed by Johanna Simon).

Figure 53.A shows the protein patterns of PS, PS-COOH and PS-NH₂ after incubation in native pooled human serum. Figure 53.B shows the respective patterns after incubation in heat inactivated pooled human serum. As was already shown in Table 12, the protein corona of the amino-functionalized polystyrene particle formed in pooled human serum

contains mostly clusterin (averaged amount $\sim 54\%$). The same is valid for the non-functionalized one. Interestingly, the corresponding protein band at 38 kDa disappears in the corona pattern, when the serum pool was heat-inactivated prior to use. One possible explanation could be the denaturation of clusterin during the heat inactivation of pooled human serum. The difference in the protein corona composition depending on serum treatment prior to incubation is also shown in Table 13 that summarizes the TOP 20 identified proteins in the protein coronas formed on PS-NH₂ after incubation in native and heat inactivated human serum.

Table 13. TOP 20 identified proteins of the protein coronas (values in %) formed on PS-NH₂ nanoparticles after incubation with native pooled human serum (A) and heat inactivated human serum (B) obtained by LC-MS (LC-MS measurements performed by Johanna Simon).

A	TOP 20 (nativ serum)	%	B	TOP 20 (heat inactivated serum)	%
	Clusterin	49.36		Apolipoprotein A-I	32.42
	Apolipoprotein A-I	16.4		Serum albumin	11.37
	Kininogen-1	9.53		Alpha-1-antitrypsin	5.67
	Complement C3	3.12		Ig kappa chain C region	3.73
	Serum albumin	3.00		Ig mu chain C region	2.88
	Phospholipid transfer protein	2.98		Apolipoprotein A-IV	2.45
	Vitronectin	1.54		Complement C4-A	2.37
	Coiled-coil domain-containing protein 158	1.5		Clusterin	2.21
	L-lactate dehydrogenase C chain	1.49		Complement C4-B	2.17
	Ig mu chain C region	1.39		Ig alpha-1 chain C region	1.72
	Apolipoprotein E	1.39		Ig gamma-1 chain C region	2.07
	Ig kappa chain C region	1.37		Ig gamma-3 chain C region	1.85
	Apolipoprotein A-IV	1.12		Ig lambda-2 chain C regions	1.54
	Ig gamma-1 chain C region	0.74		Apolipoprotein C-III	1.37
	Keratin, type I	0.54		Haptoglobin	1.22
	Alpha-1-antitrypsin	0.4		Alpha-1-antichymotrypsin	1.19
	Properdin	0.33		Vitronectin	1.11
	Microtubule-associated protein	0.29		Beta-2-glycoprotein 1	1.07
	Mannan-binding lectin serine protease 1	0.28		Antithrombin-III	1
	Ig gamma-2 chain C region	0.28		Leucine-rich alpha-2-glycoprotein	0.92

Emanated from Table 13, the amount of clusterin in the protein corona of amino-functionalized PS particles is dramatically reduced after incubation in heat inactivated

serum, while human serum albumin is enriched. The same is valid for the Ig kappa chain C region (marked in green).

To study this effect, the melting points (and with this denaturation temperature) of clusterin, HSA, IgG and fibrinogen (fibrinogen only for completeness and further discussion) were determined using Differential Scanning Fluorimetry (DSF). A solution of each protein with $c = 1$ g/L in DPBS (clusterin $c = 0.14$ g/L) was heated from 20 °C up to 95 °C with a heating rate of 1 °C/min. The auto fluorescence at 350 nm as well at 330 nm was measured. Figure 54 shows the detected fluorescence at 350 nm in dependency of the temperature.

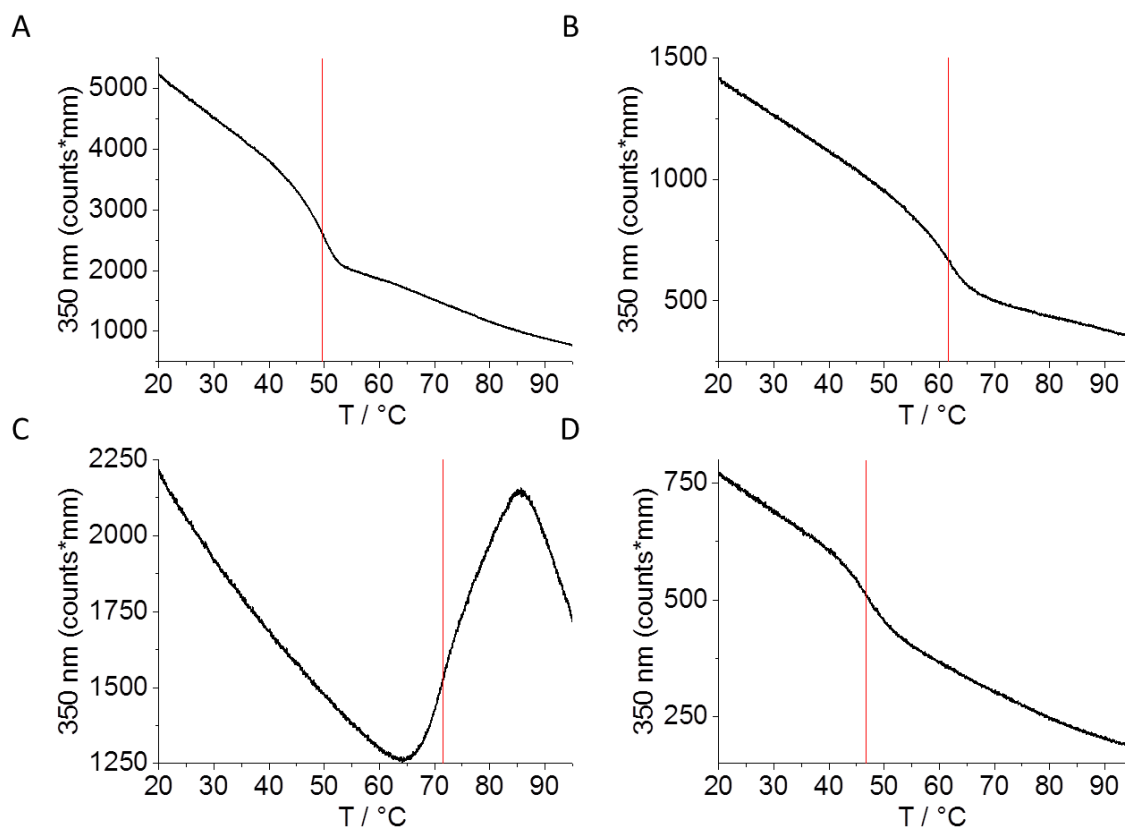


Figure 54. Fluorescence at 350 nm determined by nanoDSF of fibrinogen (A), HSA (B), IgG (C) and clusterin (C) in PBS (clusterin was measured by Julius Müller, PhD student, AK Landfester, MPIP).

For fibrinogen a denaturation point of $T = 49.6$ °C was determined, for HSA a value of $T = 61.7$ °C, for IgG a temperature of $T = 71.6$ °C, and for clusterin a melting point of $T = 46.7$ °C. This means, that the denaturation temperature of clusterin is below the temperature

that is used for heat inactivation of serum, while the corresponding points of HSA and IgG are above. The unfolding point for human serum albumin is in good agreement with the literature. Barone *at al.* determined the mid-point denaturation temperature of HSA in 0.2 M Tris-HCl (pH = 7.3) using differential scanning calorimetry (DSC) to be at $T_d = 337$ K (63.85 °C).¹⁴⁰ Vermeer *et al.* reported two transition temperatures for IgG. A lower transition temperature of the F_{ab} segments at $T = 61$ °C and a higher transition state at $T = 71$ °C for the F_c segment of IgG.¹⁴¹ The second transition temperature is in good agreement with the detected denaturation temperature of $T = 71.6$ °C using DSF. Arising from Figure 54.C, the denaturation or unfolding of IgG starts at ~ 65 °C which is in good agreement with the unfolding temperature of F_{ab} . This indicates that both processes merge. Nevertheless, both transition temperatures are above the used temperature of 56 °C for serum inactivation. As no precipitation occurs during heat inactivation, the compositions of native and inactivated serum should be identical. Only the degree of distinct protein denaturation differs. This leads to the assumption that the absence of clusterin in the protein pattern in Figure 53 is originated only in the lack of interactions between unfolded protein and particle, while clusterin in the native state has a high affinity to the same nanomaterial. The observed denaturation temperatures for HSA and IgG are also in good agreement with the results observed from LC-MS. Both proteins are not unfolded during heat inactivation of serum and are enriched in the corona of PS-NH₂ (Table 13.B).

The difference in protein-corona formation with or without heat inactivation is also mirrored by the zeta potential of the coated particles (see Table 14).

Table 14. Zeta potential of the different polystyrene particles without incubation and after incubation in native or heat inactivated pooled human serum.

zeta potential	PS	PS-COOH	PS-NH ₂
naked	-3.7 ± 0.7 mV	-27.3 ± 0.5 mV	4.3 ± 0.2 mV
heat inactivated corona	-14.1 ± 0.2 mV	-20.3 ± 0.1 mV	-15.7 ± 0.8 mV
native corona	-21.0 ± 2.3 mV	-23.5 ± 0.6 mV	-23.5 ± 0.8 mV

For all coated particles after incubation in native pooled human serum a more negative surface charge could be detected than for the ones incubated in heat inactivated pooled human serum. In addition, the zeta potentials of the coated particles in inactive human serum differ, while the ones of coated particles in native serum are similar in a range between $\zeta = - (21.0 - 23.5)$ mV. After incubation in inactive human serum, the zeta potentials of PS and PS-NH₂ particles show values of $\zeta = -14.1$ mV for PS or rather $\zeta = -15.7$ mV for PS-NH₂ that are significant higher than the value for PS-COOH particles ($\zeta = -20.3$ mV). There are two possible explanations for the observed phenomenon. On the one hand, the differences in zeta potential could be originated in a stronger impact of initial surface change of the “naked” particles on protein adsorption. On the other hand it is also possible, that the formed protein coronas on the polystyrene particles are not able to mask the initial surface charge completely.

These interesting results lead to the question, whether this causes a change of stability against aggregation of the PS particles in the serum pool as well. Figure 55 compares the observed size increases determined by DLS of the three particles under investigation when introduced into native or rather heat inactivated pooled human serum.

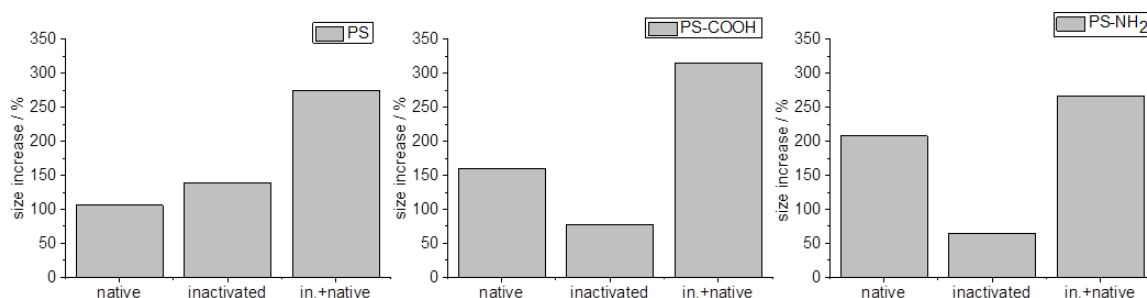


Figure 55. Size increase of the polystyrene particles in native or heat inactivated human serum pool obtained by DLS in comparison with the size increase in native human serum pool after coating with inactive human serum pool.

All three particles under investigation showed a difference in aggregation behavior. While non-functionalized polystyrene showed a slightly pronounced size increase in heat inactivated serum compared to the one in native serum, PS-COOH and PS-NH₂ formed

smaller species with size increases in the range between + 78% (PS-COOH) and + 65% (PS-NH₂). This lead to the question whether a pre-coating with heat inactivated serum pool could lead to stabilization against aggregation of the functionalized PS-particles when introduced into native serum. The results are also shown in Figure 55 (denoted as “in. + active”). Interestingly, the pre-coating lead to a size increase that is even bigger than for the uncoated particles. This effect was most obvious for PS-COOH.

In conclusion, the protein corona of the PS-particles under investigation strongly depends on the preparation of pooled human serum prior to use. Clusterin, which is high abundant in the protein corona of PS and PS-NH₂ after incubation in native human serum pool, completely disappears, when the serum pool is heat inactivated prior to incubation. The denaturation of proteins upon heat inactivation leads to conformal changes of the proteins that also cause changes in their properties. This results in a change of stability against aggregation of the particles under investigation, but pre-coating cannot stabilize the particles against the same when re-introduced in native serum. The results presented in this chapter underline the already discussed strong dependency between serum composition and the interactions of nanomaterials exposed to them. Despite not leading to full stability against aggregation in pooled human serum of polystyrene particles when precoated with inactivated serum, the data presented in this chapter demonstrate, that the heat inactivation of a given protein source alters its interactions with nanomaterials. This way, the heat inactivation is another suitable tool for the adjustment of a nanomaterial's physicochemical properties.

3.4.5 DILUTION AS A TOOL FOR PRE-COATING OF NANOPARTICLES

As already shown in chapter 3.2.2, the amount of proteins per given surface area of nanomaterial plays a critical role when looking at stability against aggregation. The amount of present proteins in chapter 3.2.2 was varied by the dilution of plasma. The question arose, whether the dilution of proteins plays a role, even when the amount of proteins per m² surface area is kept constant. With this, the equilibrium between associated proteins on the particle surface and dissociated proteins in solution is influenced. It was monitored, whether this shift critically affects the stability against

aggregation and the resulting size increase of polystyrene particles. In addition, the resulting spatial separation of particles upon dilution was assumed to decrease interactions with each other like clotting. As the precoating procedure already qualified for particle stabilization, the approach was adapted to the coating of PS particles under diluted conditions. DLS was used to investigate, whether this precoating also leads to a stabilization of particles under investigation under physiological conditions. To address this question, Lutensol stabilized PS-COOH and PS-NH₂ were introduced in pooled human serum at a constant ratio of $5 \times 10^{-3} \text{ m}^2$ per mg serum. The overall mixture was diluted 1:2, 1:5, and 1:10. The results for stability evaluation against aggregation of each nanoparticle are shown in Figure 56.

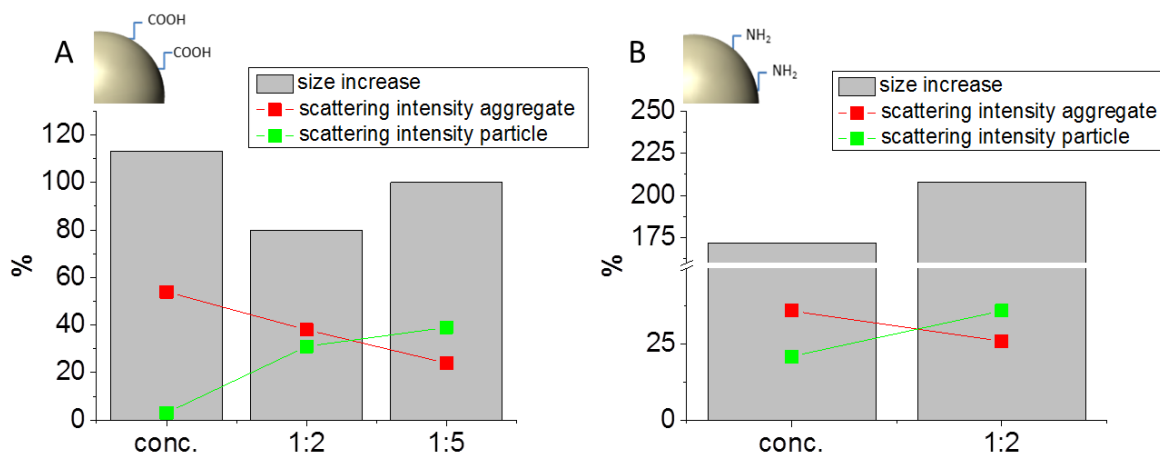


Figure 56. A) Size increase of PS-COOH in concentrated as well as diluted human serum obtained by DLS together with the scattering intensity of particle or rather aggregate at $\Theta = 30^\circ$. B) Size increase of PS-NH₂ in concentrated as well as diluted human serum obtained by DLS together with the scattering intensity of particle or rather aggregate at $\Theta = 30^\circ$.

For PS-COOH nanoparticles, an aggregate formation could be detected in the concentrated particle/serum-mixture and dilution up to 1:5. For a tenfold dilution, no aggregates could be detected anymore. The size of the formed aggregates does not diversify that much, but the intensity contribution of the different species within the respective mixture to the overall scattered light shows a trend. With stronger dilution, the intensity contribution of aggregates declines, while the ones of the particles increase. The

same phenomenon was observed for PS-NH₂ nanoparticles. In addition, no aggregate formation could be observed for a fivefold dilution. The absence of aggregation for diluted samples was utilized for coating of the respective particles. PS-COOH nanoparticles were incubated in serum pool in tenfold dilution, PS-NH₂ nanoparticles in five- and tenfold dilution. Afterwards, the coated particles were introduced into concentrated pooled serum and investigated in regards of stability against aggregation.

Figure 57 shows the ACFs at $\Theta = 30^\circ$ of uncoated PS-COOH and PS-NH₂ nanoparticles in the concentrated human serum pool in comparison to the coated ones. For all samples, aggregates were observed that represent as significant size increases. Therefore, it can be reasoned, that dilution is not a suitable tool for pre-coating of polystyrene particles when it comes to stability against aggregation.

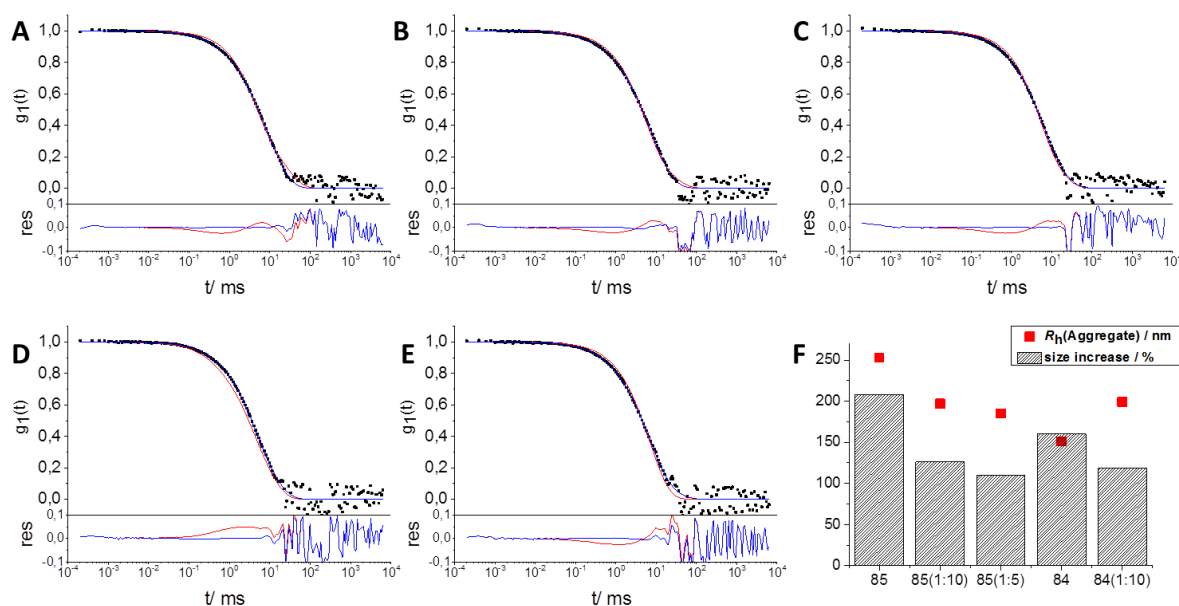


Figure 57. ACF at $\Theta = 30^\circ$ of A) PS-COOH in serum pool as concentrated mixture, B) PS-COOH in serum pool as diluted mixture 1:2, C) PS-COOH in serum pool as diluted mixture 1:5, D) PS-NH₂ in serum pool as concentrated mixture and E) PS-NH₂ in serum pool as diluted mixture 1:2 obtained by dynamic light scattering. F) Summary of determined aggregate radii and the corresponding size increase.

By dilution, the equilibrium between associated and dissociated proteins at the particle surface is shifted. In addition, the particles in higher dilution are in bigger distances to each other. This way, the possibility of interaction that leads to agglomeration is decreased. The results presented show that with increasing distance of PS particles to each other, the dimension of aggregate formation decreases. Although a pre-coating did not lead to stabilization of PS-COOH and PS-NH₂ nanoparticles under concentrated conditions, the dependence of aggregation and dilution could be of great interest for experiments that strongly depend on particle size like cellular uptake studies.

3.4.6 SUMMARY

This chapter focussed on the consequences on particle stability and protein corona formation upon a fluctuation in blood serum composition. Many approaches were introduced that should overcome the aggregation or size increase of particles in pooled human serum. In the style of pre-coating nanoparticles with certain stabilizing protein mixtures that was already introduced in chapter 3.2, the incubation in individual sera causing no size increases was utilized for the stabilization of polystyrene particles in human serum pool. Even though the same goal could not be achieved by pre-coating in heat inactivated serum, the method also demonstrated the strong correlation between a protein source's composition and the interactions with particles. Again, new opportunities for the adjustment of physicochemical parameters of nanomaterials were introduced.

3.5 THE TRANSFER OF A PROTEIN CORONA

In order to increase the blood circulation time of a nanocarrier designed for biomedical application, protein-repellent polymers have been used for surface modification. Recently it has been shown, that materials like poly (ethylene glycol) (PEG) show reduced protein adsorption, but that the presence of distinct proteins is necessary to prevent non-specific cellular uptake.¹⁰⁷ These so-called “stealth” materials possess prolonged blood-circulation time and avoid activation of the immune system. This chapter focuses on the question, whether a formed protein corona on PEGylated materials can be transferred onto a nanomaterial without PEG modification in order to stabilize it against aggregation and to retain its cell uptake. The principle of corona transfer is illustrated in Figure 58. A nanomaterial A is used for the formation of a protein corona. The protein corona afterwards can be dissolved by the use surfactants like SDS for instance. After removal of particles A and surfactant, the proteins can further be used in order to coat a nanomaterial B.

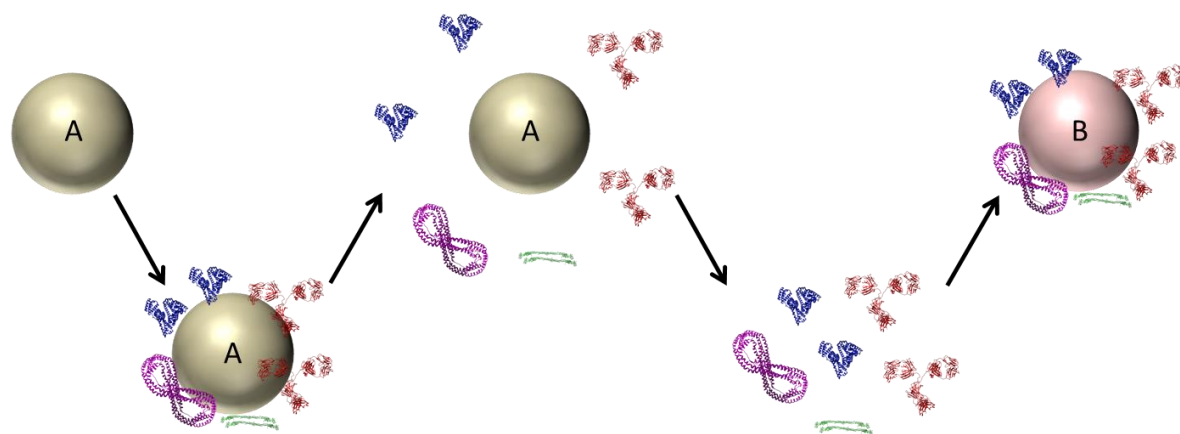


Figure 58. Illustration of protein corona transfer.

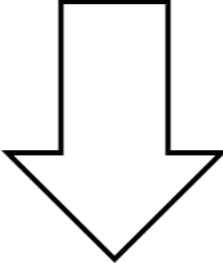
3.5.1 THE STEALTH NANOCARRIER

A requirement for this study is a PEGylated nanomaterial that is stable against aggregation in concentrated human plasma. For that purpose, PEG₅₀₀₀-NHS ester was used to modify

CTMA-Cl stabilized PS-NH₂ particles via covalent attachment of the PEG molecules. Particle functionalization was performed by Thomas Wolf (PhD student AK Landfester, MPIP Mainz). After functionalization, the particles were purified by subsequent centrifugation (20.000 g, 1 h) and redispersion of the particle pellet thrice. In addition, the dispersion was afterwards dialyzed against water with a cut off of MW = 50 kDa. The physicochemical parameters of the PEGylated nanoparticles as well as original PS-NH₂ particles are shown in Table 15.

Table 15. Physicochemical characterization of PS-NH₂ (top) and purified PS-PEG₅₀₀₀ (bottom).

particle parameter	PS-NH ₂
surfactant	CTMA-Cl
groups per NP	3500
$\langle 1/R_h \rangle_z^{-1} / \text{nm}$	51
ζ potential / mV	33.4 ± 0.1



particle parameter	PS-PEG5000
PEG chains / particle	3000
solid content in mg/mL	10
$\langle 1/R_h \rangle_z^{-1} / \text{nm}$	67
ζ potential / mV	12.9 ± 0.1

DLS was used to determine size as well as stability of the purified particles in concentrated human plasma. Figure 59 shows the results.

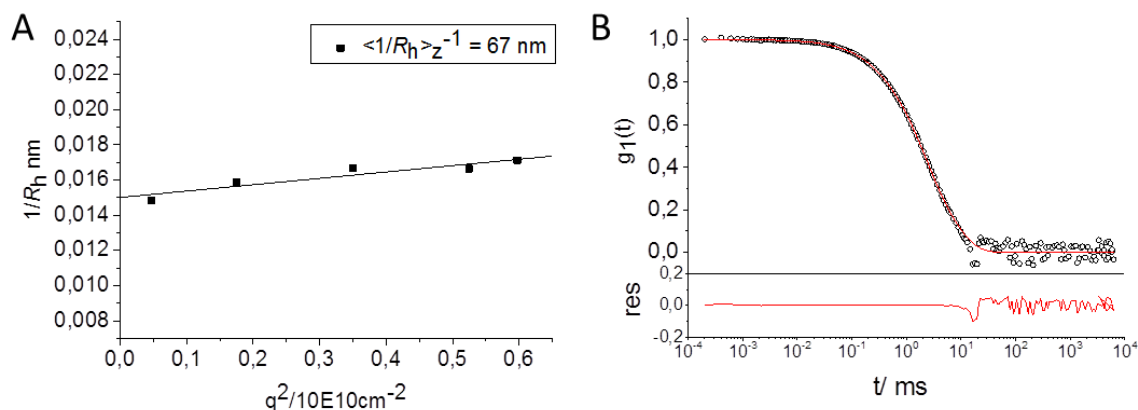


Figure 59. A) Angular dependency of the inverse hydrodynamic radius of PS-PEG₅₀₀₀ obtained by DLS. B) ACF at $\Theta = 30^\circ$ of PS-PEG₅₀₀₀ in concentrated human plasma including data points and force fit.

The particle itself shows a relatively low polydispersity as indicated by the moderate angular dependency of the hydrodynamic radius (see Figure 59) and remains stable against aggregation when introduced in concentrated human plasma.

The particle was then incubated in plasma in order to form a “stealth”-protein corona enriched with clusterin as previously described.¹⁰⁷ Table 16 shows the top 20 identified proteins by LC-MS that are present in the particles’ hard corona.

As shown in Table 16, the “stealth” corona contains mostly lipoproteins. Clusterin makes up over 50% of the total protein composition, but also apolipoproteins A-IV, A-I, and E are present in a significant manner. This is in good agreement with the literature.¹⁰⁷

Table 16. Top 20 identified proteins of the protein corona formed on PS-PEG₅₀₀₀ upon incubation in human plasma (LC-MS measurement was performed by Johanna Simon).

Description (TOP 20 based on total amount %)	TW157
Clusterin	52.82
Apolipoprotein A-IV	5.47
Apolipoprotein A-I	5.26
Vitronectin	3.72
PH and SEC7 domain-containing protein 1	3.31
Zinc finger protein basonuclin-2	3.22
Serum albumin	2.71
Apolipoprotein E	2.25
Lumican	1.5
Fibrinogen gamma chain	1.19
Ig alpha-1 chain C region	1.07
Trypsin-1	0.9
Fibrinogen alpha chain	0.93
Pregnancy zone protein	0.88
Transthyretin	0.85
Fibrinogen beta chain	0.78
Complement C1r subcomponent	0.78
Inter-alpha-trypsin inhibitor heavy chain H2	0.72
Phospholipid transfer protein	0.66
Apolipoprotein C-III	0.58

The protein corona was detached via SDS-addition and the surfactant removed via subsequent use of the Pierce® Detergent Removal Spin Column. The protein amount before and after column use was determined. In addition it was analyzed whether the PEGylated particle can be recycled and reused for corona preparation. Three cycles of incubation and corona-detachment were carried out and the process monitored via SDS-PAGE. The particle recycling would offer the possibility of using the particles as a resin in HPLC chromatography like the Protein A- or AF-Blue-column introduced in chapter 3.1. Figure 60 sums up the results.

The zeta potential of PS-PEG₅₀₀₀ mirroring the surface charge changed significantly from $(+12.9 \pm 0.1)$ mV to (-14.5 ± 0.1) mV after incubation in human plasma due to adsorption of mostly negatively charged plasma proteins. The protein patterns before and after application of the Pierce® Detergent Removal Spin Column look similar. In addition, all patterns exhibit the intense clusterin band at ~ 38 kDa (marked in red) and seem to be largely identical. Thus, the desired protein corona pattern with the enrichment of clusterin leading to potentially “stealth” properties is achieved. Also visible in the protein patterns shown in Figure 60.A are protein bands in the low molecular range between 6 and 14 kDa. These protein bands correspond amongst others to apolipoprotein C3 (~ 9 kDa).

Protein quantification determined 20% protein loss by removing SDS, but according to SDS-PAGE without significantly changing the protein composition. The zeta potential of coated PS-PEG₅₀₀₀ after the third cycle with a value of $\zeta = -(15.1 \pm 0.7)$ mV is similar to the one after the first cycle. This means, that protein adsorption takes place in a comparable manner and offers the possibility of particle recycling.

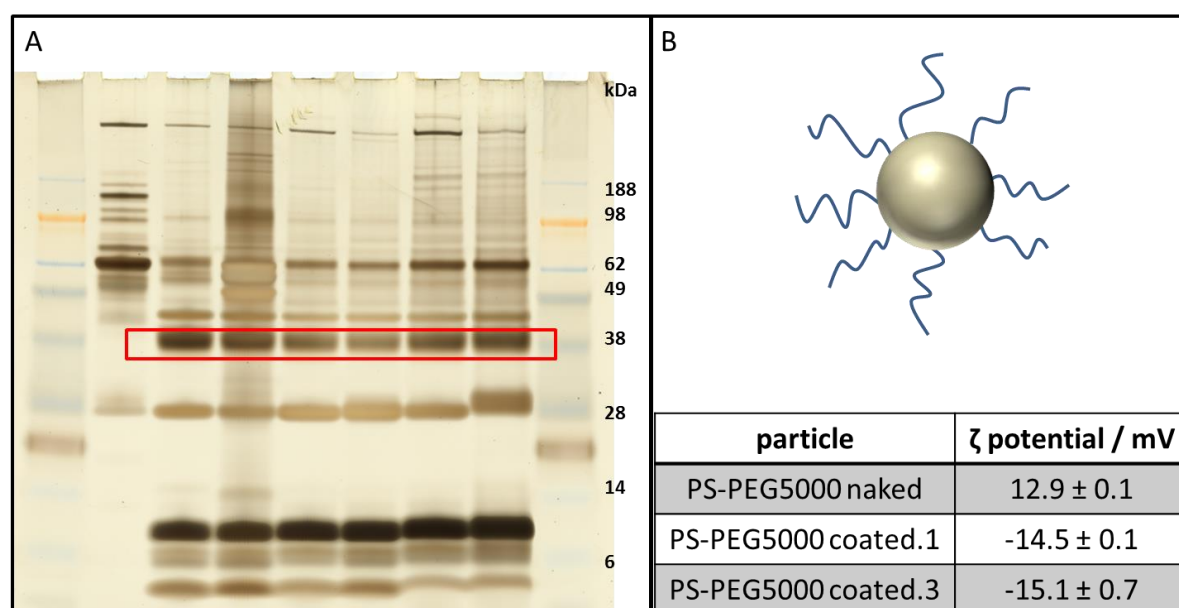


Figure 60. A) SDS-PAGE of human plasma with subsequent silver staining (1); the protein corona formed on PS-PEG₅₀₀₀ after incubation in human plasma with (2) and without (3) SDS; the protein corona formed on the second use of PS-PEG₅₀₀₀ after incubation in human plasma with (4) and without (5) SDS and the protein corona formed on the third use of PS-PEG₅₀₀₀ after incubation in human plasma with (6) and without (7) SDS. B) Zeta potential of uncoated PS-PEG₅₀₀₀ as well as of the coated ones after first and third use.

NanoDSF was utilized in regards of protein denaturation for the investigation of the “stealth” corona after detachment from PS-PEG₅₀₀₀ and SDS removal. Figure 61.A shows the auto fluorescence measured at 350nm, Figure 61.B the auto fluorescence measured at 330 nm, and Figure 61.C the ratio of both. For all three examinations no protein unfolding could be obtained. This means, that the proteins are fully denaturated after detaching them from PS-PEG₅₀₀₀ using SDS.

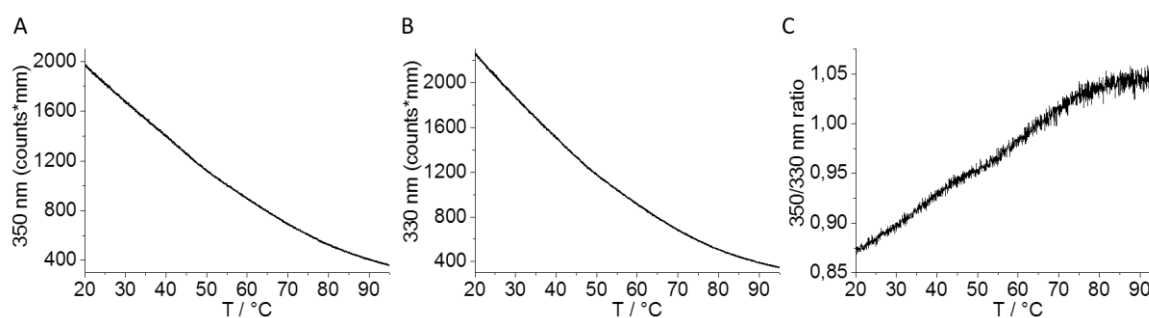


Figure 61. A) Fluorescence at 350 nm determined by nanoDSF of “stealth” proteins, B) Fluorescence at 330 nm determined by nanoDSF , and C) the 350/330 nm ratio determined by nanoDSF.

3.5.2 CORONA TRANSFER

Especially for nanomaterials designed for biomedical applications, a long blood circulation time and stability against aggregation are desired. The surface modification with protein repellent polymers such as PEG is a time consuming process that needs several purification steps subsequent to the particle synthesis itself. In addition, functional groups at the nanomaterial’s surface are needed for the covalent attachment of polymers that limits the applicability. In chapter 3.2 and 3.4 it was shown, that the adsorption of proteins on a nanomaterial’s surface also alters its physiochemical properties. The adsorption takes place upon an (in comparison) simple incubation process of particles in protein solution. No functional groups for a covalent modification are needed during this process, what makes this approach applicable for a diverse and broad range of different nanomaterials. Since the “stealth” properties of PEGylated polystyrene has recently been shown to be depending on the presence of distinct proteins, the question arose whether a

transfer of a formed “stealth corona” onto a foreign nanomaterial by adsorption is possible and whether this adsorption changes the physicochemical properties of a nanomaterial towards stability against aggregation and reduced non-specific cellular uptake of macrophages. As shown in chapter 3.4.4, the denaturation of proteins can lead to changes in their interactions with nanomaterials. This leads also to a change in properties. The question was addressed, whether this has an impact on the “stealth properties regarding cellular uptake as well.

As transfer particle CTMA-chloride stabilized PS-NH₂ particles (see Table 15 top) were chosen as they were used for PEG modification as well. Particles with a surface area of 0.05 m² were introduced in 200 µg of protein dissolved in PBS. After one hour, free and weakly bound proteins were removed via centrifugation and washing of the particle pellet. First it had to be analyzed, whether protein adsorption on the transfer particle took place at all. This was done by using SDS-PAGE as well zeta potential measurement in order to monitor changes in the particle’s surface charge. SDS-PAGE was used to study whether proteins could be detected in the particles’ hard corona and whether the pattern looks similar to the one of PS-PEG₅₀₀₀. In addition, zeta potential measurements were utilized for detection of changes on the nanomaterials surface after incubation in protein solution. Figure 62 gives an overview of the results.

First of all it has to be noted, that proteins could be detected after incubation of PS-NH₂ in the proteins detached from PS-PEG₅₀₀₀. This means that despite of losing their tertiary structure when SDS was used to detach the proteins from PEGylated polystyrene, they adsorb to amino-functionalized PS when being exposed to it. This is also mirrored in the significant change of the zeta potential of the respective particle after incubation. The protein pattern formed on PS-NH₂ after incubation in corona proteins differs from the one formed in full plasma. The most abundant protein in the higher molecular range after incubation in full plasma is albumin at 66 kDa (see Figure 62, band marked yellow in Lane 2) whereas the hard corona after incubation in “stealth-proteins” shows the most intense band at ~38 kDa (see Figure 62, marked in red in Lane 3 and 4) in the higher molecular range. This is similar to the pattern of PS-PEG₅₀₀₀.

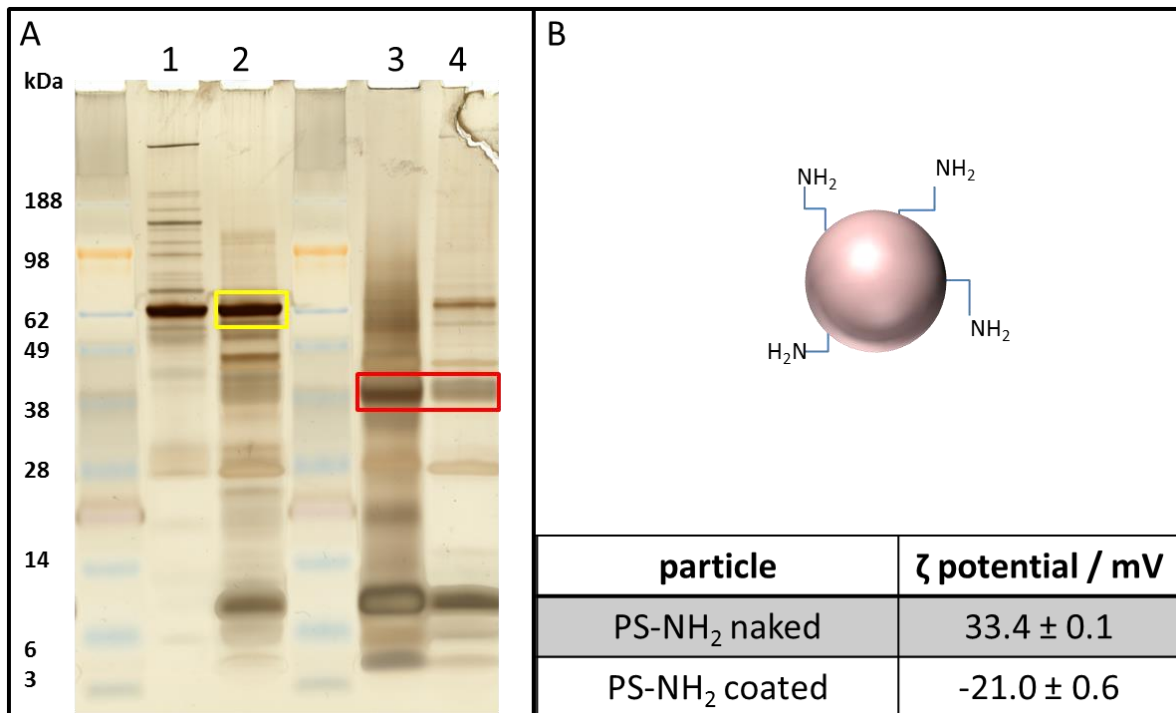


Figure 62. A) SDS-PAGE of human plasma (1), the protein corona of PS-NH₂ formed in human plasma (2), the protein corona of PS-NH₂ formed in the “stealth” proteins (3) and the “stealth” proteins (4). B) Zeta potential of uncoated PS-NH₂ as well as of coated PS-NH₂ with “stealth” proteins.

The results so far show, that the transfer of a protein corona in general is possible. Going one step further, it was analyzed whether this artificially created protein corona can enhance a particle’s stability against aggregation when introduced in concentrated human plasma.

Figure 63.A shows the DLS results for PS-NH₂ (CTMA-Cl) introduced in concentrated human plasma. Strong aggregate formation could be observed with aggregates in the microscopic size range. Figure 63.B shows the DLS results for PS-NH₂ after coating with “stealth proteins”. Aggregate formation could not be completely prevented, but the dimension could be dramatically decreased and thus the particles were stabilized. By pre-coating, the size increase of the respective particle when introduced into concentrated human plasma could be decreased from 1300 % to 120 %.

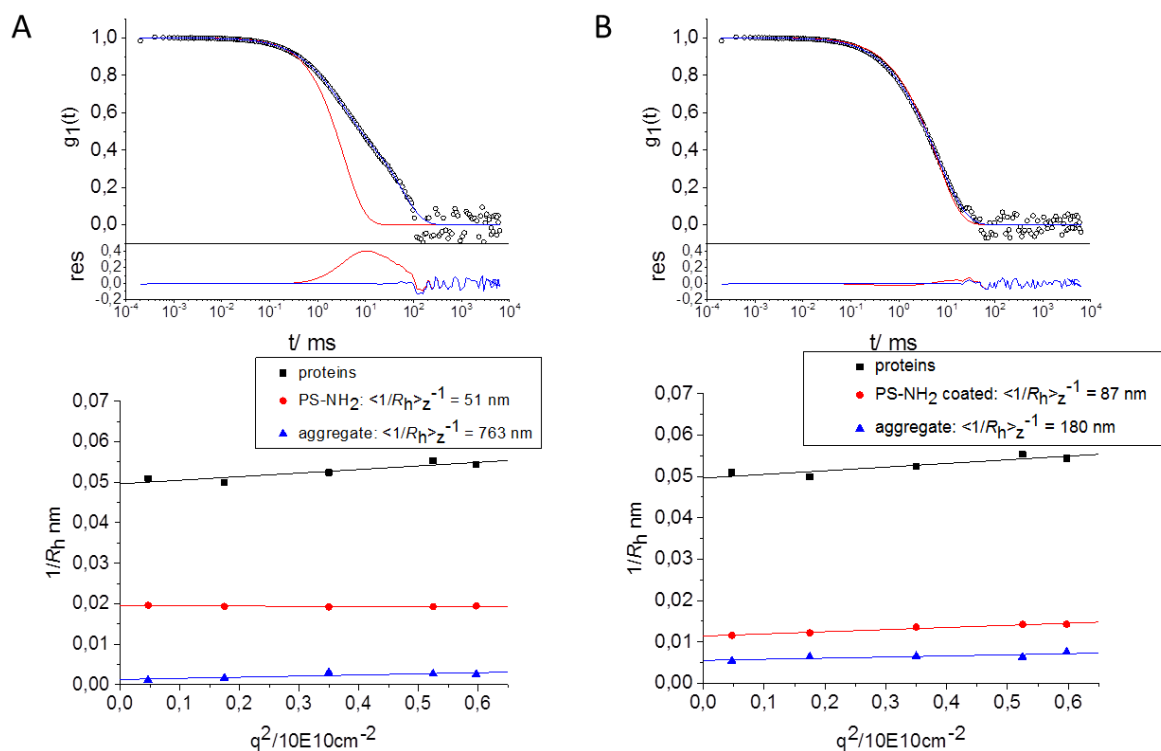


Figure 63. A) ACF at $\Theta = 30^\circ$ of PS-NH₂ in concentrated human plasma including data points (O), force fit (red) and fit with aggregate formation (blue) with the angular dependency of their inverse hydrodynamic radii. B) ACF at $\Theta = 30^\circ$ of coated PS-NH₂ in concentrated human plasma with the angular dependency of the obtained inverse hydrodynamic radii.

The effect of the transferred protein corona was additionally investigated via cellular uptake studies. RAW 264.7 macrophages were incubated with PS-NH₂ (CTMA-Cl) with and without prior pre-coating and compared to the uptake of PS-PEG. Figure 64 gives the results.

While the protein corona formed on PS-PEG₅₀₀₀ leads to a reduced uptake compared to an uncoated one (Figure 64, sample 1 vs sample 4), the inverse effect was observed for PS-NH₂ coated with the transferred protein mixture. This leads to the conclusion, that the denaturation of proteins during SDS-treatment in order to detach them from the stealth material plays a critical role during macrophage uptake. The role of macrophages as part of the immune system is to detect foreign or damaged material with subsequent cell uptake in order to remove foreign material. This could be an explanation for the increased uptake of PS-NH₂ decorated with the transferred protein mixture.

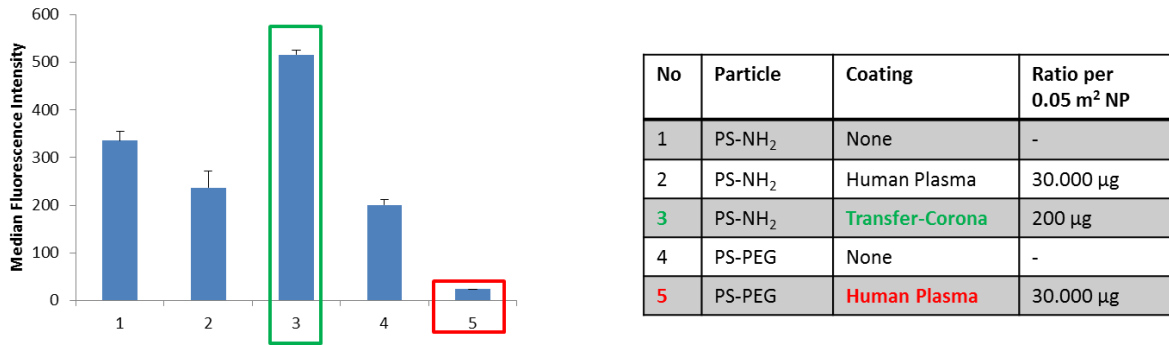


Figure 64. Flow cytometry analysis of RAW 264.7 cells incubated with nanoparticles 2 h in DMEM without additional proteins. The pre-coated nanoparticles were isolated via centrifugation and added to the cells with a nanoparticle concentration of 20 µg/mL. Relative median fluorescence intensity (rMFI) values are shown as mean ± SD of triplicates (cell experiments were performed by Johanna Simon).

As a conclusion, the transfer of a protein corona from stealth-materials to particles without stealth modification is possible. With this, the stability of a particle against aggregation in concentrated human plasma can be increased. In addition, the stealth material can be recycled and reused, opening new possibilities for protein purification via chromatography. However, the correct protein folding is necessary for achieving a “stealth effect” in regards of reducing the cellular uptake, while it is not needed for stability against aggregation. By this, the chapter underlines again the importance of protein structure on interactions with particles as was already demonstrated in chapter 3.4.4.

3.6 EVALUATION OF DIFFERENT *IN VIVO* MODELS FOR BIOMEDICAL APPLICATION

The increasing interest on nanocarriers for biomedical applications becomes apparent in the number of publications on nanomedicine that rose from ten (~1990) to more than 1200 per year (2004).¹⁴² Compared to that, the number of nanotechnology-enabled products currently on the market is very small (~38 in 2006).¹⁴² The evaluation process that a nanomaterial has to undergo prior to becoming an accepted pharmacy-medicament is very time consuming and includes several critical steps. Animal models are often used as non-human source in order to evaluate the potential nanomaterial prior to clinical trials with humans.¹⁴³ These animal tests are even required before exposure to humans.¹⁴⁴ Nevertheless, the transfer from *in vivo* to humans bears several challenges and limitations.^{145, 146} Mak *et al.* refers to that problem as “Lost in translation”.¹⁴⁷ The murine model is the most commonly used one for testing drug candidates prior to clinical trials.¹⁴⁸ Despite the very different morphology of mice compared to humans, many factors influence the outcome of *in vivo* trials. For example Cabib *et al.* showed, that the outcome of experimental results is also depending on background variables like the period of food shortage.¹⁴⁹ Very recently, Laganà and coworkers used LC-MS to investigate the protein corona formed on different liposomal formulations after incubation in mouse or rather human plasma. Their findings reported suggest that results from *in vivo* animal models are not mandatory conferrable to humans.¹⁵⁰

This chapter focusses on the transferability of different *in vivo* animal models to humans. Citrate stabilized plasma from different animals was analyzed and compared to human plasma. In addition, protein particle interactions were studied via DLS and SDS-PAGE. The so far developed pre-*in vivo* screening methods should further be modified to increase the understanding of possible differences between the outcome of *in vitro/ in vivo* experiments and clinical trials.

3.6.1 CHARACTERIZATION OF DIFFERENT BLOOD PLASMA SOURCES

Plasma from three typical *in vivo* models, namely rabbit, mouse, and sheep was chosen and compared to human plasma. As a first step, DLS was used to determine the three different size fractions for each plasma source. Figure 65 summarizes the results.

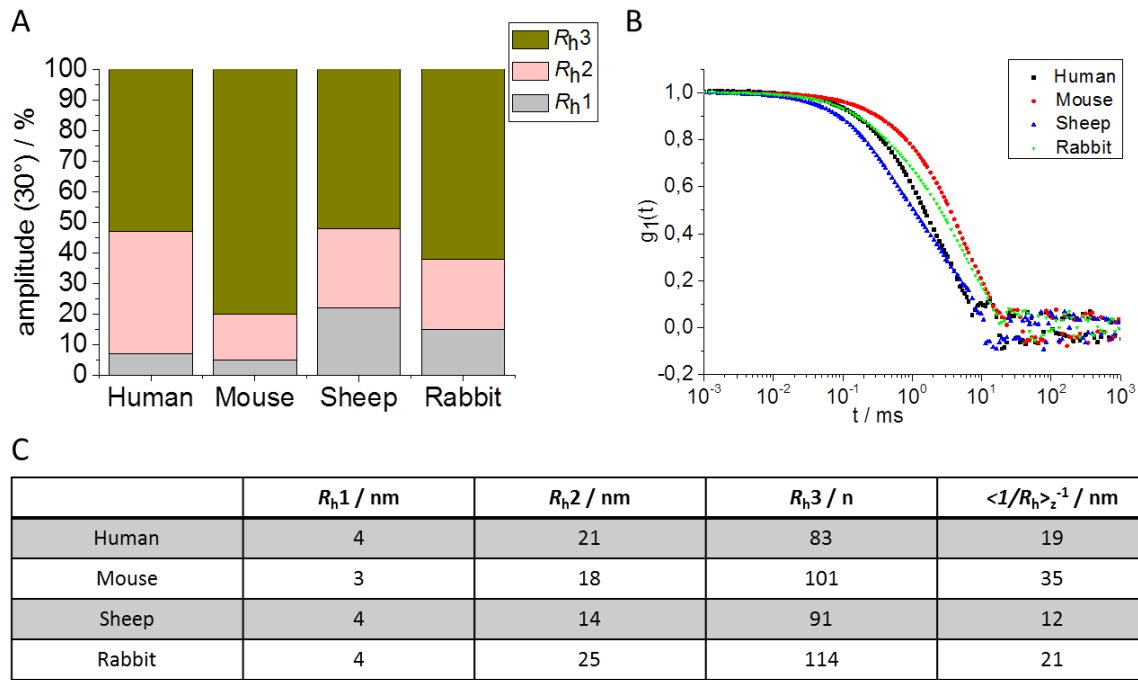


Figure 65. A) Fluctuation of the different size fractions for the different plasma sources B) The corresponding ACF at $\Theta = 30^\circ$. C) Obtained values for the different size fractions from DLS.

Each plasma source contains the already described three different size fractions. The sizes of each fraction as well as their relative intensity amplitude in % vary a lot.

Mouse plasma for example contains a lot of the biggest size fraction that is in addition very large in size. This results in the biggest inverse hydrodynamic radius $\langle 1/R_h \rangle_z^{-1} = 35 \text{ nm}$, while sheep plasma has only a determined value of $\langle 1/R_h \rangle_z^{-1} = 12 \text{ nm}$ which is less than half of the size compared to the mouse plasma proteome. One explanation for this phenomenon can be the different nutrition of animals. Cholesterol and lipids for instance can be taken up with food and are part of the lipoproteins present in plasma. These lipoproteins can form big agglomerates like chylomicrons that are part of the biggest size fraction Rh3. As DLS is very sensitive towards bigger species, this can lead to significant differences in observed size fractions and intensity contributions.

The difference between each plasma proteome becomes also apparent by SDS-PAGE. Figure 66 gives the corresponding protein patterns. Especially in the high molecular range but also between 28 – 49 kDa differences in the protein patterns can be seen.

Classification is possible for the most abundant protein bands that belong to serum albumin at ~ 66 kDa (marked in red, see Figure 66) and IgG at ~ 50 kDa for the heavy chain or rather ~ 22 kDa for the light chain (marked in green, see Figure 66). They can be found in every plasma source. In 2015, Pozzi *et. al* investigated the plasma composition of mouse and EDTA stabilized human plasma via LC-MS.¹⁵⁰ For human plasma 234 proteins were identified, for mouse plasma 354. As already indicated in the introduction, SDS-PAGE is limited in resolution. Proteins with similar molecular weights co-migrate through the gel and can therefore not be separated. That makes it very difficult to identify single proteins. Nevertheless it is a suitable method for the comparison of different protein patterns.

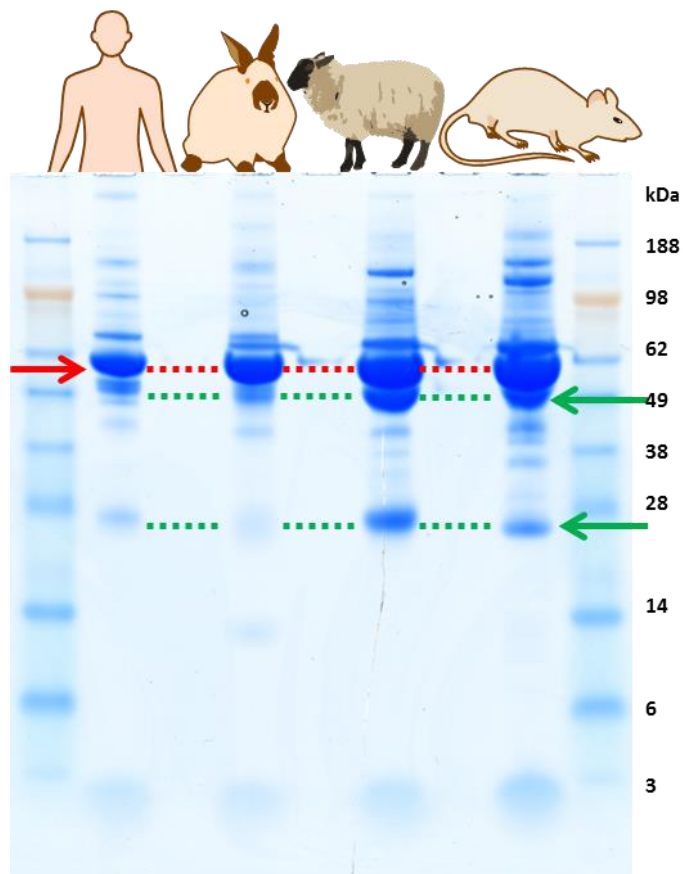


Figure 66. SDS-PAGE of human, rabbit, sheep and mouse plasma.

For better resolution, LC-MS was performed of the different plasma sources. For human as well as mouse plasma 100 proteins in total could be easily identified by our setup. For

rabbit plasma 35 and for sheep plasma 15 proteins in total could be identified due to smaller databases. Therefore, the percentaged amount of the TOP 20 identified proteins does not mirror the actual plasma composition of rabbit and sheep. Nevertheless, the most abundant proteins could be identified. Table 17 shows the TOP 20 identified proteins obtained by LC-MS in human and mouse plasma, Table 18 the corresponding results for sheep and rabbit plasma.

Table 17. Top 20 identified proteins in human and mouse plasma (LC-MS measurement was performed by Johanna Simon).

	Human		Mouse
Serum albumin	57.3	Serum albumin	50.8
Ig kappa chain C	7.21	Serotransferrin	6.63
Ig gamma-1 chain C region	6.34	Hemopexin	2.81
Serotransferrin	2.6	Pregnancy zone protein	2.46
Haptoglobin	2.01	Serine protease inhibitor A3K	1.87
Ig lambda-2 chain C regions	1.72	Alpha-1-antitrypsin 1-1	1.64
Fibrinogen gamma chain	1.58	Apolipoprotein A-I	1.6
Hemopexin	1.38	Vacuolar protein	1.15
Alpha-1-antitrypsin	1.38	Vitamin D-binding protein	1.23
Ig alpha-1 chain C region	1.3	Ig gamma-2B chain C region	1.01
Alpha-2-macroglobulin	1.19	Haptoglobin	1.03
Immunoglobulin lambda	1.01	Carboxylesterase 1C	0.88
Fibrinogen beta chain	1.01	Alpha-2-antiplasmin	0.86
Ig gamma-3 chain C region	1.08	Serum amyloid P-component	0.82
Ig gamma-2 chain C region	0.94	Fibrinogen gamma chain	0.85
Ig mu chain C region	0.84	Histidine-rich glycoprotein	0.8
Apolipoprotein A-I	0.7	Alpha-2-HS-glycoprotein	0.83
Complement C3	0.69	Alpha-1-antitrypsin 1-2	0.81
Fibrinogen alpha chain	0.59	Complement C3	0.82

In comparison to human plasma, the mouse plasma under investigation contains less albumin (~ 7%, marked in red, Table 17) and much less immunoglobulins (marked in yellow, Table 17). Both protein classes belong to the smaller globular proteins that make up the three different size fractions DLS can detect. The described deviation between human and murine plasma therefore is amongst others one factor that leads to the shift of the mouse ACF to longer correlation times (see red data points, Figure 64).

Table 18. Top 20 identified proteins in rabbit and sheep plasma (LC-MS measurement was performed by Johanna Simon).

	Rabbit		Sheep
Serum albumin	70.3	Serum albumin	86.91
Ig gamma chain C region	3.96	Ceruloplasmin	4.66
Histidine-rich glycoprotein	3.32	Antithrombin-III	3.1
Ig kappa-b4 chain C region	2.6	Alpha-2-HS-glycoprotein	2.1
Serotransferrin	2.11	Alpha-1-antiproteinase	1.59
Alpha-1-antiproteinase	2.32	Plasminogen	0.38
Hemoglobin subunit beta-1/2	2.11	Transthyretin	0.43
Vitamin D-binding protein	1.42	Inter-alpha-trypsin inhibitor	0.2
Complement component C9	1.22	Actin, cytoplasmic 1	0.2
Alpha-2-HS-glycoprotein	1.26	Homeobox protein Hox-D3	0.2
Hemopexin	0.87	Estrogen receptor	0.13
Ig kappa-b4 chain C region	0.75	Hemoglobin fetal subunit beta	0.07
Haptoglobin	0.67	Homeobox protein Hox-C9	0.04
Apolipoprotein A-I	1.05		
Hemoglobin subunit alpha-1/2	0.66		
Ig mu chain C region secreted form	0.44		
Vitronectin	0.42		
Complement C3 alpha chain	0.49		
Serum paraoxonase/arylesterase 1	0.46		

Due to the smaller numbers of identified proteins in sheep as well as rabbit plasma, the detected amount of the most abundant protein albumin is very high in both plasma

sources according to LC-MS (see Table 18). For rabbit plasma, the very high amount of ~ 70% is somehow traceable and fits the protein pattern obtained with SDS-PAGE (see also Figure 65). But for sheep plasma, a high variety of protein bands were obtained by SDS-PAGE (see Figure 65). Therefore it can be assumed that the high percentaged amount of albumin obtained via LC-MS is mostly originated in the small amount of only 15 identified proteins.

The differences in blood plasma composition can have many origins. Next to the apparent different genotype, the protein composition in blood is also influenced by outer terms and conditions. This can be physical stress during welfare or the nutrition, but also injuries. Proteins of the acute phase are for example expressed in an increased manner in the latter case.

The impact of these different plasma proteome compositions on particle stability was addressed in the next steps.

3.6.2 INVESTIGATION OF PROTEIN-PARTICLE INTERACTIONS

The three different and already described Lutensol stabilized polystyrene nanoparticles (see chapter 3.2.2) were introduced in each plasma source and their stability against aggregation investigated by using DLS. Figure 67.A summarizes the observed size increase of PS, PS-COOH and PS-NH₂ in human, mouse, rabbit, and sheep plasma.

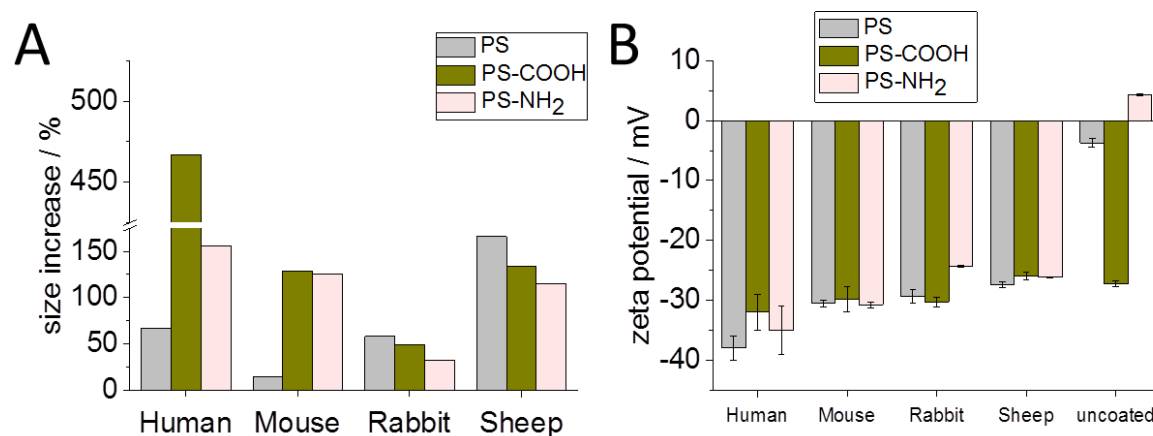


Figure 67. A) Observed size increases in % of the different PS-particles after exposure to human, mouse, rabbit and sheep plasma. B) Zeta potential of uncoated PS-particles as well as coated particles in the different plasma sources under investigation.

In general, the size increase of each particle depends a lot on the plasma source it is introduced into. Non-functionalized PS nanoparticles for example forms aggregates in sheep plasma that are 166% bigger than the original species, while the same particle increases only 14% in size when introduced into mouse plasma. A second direct observation can be made from Figure 67.A. Independent of the functionalization of the three different polystyrene particles under investigation, their size increases in rabbit plasma are very similar and in comparison to the ones in other plasma sources low. This indicates on the one hand that the protein corona formation in rabbit plasma is not depending on the surface charge of the polystyrene particles under investigation in a strong manner. On the other hand, it also means that proteins present in the corona formed in rabbit plasma do not lead to a pronounced aggregation behavior.

In addition, the change of surface charge of each particle after incubation in every plasma source was monitored (Figure 67.B). Due to the fact, that most plasma proteins are negatively charged, the measured zeta potential again becomes negative after hard-corona formation. Small differences between the animal models can be observed.

After incubation in human plasma, the values for zeta potential are most negative in the range between -32 and -38 mV, while the values after incubation in sheep plasma are around -26 mV. This could be relevant for cellular uptake and hence the body distribution.

SDS-PAGE was used in order to identify the protein patterns of the particles' hard corona that were formed after incubation in the plasma sources under investigation. Figure 68 shows the corresponding SDS-PAGE patterns.

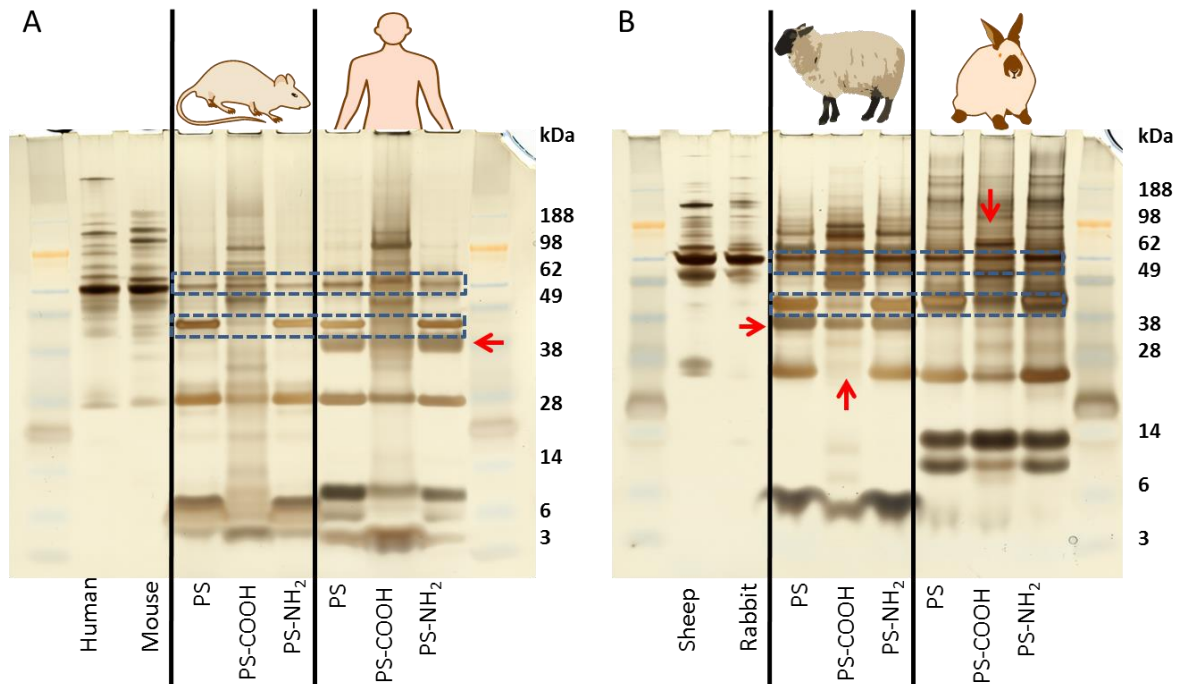


Figure 68. A) SDS-PAGE of the protein coronas formed on PS, PS-COOH and PS-NH₂ during incubation in human or mouse plasma. B) SDS-PAGE of the protein coronas formed on the respective particles during incubation in sheep or rabbit plasma.

For each particle specific protein patterns can be identified that are present in the respective hard-corona independent of the plasma source used for incubation. Two of these examples are marked in blue. One very abundant protein band is visible at ~66 kDa that probably corresponds to albumin. A second abundant protein band is detected between 38 and 48 kDa. But also very significant differences can be observed. These differences concern all particles or only one particle when comparing the different animal models. Relevant for all particles is the presence or absence of clusterin at ~38 kDa. This is marked with horizontal red arrows. This protein is highly abundant for the protein coronas formed in human or sheep plasma, but absent or only low abundant after incubation in mouse and rabbit plasma. Two additional differences only concern PS-COOH. These ones

are marked with vertical red arrows. While the protein patterns have abundant bands at ~ 28 kDa in mouse, human and rabbit plasma, the band is absent after incubation in sheep plasma. This is interesting, as the existence of the corresponding protein can be seen in the patterns of PS and PS-NH₂ after incubation in the latter plasma source. The second big difference is a protein band at ~ 98 kDa that is very weak in the protein pattern of PS-COOH after exposure to rabbit plasma, while it is intense in all other animal models.

From Figure 68 it becomes clear that there are big differences when comparing different animal models for *in vivo* application. These differences can not only be related to the animal model itself as the example of PS-COOH shows.

Secondary, the type of particles for this study was broadened. Bionized nanoferrite (BNF) particles with a shell of either crosslinked hydroxyethyl starch (HES) or dextran (DEX) were investigated in terms of transferability from the different *in vivo* models to humans.

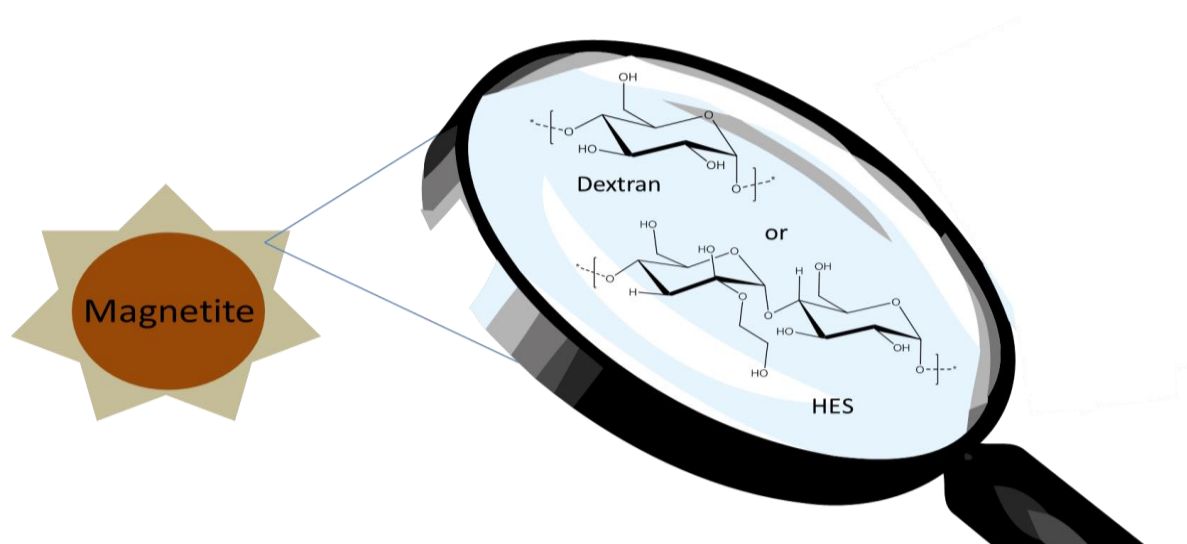


Figure 69. Schematic structure of BNF-Starch and BNF-Dextran.

The validated method of DLS was used to investigate the stability of both particles against aggregation when introduced into the different plasma sources. Table 19 summarizes the results and Figure 70 or rather 71 show the corresponding ACFs of particle/protein mixtures. The differences are significant. Both particles show distinct aggregate formation in human and sheep plasma with sizes in the micrometer range. In direct comparison, the formed aggregates in mouse and rabbit plasma are much smaller.

Table 19. Aggregate sizes formed in the different blood plasma sources obtained by DLS.

particle	aggregate human	aggregate mouse	aggregate sheep	aggregate rabbit
DEX $R_h = 82$ nm	$R_h = 394$ nm	$R_h = 201$ nm	$R_h = 515$ nm	$R_h = 268$ nm
HES $R_h = 93$ nm	$R_h = 415$ nm	$R_h = 289$ nm	$R_h = 621$ nm	$R_h = 214$ nm

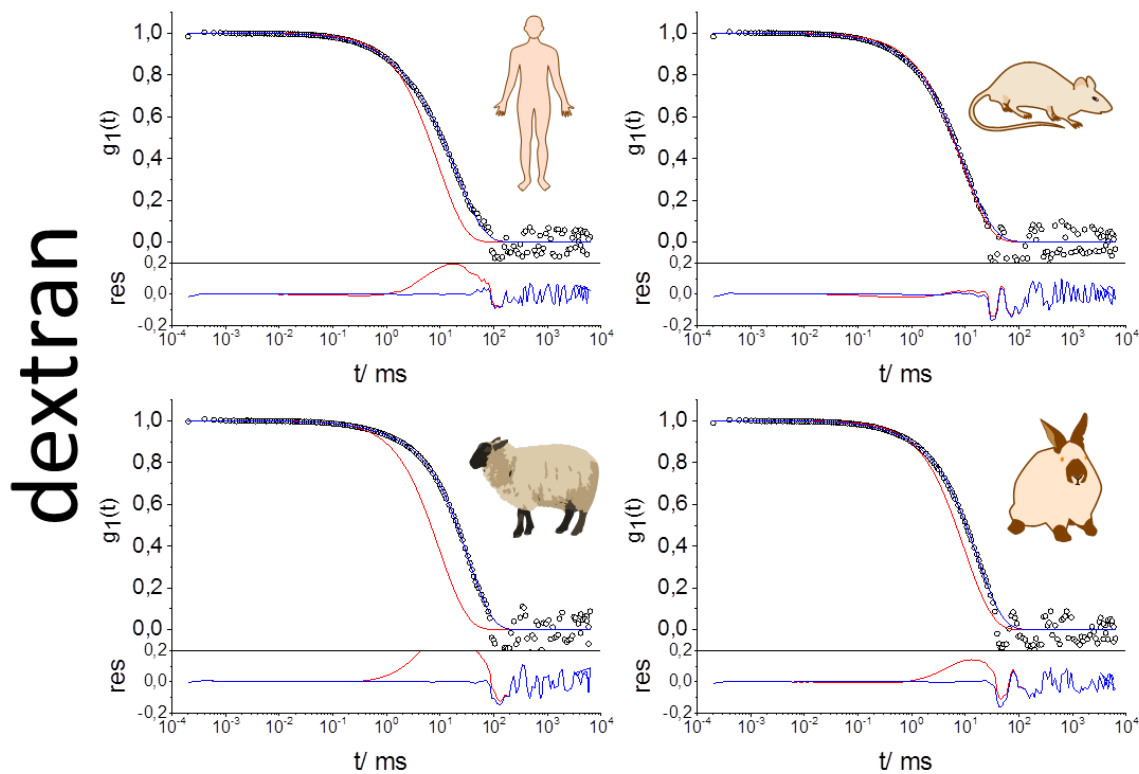


Figure 70. ACF at $\Theta = 30^\circ$ for BNF-DEX in human, mouse, sheep and rabbit plasma.

HES

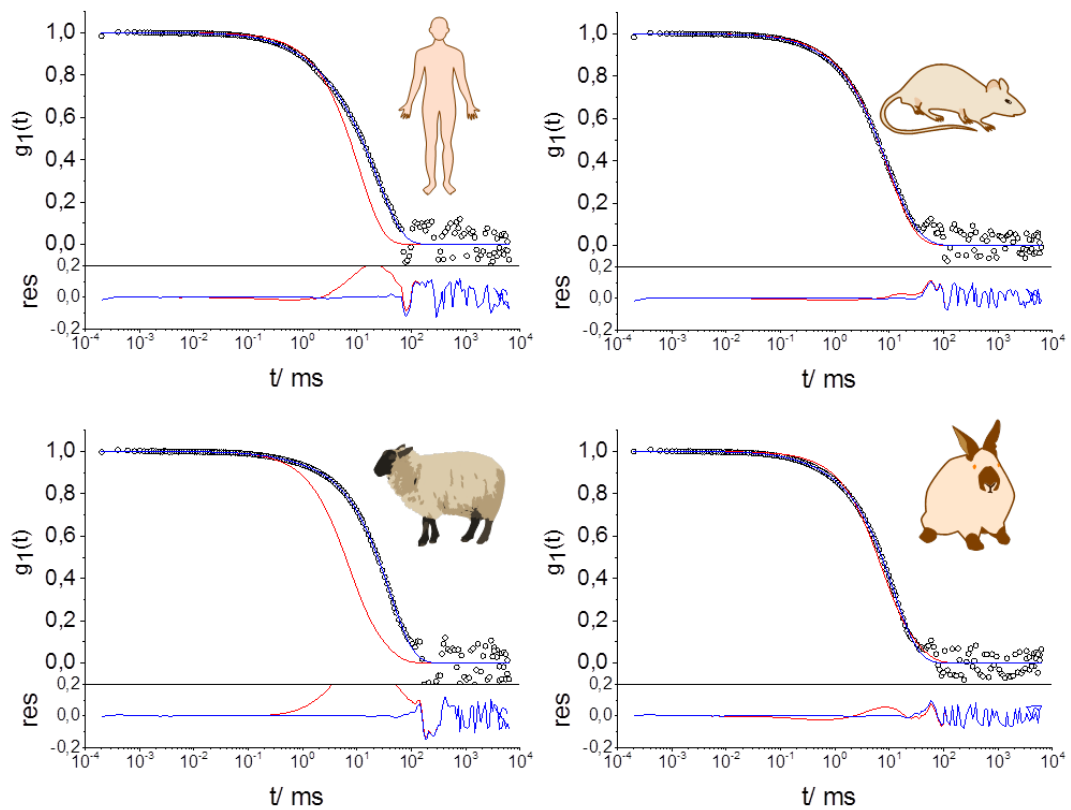


Figure 71. ACF at $\Theta = 30^\circ$ for BNF-HES in human, mouse, sheep and rabbit plasma.

Figures 70 and 71 show that huge differences for aggregate formation can be observed within the discussed *in vivo* models. Especially the significant discrepancy between mouse and human plasma implies difficulties as the mouse model is often chosen for experiments that depend on particle/aggregate size like body distribution or cellular uptake.

The hard corona formation of BNF-DEX and -HES was analyzed by SDS-PAGE and zeta potential measurements. Figure 71.A shows the respective protein patterns and Figure 71.B gives an overview of particle surface charge.

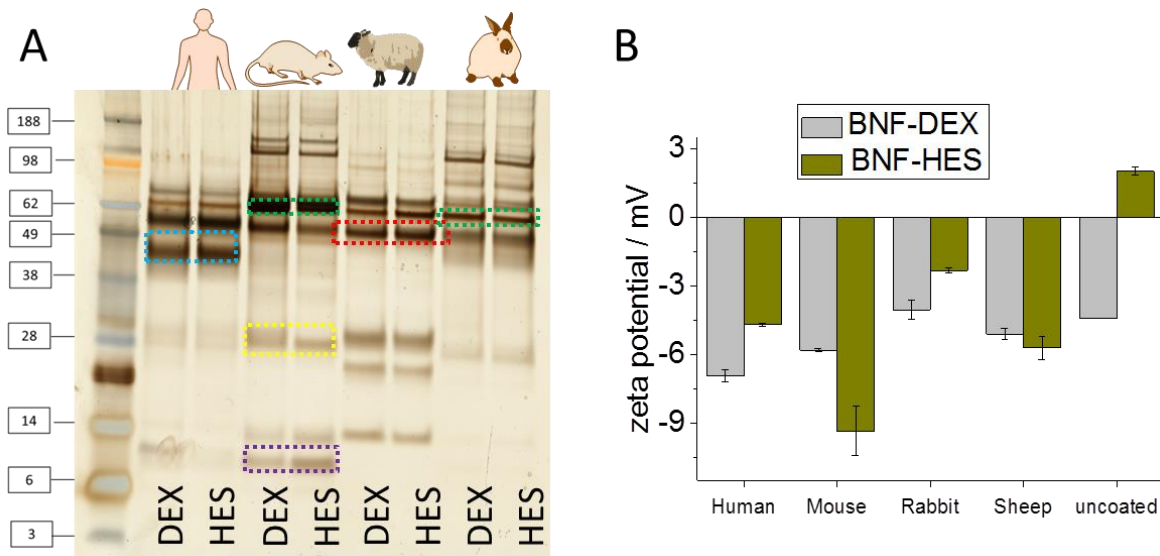


Figure 72. A) SDS-PAGE of protein coronas formed on BNF-HES and -DEX during incubation in human, mouse, sheep and rabbit plasma (performed by Johanna Simon). B) Zeta potential of uncoated as well as coated particles in the different plasma sources under investigation.

Arising from Figure 72.A, the protein patterns of BNF-DEX and BNF-HES are very similar after incubation in a respective protein source. This can be related to the fact, that both surfaces are composed of related sugar structures and do not differ much in polarity. The polarity of surfaces is of great importance when it comes to protein adsorption as already described in the introduction part. But again differences between the different animal models can be observed. The protein patterns formed during incubation in mouse and rabbit plasma look very similar. This is interesting concerning the less distinct aggregate formation of BNF-DEX and -HES in both. The marked protein bands in Figure 72.A are typically observed in many protein patterns and can therefore possibly be related to distinct proteins. The protein band at ~ 45 kDa (marked in light blue, see Figure 72.A) could correspond to apolipoprotein A-IV. The protein band at ~ 66 kDa (marked in green, see Figure 72.A) is typical for albumin adsorption. In the lower molecular range at ~ 9 kDa (marked in purple, see Figure 72.A) and ~ 28 kDa (marked in yellow, see Figure 72.A) protein bands related to potential apolipoprotein C3 or rather apolipoprotein A-I can be observed. The protein band marked in red (see Figure 72.A) at a molecular weight of ~ 56 kDa might correspond to the gamma chain of fibrinogen. Like in the previously discussed

chapter 3.4, the composition of protein source used for corona formation critically determines its composition.

The differences observed for the particles' surface charge before and after incubation mirrored by the zeta potential in Figure 72.B are smaller than the so far described ones for polystyrene particles. One explanation could be the reduced amount of adsorbed proteins calculated from Pierce 660 nm Assay. For the surface area of 0.05 m² only 13-43 µg of proteins adsorbed. Compared to the values in chapter 6.2.3 this corresponds to only ~ 10% of the amount found for PS-NPs. This can be related to the surface character as well. HES and DEX are rather hydrophilic while polystyrene is hydrophobic. As the main driving forces for protein adsorption are hydrophobic interactions, more proteins adsorb onto the latter ones.

In conclusion, the different plasma composition of the investigated *in vivo* models leads to differences in plasma protein induced aggregation of nanoparticles. These differences vary from one to another model system and cannot be generalized, but at least for BNF-HES and -DEX similar trends have been evaluated.

This means that for ideal characterization of particles used *in vivo* or rather *in vitro*, their stability against aggregation should be evaluated in the plasma of the used animal model and in addition in human plasma. Only when investigating the protein corona formation in both, animal model as well as human plasma, a transfer is possible.

Together with the results presented in chapters 3.2 and 3.3, an extensive evaluation process for nanocarriers designed for biomedical applications prior to *in vivo* experiments was demonstrated. Light was shed on different aspects that could critically affect the success of designed nanomedicines. With this, the biological identity a nanomaterial adapts upon application can be predicted in an improved manner and also adjusted by different coating procedures.

3.7 FROM THE MODEL SYSTEM TOWARDS LIPOSOMES FOR BIOMEDICAL APPLICATION

So far, the interactions of polystyrene particles as a model system with human blood plasma/serum proteins has been investigated in order to obtain a better understanding of the various factors that have an impact on protein-corona formation. In addition, the transferability from *in vivo* models towards the human plasma was analyzed. The next study changes from the model system of PS-lattices towards liposomal formulations for biomedical application.

In chapter 3.7.1, the development of stealth liposomes is focused. A novel hyperbranched polyglycerol was evaluated as alternative for PEG. Despite the prolonged blood circulation times that are usually achieved with PEGylation of nanocarriers, there are still some drawbacks. Due to its linear structure, the polymer contains only one terminal hydroxyl groups that can be used for modification with for instance antibodies. It will be demonstrated, that the novel hyperbranched structure outplays PEG in terms of liposome stabilization against aggregation.

In chapter 3.7.2, the gained insights into liposome stabilization from chapter 3.6.1 will be utilized for the development of liposomes containing a novel cationic spermine derivative. The novel compound was investigated in regards of complexation properties for siRNA. The liposomal formulations were optimized regarding their stability and investigated *in vitro* as well as *in vivo* for the delivery of siRNA to the liver of mice. It will be demonstrated that the system showed promising results *in vitro* and *in vivo* for liver accumulation and knockdown efficiency.

3.7.1 EVALUATION OF MULTIFUNCTIONAL LIPOSOMES IN HUMAN BLOOD SERUM BY DYNAMIC LIGHT SCATTERING

This chapter focusses on the development and characterization of “stealth” liposomes modified with a novel hyperbranched polyglycerol lipid (Cholesterol-PEG₃₀-hbPG₂₃). An emphasis was placed on the stability of these liposomes in comparison to those containing a linear PEG derivative (Cholesterol-PEG₄₄) directly in human blood serum, characterized via dynamic light scattering (DLS). The results presented have already been published and are reprinted (adapted) with permission from (“*Evaluation of Multifunctional Liposomes in*

Human Blood Serum by Light Scattering” Mohr et al., Langmuir 2014, 30, 14954-14962). Copyright © 2014, American Chemical Society.

Cholesterol as a natural membrane component has been widely used for the preparation of liposomes and as an anchor for polymeric lipids in lipid bilayers.¹⁵¹ Here, cholesterol was used as the initiator for the oxyanionic polymerization of various epoxides leading to Ch-PEG₄₄ and Ch-PEG₃₀-hbPG₂₃, because standard phospholipids could not be used due to their instability to extreme reaction conditions during the reaction. This technique allows for the synthesis of well-defined amphiphilic polyether-lipids with molecular weights in the range of conventional PEG-lipids used in sterically stabilized liposomes (2300 g mol⁻¹ and 3400 g mol⁻¹) and low polydispersities (M_w/M_n : 1.1 and 1.16, respectively). The structures of Ch-PEG₄₄ and Ch-PEG₃₀-hbPG₂₃ are shown in Figure 73. The synthesis of Ch-PEG and Ch-PEG-hbPG was done by Dr. Sophie Müller (AK Frey, Johannes Gutenberg University, Mainz, 2014)

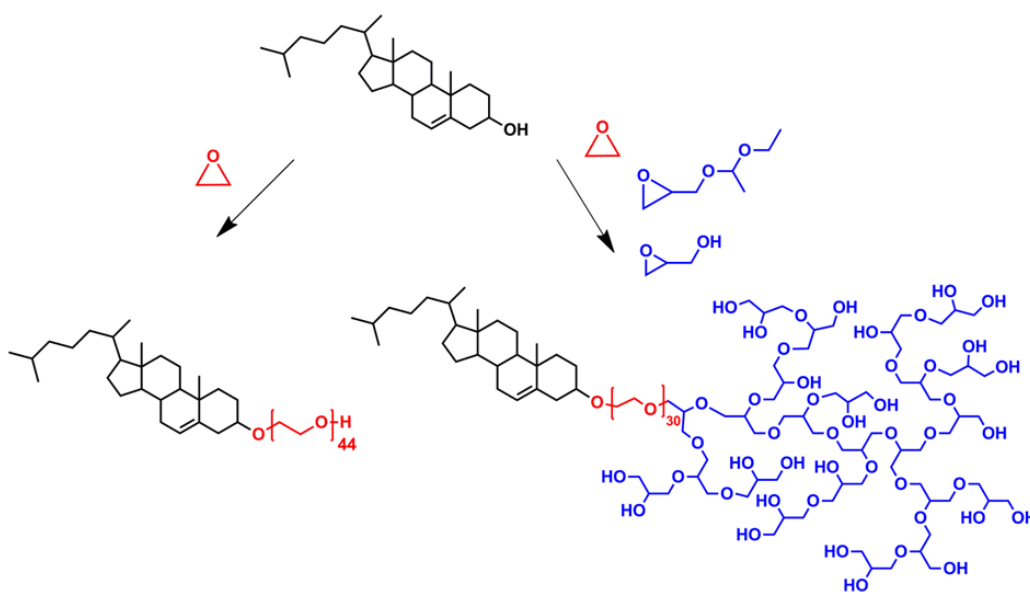


Figure 73. Molecular structures of the cholesterol-based amphiphilic lipid analogues. Reprinted (adapted) with permission from (*Evaluation of Multifunctional Liposomes in Human Blood Serum by Light Scattering*” Mohr et al., Langmuir 2014, 30, 14954-14962). Copyright © 2014, American Chemical Society.

The red PEG-part (left) represents the linear architecture of the Ch-PEG₄₄ amphiphile. The blue hydrophilic part (right) is the hyperbranched (hb) structure of the linear-hbPG lipid, which exhibits higher steric hindrance than its linear PEG analogue due to the globular structure of the hyperbranched block.

All liposomes were characterized via DLS in isotonic salt solution. The z-averaged hydrodynamic radii are summarized in Table 21. The angular dependency of the inverse apparent hydrodynamic radius for all liposomal systems is shown in the literature.²¹ Conventional liposomes (L0) without a polymer shell showed a radius of $\langle 1/R_h \rangle_z^{-1} = 115$ nm. PEGylated liposomes with polymer contents between 10-30 mol% had radii between 144 nm (L10-PEG) and 92 nm (L30-PEG), indicating that increasing the polymer content resulted in a slight decrease in the size of the structures. Liposomes containing Ch-PEG₃₀-hbPG₂₃ exhibited radii between 81 nm (L15-hbPG) and 102 nm (L30-hbPG), and a correlation between the radii and polymer content was not observed. However, the detected sizes of the liposomes are generally smaller than those with linear Ch-PEG₄₄, which may be attributed to a stronger effect on the liposome curvature by the bulky hyperbranched segments.

Table 21. Summary of the z-averaged hydrodynamic radii of all investigated liposomes. Reprinted (adapted) with permission from (*Evaluation of Multifunctional Liposomes in Human Blood Serum by Light Scattering* Mohr et al., Langmuir 2014, 30, 14954-14962). Copyright © 2014, American Chemical Society.

	L0	L10-hbPG	L10-PEG	L15-hbPG	L15-PEG	L20-hbPG	L20-PEG	L30-hbPG	L30-PEG
$\langle 1/R_h \rangle_z^{-1} / \text{nm}$	115	97	144	81	120	96	112	102	92

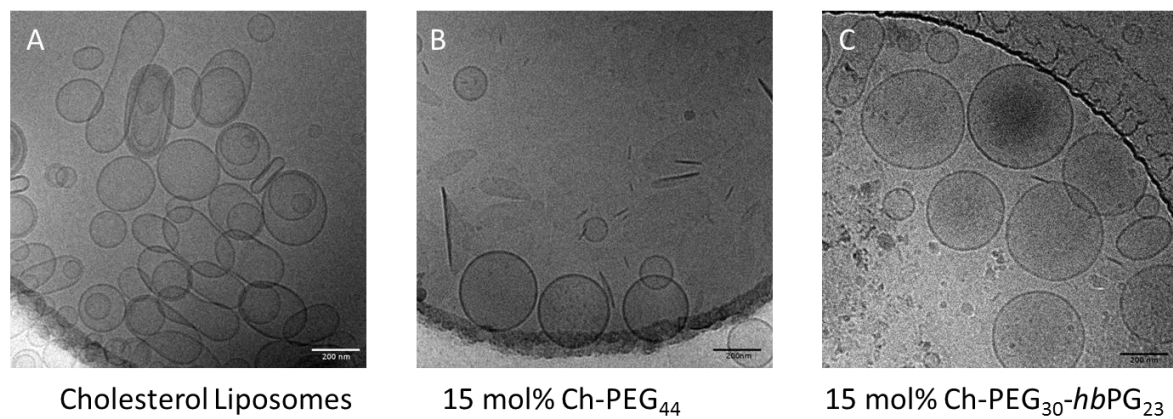


Figure 75. Cryo-Tem images of three different liposomes. Reprinted (adapted) with permission from (“Evaluation of Multifunctional Liposomes in Human Blood Serum by Light Scattering” Mohr et al., Langmuir 2014, 30, 14954-14962). Copyright © 2014, American Chemical Society (performed by Kristiane Rusitzka, Biology Department, Johannes Gutenberg University, Mainz).

Cryo-TEM measurements of liposomes with the different polymers incorporated showed the existence of vesicular structures and the successful formation of primarily unilamellar assemblies. As an example, Figure 75 depicts the respective images for EPC/cholesterol liposomes with (15 mol% Ch-PEG₄₄ (B) or Ch-PEG₃₀-hbPG₂₃ (C)) or without polymer (A). The non-stabilized (conventional) liposomes formed both spherical and non-spherical vesicles, whereas sterically stabilized liposomes predominantly showed spherical vesicles with a narrower size distribution. Additionally, it was observed that the conventional liposomes tended to overlap, possibly aggregate, whereas those that were stabilized by polymers maintained spatial separation.

It is imperative to characterize the aggregation behavior of any potential drug carrier in human blood serum, so the functionalized liposomes were analyzed by DLS. Size changes can be either caused by liposome-liposome bridging or by the formation of a protein (multi-)layer at the liposome surface. Since the investigation of L0 resulted in macroscopic precipitation, it was not possible to investigate these interactions with dynamic light scattering. Figure 76 gives an overview of the multicomponent analysis of the different PEGylated liposomes in human blood serum.

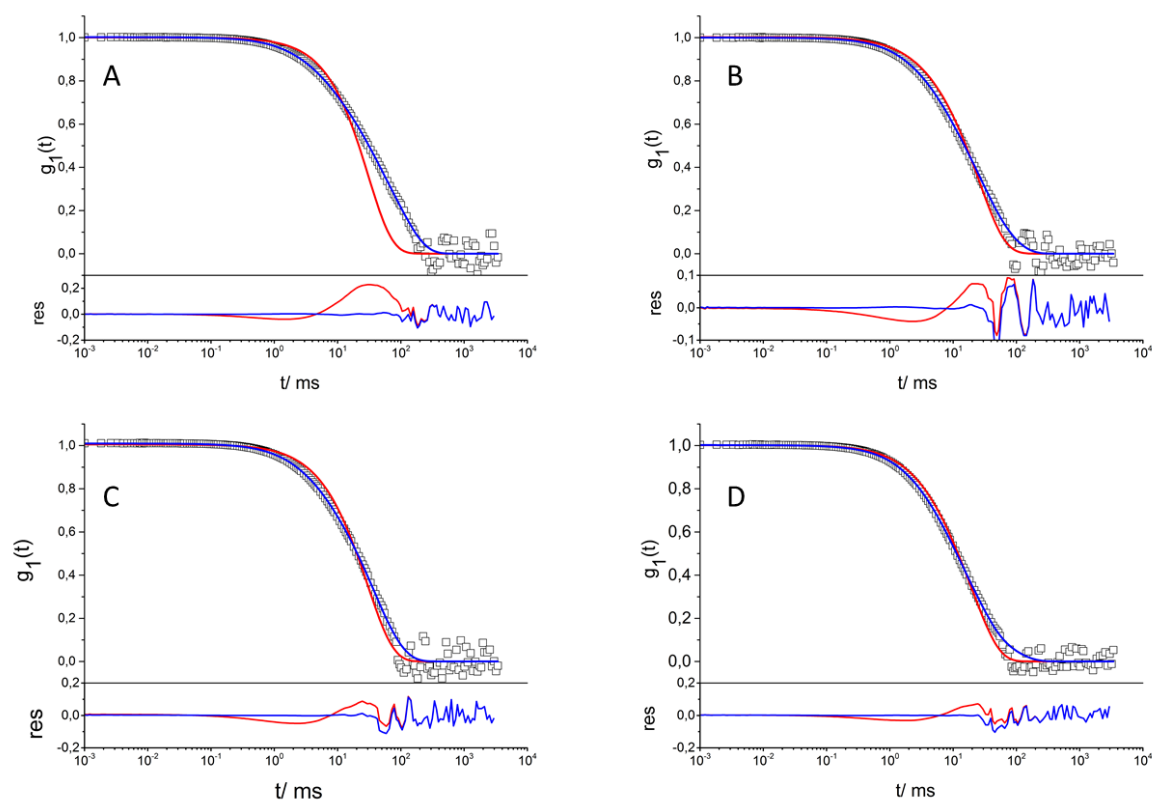


Figure 76. Liposomes containing Ch-PEG₄₄ in human serum: A) L10-PEG, B) L15-PEG, C) L20-PEG and D) L30-PEG. ACF at $\Theta = 30^\circ$ including data points, force fit (red) and aggregate fit (blue). Reprinted (adapted) with permission from (*"Evaluation of Multifunctional Liposomes in Human Blood Serum by Light Scattering"* Mohr et al., *Langmuir* 2014, 30, 14954-14962). Copyright © 2014, American Chemical Society (measurements performed by Dr. Kristin Mohr, Max Planck Institute for Polymer Research, Mainz).

There is aggregation for the PEGylated liposomes when they are introduced into human blood serum with $R_{h,Agg} = 330$ nm (10 mol% lipid), but the size of the aggregates decreased (170 nm), as the amount of Ch-PEG₄₄ (30 mol%) was increased. These values are much smaller than those for unmodified liposomes, which formed macroscopic aggregates and demonstrated the stabilizing and shielding effects of the Ch-PEG₄₄ on the assemblies.

Yet, liposomes stabilized with Ch-PEG₃₀-hbPG₂₃ showed an even better result when mixed with human blood serum, where the liposomes had no significant increase in their size in DLS. The corresponding ACFs are shown in the Figure below (Figure 77).

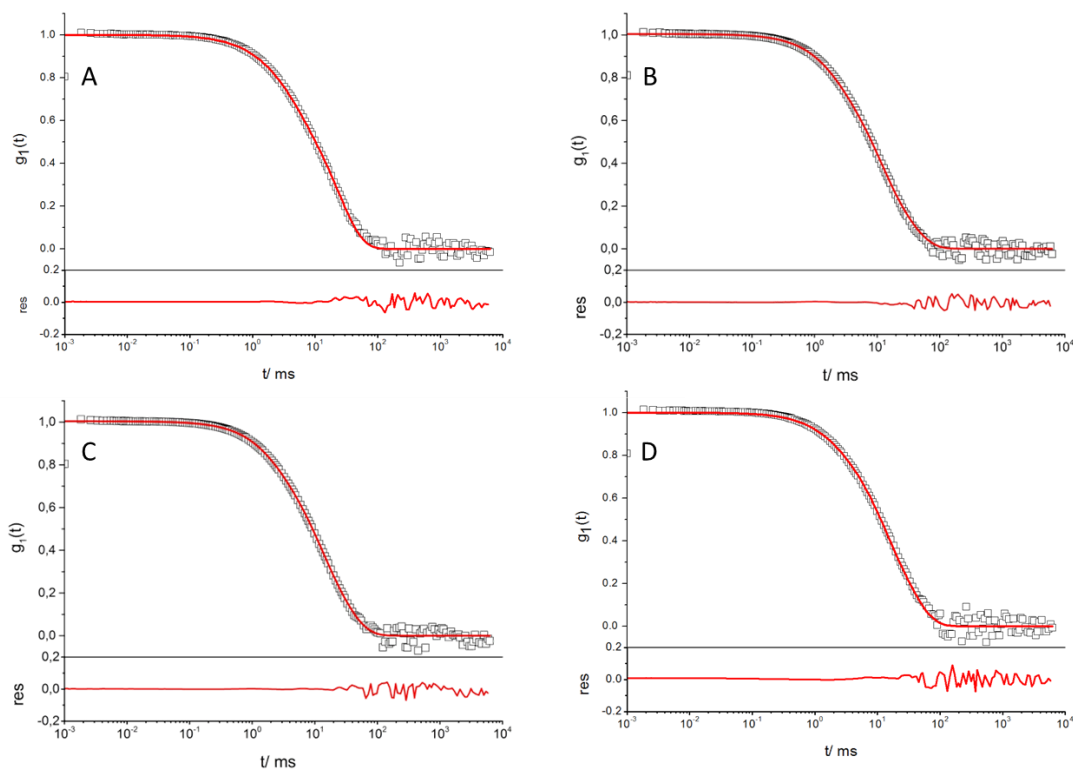


Figure 77. Liposomes containing Ch-PEG₃₃-hbPG₂₃ in human serum: A) L10-hbPG, B) L15-hbPG, C) L20-hbPG and D) L30-hbPG. ACF at $\Theta = 30^\circ$ including data points, force fit (red) and aggregate fit (blue). Reprinted (adapted) with permission from (*"Evaluation of Multifunctional Liposomes in Human Blood Serum by Light Scattering"* Mohr et al., *Langmuir* 2014, 30, 14954-14962). Copyright © 2014, American Chemical Society.

To conclude, it was the first time that the interaction between sterically stabilized liposomes and human blood serum was investigated via dynamic light scattering (DLS). This technique is a very sensitive method for the detection of aggregates and provides an efficient tool to monitor their formation, when polymer drug-delivery systems come into contact with complex biological media. In this work, the behavior of two different kinds of sterically stabilized liposomes was investigated, containing either cholesterol-PEG₄₄ or linear-hyperbranched cholesterol-PEG₃₀-hbPG₂₃ with contents between 10-30 mol%, EPC, and cholesterol. The systems were compared concerning their aggregation profile in blood serum. Liposomes containing Ch-PEG₄₄ led to the formation of aggregates in the size range between 170 nm to 330 nm (R_h), depending on the polymer amount, while the Ch-PEG₃₀-hbPG₂₃ modified liposomes were stable against aggregation despite the polymer content. Here, the adsorption of plasma proteins is assumed to be less likely due to the dense packing and multiple hydroxyl groups. The results show the steric stabilizing effect

of the novel, hyperbranched polyether lipids. Thus, based on the ability of hyperbranched polyethers to minimize interactions between liposomes and human blood serum, their relevance and potential advantages as drug delivery systems was demonstrated. From the data it is obvious that amphiphilic hyperbranched structures constitute a promising alternative to PEGylated “stealth” liposomes while showing favorable behavior in blood serum and introducing multiple functional groups at the vesicles’ surfaces.

3.7.2 MULTICOMPONENT LIPOSOMES FOR siRNA DELIVERY TO THE LIVER

This chapter focusses on the development of a liposomal system for siRNA delivery consisting of cholesterol (Chol), distearoylphosphatidylcholine (DSPC) and surfactant TF (1-hydroxy-50-amino-3,4,7,10,13,16,19,22-octaoxa-37,41,45-triaza-pentacontane), a novel spermine derivative (HO-EG8-C12-spermine) for improved siRNA delivery to cells *in vitro* and *in vivo*. The *in vitro* / *in vivo* experiments were performed by Leonard Kaps, University medical center, JGU. The work presented in this chapter is already submitted as full article.² The structure of TF is shown in Figure 78. It was synthesized by Dr. Chai Wenqiang (AK Schmidt, Johannes Gutenberg University, Mainz). It resembles an ABC structure with A being the non-ionic hydrophilic PEG block, B the hydrophobic alkyl middle block and C the hydrophilic cationic spermine block. The light yellow solid was characterized by ¹H NMR and mass spectrometry. ESI-MS shows a single peak with a mass to charge ratio of 739.63. The amine groups of the spermine part were used to label the surfactant TF with CW800-NHS ester. The HPLC elugram showed exclusively the mono-functionalized product (see Figure 79).

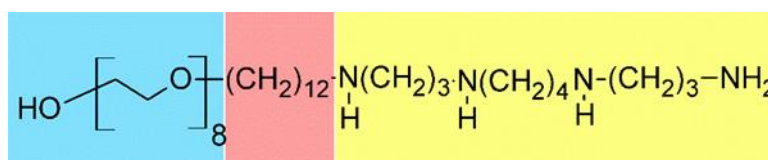


Figure 78. Chemical structure of surfactant TF.

² “Physicochemical and Preclinical Evaluation of Spermine-derived Surfactant Liposomes for *in vitro* and *in vivo* siRNA-Delivery to Liver Macrophages”

Laura K. Müller, Leonard Kaps, Detlef Schuppanb, Alexander Brose, Chai Wenqiang, Karl Fischer, Sophie Müller, Holger Frey, Manfred Schmidt, Kristin Mohr*

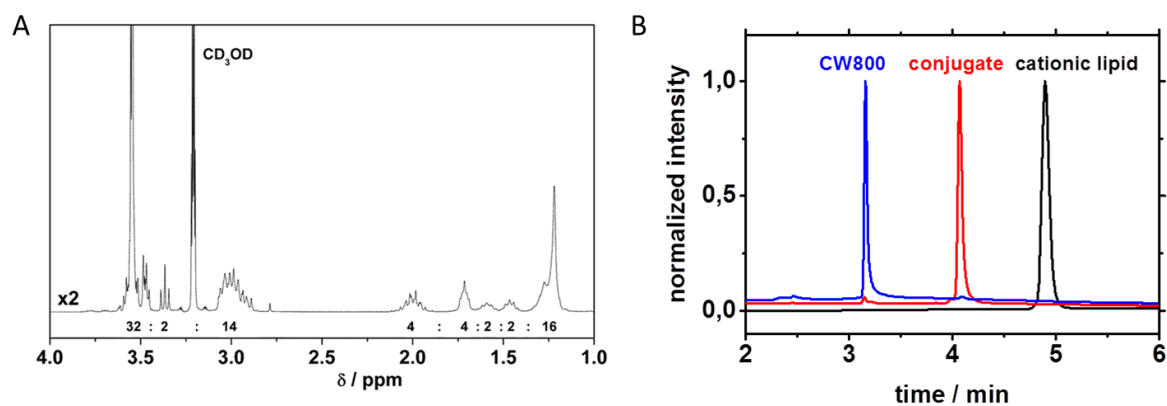


Figure 79. A) ^1H NMR of surfactant TF in CD_3OD . B) HPLC of dye, cationic lipid TF and TF-dye conjugate; MN-HD8-column 125/4/5 μm l, $T=20^\circ\text{C}$, 10 min: 5/95-100/0 (THF/water+0.1%TFA) (performed by Beate Müller, AK Landfester, MPIP).

This novel surfactant contains two hydrophilic head groups, a cationic and a non-ionic one, that are interconnected by a C12 linker. The surfactant was anticipated to combine protein repellent characteristics of PEG with cationic charges required for siRNA complexation/encapsulation. The surfactant TF was introduced into well-known liposomal formulations (comprising cholesterol and DSPC) as a novel cationic component. Moreover, the previously described hyperbranched lipid, hbPG, consisting of cholesterol as the hydrophobic and a hyperbranched polyglycerol as the hydrophilic part, was utilized since it effectively provided steric shielding of liposomes against aggregate formation induced by serum proteins. The composition and absolute concentrations of all investigated liposomes are given in Table 22.

Table 22. Composition of investigated liposomes.

Liposome	L-1:1:0	L-1:1:1	L-1:1:2	L-1:1:4	L-1:1:4-hbPG
Weight ratio (Chol:DSPC:TF)	1:1:0	1:1:1	1:1:2	1:1:4	1:1:4*
Molar ratio (Chol:DSPC:TF)	2:1:0	2:1:1	2:1:2	2:1:4	2:1:4*
c(Chol) in EtOH (g/L)	20	20	20	20	16
c(DSPC) in EtOH (g/L)	20	20	20	20	20
c(TF) in EtOH (g/L)	0	20	40	80	80
Ch-PEG ₂₂ -hbPG ₃₅ in EtOH (g/L)	0	0	0	0	36
c (total) in EtOH (g/L)	40	60	80	120	152
c(total) in DPBS (g/L)	0.87	1.33	1.33	1.33	1.33
c(TF) in DPBS (g/L)	0	0.44	0.67	0.89	0.89

* 17.5 mol% of cholesterol was replaced by hbPG corresponding to 5 mol% hbPG of total lipid content.

It is known that size and inner structure of liposomes are controllable by extrusion through membranes, i.e. by the pore diameter of the extrusion membrane⁷² and by the extrusion speed. Repeated extrusion through 50 nm pore size filters yielded mostly unilamellar liposomes with a size range of 100-150 nm that is considered to be appropriate for surpassing the fenestrated endothelium of liver cells. All liposomes were characterized by dynamic (DLS) and static light scattering (SLS) as well as by zeta potential measurements (see Table 23, Figure 80). For the uncharged liposome L-1:1:0 the angular dependence of both, the apparent hydrodynamic radii $\langle 1/R_h \rangle_{app}$, and the reduced scattering intensities $\ln(Kc/R)$, are very pronounced and curved downwards at low q , typically observed for samples with a very broad size distribution. In contrast, all other samples exhibit linear dependencies of $\langle 1/R_h \rangle_{app}$ as function of q^2 , the slopes of which are small but significantly larger than zero (expected for monodisperse spheres). Except for samples L-1:1:0 the normalized second cumulants, μ^2 , were determined to $0.1 < \mu^2 < 0.2$, indicating moderately broad size distributions in qualitative agreement with the small slopes of $\langle 1/R_h \rangle_{app}$ versus q^2 . The ρ -ratios defined by the ratio of the radius of gyration (R_g) and the hydrodynamic radius (R_h) indicate the liposomes to form mostly unilamellar vesicles that are also proven by cryo-TEM measurements (Figure 80).

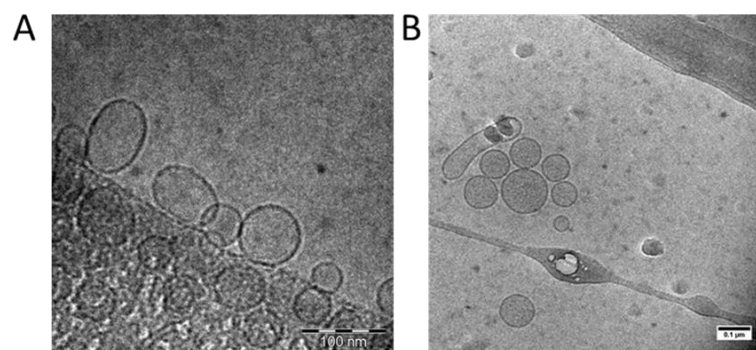


Figure 80. Cryo-TEM images of A) L-1:1:1 loaded with siRNA and B) unloaded L-1:1:4-hbPG (performed by Dr. Max Bernhard³).

³ Dr. Max Bernhard, Ak Prof. Dr. Katharina Landfester, 2015

The zeta potentials of all liposomes (see Table 23) are slightly negative despite the presence of the cationic component TF. Only the hbPG stabilized liposome exhibits neutral charge. At present these data cannot be properly explained. It might indicate that the spermine part of TF is predominantly located at the inner liposome surface, although simple volume considerations of spermine as compared to PEG₈ do not necessarily support this scenario.

Table 23. Zeta potential, DLS- and SLS-results of liposomes.

liposome	$\langle 1/R_h \rangle_z^{-1} / \text{nm}$	$\langle R_g^2 \rangle_z^{1/2} / \text{nm}$	ρ	zeta potential / mV
L-1:1:0	130	-*	-	-9.8 ± 5.5
L-1:1:1	53	55	1.04	-5.3 ± 5.7
L-1:1:2	59	58	0.98	-
L-1:1:4	63	63	1.00	-7.7 ± 5.3
L-1:1:4-hbPG	63	63	1.00	1.3 ± 4.4

* Could not be determined due to strongly curved Guinier plot.

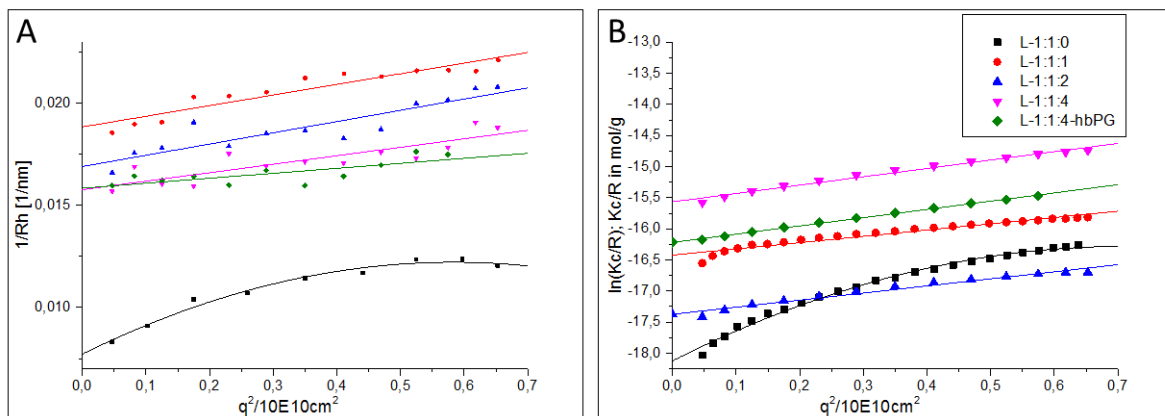


Figure 81. Angular dependency of the inverse hydrodynamic radius (A) and Guinier-plots (B) of liposomes.

For further investigation, the liposomal systems were analyzed by DLS regarding their stability against aggregation in human blood serum by mixing equal volumes of liposome and serum solution. Figure 82 shows the corresponding ACFs including data points, force fit and fit in regards of aggregate formation.

The stability of liposomes in serum depends strongly on their composition. Liposomes without incorporated cationic lipid formed aggregates in human serum with a size $R_h = 380$ nm (measured at a scattering angle of 30°) and contributed 56% to the total scattering intensity. From literature it is already known that liposomal formulations only built up by cholesterol and phosphatidylcholines are not stable in biological environments due to their similarity to naturally occurring lipoproteins.⁶⁰ When cationic lipid was added to the liposomal formulation, aggregation also took place, but the size as well as the contribution of the formed aggregates to the total scattering intensity decreased with increasing amount of surfactant TF. For example, for liposome L-1:1:4 the aggregates in human serum were significantly smaller ($R_h = 195$ nm) and contributed little to the total intensity of the scattering (31%).

As was shown before for liposomal formulations consisting of egg phosphatidylcholine (EPC) and cholesterol, the steric stabilization of liposomes by incorporation of hyperbranched polyglycerol structures more effectively prevents aggregate formation in human blood serum as compared to linear PEG surfactant. Liposomes containing PEGylated surfactant of up to 30 mol% still showed aggregate formation in human serum while those with 10, 15, 20 and 30 mol% hyperbranched surfactant were stable. Thus, in the present work 5 mol% hyperbranched polyglycerol was added to the lipid mixture in order to completely prevent aggregate formation in human serum as revealed by Figure 82.

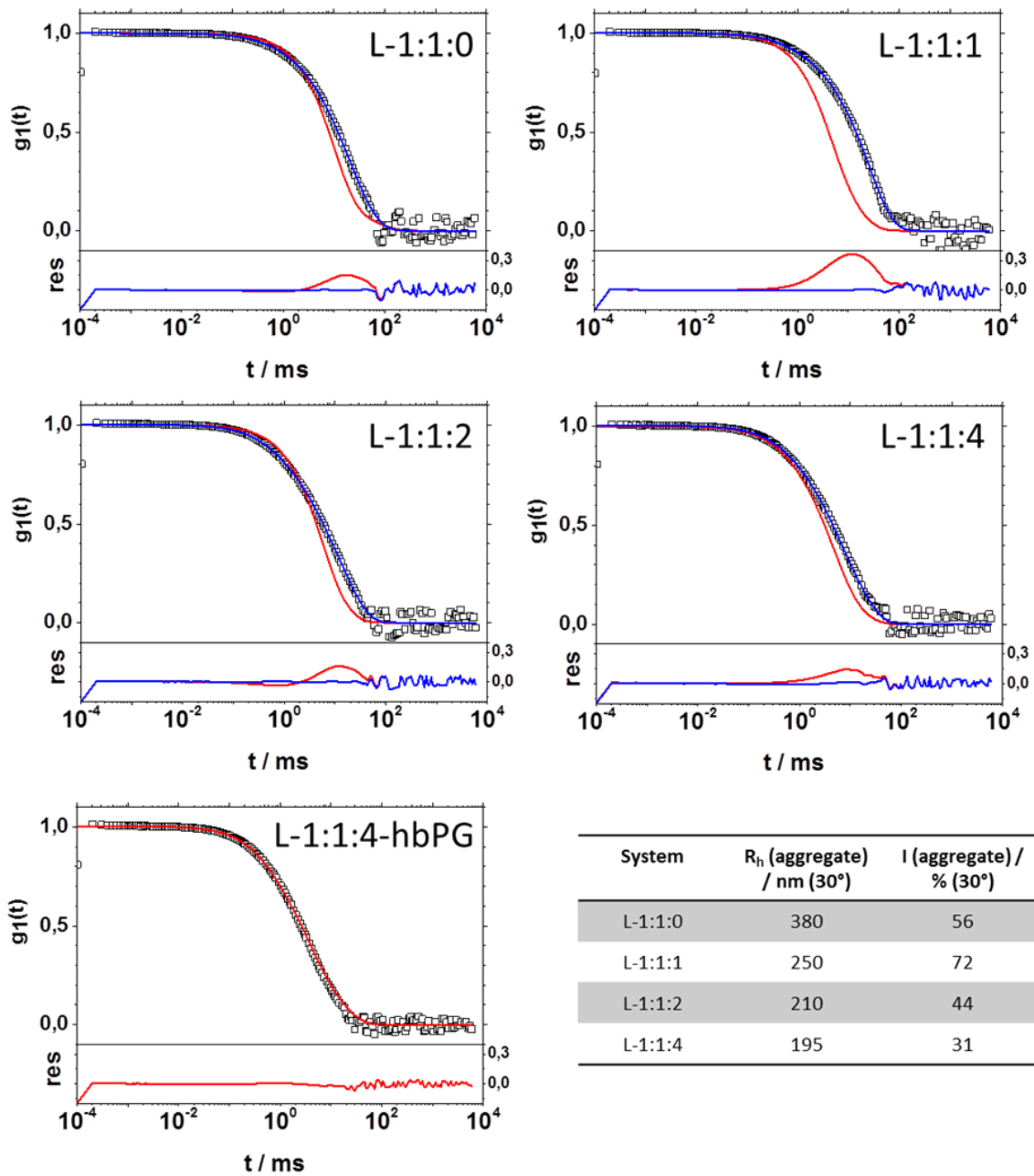


Figure 82. Autocorrelation functions of the different liposomal systems in human serum at 30° and the respective aggregate size with its impact on the scattering intensity. Red lines: Force fit with the pure component correlation, blue lines: Fit with an additional aggregate term. Residues of the respective fits are shown in the lower part of the graphs.

When siRNA (anti-CD68) was dissolved in the aqueous phase prior to liposome formation it was encapsulated to a very large extent by all liposomes, i.e. between 81 and 97%, as proven by a Quant-iT™ RiboGreen® assay (Table 24). As shown by *cryo*-TEM (see Figure 80) the siRNA loaded liposomes preserved their unilamellar structure. Quantitative light

scattering results confirmed this observation, since the ρ -ratios of liposomes loaded with siRNA remained at values close to 1 (see Table 24 and Figure 83). Such high encapsulation efficiencies are usually not achieved if the siRNA is just sterically trapped within the vesicles. Rather, electrostatically driven complex formation is required to explain the high siRNA load. The latter scenario was also supported by the large N/P ratio calculated from the liposome composition. Thus, in the following the siRNA loaded liposomes are termed lipoplexes.

Table 24. Zeta potential, DLS -, SLS results and encapsulated amount of siRNA of loaded liposomes.

liposome	$\langle 1/R_h \rangle_z^{-1}$ /nm	$\langle R_g^2 \rangle_z^{1/2}$ /nm	ρ	zeta potential	encapsulated siRNA	N/P
L-1:1:1 siRNA	52	48	0.92	-6.3±6.8	97%	17
L-1:1:2 siRNA	57	56	0.98	-3.7±7.6	81%	25
L-1:1:4 siRNA	61	58	0.95	-5.2±9.6	90%	34
L-1:1:4-hbPG siRNA	62	-	-	-7.7±5.9	90%	34

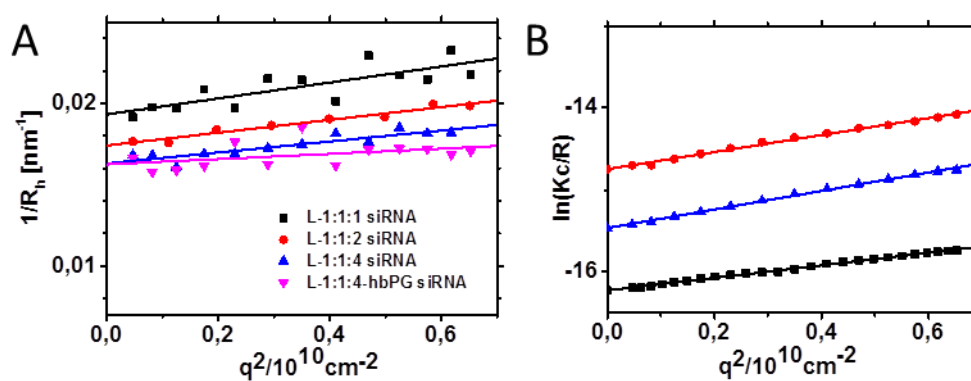


Figure 83. A) Angular dependency of the inverse hydrodynamic radius of siRNA loaded liposomes. B) Guinier-plots of siRNA-loaded liposomes.

As shown in Figure 84, complex size and zeta potential were reproducible and did not depend on the type of siRNA used.

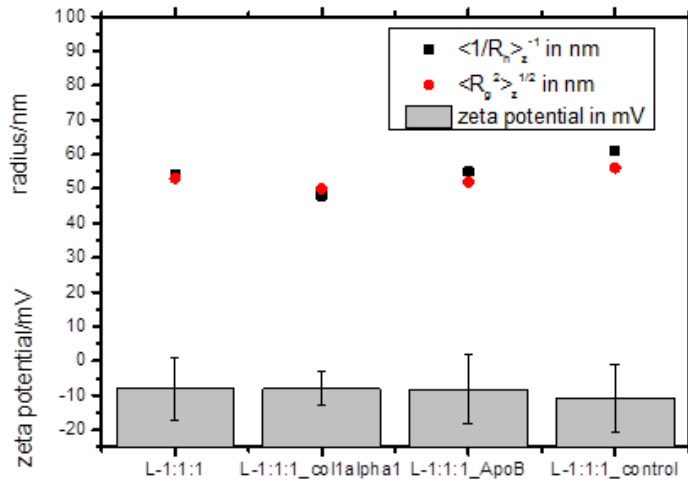


Figure 84. Zeta potential of L-1:1:1 in comparison to the zeta potential of L-1:1:1 loaded with different types of siRNA.

Prior to biological experiments the small but significant amount of free siRNA needs to be removed by either dialysis and or by centrifugal filters. Both methods were tested for liposome L-1:1:1 and the results are shown in Figure 85. The size of the lipoplexes did not change significantly during purification by centrifugal filters, whereas the sizes decreased by approximately 20% after dialysis. Since application of centrifugal filter devices decreased the free siRNA concentration to a lower level (0.1% as compared to 0.3% by dialysis) this method was applied to all samples discussed below.

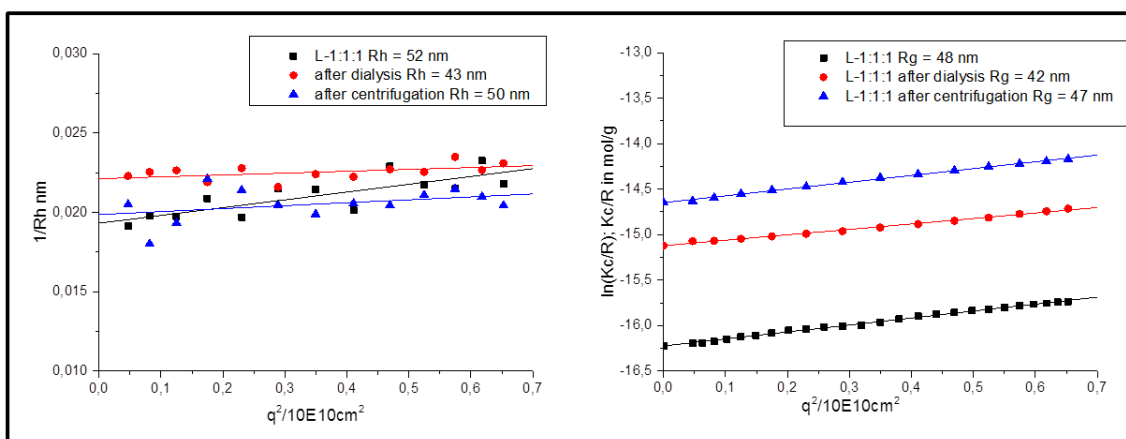


Figure 85. Comparison of two different work-up procedures for L-1:1:1.

Again, the stability of lipoplexes against aggregation was evaluated by using dynamic light scattering. It was recently reported that aggregate formation of cationically charged nanogels in serum depends on the siRNA loading, i.e. aggregates were observed for bare nanogels, whereas no aggregates could be detected for siRNA loaded nanogels. Thus, a direct comparison was made for liposomes/lipoplexes L-1:1:4 and L-1:1:4-*hbPG* added to pooled human blood plasma (see Figure 86). In contrast to Nuhn *et. al.*,¹⁵² no significant differences were observed between the bare liposomes and the lipoplexes loaded with siRNA. Again, *hbPG* stabilized lipoplexes L-1:1:4-*hbPG* did not aggregate in plasma, whereas for L-1:1:4 lipoplex aggregates of $R_h = 250$ nm were detected that were in a similar size range as those observed in serum.

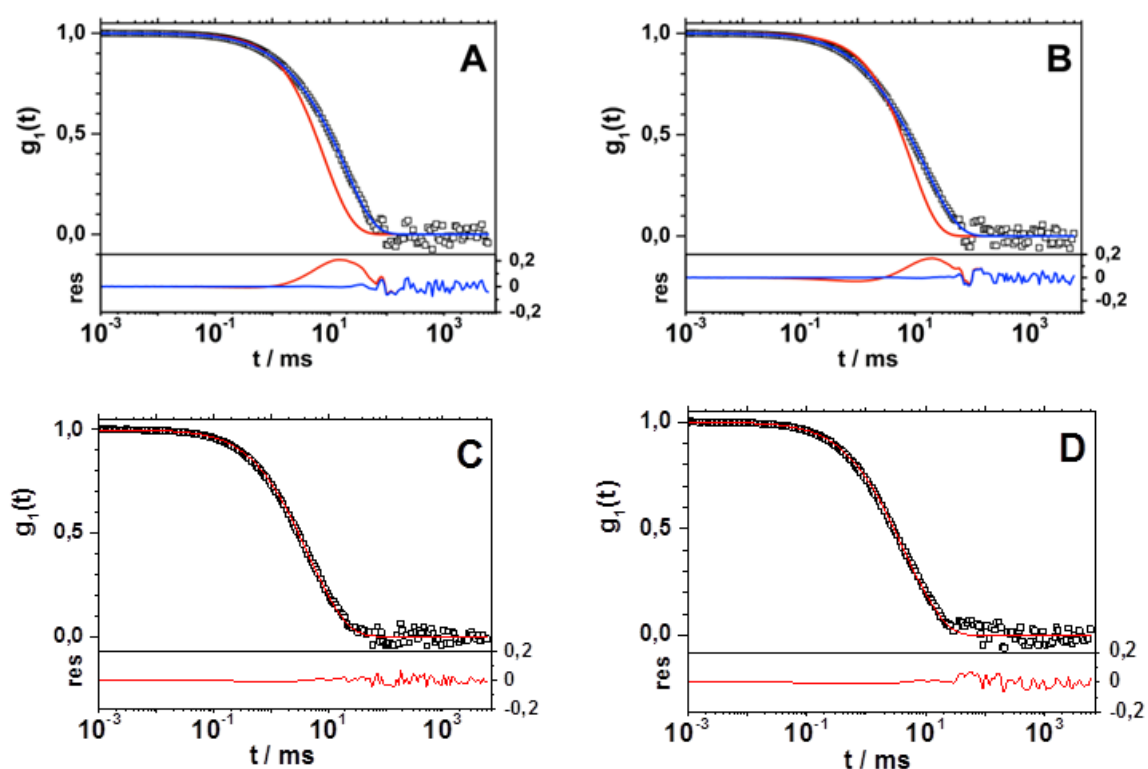


Figure 86. Correlation functions (recorded 30° scattering angle) of liposomes and siRNA loaded liposomes in 50% human plasma. A) liposome consisting of DSPC, Chol and lipid TF, B) liposome in A loaded with siRNA (N/P = 34), C) liposome consisting of Chol, DSPC, TF and *hbPG*, D) liposome in C loaded with siRNA (N/P = 34). Red lines: Force fit with the pure component correlation function, blue lines: Fit with an additional aggregate ter. Residues of the respective fits are shown in the lower part of the graphs.

Prior to *in vivo* applications, cytotoxicity and *in vitro* knockdown efficiency of lipoplex L-1:1:4 was evaluated. As shown in Figure 87a), L-1:1:4 lipoplexes loaded with scrambled siRNA (scsiRNA) caused no *in vitro* cytotoxicity in MHS macrophages, even at concentrations corresponding to 600 nM siRNA that are far above the concentrations required for *in vitro* or *in vivo* gene knockdown. L-1:1:4 loaded with 100 nM anti-CD68 siRNA achieved a significant CD68 knockdown (40% vs the PBS control) in MHS cells, whereas L-1:1:4 lipoplexes loaded with scrambled siRNA (scsiRNA) revealed no effect (Figure 87b)).

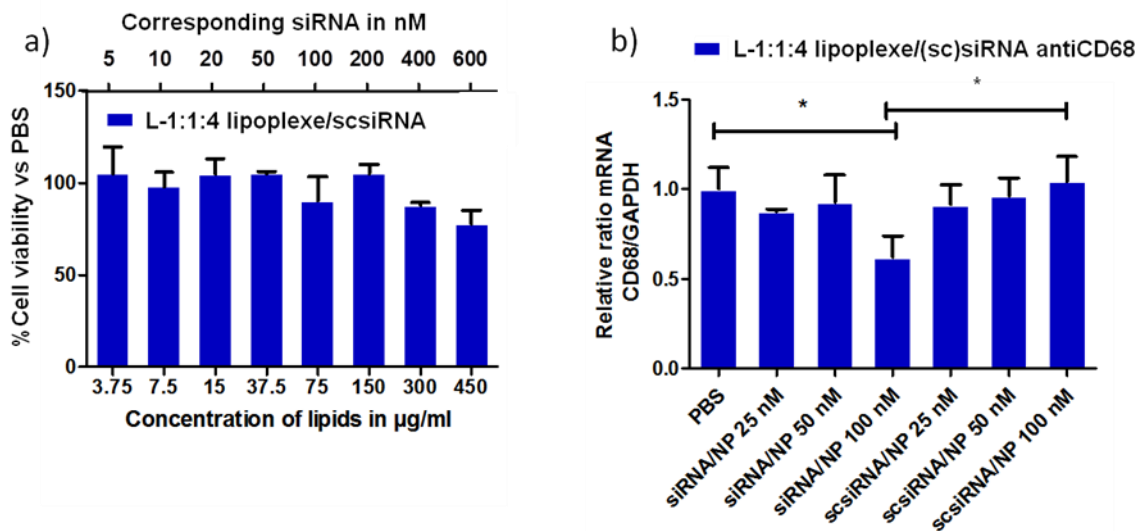


Figure 87. a) Viability of MHS macrophages in response to increasing amounts of L-1:1:4 lipoplex loaded with scrambled siRNA normalized to PBS; incubation time 24 h (n = 3); MEAN \pm SD; b) *In vitro* knockdown by L-1:1:4 (NP) loaded with anti-CD68 siRNA after 24 h. scsiRNA, negative control; * p < 0.05 (n =3); MEAN \pm SD (measurements performed by Leonard Kaps, Medical department of the Johannes Gutenberg University, Mainz).

Macrophages are a central part of the innate immune system expressing a variety of danger sensing receptor, such as the toll like receptors (TLRs) that are involved in anti-bacterial and anti-viral immune defense. L-1:1:4 loaded with antiCD68 siRNA did show a robust knockdown at a reasonable siRNA concentration of 100 mM without signs of off-target effects *in vitro*, the liposomal formulations qualified for further investigations. Both lipoplexes, L-1:1:4 and L-1:1:4-hbPG were tested *in vivo*, to assess efficacy in macrophage

targeting and to elucidate potential effects of serum-induced aggregate formation on *in vivo* performance.

In vivo particle biodistribution studies require a detectable dye with an emission in the near infrared (NIR) wavelength spectrum that is being less absorbed by tissue and blood than emission in the visible range. Therefore, 5 mol% of TF was replaced by CW800-labeled lipid TF in both liposomal formulations.

Mice (n = 3 per group) received two retroorbital injections 48 h apart of 1 or 2 mg/kg anti-CD68 siRNA loaded into L-1:1:4 or L-1:1:4-hbPG, or an equivalent volume of PBS (Figure 88 top).

Figure 88 (bottom) shows the biodistribution of CW800 labeled L-1:1:4 and L-1:1:4-hbPG lipoplexes at 0, 1, 3, 6, 24 and 48 h after injection. At 0 to 6 h after intravenous injection both lipoplexes displayed some disassembly, since free NIR dye was cleared by the kidneys and further ended up in the bladder. However at 48 h the cleared dye accumulated predominantly in the liver, suggesting that stable lipoplexes are sequestered in the liver, while degraded lipoplexes are rapidly cleared via the kidney.

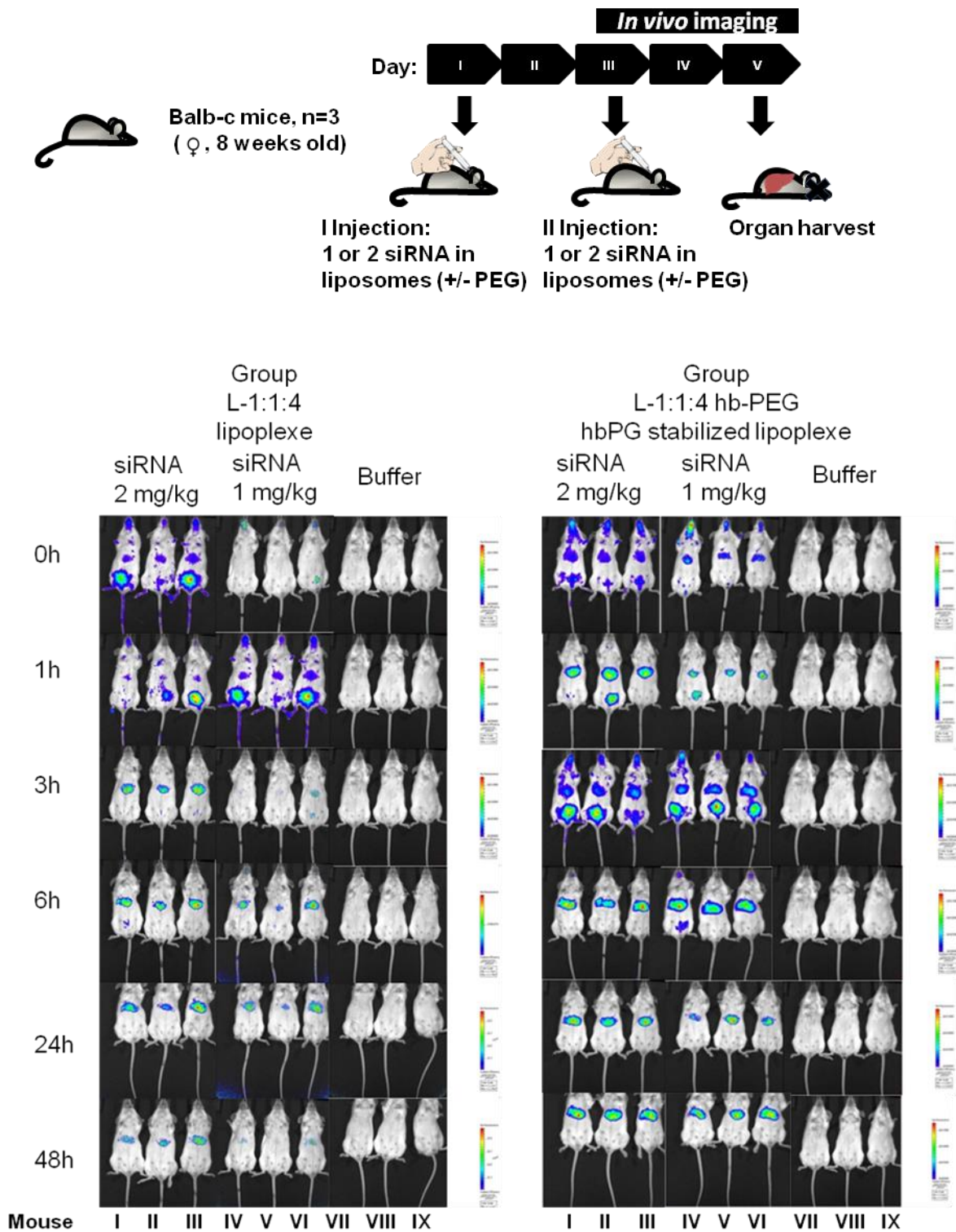


Figure 88. Top) *In vivo* knockdown outline. Mice received two retroorbital injections of 1 or 2 anti-CD68 siRNA encapsulated in L-1:1:4 or L-1:1:4-hbPG; *in vivo* imaging period indicated above timeline. Bottom) *In vivo* images system (IVIS) pictures of mice injected with 1 mg/kg or 2 mg/kg antiCD68 siRNA loaded in L-1:1:4 lipoplexes (left) or L-1:1:4-hbPG hbPG stabilized lipoplexe (right) labeled with CW800 near infrared dye at 0, 1, 3, 24 and 48h (measurements performed by Leonard Kaps).

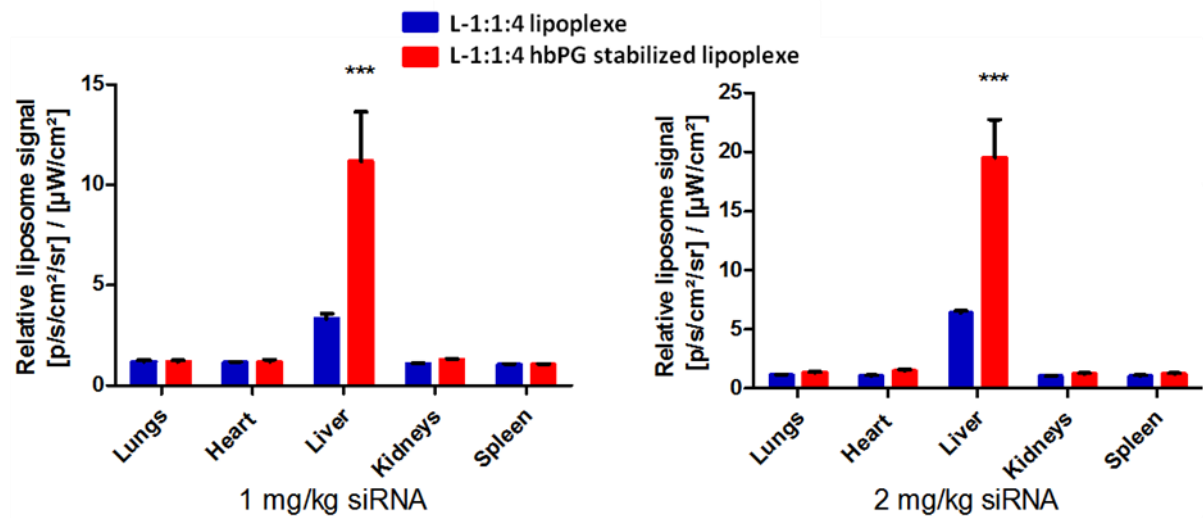


Figure 89. *Ex vivo* organ quantification of L-1:1:4 lipoplex (blue) and L-1:1:4-hbPG (red) labeled with near infrared dye 48 h after the second injection, *** $p < 0.001$; MEAN \pm SD (measurements performed by Leonard Kaps).

48 h after the second lipoplex injection organs were imaged *ex vivo* (see Figure 90). Such *ex vivo* organ images allow a more accurate quantification of lipoplex biodistribution. Both the simple lipoplex L-1:1:4 and the hbPG derivatized L-1:1:4-hbPG lipoplex accumulated in the liver in a dose-dependent manner, with L-1:1:4-hbPG showing a higher signal (Figure 89), which may be due to their longer blood circulation time originating from better stealth properties against *in vivo* serum protein interaction.

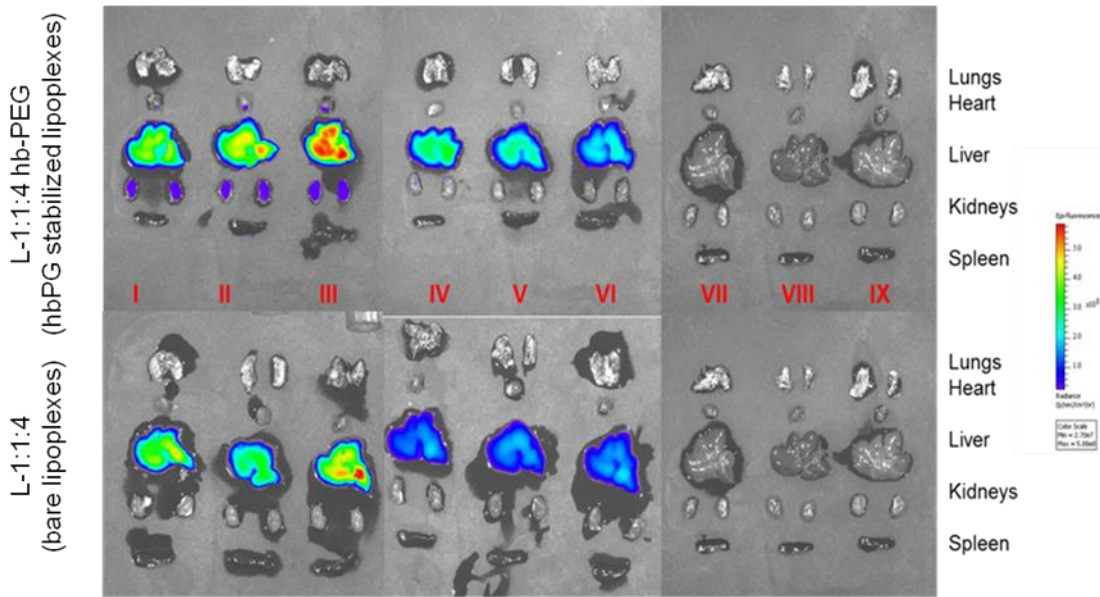


Figure 90. IVIS pictures of ex vivo organs from mice that were injected with 1 mg/kg or 2 mg/kg antiCD68 siRNA loaded in L-1:1:4 or L-1:1:4-*hbPG* respectively labeled with near infrared dye 48h after injection (measurements performed by Leonard Kaps).

After the second injection of the lipoplexes, liver macrophages (CD45+, F4/80+-cells) were isolated and subjected to FACS analysis to determine the *in vivo* macrophage-specific uptake of the lipoplexes. 48 h after the second injection approximately 3-6% of both lipoplexes were taken up to by liver resident macrophages (Figure 91). This dose-dependent uptake of both lipoplexes is lower than that of siRNA loaded nanogels that were recently investigated.

The two lipoplex formulations loaded with two concentrations of anti-CD68 siRNA (1 and 2 mg/kg siRNA) induced a significant *in vivo* knockdown of up to 70%, while lipoplexes loaded with scrambled siRNA did not show any off target knockdown (Figure 92).

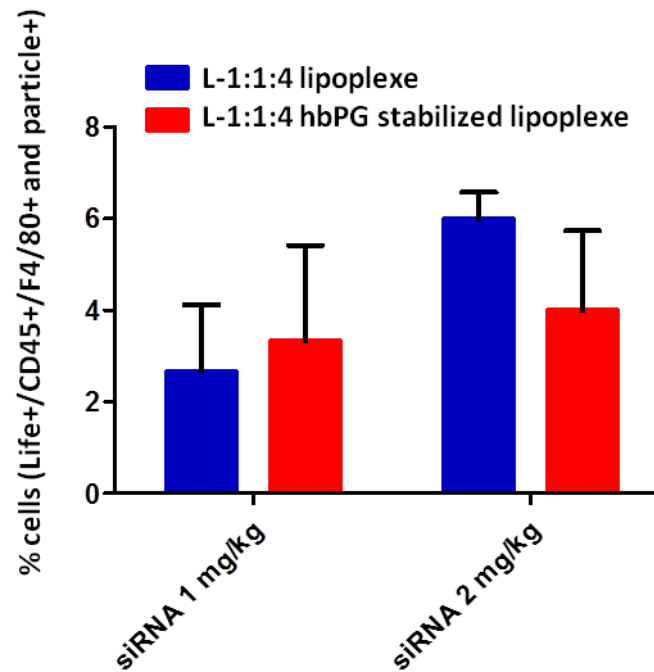


Figure 91. *In vivo* liver resident macrophage uptake of L-1:1:4 lipoplex (blue) and L-1:1:4-hbPG lipoplex (red) labeled with NIR dye 48 h after the second injection; MEAN \pm SD (measurements performed by Leonard Kaps).

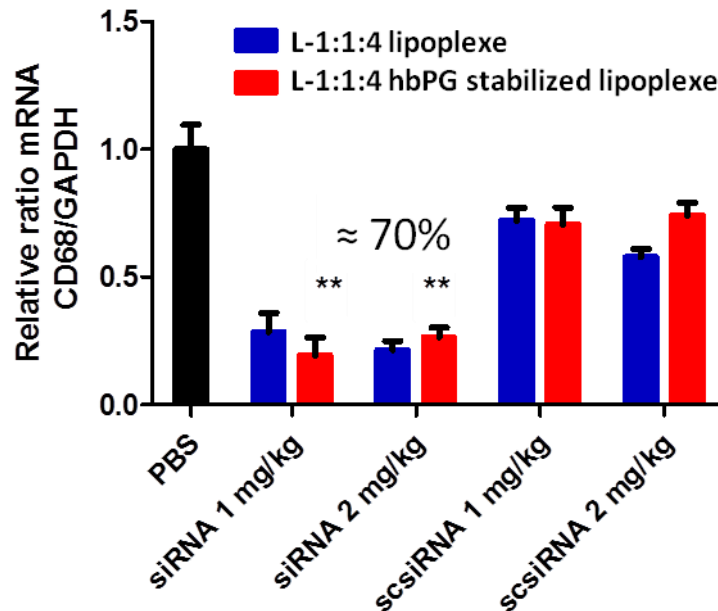


Figure 92. *In vivo* knockdown of the macrophage specific gene CD68 in the liver of mice that were injected twice with 1 mg/kg or 2 mg/kg anti-CD68 siRNA loaded into L-1:1:4 (blue) or L-1:1:4-hbPG lipoplex (red). ** $p < 0.01$ for anti-CD68 siRNA vs negative controls; MEAN \pm SD (measurements performed by Leonard Kaps).

The successful *in vivo* knockdown demonstrates a functional siRNA delivery of both liposomal formulations in liver macrophages *in vitro* and notably *in vivo*. Interestingly the applied 1 mg/kg dose appears to be equally potent as the 2 mg/kg siRNA dose, and lower concentrations may still be effective.

In conclusion, it could be demonstrated, that serum or blood plasma induced aggregate formation of liposomes and liposome-siRNA complexes (lipoplexes) may be avoided if the surface is sterically shielded by incorporation of appropriate lipids that contain a short polymer chain. In the present work aggregate formation could be completely suppressed by introduction of a novel lipid consisting of a cholesterol anchor and hyperbranched polyglycerol. Simple and sterically shielded liposomes almost quantitatively encapsulated siRNA at N/P = 34. The resulting lipoplexes showed promising results in *in vitro* and *in vivo* studies of liver accumulation and knockdown efficiency towards the macrophage-specific CD68 mRNA. Another important conclusion is that for the investigated lipoplexes serum/plasma induced aggregates of as large as 500 nm in size ($R_h = 250$ nm) increase cellular uptake and have no detectable effect on knockdown efficiency. Likewise, no obvious side effects were observed for mice during the experimental time of up to 96 hours.

4 SUMMARY AND OUTLOOK

Within this work, effort was taken towards a better understanding of the interactions between nanomaterials and proteins of the human plasma proteome. A closer look was taken on the gap between the synthetic and biological identity of nanomaterials that limits the biomedical application of nanocarriers so far.

The most abundant proteins HSA and IgG were removed from human blood plasma effectively. This allowed the investigation of the single proteins but more importantly also of various low abundant protein mixtures. Plain polystyrene as well as amino-functionalized polystyrene particles have been coated with $F_{\text{Plasma-w/o-IgG-HSA}}$ in order to successfully prevent the particles from aggregation under *in vivo* conditions. In addition it turned out, that those decorated particles also were taken up by macrophages very weakly, meaning that the introduced pre-coating could also prolong blood circulation time when it comes to administration. For carboxy-functionalized polystyrene particles, the stabilizing against aggregation was possible with IgG, but the coating and subsequent redispersion lead to an increase in size.

$F_{\text{Plasma-w/o-IgG}}$ that was also obtained by plasma fractionation could be used for particle stabilization when used as surfactant during polystyrene synthesis. While the aggregation behaviour was comparable to Lutensol-stabilized particles, this offers the possibility of passing on chemical surfactants completely.

The concept of pre-coating nanoparticles in order to tune their stability against aggregation was also utilized to overcome the fluctuation in the blood proteome composition when looking at different individuals. Once formed protein coronas on the polystyrene particles under investigation remained stable even when re-introduced into another protein source (in this case pooled human serum). This could be of special interest for drug carrier preparation prior to administration.

The above mentioned transfer of a protein corona was not only limited to the change from one protein medium into another. It was also possible to transfer the protein corona that was formed on “stealth” nanocarriers onto non-modified nanoparticles. The transfer was successful in order to stabilize a respective particle against aggregation, but the

reduced cellular uptake that is characteristic for the “stealth” effect could not be achieved. This could have originated in the denaturation of proteins when detaching them from the particles with SDS. The introduced method offers new possibilities for blood plasma fractionation by resins that can be inserted into an HPLC system. In addition, the possibility of corona transfer could be useful for nanocarriers that are not suitable for surface modification with “stealth” polymers.

Light was shed on the gap between different *in vivo* models and humans. The protein corona formation and the stability of particles under investigation strongly depends on the protein source that is used as a model. Results shown in this work suggest that the investigation of particles regarding their stability against aggregation in plasma of the used *in vivo* / *in vitro* model as well as in human plasma is necessary to obtain a full understanding of the protein particle interactions.

Liposomes for siRNA delivery *in vivo* were optimized regarding their stability in human serum / plasma by modifying their surface with a novel hyperbranched polyglycerol. The encapsulation efficiency for siRNA of the liposomal structures was excellent. The resulting lipoplexes showed promising results in knockdown efficiency towards the macrophage specific CD-68 mRNA *in vivo*.

Altogether, this study throws light on different parameters effecting the protein corona formation as well as protein-induced aggregation of nanoparticles. Moreover, suggestions were introduced of how these interactions could be used, in order to control a particles response upon introduction in biological media.

5 EXPERIMENTAL SECTION

5.1 LIST OF EQUIPMENT

Equipment	Purchaser
ToyoScreen AF-rProtein A HC-650F	tosohbioscience, DE
ToyoScreen AF-Blue HC-650M	tosohbioscience, DE
ToyoScreen DEAE-650M	tosohbioscience, DE
Agilent Technologies 1200 series	Agilent Technologies, USA
UV-detector	Agilent Technologies, USA
Diode Array Detector	Agilent Technologies, USA
MN HD8 125/4/5 μ m column	Macherey-Nagel, DE
Evaporative Lightscattering Detector 385-LC	Varian, USA
ALV/CGS 3	ALV GmbH, DE
ALV-5004 multiple tau full digital correlator	ALV GmbH, DE
ALV-CGS 8F SLS/DLS 5022F goniometer	ALV GmbH, DE
ALV-7004 correlators	ALV GmbH, DE
QEAPD Avalanche photodiode detector	ALV GmbH, DE
ALV-5000 multiple tau full digital correlator	ALV GmbH, DE
Prometheus NT.48	Nanotemper Technologies, DE
HeNe-Laser	JDS Uniphase, USA
Liposofast Extruder	Avestin Europe GmbH, DE
Liposofast Stabilizer	Avestin Europe GmbH, DE
Polycarbonate membranes	Avestin Europe GmbH, DE

Gas tight syringe	Avestin Europe GmbH, DE
Branson W450 digital sonifier	G.HEINEMANN, DE
JEM-1400 electron microscope	JEOL, DE
Zetasizer Nano Z	Malvern Instruments GmbH, DE
Mütek particle charge detector	BTG, DE
Titrimo Automatic Titrator	Metrohm AG, CHE
cLSM Leica SP5 II with CW-STED	Leica, DE
Flow cytometer CyFlow ML	Partec, DE
Plate Reader Infinite M1000	Tecan, DE
Power Supply	Bio-Rad, USA
SDS-PAGE Chamber MiniGel Tank	Lifetechnologies, USA
nanoACQUITY UPLC	Waters, USA
Synapt G2-Si mass spectrometer	Waters, USA
Bruker Avance 300 Spectrometer	Bruker Corporation, USA
Jasco J-815 spectrometer	JASCO, USA
NuPAGE 10% BisTris Protein Gel	Novex, ThermoFisher Scientific, USA
NuPAGE LDS sample buffer	Novex, ThermoFisher Scientific, USA
NuPAGE sample reducing agent	Novex, ThermoFisher Scientific, USA
NuPAGE MES SDS running buffer	Novex, ThermoFisher Scientific, USA
SeeBlue Plus2 Pre-Stained Standard	Invitrogen, USA
Simply Blue SafeStain	Novex, ThermoFisher Scientific, USA
SilverQuest™ Silver Staining Kit	ThermoFisher Scientific, USA
Pierce® 660 nm assay	ThermoScientific, USA

Pierce® Detergent removal Spin Column	ThermoScientific, USA
Quant-it™ RiboGreen Assay	Invitrogen, USA
BCA Protein Macro Assay Kit	SERVA Electrophoresis, DE
Millex-LCR450nm filter	Millipore, IRL
Millex-GS220nm filter	MerckMillipore, DE

5.2 METHODS

5.2.1 FRACTIONATION OF HUMAN BLOOD PLASMA

Dulbecco's phosphate buffered saline (DPBS) without calcium and magnesium was purchased from Gibco/lifetechnologies, Germany. The human blood plasma (citrate stabilized) was prepared according to standard guidelines, was obtained from the blood transfusion service at the University Clinic of Mainz/Germany and aliquots stored at -80 °C before used. Human Serum Albumin (HSA) as well as Trizma® hydrochloride solution was purchased from Sigma Aldrich, USA. The protein fibrinogen was purchased from Aventis Behring and immunoglobulin G from privigen® (10% solution, CSL Behring, USA).

For separation of IgG a ToyoScreen AF-rProtein A HC-650F column (1 mL; tosohbioscience, Germany) was used with 0.01M Tris·HCl (pH=7.4) as running buffer (RB). The column was run as recommended by the manufacturer at 3 bar which was achieved with a flow rate of 0.5 mL/min. Before loading a sample, the HPLC system was purged with running buffer for 30 min until the baseline was constant over time.

The human plasma was diluted 1:3 and filtered with LCR 450 nm filters to remove possible protein-aggregates. To avoid overload, only 0.5 mL of sample were loaded on the column. The maximum load was determined prior to use at 0.7 mL 1:3 diluted plasma which corresponds to 2.3 mg IgG. The flow through was collected between 60 s and 270 s. After waiting for several minutes, 2 mL of 0.2 M citric acid were injected. One minute after injection IgG was collected for 2 min and the fraction neutralized with 330 µL 1M tris base solution.

For separation of albumin a ToyoScreen AF-Blue HC-650M column (5mL; tosohbioscience, Germany) was used with the similar running buffer as described earlier. Prior to use, the column was washed with 20 mL deuterium oxide as well as 20 mL 2M guanidine. After running the system for 30 min with running buffer (3 bar, 0.5 mL/min) until the baseline was constant over time, 0.5 mL of 1:2 diluted plasma was injected in order to achieve a concentrated flowthrough. The flowthrough was collected between 4:00 and 12:00 min. 4.5 min after the injection of 7 mL 2 M NaCl albumin was collected for 6 min.

For anion exchange chromatography, a ToyoScreen DEAE-650M column (1 mL, tosohbioscience, Germany) was used. Plasma was diluted 1:10 and filtered with LCR 450 nm filters prior to use. 0.5 mL of sample were loaded on the column and the flow through caught between 1 and 4 min. The flow through was recirculated two times. The four elution fractions were obtained by subsequent injection of 0.155 M, 0.3 M, 0.5 M and 1 M NaCl 0.1 mL each.

Protein concentrations in human plasma as well as in different fractions were determined with a BCA Protein Macro Assay Kit from SERVA electrophoresis, Germany, according to manufacturer. Absorption at 562 nm was measured with a Tecan infinite M1000.

For SDS PAGE 6.5 μ L of the protein sample was mixed with 2.5 μ L NuPAGE LDS Sample Buffer and 1 μ L NuPAGE Sample Reducing Agent and applied onto a NuPAGE 10% Bis Tris Protein Gel (all Novex, Thermo Fisher Scientific, USA). The electrophoresis was carried out in NuPAGE MES SDS Running Buffer at 100 V for 2 h with SeeBlue Plus2 Pre-Stained Standard (Invitrogen, USA) as a molecular marker. The gel was stained using SimplyBlue SafeStain (Novex, Thermo Fisher Scientific).

For LC-MS analysis (performed by Susanne Schöttler or Johanna Simon), proteins were digested following the protocol of Tenzer *et al.*¹²² with following modifications: 25 μ g of each protein sample was precipitated and trypsin was used with a 1:50 ratio (enzyme:protein). For LC-MS analysis the samples were diluted 10-fold with aqueous 0.1% formic acid and spiked with 50 fmol/ μ L Hi3 EColi Standard (Waters Corporation, Germany) for absolute quantification. Quantitative analysis of protein samples was performed using a nanoACQUITY UPLC system coupled with a Synapt G2-Si mass spectrometer (Waters Corporation). Tryptic peptides were separated on the nanoACQUITY system equipped

with a C18 analytical reversed-phase column (1.7 μm , 75 μm x 150 mm, Waters Corporation) and a C18 nanoACQUITY Trap Column (5 μm , 180 μm x 20 mm, Waters Corporation). Samples were processed with mobile phase A consisting of 0.1% (v/v) formic acid in water and mobile phase B consisting of acetonitrile with 0.1% (v/v) formic acid. The separation was performed at a sample flow rate of 0.3 $\mu\text{L}/\text{min}$, using a gradient of 2-37% mobile phase B over 70 min. As a reference compound 150 fmol/ μL Glu-Fibrinopeptide was infused at a flow rate of 0.5 $\mu\text{L}/\text{min}$.

Data-independent acquisition (MSE) experiments were performed on the Synapt G2-Si operated in resolution mode. Electrospray Ionization was performed in positive ion mode using a NanoLockSpray source. Data was acquired over a range of m/z 50-2000 Da with a scan time of 1 s, ramped trap collision energy from 20 to 40 V with a total acquisition time of 90 min. All samples were analyzed in two technical replicates. Data acquisition and processing was carried out using MassLynx 4.1 and TansOmics Informatics software was used to process data and identify peptides. Data were post acquisition lock mass corrected. Noise reduction thresholds for low energy, high energy and peptide intensity were fixed at 120, 25, and 750 counts, respectively. During database searches, the protein false discovery rate was set at 4%. The generated peptide masses were searched against a reviewed human protein sequence database downloaded from Uniprot. The following criteria were used for the search: one missed cleavage, maximum protein mass 600 kDa, fixed carbamidomethyl modification for cysteine and variable oxidation for methionine. For identification a peptide was required to have at least three assigned fragments and a protein was required to have at least two assigned peptides and five assigned fragments. Quantitative data were generated based on the TOP3/Hi3 approach.[32] Quantitative data were generated based on the TOP3/Hi3 approach,[32] providing the amount of each protein in fmol.

5.2.2 FRACTIONS OF PROTEIN MIXTURE DIFFERENTIALLY AGGREGATE NANOPARTICLES AND INFLUENCE THE CELLULAR UPTAKE

5.2.2.1 SYNTHESIS OF PS PARTICLES (BY KATJA KLEIN⁴)

A direct miniemulsion co-polymerization method according to previously published work was used to synthesize functionalized as well as non-functionalized polystyrene nanoparticles (NP). Briefly, a total monomer amount of 6 g was used for each particle. In case of the non-functionalized NP this means 6 g styrene (Merck, Germany). For the functionalized particles, 5.88 g styrene and 0.12 g functionalized co-monomer were used. For the preparation of negatively charged polystyrene nanoparticles, acrylic acid (Aldrich, USA), 252 mg hexadecane (Aldrich), 5 mg arcBODIPY (for measurements that did not need a fluorescent dye it was omitted) and 100 mg V59 (Wako chemicals, Japan) as initiator were added to a solution of 0.6 g Lutensol AT50 (BASF, Germany) in 24 mL water under vigorous stirring to prepare PS-COOH NPs. For the synthesis of positively charged polystyrene nanoparticles, 2-aminoethyl methacrylate hydrochloride (AEMH; Aldrich, Germany)) was added to the water phase and combined with the disperse phase as described above to prepare PS-NH₂. After combining water and disperse phase, each preparation was stirred for one hour and the emulsions afterwards ultrasonicated for two minutes at 90% intensity (Branson Sonifier, 1/2" tip, 450 W). After polymerization at 72 °C for 12 h, the NPs were purified by centrifugation and redispersion in water three times (13.000 rpm, 3-4 h).

5.2.2.2 TRANSMISSION ELECTRON MICROSCOPY (TEM) (PERFORMED BY CHRISTOPH SIEBERT⁵)

Transmission electron microscopy was carried out with a JEOL JEM-1400 electron microscope operating at an acceleration voltage of 120 kV. The samples were prepared by diluting the 1 wt% dispersion 1:50 with water. One droplet was placed on a 300 mesh carbon-coated copper grid and dried overnight.

⁴ Katja Klein, AK Prof. Dr. Katharina Landfester, MPIP

⁵ Christoph Siebert, AK Prof. Dr. Katharina Landfester, MPIP

5.2.2.3 DYNAMIC LIGHT SCATTERING (DLS)

All light scattering experiments were done on a commercially available instrument from ALV GmbH (Langen, Germany) consisting of an electronically controlled goniometer and an ALV-5000 multiple tau full-digital correlators with 320 channels, equipped with an HeNe Laser. 1 mL protein solutions as well as concentrated human plasma were filtered through Millex GS 220nm filters into cylindrical quartz cuvettes (20 mm diameter, Hellma, Müllheim). Particle dispersions were diluted 1:1000 with PBS, running buffer or protein solution and measured without filtering to avoid changes within the system under investigation ($5 \times 10^{-4} \text{ m}^2$ particle surface area per mg protein).

5.2.2.4 PARTICLE CHARGE DETECTION (PCD) (PERFORMED BY ELKE MUTH⁶)

The amount of amine or carboxyl groups on the particle surface was calculated from titration performed on a particle charge detector PCD 02 (Mütek GmbH Germany) combined with a Titrimo Automatic Titrator 702 SM (Metrohm AG Switzerland). Carboxyl groups were titrated against positively charged poly(diallyl dimethyl ammonium chloride) (PDADAMC) while amino groups were titrated against negatively charged polyelectrolyte standard sodium poly(ethylene sulfonate) (Pes-Na). 10 mL of the dispersion under investigation with a solid content of 1 g/L were titrated.

5.2.2.5 ZETA POTENTIAL

For determination of the zeta (ζ) potential of the different polystyrene nanoparticles a Malvern zetasizer nano series instrument was used. 20 μL of the respective dispersion was diluted in 2 mL 1 mM KCl and filled into appropriate disposable folded capillary cells.

5.2.2.6 PROTEIN CORONA PREPARATION

Each nanoparticle was incubated with human plasma or the obtained protein fractions at constant ratio of particle surface area to protein amount ($5 \times 10^{-3} \text{ m}^2$ particle surface area per mg protein) for one hour at 37 °C. Unbound proteins in the supernatant were separated from particles by centrifugation at 20,000g for 30 min. The coated particle

⁶ Elke Muth, AK Prof. Dr. Katharina Landfester, MPIP

pellet was resuspended in running buffer and in case for SDS-Page, washed by three centrifugation steps at 20,000g for 30 min and subsequent redispersion in buffer. For LC-MS and protein quantification, proteins were eluted from the nanoparticles by dissolving the pellet in 300 μ L of buffer (7M Urea, 2 M Thiourea, 4% CHAPS). The amount of proteins was quantified using Pierce 660nm protein Assay (Thermo Scientific; Germany) according to manufacturer's instructions and absorption at 660 nm was measured with a Tecan infinite M1000.

5.2.2.7 CIRCULAR DICHROISM SPECTROSCOPY

CD spectra were recorded with a Jasco J-815 spectrometer equipped with a PTC-423S Peltier type temperature-control system. Measurements were performed at 37 °C in a 10 mm cell from 300 to 190 nm with a band width of 1 nm and a scanning speed of 20 nm/s. Proteins were dissolved in PBS or running buffer with a concentration of 1 g/L.

5.2.2.8 MACROPHAGES

Murine macrophage-like cells (RAW 264.7) were kept in Dulbecco's modified eagle medium (DMEM, Invitrogen, USA) supplement with 10% fetal bovine serum (FBS, Sigma Aldrich, USA) and 1% penicillin/streptomycin (Invitrogen, USA). Cells were grown in humidified incubator at 37 °C and 5% CO₂.

5.2.2.9 FLOW CYTOMETRY (PERFORMED BY JOHANNA SIMON)

1×10^5 cells/mL (RAW 264.7) were allowed to attach in six-well plates (2 mL per well). After 12 h the cells were washed with DPBS to remove all proteins from FBS and kept in DMEM without additional proteins. Pre-coated nanoparticles (75 μ g/mL) were added to cells and incubated for 2 h. For further flow cytometry analysis, cells were washed with DPBS, detached with trypsin (Invitrogen, USA), centrifuged (4 min, 266 g) and resuspended in DPBS. Flow cytometry measurements were performed on a CyFlow ML cytometer (Partec, Germany) with a 488 nm laser to excite the fluorescent labelled nanoparticles and a 527 nm pass filter for emission detection (fluorescence channel 1 FL1). With FCS Express V4 (DeNovo Software, USA) cells were selected on a forward scatter/sideward scatter plot, thereby excluding cell debris. The gated events were further

analyzed in the FL1 channels. The median in the FL1 channel (MFI) was determined from a 1D histogram as a relative figure for the amount of nanoparticles taken up or associated with cells.

As different nanoparticles contained different amounts of dye, the fluorescence intensity for each particle was measured with a Tecan Infinite R M1000 PRO microplate reader with standard settings of the software iconcontrol[®] at an excitation and emission wavelengths of 523 nm and 536 nm. The fluorescence intensity values of each nanoparticle (FI_{NP}) were further normalized (nFI_{NP}) to the fluorescence intensity value for PS particles (FI_{PS}) to further normalize the median fluorescence intensity (MFI) obtained from flow cytometry measurements. The following equations were used:

$$n(FI)_{NP} = FI_{NP} / FI_{PS}$$

$$nMFI = MFI / (n(FI)_{NP})$$

For each cell uptake experiment the normalized median fluorescence intensity values $nMFI$ of uncoated nanoparticles ($nMFI_{-}$) was determined to compare $nMFI$ values of pre-coated particles from different cell experiments. According to this, relative fluorescence intensity values $rMFI$ were calculated with the equation:

$$rMFI = nMFI / nMFI_{-}$$

5.2.2.10 CONFOCAL LASER SCANNING MICROSCOPY (CLSM) (PERFORMED BY DR. ANKE KALTBEITZEL⁷)

1×10^5 cells/mL (RAW 264.7) were seeded in Ibidi iTreat μ -dishes (IBIDI, Germany) for 24 h, washed with PBS and kept in DMEM without additional proteins. $75 \mu\text{g/mL}$ pre-incubated nanoparticles were added to cells for 2 h. Afterwards cells were washed with PBS three times and stained with CellMask Orange (CMO, stock solution: 5 mg/mL in DMSO, Invitrogen, USA) which labeled the cell membrane red. CMO ($0.2 \mu\text{L}$) was diluted with one mL of Hanks' Balanced Salt solution (HBSS, Life technologies, USA). After adding the diluted staining solution ($400 \mu\text{L}$) to cells, live cell images were taken on a Leica TCS

⁷ Dr. Anke Kaltbeitzel, AK Prof. Dr. Katharina Landfester

SP5 II microscope with an HC PL APO CS 63x/1.4 oil objective using the software LAS AF 3000 software. The fluorescence signals of nanoparticles (excitation: 488 nm, pseudo colored green) and CMO (excitation: 561 nm, pseudo colored red) were detected in a serial scan mode at 502 – 534 nm and 579 – 642 nm.

5.2.2.11 SDS-PAGE AND LC-MS

Experiments were performed according to chapter 5.2.1.

5.2.2.12 SYNTHESIS OF POLYSTYRENE WITH PROTEINS AS SURFACTANT

The CMC of IgG depleted Plasma at the air water interface was determined using DCAT 21 from DataPhysics with a Du Noüy-Ring RG11. Protein solution in water was added dropwise up to a concentration of 0.5 g/L and the change in surface tension detected.

A direct miniemulsion co-polymerization method according to previously published work was used to synthesize non-functionalized polystyrene nanoparticles (NP). Briefly, 5 mg of initiator V59 (Wakoo chemicals, Japan) was dissolved in 560 μ L styrene (Merck, Germany) with 32 μ L hexadecane (> 99%, Sigma Aldrich) as osmotic pressure reagent. 59 μ L of this stock solution was added to 2 mL of protein solution in water ($c= 1$ mg/mL). The mixture was stirred for 1 hour at room temperature and 1000 rpm. Afterwards, the emulsion was ultrasonicated for two minutes at 70% intensity (indirect ultrasonifier, branson digital sonifier) and the polymerization carried out at 65 °C for 12 h. The dispersion was diluted and purified by centrifugation at 4000 rpm for 10 minutes. The solid content of the resulting dispersion was determined to be 0.5%.

Cell toxicity of the particles was determined by using a CellTiter-Glo[®] Assay according to manufacturer for particle concentrations from 75 up to 1200 μ g/mL. For the SDS-Page, the SilverQuest™ Silver Staining Kit from ThermoFisher Scientific was used as recommended by manufacturer.

5.2.2.13 FLUORESCENT CORRELATION SPECTROSCOPY (FCS) (PERFORMED BY JENNIFER SCHULTZE, MPIP)

FCS experiments were performed using a commercial setup (Zeiss, Germany) consisting of the module ConfoCor 2 and an inverted microscope model Axiovert 200 with a Zeiss C-Apochromat 40×/1.2W water immersion objective.

Dyes were excited by an argon laser (488 nm). Fluorescence light was filtered (LP 505 long pass emission filter) and collected by an avalanche photodiode that enables single-photon counting. Eight-well polystyrene-chambered coverglass (Laboratory-Tek, Nalge Nunc International) was used as a sample cell.

For each solution, a series of 50 measurements (10 s each) were performed.

The confocal observation volume was calibrated using AlexaFlour488 as a reference dye with a known diffusion coefficient.

5.2.3 HUMAN BLOOD PLASMA VERSUS SERUM

DLS measurements were performed according to chapter 5.2.1-2. All protein sources were centrifuged prior to DLS measurements (20.000 g, 30 min). The experimental setup of cited cell experiments as well as the origin of the protein sources and particles is already published.¹³⁷

5.2.4 EVALUATION OF NP STABILITY IN HUMAN BLOOD SERUM

DLS, LC-MS, SDS-PAGE and zeta potential experiments were performed according to chapter 5.2.1-2. The human serum pool was centrifuged prior to the introduction of coated particles (20.000 g, 30 min).

5.2.4.1 PROTEIN CORONA FORMATION

0.05 m² or particle surface area were introduced into 500 µL individual serum or pooled human serum and incubated for 1 h at 37 °C. For light scattering experiments, the particles were separated from unbound proteins via centrifugation for 30 min at 20.000 g and the pellet resuspended in PBS. For SDS-PAGE, LC-MS analysis and zeta potential determination the pellet was washed thrice with PBS and subsequent centrifugation at 20.000 g for 30 min. For SDS-Page proteins were eluted from the nanoparticles by dissolving the pellet in 300 µL of buffer (7M Urea, 2 M Thiourea, 4% CHAPS); for LC-MS 2% SDS (> 95 %, Merck) (solution (w/v) in 62.5 mM Tris•HCl) was used. The amount of proteins was quantified using Pierce 660nm protein Assay (Thermo Scientific; Germany) according to manufacturer's instructions and absorption at 660 nm was measured with a Tecan infinite M1000. The human serum pool was centrifuged prior to the introduction of coated particles (20.000 g, 30 min).

5.2.4.2 HEAT INACTIVATION OF HUMAN SERUM

Serum was heated up to 56 °C for one hour and centrifuged for 30 min at 20.000 g prior to use.

5.2.4.3 NANO-DSF MEASUREMENTS

All proteins were dissolved with $c = 1$ g/L in PBS. Clusterin (recombinant, AG Koch-Brandt, JGU Mainz) was an exception and was dissolved with $c = 0.14$ g/L. The samples were heated up from 20 °C to 95 °C with a heating rate of 1 °C/ min.

5.2.4.4 DILUTION AS TOOL FOR PRE-COATING

For DLS measurements, the particles were introduced into concentrated human plasma (centrifuged for 30 min at 20.000 g and filtered with GS 220 nm filters into the cuvette) at a constant ratio of 5×10^{-3} m² per mg serum. The overall solution was diluted 1:2, 1:5, and 1:10. The dilution was done by diluting the plasma prior to particle introduction.

5.2.5 THE TRANSFER OF A PROTEIN CORONA

LC-MS as well as nanoDSF and DLS measurements were performed as previously described. The protein concentration for nanoDSF measurements in PBS was $c = 0.3$ g/L.

PS-NH₂ with CTMA-Cl as surfactant was synthesized by Katja Klein according to literature.¹⁰⁷ The NH₂-functionalization was determined by a fluorescamine assay. The NHS-coupling was performed by Thomas Wolf. 5 mL of 1% particle dispersion (pH = 8) were stirred at room temperature and 5 eq (in relation to the amine groups) PEG-ester added in three equivalents with 20 min time lag. After additional stirring for one hour, the particles were purified by subsequent centrifugation (20.000 g, 1 h) and redispersion of the particle pellet thrice. In addition, the dispersion was afterwards dialyzed against water with a cut off of MW = 50 kDa. PEG functionalization was determined by NMR spectroscopy.

5.2.5.1 OBTAINING STEALTH PROTEINS

0.05 m² of PS-PEG₅₀₀₀ surface area were incubated in 500 μL human plasma for 1 hour at 37 °C. Afterwards, unbound and weakly bound proteins were removed via centrifugation at 20.000 g for 30 min. The pellet was washed via resuspension in PBS and subsequent centrifugation thrice. After the last centrifugation step, the pellet was resuspended in 100 μL of 2% SDS (> 95 %, Merck) (solution (w/v) in 62.5 mM Tris•HCl. The particles were separated from the supernatant by centrifugation at 20.000 g for 1 h. Afterwards, the protein solution was obtained.

5.2.5.2 REMOVAL OF SDS

SDS was removed from the protein solution via the use of Pierce® Detergent Removal Spin Column (0.5 mL, ThermoScientific). The centrifugal column was placed in an 2 mL Eppendorf tube and the storage buffer removed via centrifugation at 1.500 g for 1 min. Afterwards, the column was washed three times with 0.4 mL DPBS and centrifugation at 1.500 g for 1 min. 100 μL of sample were added and incubated at RT for 2 min. After centrifugation at 1.500 g for 2 min the detergent free protein solution was obtained. Protein concentrations were determined using Pierce 660 nm protein assay according to

manufacturer's instructions and absorption at 660 nm measured with a Tecan infinite M1000.

5.2.5.3 PARTICLE RECYCLING

For particle recycling, the already used particle pellet was resuspended in 1 mL DPBS and incubated overnight. Afterwards, the supernatant was removed via centrifugation at 20.000 g for 30 min. The pellet was washed additional three times with PBS and afterwards used again for incubation in human plasma.

5.2.5.4 TRANSFER OF THE PROTEIN CORONA ON PS-NH₂

0.05 m² of particle surface area were incubated in a solution of 200 µg proteins in PBS. After one hour at 37 °C, the supernatant was removed via centrifugation at 20.000 g for 30 min. The pellet was resuspended in the original amount of MilliQ water. For zeta potential determination and SDS-PAGE, the particle pellet was washed with PBS and subsequent centrifugation at 20.000 g for 30 min thrice.

5.2.5.5 CELL UPTAKE (PERFORMED BY JOHANNA SIMON)

Flow cytometry was performed as described in chapter 5.2.2. This time, pre-coated nanoparticles were added to cells and incubated for 2 h with a nanoparticle concentration of 20 µg/mL.

5.2.6 EVALUATION OF DIFFERENT *IN VIVO* MODELS

BNF-Dextran-redF and BNF-Starch-redF were obtained by MicroMod, Germany with a solid content of 10 mg/mL.

Rabbit, sheep and mouse plasma were purchased from GeneTex, distributed by Biozol, Eching, Germany. In each case, citrate was added as anti-coagulant.

Protein corona formation as well as analysis was done as described before. The proteins were dissolved from the particles by using the above described urea buffer. The only

difference was the staining of SDS-PAGEs. Instead of comassie brilliant blue, the silverstaining was applied. The SilverQuest™ Silver Staining Kit from ThermoFisher Scientific was used as recommended by manufacturer.

5.2.7 EVALUATION OF MULTIFUNCTIONAL LIPOSOMES IN HUMAN BLOOD SERUM BY DYNAMIC LIGHT SCATTERING

The detailed information about materials and methods has already been published and can be seen in “Evaluation of Multifunctional Liposomes in Human Blood Serum by Light Scattering” Mohr *et al.*, Langmuir 2014, 30, 14954-14962).²¹

5.2.8 MULTICOMPONENT LIPOSOMES FOR siRNA DELIVERY TO THE LIVER

5.2.8.1 REAGENTS

All solvents and reagents were purchased from Acros and Sigma Aldrich and used as received, unless mentioned otherwise. Deuterated methanol-*d*₄ was purchased from Deutero GmbH. Dulbecco’s phosphate buffered saline (DPBS) without calcium and magnesium was purchased from Gibco/lifetechnologies. Human blood serum and blood plasma, prepared according to standard guidelines, was obtained from the blood transfusion service at the University Clinic of Mainz/Germany. Human plasma was pooled from 6 patients, whereas serum originated from one patient. Extruder, stabilizer and polycarbonate membranes were purchased from Avestin Europe GmbH. The Quant-it™ RiboGreen® assay was obtained from Invitrogen. CW800 NHS ester was procured from LICOR Biotechnology.

5.2.8.2 SYNTHESIS OF SURFACTANT TF AND DYE LABELING

Surfactant TF was synthesized according to Figure 93 by Dr. Chai Wenquiang. Detailed information is provided in the dissertation of Dr. Wenquiang.¹⁵³

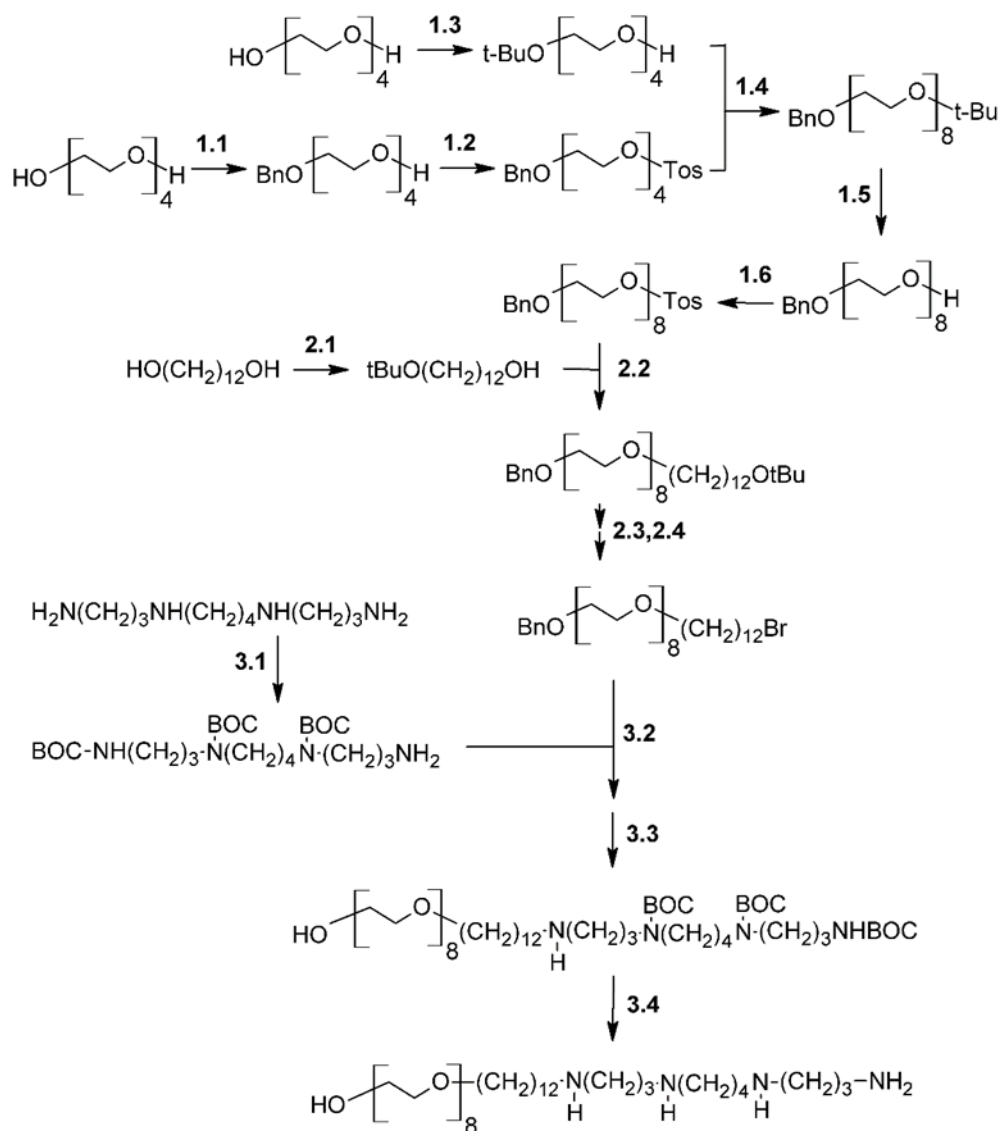


Figure 93. Synthesis of surfactant TF according to [153].

For dye labeling, 1 eq CW800 NHS ester (LI-COR Biotechnology) was reacted with 1.05 eq surfactant TF in DMSO for 70 h under stirring.

5.2.8.3 SYNTHESIS OF A HYPERBRANCHED POLYGLYCEROL (HBPG) SURFACTANT

The synthesis was conducted by Dr. Sophie Müller as reported elsewhere.²¹

5.2.8.4 LIPOSOME FORMULATION

The cationic lipid TF as well as cholesterol and DSPC were dissolved in ethanol at room temperature with different weight ratios. The ethanolic solution of lipids was dropped into an aqueous solution of Dulbecco's phosphate-buffered saline (DPBS) under vigorous stirring for several minutes. The resulting liposomal mixture was extruded through a polycarbonate membrane with a nominal pore-size of 50 nm. In order to achieve reproducible liposome preparation, a semi-automatic controllable extruder was designed for syringe volumes of 0.5 and 1 mL. The homebuilt mechanical set-up utilizes the LiposoFast Basic filter housing from AVESTIN Europe GmbH. The syringes are electronically driven by a stepping motor that enables a continuously tunable speed of the syringe plunger between 7 mm/s and 0.4 mm/s. Mostly unilamellar liposomes were obtained at constant extrusion speed (4.9 mm/s corresponding to 5.2 mL/min) and 30 extrusion cycles. For light scattering measurements the extruded liposomes were filtered through a Millex LCR 450nm filter into a dust-free Suprasil light scattering cuvette (Hellma, Mülheim).

5.2.8.5 LOADING OF LIPOSOMES WITH SIRNA

A desired amount of siRNA was dissolved in aqueous DPBS. After adding the ethanolic solution of lipids under vigorous stirring, siRNA loaded liposomes (mass ratio TF:siRNA = 5:1, 7.5:1, 10:1 corresponding to N/P = 17, 25, 34) were produced by repeated extrusion as described before. The amount of encapsulated siRNA was determined as described⁶ using the Quant-it™ RiboGreen® assay from Invitrogen. Purification of non-encapsulated siRNA was performed using Amicon Ultra-2 mL Centrifugal filter devices (30K) or by dialysis (MW 20K).

5.2.8.6 DYNAMIC AND STATIC LIGHT SCATTERING

All dynamic light scattering experiments were performed with an instrument consisting of HeNe laser (632.8 nm, 25 mW output power), an ALV-CGS 8F SLS/DLS 5022F goniometer equipped with eight simultaneously working ALV 7004 correlators and eight QEAPD Avalanche photodiode detectors. Static light scattering (SLS) experiments were carried out on an ALV/CGS3 instrument consisting of a HeNe laser, a goniometer and an ALV-5004

multiple-tau full-digital correlator. Measurements were performed at scattering angles between $\Theta = 30 - 150^\circ$ with steps of 10° .

For DLS and SLS the liposomal solutions were diluted 1:20 v/v by aqueous PBS to a total lipid concentration of 0.03 g/L and subsequently filtered through LCR 450 nm filters (Millipore). Human serum as well as plasma was filtered through Millex GS filters, 220 nm nominal pore size, (Millipore) into cylindrical Suprasil quartz cuvettes (20 mm diameter, Hellma, Müllheim) in a dust-free flow hood. By adding the liposomal solution in PBS, the human serum was diluted 1:1 resulting in a total protein concentration approximately 3%. After incubation for 30 min at room temperature, DLS measurements were performed at 20 °C.

For the liposomes and lipoplexes in buffer the correlation functions showed a monomodal decay and were fitted by a sum of two exponentials, from which the first cumulant Γ was calculated. The z-average diffusion coefficient D_z was obtained by extrapolation of Γ/q^2 for $q = 0$ leading to the inverse z-average hydrodynamic radius $R_h \equiv \langle 1/R_h \rangle_z^{-1}$ by formal application of Stokes law.

For the measurements in serum/plasma the correlation functions were analyzed according to the method introduced by Rausch *et al.*¹¹⁴ which is described in detail in the introduction.

5.2.8.7 ZETA POTENTIAL

For determination of the zeta potential of the different liposomal systems a Malvern nano zeta sizer was utilized. 20 μ L of liposomal solution was diluted in 2 mL 1mM KCl and filled into disposable folded capillary cells (DTS 1060).

5.2.8.8 CELL CULTURE (LEONARD KAPS)

Murine MHS alveolar macrophages (ATCC, Teddington, UK) were cultured in Dulbecco's modified Eagle's medium supplemented with 10% FBS, 1% penicillin, 1% L-glutamine, and 1% streptomycin in 5% CO₂ at 37 °C. The medium was routinely changed every 2 days and the cells were separated by cell scraping before reaching confluency.

5.2.8.9 *IN VITRO* CYTOTOXICITY (PERFORMED BY LEONARD KAPS)

The MTT (3-(4,5-dimethylthiazol-2-yl)-2,5-diphenyltetrazoliumbromide) assay was used to assess potential cytotoxicity of the L-1:1:4 loaded with control scrambled siRNA (scsiRNA, see below) on MHS macrophages. In brief, the cells were seeded into 96-well plates at a density of ~10,000 cells per well. After a 24 h incubation period, supplement (as described in detail above) containing medium with serial concentrations of L-1:1:4 (loaded with control scsiRNA) corresponding to 5, 10, 20, 50, 100, 200, 400 and 600 nM scsiRNA formulation was added to replace the cell culture medium. After a 48 h incubation time, 20 µL of MTT dissolved in PBS (4 mg/mL) was added and incubated for another 4 h to quantify the living cells, followed by removal of the medium and addition of 150 µL DMSO. Finally, the 96-well plates were read on an Infinite M200Pro spectrofluorometer (TECAN, Männerdorf, Switzerland) at 570 nm.

5.2.8.10 *IN VITRO* KNOCKDOWN (PERFORMED BY LEONARD KAPS)

Anti-CD68 siRNA with the sequence:

5'-G6A 6U8 C6A 8C6 U6G 5U7 U-3'

5'-6G6 A7U 6U8 C5U 8C6 U5U 70-3'

containing the following chemical modifications (methylations) at the 2' position of the ribose ring:

0: 3'Amino-C6; 5: 2'OMe-rU; 6: 2'OMe-rA; 7: 2'OMe-rC; 8: 2'OMe-rG

was purchased from BioSpring (Germany, Frankfurt).

As scramble siRNA siGENOME Non-Targeting siRNA #2 with the following sequence:

5'-UAAGGCUAUGAAGAGAUACUU-3'

5'-GUAUCUCUUCAUAGCCUUAUU-3'

was purchased from Dharmacon (Dharmacon GE Healthcare, Germany, Freiburg). Chemical modifications of the scsiRNA as intellectual property of Dharmacon were not disclosed in the datasheet.

As positive in vitro transfection control anti-CD68 siRNA was mixed with INTERFERin from Polyplus transfection (Illkirch-Graffenstaden, France) according to the manufactures protocol.

Before transfection, MHS cells were seeded in 12-well culture plates at a density of ~100,000 cells per well and allowed to adhere overnight. After the plates were washed three times with PBS, the cells were incubated with a final liposomal siRNA concentration of 25 nM, 50 nM, 100 nM in 1 mL supplement containing medium for 48 h.

5.2.8.11 QUANTITATIVE RT-PCR (PERFORMED BY LEONARD KAPS)

After transfection cellular RNAs was extracted with GeneMATRIX Universal RNA Purification Kit from EURX (Berlin, Germany) according to the manufactures protocol. 1 µg of total RNA was reverse transcribed into cDNA using the iScript cDNA Synthesis Kit (Bio-Rad, Hercules, USA) according to the manufacturer's protocol.

The following Primers and probes were obtained from Eurofins (Mannheim, Germany):

Glycerinaldehyd-3-phosphat-Dehydrogenase (GAPDH)

forward 5'-AAGGTGAAGGTCGGAGTCAAC-3'

reverse 5'-GGGGTCATTGATGGCAACAATA-3',

Pan macrophages marker CD68

forward 5'-ACCGCCATGTAGTCCAGGTA-3'

reverse 5'-ATCCCCACCTGTCTCTCTCA-3'

were purchased from Applied Biosystems (Carlsbad, CA, USA).

Syber Green reaction mixtures were purchased by Applied Biosystems (Germany, Darmstadt). GAPDH transcript levels were used to normalize data and to control for RNA integrity. The Syber Green reactions were performed using a Step One Plus sequence amplification system. Results are expressed as the ratio of the copy number of the target gene divided by the number of copies of the housekeeping gene (GAPDH) within a single PCR run.

5.2.8.12 *IN VIVO* KNOCKDOWN (PERFORMED BY LEONARD KAPS)

All animal studies were approved by the committee on animal care (Government of Rhineland Palatinate, Germany). 8 week old Balb/c mice were kept under 12 h light-dark cycles, treated with human care and sacrificed by cervical dislocation. Mice (n=3 per group) were anaesthetized with isoflurane and injected retroorbitally with 1 mg/kg or 2 mg/kg anti-CD68 siRNA, the scrambled control RNA loaded in L-1:1:4 or L-1:1:4-*hbPG*, or received buffer alone (250 μ l PBS). All mice were injected twice 48 h apart. Liver RNA was extracted, reverse transcribed and analyzed by quantitative RT-PCR as described above.

5.2.8.13 *IN VIVO* IMAGING (PERFORMED BY LEONARD KAPS)

In vivo near infrared fluorescence imaging of CW-800-labeled liposomes loaded with siRNA was performed with the IVIS Spectrum Imaging system (Caliper LifeSciences). Fluorescence source and filters were set for IR-excitation at 745 nm and emission at 800. 48 h after the second injection the mice were sacrificed, liver, spleen, lungs, heart and kidneys removed and transferred immediately into the image chamber for ex vivo imaging. Acquisition of images was performed with an integration time of 4 s.

5.2.8.14 ISOLATION OF LIVER NON-PARENCHYMAL CELLS (PERFORMED BY LEONARD KAPS)

The nonparenchymal liver cell population was isolated and purified from the liver of female Balb/c mice according as described by us.¹⁹ Briefly, mice were anesthetized with Ketamine/Xylazine, the livers were rinsed with PBS and after removal of the gall bladder carefully homogenized and digested with 5,000 U Collagenase IV from Sigma-Aldrich (Munich, Germany) in Krebs-Ringer-Buffer, pH 7.4, for 30 min at 37 °C, followed by

another homogenization and digestion step. The cell suspension was filtered over a 100 µm cell strainer to remove non-digested particles and centrifuged at 17–21×g for 4 min at 4 °C to remove hepatocytes. The supernatant suspension was transferred into new tubes and centrifuged again at 300×g for 10 min and the cell pellet resuspended in 10 mL 1× Red Blood Cell Lysis Solution from Milteny (Bergisch-Gladbach, Germany) for 5 min at RT, followed by thorough washing with PBS.

5.2.8.15 FACS ANALYSIS (PERFORMED BY LEONARD KAPS)

In vivo macrophage uptake of CW-800-labeled siRNA loaded liposomes was measured by FACS analysis using antibodies to CD45 (clone 30-F11), F4/80 (clone BM8) from eBioscience (San Diego, USA) and Fixable Viability Dye eFluor 506 (eBioscience, San Diego, USA) to exclude dead cells. Cells were fixed with 4% paraformaldehyde (Histofix, Roth, Germany) for 15 min at 37 °C, and analyzed on a BD FACSCanto II flow cytometer BD Bioscience (Mississauga, Canada). Compensation was performed automatically with FACSDiva software using corresponding single stained controls. 50,000 cells were measured per staining. Further analysis of flow cytometry data was performed with open source Flowing Software 2.5.0 (Perttu Terho, Turku Centre for Biotechnology, Finland).

5.2.8.16 STATISTICAL ANALYSIS (PERFORMED BY LEONARD KAPS)

Statistical comparisons were performed with student t-test analysis using the GraphPad Prism (La Jolla, USA) program.

5.2.8.17 ¹H NMR

¹H NMR spectrum of the surfactant F was recorded on a Bruker AVANCE 300 spectrometer. As deuterated solvent CD₃OD was used. For analysis MestReNova 8 from Mestrelab Research S.L. was used. The spectra were calibrated against the solvent signal.

5.2.8.18 HPLC (BEATE MÜLLER)

The high pressure liquid chromatograms of dye, cationic lipid TF and TF-dye conjugate were measured by using an Agilent Series 1200 HPLC system with a MN-HD8-column (125/4/5µm), an evaporative light scattering detector 385-LC (Varian) and a diode array

detector (Agilent). The measurement was run at 20°C and a flow-rate of 1 mL/min. As liquid phase, a THF water mixture was used (5% THF, 95% water + 0.1% TFA). The THF amount was increased within 10 minutes to 100%.

5.2.8.19 CRYO-TEM (PERFORMED BY MAX BERNHARD)

For cryo-TEM imaging a JEOL 1400 transmission electron microscope equipped with a cryogenic holder (Gatan, USA) was used.

6 REFERENCES

1. Zolnik, B. S.; Sadrieh, N. Regulatory perspective on the importance of ADME assessment of nanoscale material containing drugs. *Adv. Drug Deliv. Rev.* **2009**, 61, 422-427.
2. Duncan, R. Polymer conjugates as anticancer nanomedicines. *Nat. Rev. Cancer* **2006**, 6, 688-701.
3. Pieper, R.; Gatlin, C. L.; Makusky, A. J.; Russo, P. S.; Schatz, C. R.; Miller, S. S.; Su, Q.; McGrath, A. M.; Estock, M. A.; Parmar, P. P. The human serum proteome: Display of nearly 3700 chromatographically separated protein spots on two-dimensional electrophoresis gels and identification of 325 distinct proteins. *Proteomics* **2003**, 3, 1345-1364.
4. Anderson, N. L. The clinical plasma proteome: a survey of clinical assays for proteins in plasma and serum. *Clin. Chem.* **2010**, 56, 177-185.
5. Kim, M.-R.; Kim, C.-W. Human blood plasma preparation for two-dimensional gel electrophoresis. *J. Chromatogr. B* **2007**, 849, 203-210.
6. Andrade, J. D.; Hlady, V. Plasma Protein Adsorption: The Big Twelve. *Ann. N.Y. Acad. Sci.* **1987**, 516, 158-172.
7. Varlan, A.; Hillebrand, M. Bovine and human serum albumin interactions with 3-carboxyphenoxathiin studied by fluorescence and circular dichroism spectroscopy. *Molecules* **2010**, 15, 3905-3919.
8. <http://www.management-krankenhaus.de/produkte/labor-diagnostik/igy-so-tief-wie-nie-zuvor-ins-plasma-proteom-schauen>.
9. Vermeer, A. W.; Norde, W. The thermal stability of immunoglobulin: unfolding and aggregation of a multi-domain protein. *Biophys. J.* **2000**, 78, 394-404.
10. Gauldie, J.; Richards, C.; Harnish, D.; Lansdorp, P.; Baumann, H. Interferon beta 2/B-cell stimulatory factor type 2 shares identity with monocyte-derived hepatocyte-stimulating factor and regulates the major acute phase protein response in liver cells. *Proceedings of the National Academy of Sciences* **1987**, 84, 7251-7255.
11. Marguerie, G. A.; Plow, E. F.; Edgington, T. S. Human platelets possess an inducible and saturable receptor specific for fibrinogen. *J. Biol. Chem.* **1979**, 254, 5357-5363.
12. Furie, B.; Furie, B. C. The molecular basis of blood coagulation. *Cell* 53, 505-518.
13. Bathen, T. F.; Engan, T.; Krane, J.; Axelson, D. Analysis and classification of proton NMR spectra of lipoprotein fractions from healthy volunteers and patients with cancer or CHD. *Anticancer Res.* **1999**, 20, 2393-2408.
14. Maeda, H.; Wu, J.; Sawa, T.; Matsumura, Y.; Hori, K. Tumor vascular permeability and the EPR effect in macromolecular therapeutics: a review. *J. Controlled Release* **2000**, 65, 271-284.
15. Muggia, F. M. Doxorubicin-polymer conjugates: further demonstration of the concept of enhanced permeability and retention. *Clin. Cancer. Res.* **1999**, 5, 7-8.
16. Fang, J.; Nakamura, H.; Maeda, H. The EPR effect: Unique features of tumor blood vessels for drug delivery, factors involved, and limitations and augmentation of the effect. *Adv. Drug Deliv. Rev.* **2011**, 63, 136-151.

17. Byrne, J. D.; Betancourt, T.; Brannon-Peppas, L. Active targeting schemes for nanoparticle systems in cancer therapeutics. *Adv. Drug Deliv. Rev.* **2008**, 60, 1615-1626.
18. Maeda, H.; Nakamura, H.; Fang, J. The EPR effect for macromolecular drug delivery to solid tumors: Improvement of tumor uptake, lowering of systemic toxicity, and distinct tumor imaging in vivo. *Adv. Drug Deliv. Rev.* **2013**, 65, 71-79.
19. Betancourt, T.; Brown, B.; Brannon-Peppas, L. Doxorubicin-loaded PLGA nanoparticles by nanoprecipitation: preparation, characterization and in vitro evaluation. **2007**.
20. Schroeder, A.; Levins, C. G.; Cortez, C.; Langer, R.; Anderson, D. G. Lipid-based nanotherapeutics for siRNA delivery. *Journal of internal medicine* **2010**, 267, 9-21.
21. Mohr, K.; Müller, S. S.; Müller, L. K.; Rusitzka, K.; Gietzen, S.; Frey, H.; Schmidt, M. Evaluation of Multifunctional Liposomes in Human Blood Serum by Light Scattering. *Langmuir* **2014**, 30, 14954-14962.
22. Gavrillov, K.; Saltzman, W. M. Therapeutic siRNA: principles, challenges, and strategies. *The Yale journal of biology and medicine* **2012**, 85, 187.
23. Jin, S.; Leach, J. C.; Ye, K. Nanoparticle-mediated gene delivery. *Micro and Nano Technologies in Bioanalysis: Methods and Protocols* **2009**, 547-557.
24. Patil, M. L.; Zhang, M.; Betigeri, S.; Taratula, O.; He, H.; Minko, T. Surface-modified and internally cationic polyamidoamine dendrimers for efficient siRNA delivery. *Bioconjugate Chem.* **2008**, 19, 1396-1403.
25. Sutton, D.; Nasongkla, N.; Blanco, E.; Gao, J. Functionalized micellar systems for cancer targeted drug delivery. *Pharm. Res.* **2007**, 24, 1029-1046.
26. Francis, M. F.; Cristea, M.; Winnik, F. M. Polymeric micelles for oral drug delivery: why and how. *Pure Appl. Chem.* **2004**, 76, 1321-1335.
27. Moore, A.; Medarova, Z.; Potthast, A.; Dai, G. In Vivo Targeting of Underglycosylated MUC-1 Tumor Antigen Using a Multimodal Imaging Probe. *Cancer Res.* **2004**, 64, 1821-1827.
28. Flenniken, M. L.; Liepold, L. O.; Crowley, B. E.; Willits, D. A.; Young, M. J.; Douglas, T. Selective attachment and release of a chemotherapeutic agent from the interior of a protein cage architecture. *Chem. Commun.* **2005**, 447-449.
29. Müller, L. K.; Landfester, K. Natural liposomes and synthetic polymeric structures for biomedical applications. *Biochem. Biophys. Res. Commun.* **2015**.
30. Fire, A.; Xu, S.; Montgomery, M. K.; Kostas, S. A.; Driver, S. E.; Mello, C. C. Potent and specific genetic interference by double-stranded RNA in *Caenorhabditis elegans*. *Nature* **1998**, 391, 806-811.
31. Elbashir, S. M.; Harborth, J.; Lendeckel, W.; Yalcin, A.; Weber, K.; Tuschl, T. Duplexes of 21-nucleotide RNAs mediate RNA interference in cultured mammalian cells. *Nature* **2001**, 411, 494-498.
32. Elbashir, S. M.; Lendeckel, W.; Tuschl, T. RNA interference is mediated by 21- and 22-nucleotide RNAs. *Genes Dev.* **2001**, 15, 188-200.
33. Gao, Y.; Liu, X.-L.; Li, X.-R. Research progress on siRNA delivery with nonviral carriers. *Int J Nanomedicine* **2011**, 6, 1017-1025.
34. Choung, S.; Kim, Y. J.; Kim, S.; Park, H.-O.; Choi, Y.-C. Chemical modification of siRNAs to improve serum stability without loss of efficacy. *Biochem. Biophys. Res. Commun.* **2006**, 342, 919-927.

35. Ghosn, B.; Singh, A.; Li, M.; Vlassov, A. V.; Burnett, C.; Puri, N.; Roy, K. Efficient gene silencing in lungs and liver using imidazole-modified chitosan as a nanocarrier for small interfering RNA. *Oligonucleotides* **2010**, *20*, 163-172.
36. Howard, K. A.; Rahbek, U. L.; Liu, X.; Damgaard, C. K.; Glud, S. Z.; Andersen, M. Ø.; Hovgaard, M. B.; Schmitz, A.; Nyengaard, J. R.; Besenbacher, F. RNA interference in vitro and in vivo using a chitosan/siRNA nanoparticle system. *Mol. Ther.* **2006**, *14*, 476-484.
37. Buyens, K.; De Smedt, S. C.; Braeckmans, K.; Demeester, J.; Peeters, L.; van Grunsven, L. A.; du Jeu, X. d. M.; Sawant, R.; Torchilin, V.; Farkasova, K. Liposome based systems for systemic siRNA delivery: stability in blood sets the requirements for optimal carrier design. *J. Controlled Release* **2012**, *158*, 362-370.
38. Gurr, M. I.; Harwood, J. L.; Frayn, K. N. Index. *Lipid Biochemistry*, Blackwell Science Ltd: 2008; pp 315-320.
39. Heinrich, P. C.; Müller, M.; Graeve, L. *Löffler/Petrides Biochemie und Pathobiochemie*. Springer-Verlag: 2014.
40. Israelachvili, J. N.; Mitchell, D. J.; Ninham, B. W. Theory of self-assembly of hydrocarbon amphiphiles into micelles and bilayers. *Journal of the Chemical Society, Faraday Transactions 2: Molecular and Chemical Physics* **1976**, *72*, 1525-1568.
41. Lasic, D. D. *Liposomes: from physics to applications*. Elsevier Science Ltd: 1993.
42. Lasic, D. D.; Needham, D. The "stealth" liposome: a prototypical biomaterial. *Chem. Rev.* **1995**, *95*, 2601-2628.
43. Crommelin, D. J. A.; Metselaar, J. M.; Storm, G. Liposomes: The Science and the Regulatory Landscape. *Non-Biological Complex Drugs*, Crommelin, D. J. A.; de Vlieger, J. S. B., Eds. Springer International Publishing: 2015; Vol. 20, pp 77-106.
44. Singer, S. J.; Nicolson, G. L. The fluid mosaic model of the structure of cell membranes. *Science* **1972**, *175*, 720-731.
45. Zhang, Y.; Cristofaro, P.; Silbermann, R.; Pusch, O.; Boden, D.; Konkin, T.; Hovanesian, V.; Monfils, P. R.; Resnick, M.; Moss, S. F. Engineering mucosal RNA interference in vivo. *Mol. Ther.* **2006**, *14*, 336-342.
46. Wu, S.; McMillan, N. J. Lipidic Systems for In Vivo siRNA Delivery. *The AAPS Journal* **2009**, *11*, 639-652.
47. Moore, C. C.; Martin, E. N.; Lee, G.; Taylor, C.; Dondero, R.; Reznikov, L. L.; Dinarello, C.; Thompson, J.; Scheld, W. M. Eukaryotic Translation Initiation Factor 5A Small Interference RNA-Liposome Complexes Reduce Inflammation and Increase Survival in Murine Models of Severe Sepsis and Acute Lung Injury. *J. Infect. Dis.* **2008**, *198*, 1407-1414.
48. Ren, T.; Song, Y.; Zhang, G.; Liu, D. Structural basis of DOTMA for its high intravenous transfection activity in mouse. *Gene Ther.* **2000**, *7*, 764-768.
49. Dokka, S.; Toledo, D.; Shi, X.; Castranova, V.; Rojanasakul, Y. Oxygen radical-mediated pulmonary toxicity induced by some cationic liposomes. *Pharm. Res.* **2000**, *17*, 521-525.
50. Harris, T. J.; Green, J. J.; Fung, P. W.; Langer, R.; Anderson, D. G.; Bhatia, S. N. Tissue-specific gene delivery via nanoparticle coating. *Biomaterials* **2010**, *31*, 998-1006.

51. Allen, T.; Chonn, A. Large unilamellar liposomes with low uptake into the reticuloendothelial system. *FEBS Lett.* **1987**, 223, 42-46.
52. Love, K. T.; Mahon, K. P.; Levins, C. G.; Whitehead, K. A.; Querbes, W.; Dorkin, J. R.; Qin, J.; Cantley, W.; Qin, L. L.; Racie, T.; Frank-Kamenetsky, M.; Yip, K. N.; Alvarez, R.; Sah, D. W. Y.; de Fougerolles, A.; Fitzgerald, K.; Koteliansky, V.; Akinc, A.; Langer, R.; Anderson, D. G. Lipid-like materials for low-dose, in vivo gene silencing. *Proceedings of the National Academy of Sciences* **2010**, 107, 1864-1869.
53. Zhang, Y.; Anchordoquy, T. J. The role of lipid charge density in the serum stability of cationic lipid/DNA complexes. *Biochimica et Biophysica Acta (BBA)-Biomembranes* **2004**, 1663, 143-157.
54. Xu, L.; Anchordoquy, T. J. Cholesterol domains in cationic lipid/DNA complexes improve transfection. *Biochimica et Biophysica Acta (BBA)-Biomembranes* **2008**, 1778, 2177-2181.
55. Allen, T.; Hansen, C.; Martin, F.; Redemann, C.; Yau-Young, A. Liposomes containing synthetic lipid derivatives of poly (ethylene glycol) show prolonged circulation half-lives in vivo. *Biochimica et Biophysica Acta (BBA)-Biomembranes* **1991**, 1066, 29-36.
56. Allen, C.; Dos Santos, N.; Gallagher, R.; Chiu, G.; Shu, Y.; Li, W.; Johnstone, S. a.; Janoff, A.; Mayer, L.; Webb, M. Controlling the physical behavior and biological performance of liposome formulations through use of surface grafted poly (ethylene glycol). *Biosci. Rep.* **2002**, 22, 225-250.
57. Woodle, M.; Matthay, K.; Newman, M.; Hidayat, J.; Collins, L.; Redemann, C.; Martin, F.; Papahadjopoulos, D. Versatility in lipid compositions showing prolonged circulation with sterically stabilized liposomes. *Biochimica et Biophysica Acta (BBA)-Biomembranes* **1992**, 1105, 193-200.
58. Torchilin, V. P.; Omelyanenko, V. G.; Papisov, M. I.; Bogdanov, A. A.; Trubetskoy, V. S.; Herron, J. N.; Gentry, C. A. Poly (ethylene glycol) on the liposome surface: on the mechanism of polymer-coated liposome longevity. *Biochimica et Biophysica Acta (BBA)-Biomembranes* **1994**, 1195, 11-20.
59. Blume, G.; Cevc, G. Liposomes for the sustained drug release in vivo. *Biochimica et Biophysica Acta (BBA)-Biomembranes* **1990**, 1029, 91-97.
60. Immordino, M. L.; Dosio, F.; Cattel, L. Stealth liposomes: review of the basic science, rationale, and clinical applications, existing and potential. *International journal of nanomedicine* **2006**, 1, 297.
61. Cabanes, A.; Tzemach, D.; Goren, D.; Horowitz, A. T.; Gabizon, A. Comparative study of the antitumor activity of free doxorubicin and polyethylene glycol-coated liposomal doxorubicin in a mouse lymphoma model. *Clin. Cancer. Res.* **1998**, 4, 499-505.
62. Torchilin, V. P. Recent advances with liposomes as pharmaceutical carriers. *Nat. Rev. Drug Discov.* **2005**, 4, 145-160.
63. Sharma, A.; Sharma, U. S. Liposomes in drug delivery: progress and limitations. *Int. J. Pharm.* **1997**, 154, 123-140.
64. Müller, S. S.; Wurm, F. R. Nanovesicles as Drug Delivery Vehicles: Liposomes and Polymersomes. *Encyclopedia of Polymeric Nanomaterials* **2015**, 1372-1377.
65. Kremer, L. C. M.; van Dalen, E. C.; Offringa, M.; Ottenkamp, J.; Voûte, P. A. Anthracycline-Induced Clinical Heart Failure in a Cohort of 607 Children: Long-Term Follow-Up Study. *Journal of Clinical Oncology* **2001**, 19, 191-196.

66. Gabizon, A.; Catane, R.; Uziely, B.; Kaufman, B.; Safra, T.; Cohen, R.; Martin, F.; Huang, A.; Barenholz, Y. Prolonged Circulation Time and Enhanced Accumulation in Malignant Exudates of Doxorubicin Encapsulated in Polyethylene-glycol Coated Liposomes. *Cancer Res.* **1994**, *54*, 987-992.
67. Papahadjopoulos, D.; Allen, T.; Gabizon, A.; Mayhew, E.; Matthay, K.; Huang, S.; Lee, K.; Woodle, M.; Lasic, D.; Redemann, C. Sterically stabilized liposomes: improvements in pharmacokinetics and antitumor therapeutic efficacy. *Proceedings of the National Academy of Sciences* **1991**, *88*, 11460-11464.
68. Buyens, K.; Demeester, J.; De Smedt, S. S.; Sanders, N. N. Elucidating the encapsulation of short interfering RNA in PEGylated cationic liposomes. *Langmuir* **2009**, *25*, 4886-4891.
69. Kasahara, M.; Hinkle, P. C. Reconstitution and purification of the D-glucose transporter from human erythrocytes. *J. Biol. Chem.* **1977**, *252*, 7384-7390.
70. Pick, U. Liposomes with a large trapping capacity prepared by freezing and thawing of sonicated phospholipid mixtures. *Arch. Biochem. Biophys.* **1981**, *212*, 186-194.
71. Maguire, L. A.; Zhang, H.; Shamlou, P. A. Preparation of small unilamellar vesicles (SUV) and biophysical characterization of their complexes with poly-L-lysine-condensed plasmid DNA. *Biotechnol. Appl. Biochem.* **2003**, *37*, 73-81.
72. Olson, F.; Hunt, C. A.; Szoka, F. C.; Vail, W. J.; Papahadjopoulos, D. Preparation of liposomes of defined size distribution by extrusion through polycarbonate membranes. *Biochim. Biophys. Acta* **1979**, *557*, 9-23.
73. Miller, A. D. Cationic liposomes for gene therapy. *Angew. Chem. Int. Ed.* **1998**, *37*, 1768-1785.
74. Akinc, A.; Zumbuehl, A.; Goldberg, M.; Leshchiner, E. S.; Busini, V.; Hossain, N.; Bacallado, S. A.; Nguyen, D. N.; Fuller, J.; Alvarez, R. A combinatorial library of lipid-like materials for delivery of RNAi therapeutics. *Nat. Biotechnol.* **2008**, *26*, 561-569.
75. Dong, Y.; Eltoukhy, A. A.; Alabi, C. A.; Khan, O. F.; Veisheh, O.; Dorkin, J. R.; Sirirungruang, S.; Yin, H.; Tang, B. C.; Pelet, J. M.; Chen, D.; Gu, Z.; Xue, Y.; Langer, R.; Anderson, D. G. Lipid-Like Nanomaterials for Simultaneous Gene Expression and Silencing In Vivo. *Advanced Healthcare Materials* **2014**, *3*, 1392-1397.
76. Zhang, Y.; Arrington, L.; Boardman, D.; Davis, J.; Xu, Y.; DiFelice, K.; Stirdivant, S.; Wang, W.; Budzik, B.; Bawiec, J. The development of an in vitro assay to screen lipid based nanoparticles for siRNA delivery. *J. Controlled Release* **2014**, *174*, 7-14.
77. Ewe, A.; Schaper, A.; Barnert, S.; Schubert, R.; Temme, A.; Bakowsky, U.; Aigner, A. Storage stability of optimal liposome-polyethylenimine complexes (lipopolyplexes) for DNA or siRNA delivery. *Acta Biomater.* **2014**, *10*, 2663-2673.
78. Lerch, S.; Dass, M.; Musyanovych, A.; Landfester, K.; Mailander, V. Polymeric nanoparticles of different sizes overcome the cell membrane barrier. *Eur J Pharm Biopharm* **2013**, *84*, 265-74.
79. Florez, L.; Herrmann, C.; Cramer, J. M.; Hauser, C. P.; Koynov, K.; Landfester, K.; Crespy, D.; Mailander, V. How Shape Influences Uptake: Interactions of Anisotropic Polymer Nanoparticles and Human Mesenchymal Stem Cells. *Small* **2012**, *8*, 2222-2230.
80. Schrade, A.; Mailander, V.; Ritz, S.; Landfester, K.; Ziener, U. Surface roughness and charge influence the uptake of nanoparticles: fluorescently labeled pickering-type versus surfactant-stabilized nanoparticles. *Macromol. Biosci.* **2012**, *12*, 1459-71.

81. Monopoli, M. P.; Aberg, C.; Salvati, A.; Dawson, K. A. Biomolecular coronas provide the biological identity of nanosized materials. *Nat Nanotechnol* **2012**, *7*, 779-86.
82. Liu, Z. H.; Jiao, Y. P.; Wang, T.; Zhang, Y. M.; Xue, W. Interactions between solubilized polymer molecules and blood components. *J. Controlled Release* **2012**, *160*, 14-24.
83. Salvati, A.; Pitek, A. S.; Monopoli, M. P.; Prapainop, K.; Bombelli, F. B.; Hristov, D. R.; Kelly, P. M.; Aberg, C.; Mahon, E.; Dawson, K. A. Transferrin-functionalized nanoparticles lose their targeting capabilities when a biomolecule corona adsorbs on the surface. *Nature Nanotechnology* **2013**, *8*, 137-143.
84. Musyanovych, A.; Dausend, J.; Dass, M.; Walther, P.; Mailander, V.; Landfester, K. Criteria impacting the cellular uptake of nanoparticles: a study emphasizing polymer type and surfactant effects. *Acta Biomater.* **2011**, *7*, 4160-8.
85. Baier, G.; Baumann, D.; Siebert, J. M.; Musyanovych, A.; Mailander, V.; Landfester, K. Suppressing Unspecific Cell Uptake for Targeted Delivery Using Hydroxyethyl Starch Nanocapsules. *Biomacromolecules* **2012**, *13*, 2704-2715.
86. Walkey, C. D.; Chan, W. C. Understanding and controlling the interaction of nanomaterials with proteins in a physiological environment. *Chem. Soc. Rev.* **2012**, *41*, 2780-2799.
87. Monopoli, M. P.; Walczyk, D.; Campbell, A.; Elia, G.; Lynch, I.; Baldelli Bombelli, F.; Dawson, K. A. Physical-Chemical Aspects of Protein Corona: Relevance to in Vitro and in Vivo Biological Impacts of Nanoparticles. *JACS* **2011**, *133*, 2525-2534.
88. Walczyk, D.; Bombelli, F. B.; Monopoli, M. P.; Lynch, I.; Dawson, K. A. What the Cell "Sees" in Bionanoscience. *JACS* **2010**, *132*, 5761-5768.
89. Vroman, L. Effect of adsorbed proteins on the wettability of hydrophilic and hydrophobic solids. **1962**.
90. Vroman, L.; Adams, A.; Fischer, G.; Munoz, P. Interaction of high molecular weight kininogen, factor XII, and fibrinogen in plasma at interfaces. *Blood* **1980**, *55*, 156-159.
91. Lynch, I.; Dawson, K. A.; Linse, S. Detecting Cryptic Epitopes Created by Nanoparticles. *Science Signaling* **2006**, *2006*, pe14-pe14.
92. Cedervall, T.; Lynch, I.; Lindman, S.; Berggård, T.; Thulin, E.; Nilsson, H.; Dawson, K. A.; Linse, S. Understanding the nanoparticle-protein corona using methods to quantify exchange rates and affinities of proteins for nanoparticles. *Proceedings of the National Academy of Sciences* **2007**, *104*, 2050-2055.
93. Patel, H. Serum opsonins and liposomes: Their interaction and opsonophagocytosis. *Crit. Rev. Ther. Drug Carrier Syst.* **1991**, *9*, 39-90.
94. Chonn, A.; Semple, S.; Cullis, P. Association of blood proteins with large unilamellar liposomes in vivo. Relation to circulation lifetimes. *J. Biol. Chem.* **1992**, *267*, 18759-18765.
95. Lunov, O.; Syrovets, T.; Loos, C.; Beil, J.; Delacher, M.; Tron, K.; Nienhaus, G. U.; Musyanovych, A.; Mailander, V.; Landfester, K.; Simmet, T. Differential uptake of functionalized polystyrene nanoparticles by human macrophages and a monocytic cell line. *ACS Nano* **2011**, *5*, 1657-69.
96. Åkesson, A.; Cárdenas, M.; Elia, G.; Monopoli, M. P.; Dawson, K. A. The protein corona of dendrimers: PAMAM binds and activates complement proteins in human plasma in a generation dependent manner. *Rsc Advances* **2012**, *2*, 11245-11248.

97. Roser, M.; Fischer, D.; Kissel, T. Surface-modified biodegradable albumin nano- and microspheres. II: effect of surface charges on in vitro phagocytosis and biodistribution in rats. *European Journal of Pharmaceutics and Biopharmaceutics* **1998**, *46*, 255-263.
98. Carrstensen, H.; Müller, R. H.; Müller, B. W. Particle size, surface hydrophobicity and interaction with serum of parenteral fat emulsions and model drug carriers as parameters related to RES uptake. *Clin. Nutr.* **1992**, *11*, 289-297.
99. Müller, R. H.; Wallis, K. H.; Troester, S. D.; Kreuter, J. In vitro characterization of poly (methyl-methacrylate) nanoparticles and correlation to their in vivo fate. *J. Controlled Release* **1992**, *20*, 237-246.
100. Teichroeb, J.; Forrest, J.; Ngai, V.; Jones, L. Anomalous thermal denaturing of proteins adsorbed to nanoparticles. *The European Physical Journal E* **2006**, *21*, 19-24.
101. Karajanagi, S. S.; Vertegel, A. A.; Kane, R. S.; Dordick, J. S. Structure and function of enzymes adsorbed onto single-walled carbon nanotubes. *Langmuir* **2004**, *20*, 11594-11599.
102. Norde, W.; Giacomelli, C. E. BSA structural changes during homomolecular exchange between the adsorbed and the dissolved states. *J. Biotechnol.* **2000**, *79*, 259-268.
103. Wan, S.; Kelly, P. M.; Mahon, E.; Stöckmann, H.; Rudd, P. M.; Caruso, F.; Dawson, K. A.; Yan, Y.; Monopoli, M. P. The "Sweet" Side of the Protein Corona: Effects of Glycosylation on Nanoparticle-Cell Interactions. *ACS Nano* **2015**, *9*, 2157-2166.
104. Gref, R.; Lück, M.; Quellec, P.; Marchand, M.; Dellacherie, E.; Harnisch, S.; Blunk, T.; Müller, R. H. 'Stealth' corona-core nanoparticles surface modified by polyethylene glycol (PEG): influences of the corona (PEG chain length and surface density) and of the core composition on phagocytic uptake and plasma protein adsorption. *Colloids Surf. B. Biointerfaces* **2000**, *18*, 301-313.
105. Peracchia, M.; Harnisch, S.; Pinto-Alphandary, H.; Gulik, A.; Dedieu, J.; Desmaele, D.; d'Angelo, J.; Müller, R.; Couvreur, P. Visualization of in vitro protein-rejecting properties of PEGylated stealth® polycyanoacrylate nanoparticles. *Biomaterials* **1999**, *20*, 1269-1275.
106. Kim, H. R.; Andrieux, K.; Delomenie, C.; Chacun, H.; Appel, M.; Desmaële, D.; Taran, F.; Georgin, D.; Couvreur, P.; Taverna, M. Analysis of plasma protein adsorption onto PEGylated nanoparticles by complementary methods: 2-DE, CE and Protein Lab-on-chip® system. *Electrophoresis* **2007**, *28*, 2252-2261.
107. Schöttler, S.; Becker, G.; Winzen, S.; Steinbach, T.; Mohr, K.; Landfester, K.; Mailänder, V.; Wurm, F. R. Protein adsorption is required for stealth effect of poly(ethylene glycol)- and poly(phosphoester)-coated nanocarriers. *Nat Nano* **2016**, advance online publication.
108. Winzen, S.; Schoettler, S.; Baier, G.; Rosenauer, C.; Mailänder, V.; Landfester, K.; Mohr, K. Complementary analysis of the hard and soft protein corona: sample preparation critically effects corona composition. *Nanoscale* **2015**, *7*, 2992-3001.
109. Bouchemal, K. New challenges for pharmaceutical formulations and drug delivery systems characterization using isothermal titration calorimetry. *Drug Discovery Today* **2008**, *13*, 960-972.
110. Lindman, S.; Lynch, I.; Thulin, E.; Nilsson, H.; Dawson, K. A.; Linse, S. Systematic investigation of the thermodynamics of HSA adsorption to N-iso-propylacrylamide/N-tert-butylacrylamide copolymer nanoparticles. Effects of particle size and hydrophobicity. *Nano Lett.* **2007**, *7*, 914-920.
111. Tsai, D.-H.; DelRio, F. W.; Keene, A. M.; Tyner, K. M.; MacCuspie, R. I.; Cho, T. J.; Zachariah, M. R.; Hackley, V. A. Adsorption and Conformation of Serum Albumin Protein on Gold Nanoparticles Investigated Using Dimensional Measurements and in Situ Spectroscopic Methods. *Langmuir* **2011**, *27*, 2464-2477.

112. Siegert, A. Radiation Laboratory report no. 465. *Massachusetts Institute of Technology, Cambridge* **1943**.
113. Burchard, W.; Richtering, W. Dynamic light scattering from polymer solutions. *Relaxation in Polymers*, Pietralla, M.; Pechhold, W., Eds. Steinkopff: Darmstadt, 1989; pp 151-163.
114. Rausch, K.; Reuter, A.; Fischer, K.; Schmidt, M. Evaluation of nanoparticle aggregation in human blood serum. *Biomacromolecules* **2010**, *11*, 2836-2839.
115. Mohr, K.; Sommer, M.; Baier, G.; Schöttler, S.; Okwieka, P.; Tenzer, S.; Landfester, K.; Mailänder, V.; Schmidt, M.; Meyer, R. Aggregation behavior of polystyrene-nanoparticles in human blood serum and its impact on the in vivo distribution in mice. *J. Nanomed. Nanotechnol* **2014**, *5*.
116. Koynov, K.; Butt, H.-J. Fluorescence correlation spectroscopy in colloid and interface science. *Current Opinion in Colloid & Interface Science* **2012**, *17*, 377-387.
117. Rocker, C.; Potzl, M.; Zhang, F.; Parak, W. J.; Nienhaus, G. U. A quantitative fluorescence study of protein monolayer formation on colloidal nanoparticles. *Nat Nano* **2009**, *4*, 577-580.
118. Smith, P. K.; Krohn, R. I.; Hermanson, G. T.; Mallia, A. K.; Gartner, F. H.; Provenzano, M. D.; Fujimoto, E. K.; Goeke, N. M.; Olson, B. J.; Klenk, D. C. Measurement of protein using bicinchoninic acid. *Anal. Biochem.* **1985**, *150*, 76-85.
119. Reynolds, J. A.; Tanford, C. The gross conformation of protein-sodium dodecyl sulfate complexes. *J. Biol. Chem.* **1970**, *245*, 5161-5165.
120. Gygi, S. P.; Corthals, G. L.; Zhang, Y.; Rochon, Y.; Aebersold, R. Evaluation of two-dimensional gel electrophoresis-based proteome analysis technology. *Proceedings of the National Academy of Sciences* **2000**, *97*, 9390-9395.
121. Burkhart, J. M.; Schumbrutzki, C.; Wortelkamp, S.; Sickmann, A.; Zahedi, R. P. Systematic and quantitative comparison of digest efficiency and specificity reveals the impact of trypsin quality on MS-based proteomics. *Journal of proteomics* **2012**, *75*, 1454-1462.
122. Tenzer, S.; Docter, D.; Kuharev, J.; Musyanovych, A.; Fetz, V.; Hecht, R.; Schlenk, F.; Fischer, D.; Kiouptsi, K.; Reinhardt, C.; Landfester, K.; Schild, H.; Maskos, M.; Knauer, S. K.; Stauber, R. H. Rapid formation of plasma protein corona critically affects nanoparticle pathophysiology. *Nat Nanotechnol* **2013**, *8*, 772-81.
123. Hunter, R. J. *Zeta potential in colloid science: principles and applications*. Academic press: 2013; Vol. 2.
124. Ritz, S.; Schöttler, S.; Kotman, N.; Baier, G.; Musyanovych, A.; Kuharev, J.; Landfester, K.; Schild, H.; Jahn, O.; Tenzer, S.; Mailänder, V. Protein corona of nanoparticles: distinct proteins regulate the cellular uptake. *Biomacromolecules* **2015**, *16*, 1311-21.
125. Baier, G.; Costa, C.; Zeller, A.; Baumann, D.; Sayer, C.; Araujo, P. H. H.; Mailänder, V.; Musyanovych, A.; Landfester, K. BSA Adsorption on Differently Charged Polystyrene Nanoparticles using Isothermal Titration Calorimetry and the Influence on Cellular Uptake. *Macromol. Biosci.* **2011**, *11*, 628-638.
126. Gianazza, E.; Arnaud, P. Chromatography of plasma proteins on immobilized Cibacron Blue F3-GA. Mechanism of the molecular interaction. *Biochem. J* **1982**, *203*, 637-641.

127. Ghiggeri, G. M.; Candiano, G.; Delfino, G.; Queirolo, C. Highly selective one-step chromatography of serum and urinary albumin on immobilized Cibacron Blue F3GA. Studies on normal and glycosyl albumin. *Clin. Chim. Acta* **1985**, *145*, 205-211.
128. Armstrong, J.; Wenby, R.; Meiselman, H.; Fisher, T. The hydrodynamic radii of macromolecules and their effect on red blood cell aggregation. *Biophys. J.* **2004**, *87*, 4259-4270.
129. Rausch, K. Interaktions-und Aggregationsverhalten von Nanopartikeln in Blutserum. Universitätsbibliothek Mainz, 2013.
130. Rezaei-Tavirani, M.; Moghaddamnia, S. H.; Ranjbar, B.; Amani, M.; Marashi, S.-A. Conformational study of human serum albumin in pre-denaturation temperatures by differential scanning calorimetry, circular dichroism and UV spectroscopy. *BMB Reports* **2006**, *39*, 530-536.
131. Ehrenberg, M. S.; Friedman, A. E.; Finkelstein, J. N.; Oberdörster, G.; McGrath, J. L. The influence of protein adsorption on nanoparticle association with cultured endothelial cells. *Biomaterials* **2009**, *30*, 603-610.
132. Dutta, D.; Sundaram, S. K.; Teeguarden, J. G.; Riley, B. J.; Fifield, L. S.; Jacobs, J. M.; Addleman, S. R.; Kaysen, G. A.; Moudgil, B. M.; Weber, T. J. Adsorbed proteins influence the biological activity and molecular targeting of nanomaterials. *Toxicol. Sci.* **2007**, *100*, 303-315.
133. Hawkins, C. L.; Davies, M. J. Generation and propagation of radical reactions on proteins. *Biochim. Biophys. Acta* **2001**, *1504*, 196-219.
134. Honn, K. V.; Singley, J. A.; Chavin, W. Fetal bovine serum: a multivariate standard. *Exp. Biol. Med.* **1975**, *149*, 344-347.
135. Walkey, C. D.; Olsen, J. B.; Guo, H.; Emili, A.; Chan, W. C. Nanoparticle size and surface chemistry determine serum protein adsorption and macrophage uptake. *JACS* **2012**, *134*, 2139-2147.
136. Pozzi, D.; Caracciolo, G.; Capriotti, A. L.; Cavaliere, C.; La Barbera, G.; Anchordoquy, T. J.; Laganà, A. Surface chemistry and serum type both determine the nanoparticle-protein corona. *Journal of proteomics* **2015**, *119*, 209-217.
137. Schöttler, S.; Klein, K.; Landfester, K.; Mailänder, V. Protein source and choice of anticoagulant decisively affect nanoparticle protein corona and cellular uptake. *Nanoscale* **2016**.
138. Hajipour, M. J.; Laurent, S.; Aghaie, A.; Rezaee, F.; Mahmoudi, M. Personalized protein coronas: a "key" factor at the nanobiointerface. *Biomaterials Science* **2014**, *2*, 1210-1221.
139. Caracciolo, G.; Caputo, D.; Pozzi, D.; Colapicchioni, V.; Coppola, R. Size and charge of nanoparticles following incubation with human plasma of healthy and pancreatic cancer patients. *Colloids Surf. B. Biointerfaces* **2014**, *123*, 673-678.
140. Barone, G.; Giancola, C.; Verdoliva, A. DSC studies on the denaturation and aggregation of serum albumins. *Thermochim. Acta* **1992**, *199*, 197-205.
141. Vermeer, A. W.; Norde, W.; van Amerongen, A. The Unfolding/Denaturation of Immunoglobulin of Isotype 2b and its F ab and F c Fragments. *Biophys. J.* **2000**, *79*, 2150-2154.
142. Wagner, V.; Dullaart, A.; Bock, A.-K.; Zweck, A. The emerging nanomedicine landscape. *Nat Biotech* **2006**, *24*, 1211-1217.

143. Prensner, J. R.; Chinnaiyan, A. M.; Srivastava, S. Systematic, evidence-based discovery of biomarkers at the NCI. *Clin. Exp. Metastasis* **2012**, *29*, 645-652.
144. Junod, S. W. FDA and clinical drug trials: a short history. *A Quick Guide to Clinical Trials: For People Who May Not Know It All* **2014**, 21-51.
145. McGonigle, P.; Ruggeri, B. Animal models of human disease: Challenges in enabling translation. *Biochem. Pharmacol.* **2014**, *87*, 162-171.
146. Perel, P.; Roberts, I.; Sena, E.; Wheble, P.; Briscoe, C.; Sandercock, P.; Macleod, M.; Mignini, L. E.; Jayaram, P.; Khan, K. S. Comparison of treatment effects between animal experiments and clinical trials: systematic review. *BMJ* **2007**, *334*, 197.
147. Mak, I.; Evaniew, N.; Ghert, M. Lost in translation: animal models and clinical trials in cancer treatment. *Am J Transl Res* **2014**, *6*, 114-8.
148. Seok, J.; Warren, H. S.; Cuenca, A. G.; Mindrinos, M. N.; Baker, H. V.; Xu, W.; Richards, D. R.; McDonald-Smith, G. P.; Gao, H.; Hennessy, L.; Finnerty, C. C.; López, C. M.; Honari, S.; Moore, E. E.; Minei, J. P.; Cuschieri, J.; Bankey, P. E.; Johnson, J. L.; Sperry, J.; Nathens, A. B.; Billiar, T. R.; West, M. A.; Jeschke, M. G.; Klein, M. B.; Gamelli, R. L.; Gibran, N. S.; Brownstein, B. H.; Miller-Graziano, C.; Calvano, S. E.; Mason, P. H.; Cobb, J. P.; Rahme, L. G.; Lowry, S. F.; Maier, R. V.; Moldawer, L. L.; Herndon, D. N.; Davis, R. W.; Xiao, W.; Tompkins, R. G.; Inflammation, t.; Host Response to Injury, L. S. C. R. P. Genomic responses in mouse models poorly mimic human inflammatory diseases. *Proceedings of the National Academy of Sciences* **2013**, *110*, 3507-3512.
149. Cabib, S.; Orsini, C.; Moal, M. L.; Piazza, P. V. Abolition and Reversal of Strain Differences in Behavioral Responses to Drugs of Abuse After a Brief Experience. *Science* **2000**, *289*, 463-465.
150. Pozzi, D.; Caracciolo, G.; Capriotti, A. L.; Cavaliere, C.; La Barbera, G.; Anchordoquy, T. J.; Lagana, A. Surface chemistry and serum type both determine the nanoparticle-protein corona. *J Proteomics* **2015**, *119*, 209-17.
151. Zhao, X. B.; Muthusamy, N.; Byrd, J. C.; Lee, R. J. Cholesterol as a bilayer anchor for PEGylation and targeting ligand in folate-receptor-targeted liposomes. *J. Pharm. Sci.* **2007**, *96*, 2424-2435.
152. Nuhn, L.; Gietzen, S.; Mohr, K.; Fischer, K.; Toh, K.; Miyata, K.; Matsumoto, Y.; Kataoka, K.; Schmidt, M.; Zentel, R. Aggregation behavior of cationic nanohydrogel particles in human blood serum. *Biomacromolecules* **2014**, *15*, 1526-1533.
153. Chai, W. Synthese und Charakterisierung von multivalenten kationischen Tensiden und Polymeren. Universitätsbibliothek Mainz, 2012.

7 APPENDIX

7.1 ABBREVIATIONS

A	baseline
a	amplitude
AF-FFF	asymmetric flow-field flow fractionation
ACF	autocorrelation dunction
BNF	bionized nanofferite
BSA	bovine serum albumin
Chol	cholesterol
CD	circular dichroism
CMC	critical micelle concentration
cp	coated particle
D	diffusion coefficient
DEX	dextran
DOTAP	1,2-dioleoyl-3-trimethylammonio propane
DOTMA	N-[1-(2, 3-dioleyloxy)propyl]-N,N,N-trimethylammonium chloride
DOX	doxorubicin
DLS	dynamic light scattering
DSPC	distearoyl phosphatodylcholine
E	elution fraction
ϵ	dielectric constant
EPC	egg phosphatidyl choline
EPR	enhanced permeability and retention
f	intensity contribution
FBS	fetal bovine serum
FCS	fluorescence correlation spectroscopy
FT	flow through
$g_1(t)$	experimental field autocorrelation function
$g_2(t)$	intensity autocorrelation function

<i>hbPG</i>	hyperbranched polyglycerol
HES	hydroxyl ethyl starch
HI	heat inactivated
HSA	human serum albumin
IgG	immunoglobulin G
ITC	isothermal titration calorimetry
L	liposome
LC-MS	liquid chromatography-mass spectrometry
η	viscosity
NP	nanoparticles
PEG	poly (ethylene glycol)
PS	polystyrene
q	scattering angle
ρ	particle
ρ	ratio of radius of gyration and hydrodynamic radius
R_g	radius of gyration
R_h	hydrodynamic radius
RNAi	RNA interference
SDS	sodium dodecyl sulfate
SDS-PAGE	SDS polyacrylamide gel electrophoresis
T	temperature
τ	correlation time
TF	1-hydroxy-50-amino-3,4,7,10,13,16,19,22-octaoxa-37,41,45-triaza-pentacontane
TLR	toll like receptor
TNT	1,3,5-triazin-2,4,6-trione
TOF	time of flight
u_E	electrophoretic mobility
ζ	zeta potential

7.2 SUPPLEMENTARY INFORMATION

7.2.1 LC-MS DATA FOR BLOOD PLASMA FRACTIONATION

Protein name	Average percentage of total protein				
	IgG	IgG depleted plasma	HSA depleted plasma	HSA (AffiBlue only)	HSA (columns in series)
Alpha-1-acid glycoprotein 1	0,00%	0,54%	4,19%	0,00%	0,00%
Alpha-1-acid glycoprotein 2	0,00%	1,90%	1,99%	0,00%	0,00%
Alpha-1-antichymotrypsin	0,00%	0,50%	1,01%	0,13%	0,43%
Alpha-1-antitrypsin	0,00%	1,61%	13,38%	0,00%	0,00%
Alpha-2-macroglobulin	0,00%	1,20%	7,25%	0,03%	0,02%
Ceruloplasmin	0,00%	0,50%	2,54%	0,00%	0,00%
Fibronectin	0,00%	0,21%	0,00%	0,00%	0,02%
Haptoglobin	0,00%	1,05%	6,31%	0,07%	0,04%
Haptoglobin-related protein	1,66%	0,25%	1,41%	0,00%	0,01%
Serum amyloid P-component	0,00%	0,04%	0,00%	0,00%	0,05%
Alpha-2-antiplasmin	0,00%	0,21%	0,59%	0,00%	0,00%
Antithrombin-III	0,00%	0,46%	0,00%	0,11%	0,16%
Coagulation factor XII	0,06%	0,00%	0,00%	0,00%	0,00%
Fibrinogen alpha chain	0,02%	0,62%	0,00%	0,13%	0,48%
Fibrinogen beta chain	0,03%	1,85%	0,00%	0,51%	0,82%
Fibrinogen gamma chain	0,14%	1,55%	0,00%	0,42%	1,21%
Heparin cofactor 2	0,00%	0,18%	0,00%	0,00%	0,00%

Histidine-rich glycoprotein	0,10%	0,07%	0,00%	0,00%	0,00%
Kininogen-1	0,00%	0,20%	0,51%	0,15%	0,20%
Plasminogen	0,30%	0,06%	0,00%	0,00%	0,00%
Prothrombin	0,00%	0,16%	0,00%	0,51%	0,06%
C4b-binding protein alpha chain	0,45%	0,15%	0,00%	0,00%	0,00%
Complement C1q subcomponent subunit A	0,14%	0,00%	0,00%	0,00%	0,00%
Complement C1q subcomponent subunit B	0,18%	0,00%	0,00%	0,00%	0,00%
Complement C1q subcomponent subunit C	0,13%	0,00%	0,00%	0,00%	0,00%
Complement C1r subcomponent	0,11%	0,00%	0,00%	0,00%	0,00%
Complement C1s subcomponent	0,07%	0,00%	0,00%	0,00%	0,00%
Complement C3	0,40%	0,61%	1,24%	0,34%	0,74%
Complement C4-A	0,01%	0,08%	0,12%	0,81%	0,16%
Complement C4-B	0,13%	0,35%	0,74%	1,61%	0,00%
Complement component C8 gamma chain	0,04%	0,00%	0,00%	0,00%	0,00%
Complement factor B	0,07%	1,15%	0,00%	0,84%	0,24%
Complement factor H	0,17%	0,44%	0,00%	0,00%	0,00%
Complement factor H-related protein 1	0,02%	0,00%	0,00%	0,00%	0,00%
Plasma protease C1 inhibitor	0,00%	0,15%	0,00%	0,14%	0,15%
Ig alpha-1 chain C region	1,06%	0,98%	5,36%	0,45%	0,33%
Ig alpha-2 chain C region	0,24%	0,41%	2,77%	0,10%	0,07%
Ig delta chain C region	0,02%	0,00%	0,00%	0,02%	0,00%
Ig gamma-1 chain C region	37,45%	0,08%	1,02%	15,35%	0,00%
Ig gamma-2 chain C region	8,53%	0,00%	2,80%	2,27%	0,00%
Ig gamma-3 chain C region	0,73%	0,00%	0,02%	0,25%	0,00%
Ig gamma-4 chain C region	0,83%	0,00%	0,41%	0,13%	0,00%
Ig heavy chain V-I region HG3	0,14%	0,00%	0,00%	0,00%	0,00%

Ig heavy chain V-I region V35	0,05%	0,00%	0,00%	0,00%	0,00%
Ig heavy chain V-II region ARH-77	0,28%	0,00%	0,00%	0,09%	0,00%
Ig heavy chain V-II region NEWM	0,04%	0,00%	0,00%	0,00%	0,00%
Ig heavy chain V-II region WAH	0,05%	0,00%	0,00%	0,00%	0,00%
Ig heavy chain V-III region BRO	1,04%	0,11%	0,32%	0,46%	0,00%
Ig heavy chain V-III region BUT	0,22%	0,00%	0,00%	0,00%	0,00%
Ig heavy chain V-III region CAM	0,03%	0,00%	0,00%	0,00%	0,00%
Ig heavy chain V-III region GAL	0,23%	0,00%	0,00%	0,09%	0,00%
Ig heavy chain V-III region JON	0,13%	0,00%	0,00%	0,00%	0,00%
Ig heavy chain V-III region POM	0,01%	0,00%	0,00%	0,00%	0,00%
Ig heavy chain V-III region TIL	0,00%	0,00%	0,10%	0,13%	0,00%
Ig heavy chain V-III region TUR	0,29%	0,00%	0,00%	0,00%	0,00%
Ig heavy chain V-III region VH26	0,19%	0,00%	0,09%	0,14%	0,00%
Ig heavy chain V-III region WEA	0,08%	0,00%	0,01%	0,05%	0,00%
Ig kappa chain C region	17,88%	1,27%	6,47%	8,37%	1,31%
Ig kappa chain V-I region AG	0,42%	0,62%	0,11%	0,90%	0,00%
Ig kappa chain V-I region AU	0,04%	0,00%	0,00%	0,00%	0,00%
Ig kappa chain V-I region CAR	0,11%	0,00%	0,00%	0,00%	0,00%
Ig kappa chain V-I region EU	0,15%	0,00%	0,00%	0,10%	0,00%
Ig kappa chain V-I region Gal	0,01%	0,00%	0,00%	0,00%	0,00%
Ig kappa chain V-I region Hau	0,00%	0,00%	0,00%	0,00%	0,00%
Ig kappa chain V-I region HK101 (Fragment)	0,02%	0,00%	0,00%	0,00%	0,00%
Ig kappa chain V-I region Lay	0,13%	0,00%	0,07%	0,00%	0,00%
Ig kappa chain V-I region Roy	0,06%	0,00%	0,00%	0,00%	0,00%
Ig kappa chain V-I region Scw	0,05%	0,00%	0,00%	0,00%	0,00%
Ig kappa chain V-I region WEA	0,04%	0,00%	0,00%	0,01%	0,00%

Ig kappa chain V-I region Wes	0,12%	0,00%	0,00%	0,00%	0,00%
Ig kappa chain V-II region Cum	0,09%	0,00%	0,00%	0,02%	0,00%
Ig kappa chain V-II region GM607 (Fragment)	0,01%	0,00%	0,00%	0,00%	0,00%
Ig kappa chain V-II region RPMI 6410	0,07%	0,00%	0,00%	0,00%	0,00%
Ig kappa chain V-II region TEW	0,72%	0,00%	0,26%	0,28%	0,00%
Ig kappa chain V-III region GOL	0,20%	0,00%	0,00%	0,00%	0,04%
Ig kappa chain V-III region HIC	0,16%	0,00%	0,00%	0,00%	0,00%
Ig kappa chain V-III region IARC/BL41	0,06%	0,00%	0,00%	0,00%	0,00%
Ig kappa chain V-III region NG9 (Fragment)	0,04%	0,00%	0,00%	0,12%	0,00%
Ig kappa chain V-III region SIE	0,54%	0,11%	0,14%	0,30%	0,00%
Ig kappa chain V-III region Ti	0,78%	0,00%	0,09%	0,00%	0,00%
Ig kappa chain V-III region VG (Fragment)	0,34%	0,00%	0,23%	0,09%	0,00%
Ig kappa chain V-IV region JI	0,05%	0,00%	0,00%	0,00%	0,00%
Ig kappa chain V-IV region Len	0,70%	0,06%	0,19%	0,19%	0,00%
Ig kappa chain V-IV region STH (Fragment)	0,06%	0,00%	0,00%	0,00%	0,00%
Ig lambda chain V-I region HA	0,41%	0,00%	0,00%	0,00%	0,00%
Ig lambda chain V-I region WAH	0,10%	0,00%	0,00%	0,00%	0,00%
Ig lambda chain V-III region LOI	0,07%	0,00%	0,00%	0,00%	0,00%
Ig lambda chain V-III region SH	5,00%	0,00%	0,00%	0,00%	0,00%
Ig lambda-1 chain C regions	0,00%	0,00%	1,36%	0,00%	0,00%
Ig lambda-2 chain C regions	1,32%	0,35%	2,98%	1,58%	0,16%
Ig lambda-7 chain C region	2,68%	0,00%	0,00%	0,00%	0,00%
Ig mu chain C region	2,86%	0,75%	1,39%	2,57%	1,46%
Ig mu heavy chain disease protein	3,16%	0,82%	1,39%	0,00%	0,21%
Immunoglobulin J chain	0,14%	0,00%	0,10%	0,08%	0,00%
Immunoglobulin lambda-like polypeptide 5	3,93%	0,30%	0,00%	0,47%	0,00%

Apolipoprotein A-I	0,00%	0,10%	2,17%	0,00%	0,00%
Apolipoprotein A-II	0,00%	0,00%	0,28%	0,00%	0,00%
Apolipoprotein A-IV	0,00%	0,00%	0,22%	0,00%	0,00%
Apolipoprotein B-100	0,00%	0,22%	0,00%	0,00%	0,00%
Beta-2-glycoprotein 1	0,65%	5,35%	0,00%	1,96%	0,39%
Clusterin	0,00%	0,23%	0,14%	0,00%	0,00%
Phosphatidylcholine-sterol acyltransferase	0,00%	0,00%	0,05%	0,00%	0,00%
Serum paraoxonase/arylesterase 1	0,00%	0,20%	0,25%	0,00%	0,00%
Afamin	0,00%	0,04%	0,27%	0,00%	0,00%
Alpha-1B-glycoprotein	0,00%	0,34%	2,40%	0,00%	0,00%
Alpha-2-HS-glycoprotein	0,00%	0,53%	1,71%	0,00%	0,00%
Angiotensinogen	0,00%	0,08%	1,03%	0,00%	0,00%
Attractin	0,00%	0,00%	0,09%	0,00%	0,00%
Beta-Ala-His dipeptidase	0,00%	0,00%	0,05%	0,00%	0,00%
Cholinesterase	0,00%	0,00%	0,11%	0,00%	0,00%
Corticosteroid-binding globulin	0,00%	0,04%	0,52%	0,00%	0,00%
Hemopexin	0,00%	1,75%	3,36%	1,49%	1,82%
Inter-alpha-trypsin inhibitor heavy chain H1	0,00%	0,49%	0,00%	0,56%	0,12%
Inter-alpha-trypsin inhibitor heavy chain H2	0,00%	0,26%	0,00%	1,32%	0,22%
Inter-alpha-trypsin inhibitor heavy chain H4	0,00%	0,20%	0,00%	0,09%	0,05%
Leucine-rich alpha-2-glycoprotein	0,00%	0,00%	0,92%	0,00%	0,00%
N(G),N(G)-dimethylarginine dimethylaminohydrolase 1	0,00%	0,00%	0,09%	0,00%	0,00%
Pregnancy zone protein	0,00%	0,50%	0,58%	0,00%	0,00%
Protein AMBP	0,00%	0,12%	0,23%	0,18%	0,08%
Serotransferrin	0,04%	2,78%	4,51%	1,65%	2,80%
Serum albumin	0,56%	56,92%	4,08%	47,39%	84,14%

Thyroxine-binding globulin	0,00%	0,00%	0,19%	0,00%	0,00%
Transthyretin	0,00%	0,47%	2,85%	0,00%	0,00%
Vitamin D-binding protein	0,00%	0,25%	2,16%	0,00%	0,00%
Zinc-alpha-2-glycoprotein	0,00%	1,25%	0,84%	0,00%	0,00%
Acylpyruvase FAHD1, mitochondrial	0,00%	0,66%	0,00%	0,88%	1,95%
Brain and acute leukemia cytoplasmic protein	0,01%	0,00%	0,00%	0,00%	0,00%
BTB/POZ domain-containing protein KCTD12	0,00%	1,59%	0,00%	1,86%	0,00%
BTB/POZ domain-containing protein KCTD2	0,00%	0,00%	0,66%	0,00%	0,00%
CD5 antigen-like	0,24%	0,06%	0,08%	0,08%	0,00%
Coronin-1B	0,00%	0,09%	0,00%	0,00%	0,00%
DDB1- and CUL4-associated factor 8	0,00%	0,00%	0,14%	0,00%	0,00%
Hemoglobin subunit beta	0,00%	0,00%	0,16%	0,00%	0,00%
Lumican	0,00%	0,00%	0,15%	0,00%	0,00%
Lysophospholipid acyltransferase LPCAT4	0,00%	0,23%	0,00%	0,04%	0,00%
Methylglutaconyl-CoA hydratase, mitochondrial	0,00%	0,00%	0,00%	0,00%	0,06%
Methylmalonyl-CoA epimerase, mitochondrial	0,00%	0,00%	0,18%	0,00%	0,00%
N-acetylmuramoyl-L-alanine amidase	0,03%	0,00%	0,00%	0,07%	0,00%
N-alpha-acetyltransferase 10	0,00%	0,07%	0,00%	0,00%	0,00%
Potassium voltage-gated channel subfamily C member 2	0,00%	1,85%	0,00%	0,00%	0,00%
Protein Njmu-R1	0,00%	1,21%	0,00%	1,83%	0,00%
SHC-transforming protein 1	0,00%	0,00%	0,32%	0,00%	0,00%
Sorting nexin-32	0,00%	0,00%	0,07%	0,00%	0,00%
Tubulin beta-4A chain	0,00%	0,00%	0,00%	0,21%	0,00%
Tubulin beta-4B chain	0,00%	0,00%	0,17%	0,00%	0,00%
Vitronectin	0,00%	0,18%	0,00%	0,00%	0,00%

Protein name	E1	E2	E3	E4
BTB/POZ domain-containing protein KCTD12	0,00%	4,84%	0,00%	1,82%
Kv channel-interacting protein 2	0,00%	0,00%	0,00%	0,07%
Myocyte-specific enhancer factor 2A	0,00%	0,00%	0,00%	0,04%
Ribosomal RNA small subunit methyltransferase NEP1	0,00%	0,00%	0,00%	0,03%
Protein Njmu-R1	0,00%	1,14%	0,00%	0,00%
Thymidine phosphorylase	0,00%	0,09%	0,00%	0,00%
Tubulin beta-4A chain	0,00%	0,08%	0,00%	0,00%
Corticosteroid-binding globulin	0,00%	0,08%	0,00%	0,00%
Transcription factor IIIB 50 kDa subunit	0,00%	0,04%	0,00%	0,00%
Calmodulin-like protein 3	0,00%	0,02%	0,00%	0,00%
Dihydropyrimidinase	0,00%	0,02%	0,00%	0,00%
Ras-related protein Rab-4A	0,00%	0,02%	0,00%	0,00%
Leucine-rich alpha-2-glycoprotein	0,00%	0,02%	0,00%	0,00%
Alpha-1,6-mannosyl-glycoprotein 2-beta-N-acetylglucosaminyltransferase	0,33%	0,00%	0,00%	0,00%
ADP-ribosylation factor-like protein 8B	0,11%	0,00%	0,00%	0,00%
FERM and PDZ domain-containing protein 2	0,08%	0,00%	0,00%	0,00%
DNA replication factor Cdt1	0,02%	0,00%	0,00%	0,00%
UPF0160 protein MYG1, mitochondrial	0,02%	0,00%	0,00%	0,00%
Paired mesoderm homeobox protein 1	0,00%	0,00%	0,00%	0,00%
Serglycin	0,00%	0,00%	0,00%	0,00%
LysM and putative peptidoglycan-binding domain-containing protein 1	0,00%	0,00%	0,00%	0,00%
Alpha-1-antitrypsin	0,00%	2,13%	2,18%	1,35%
Haptoglobin	0,00%	1,63%	1,06%	1,14%

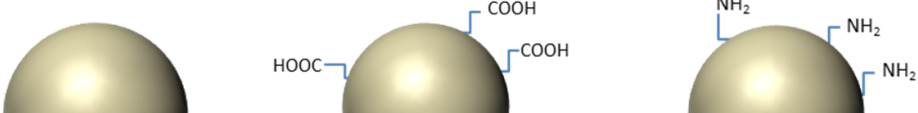
Alpha-2-macroglobulin	0,00%	1,16%	0,68%	0,86%
Ceruloplasmin	0,00%	0,03%	0,53%	0,65%
Alpha-1-antichymotrypsin	0,00%	0,14%	0,34%	0,37%
Fibronectin	0,00%	0,00%	0,19%	0,31%
Alpha-1-acid glycoprotein 1	0,00%	0,56%	0,47%	0,24%
Haptoglobin-related protein	0,00%	0,37%	0,29%	0,13%
Serum amyloid P-component	0,00%	0,00%	0,00%	0,12%
Alpha-1-acid glycoprotein 2	0,00%	1,10%	0,19%	0,06%
Fibrinogen gamma chain	0,00%	1,13%	1,34%	2,62%
Fibrinogen beta chain	0,00%	0,66%	0,90%	1,77%
Fibrinogen alpha chain	0,00%	0,50%	0,55%	0,97%
Prothrombin	0,00%	0,00%	0,00%	0,89%
Kininogen-1	0,00%	0,15%	0,22%	0,31%
Plasminogen	0,32%	0,20%	0,00%	0,04%
Antithrombin-III	0,00%	0,13%	0,07%	0,03%
Alpha-2-antiplasmin	0,00%	0,11%	0,00%	0,00%
Complement C3	0,00%	0,12%	0,90%	1,47%
Complement C4-B	0,00%	0,00%	0,33%	0,80%
Plasma protease C1 inhibitor	0,00%	0,00%	0,23%	0,29%
Complement factor H	0,00%	0,03%	0,00%	0,16%
Complement component C9	0,00%	0,00%	0,00%	0,09%
C4b-binding protein alpha chain	0,00%	0,00%	0,02%	0,06%
Complement factor B	0,08%	0,28%	0,03%	0,03%
Complement component C8 gamma chain	0,00%	0,01%	0,00%	0,00%
Complement C4-A	0,00%	0,00%	0,00%	0,00%
Ig kappa chain C region	27,34%	4,41%	3,43%	3,90%

Ig mu chain C region	0,00%	2,58%	3,09%	2,70%
Ig gamma-1 chain C region	38,04%	2,94%	1,02%	1,34%
Ig alpha-1 chain C region	0,02%	0,96%	0,88%	1,05%
Immunoglobulin lambda-like polypeptide 5	5,06%	0,00%	0,61%	0,59%
Ig heavy chain V-III region BRO	0,70%	0,34%	0,24%	0,44%
Ig lambda-3 chain C regions	0,00%	0,00%	0,00%	0,33%
Ig alpha-2 chain C region	0,00%	0,37%	0,25%	0,24%
Ig gamma-2 chain C region	8,08%	0,74%	0,23%	0,19%
Ig kappa chain V-II region TEW	0,72%	0,21%	0,15%	0,17%
Ig kappa chain V-I region AG	0,19%	0,06%	0,11%	0,14%
Immunoglobulin J chain	0,00%	0,07%	0,11%	0,13%
Ig kappa chain V-III region SIE	0,62%	0,24%	0,09%	0,09%
Ig heavy chain V-III region BUT	0,00%	0,00%	0,04%	0,00%
Ig gamma-3 chain C region	1,49%	0,21%	0,00%	0,00%
Ig heavy chain V-I region HG3	0,00%	0,02%	0,00%	0,00%
Ig lambda-7 chain C region	2,09%	0,00%	0,00%	0,00%
Ig gamma-4 chain C region	0,81%	0,00%	0,00%	0,00%
Ig kappa chain V-I region WEA	0,23%	0,00%	0,00%	0,00%
Ig heavy chain V-II region ARH-77	0,22%	0,00%	0,00%	0,00%
Ig lambda chain V-III region LOI	0,19%	0,00%	0,00%	0,00%
Ig lambda chain V-I region WAH	0,17%	0,00%	0,00%	0,00%
Ig heavy chain V-III region TUR	0,15%	0,00%	0,00%	0,00%
Ig kappa chain V-I region EU	0,14%	0,00%	0,00%	0,00%
Ig heavy chain V-III region GAL	0,13%	0,00%	0,00%	0,00%
Ig heavy chain V-III region VH26	0,12%	0,00%	0,00%	0,00%
Ig kappa chain V-III region NG9 (Fragment)	0,12%	0,00%	0,00%	0,00%

Ig kappa chain V-IV region Len	0,11%	0,00%	0,00%	0,00%
Ig lambda chain V-III region SH	0,10%	0,00%	0,00%	0,00%
Ig kappa chain V-IV region STH (Fragment)	0,10%	0,00%	0,00%	0,00%
Ig heavy chain V-III region WEA	0,09%	0,00%	0,00%	0,00%
Apolipoprotein A-I	0,00%	0,66%	0,52%	0,83%
Apolipoprotein A-IV	0,00%	0,25%	0,00%	0,30%
Apolipoprotein B-100	0,00%	0,26%	0,00%	0,19%
Serum paraoxonase/arylesterase 1	0,00%	0,00%	0,00%	0,18%
Clusterin	0,00%	0,30%	0,14%	0,18%
Beta-2-glycoprotein 1	1,81%	0,18%	0,00%	0,00%
Apolipoprotein A-II	0,00%	0,00%	0,00%	0,00%
Serum albumin	0,00%	58,08%	75,13%	64,82%
Inter-alpha-trypsin inhibitor heavy chain H2	0,00%	0,00%	0,09%	0,81%
Hemopexin	1,08%	2,70%	1,14%	0,72%
Transthyretin	0,00%	0,00%	0,18%	0,72%
Pregnancy zone protein	0,00%	0,17%	0,00%	0,58%
Inter-alpha-trypsin inhibitor heavy chain H1	0,00%	0,00%	0,00%	0,54%
Protein AMBP	0,00%	0,00%	0,00%	0,41%
Serotransferrin	9,15%	5,17%	0,95%	0,41%
Alpha-2-HS-glycoprotein	0,00%	0,59%	0,40%	0,36%
Vitamin D-binding protein	0,00%	0,39%	0,19%	0,14%
Alpha-1B-glycoprotein	0,00%	0,29%	0,27%	0,14%
Angiotensinogen	0,00%	0,09%	0,16%	0,12%
Retinol-binding protein 4	0,00%	0,00%	0,00%	0,09%
Afamin	0,00%	0,03%	0,00%	0,02%
Zinc-alpha-2-glycoprotein	0,01%	0,15%	0,06%	0,01%

Inter-alpha-trypsin inhibitor heavy chain H4	0,00%	0,05%	0,00%	0,00%
Vitronectin	0,00%	0,00%	0,00%	0,21%
CD5 antigen-like	0,00%	0,08%	0,00%	0,09%
Lumican	0,00%	0,00%	0,00%	0,05%
Keratin, type II cytoskeletal 1	0,00%	0,28%	0,00%	0,00%
Keratin, type I cytoskeletal 9	0,00%	0,18%	0,00%	0,00%
Keratin, type II cytoskeletal 2 epidermal	0,00%	0,06%	0,00%	0,00%
Keratin, type I cytoskeletal 14	0,00%	0,03%	0,00%	0,00%
Keratin, type I cytoskeletal 10	0,00%	0,03%	0,00%	0,00%
Keratin, type II cytoskeletal 6B	0,00%	0,01%	0,00%	0,00%
Keratin, type I cytoskeletal 16	0,00%	0,01%	0,00%	0,00%
Keratin, type I cytoskeletal 15	0,00%	0,00%	0,00%	0,00%

7.2.2 OVERVIEW OF SOFT CORONA ANALYSIS CHAPTER 6.2.1



	Rh / nm extrapolated		Rh / nm 30°	I / % 30°	Rh / nm extrapolated		Rh / nm 30°	I / % 30°	Rh / nm extrapolated		Rh / nm 30°	I / % 30°
naked	69			58			65					
Plasma diluted	93	87.5	126	34	80	95	68	95	74	71	110	21
	82		115	93	110		166	33	68		-	0
IgG	191	224	423	24	99	95.5	137	34	285	206.5	229	37
	257		470	30	92		84	32	128		206	21
Albumin-IgG-mixture (affi_only)	241	180	335	22	95	90.5	76	100	121	137.5	95	65
	119		184	9	86		77	100	154		80	58
Albumin (row)	125	121.5	309	15	57	61.5	57	100	67	72	70	92
	118		381	28	66		71	42	77		64	100
IgG-depleted Plasma	198	146	407	13	67	83.5	62	100	71	70	75	98
	94		765	15	100		193	19	69		84	95
Albumin-depleted Plasma	102	137	477	15	54	57.5	53	100	88	102	104	72
	172		219	16	61		62	58	116		491	18
Albumin- and IgG - depleted Plasma	59	61	59	100	57	53.5	24	9	72	77.5	-	0
	63		46	100	50		50	100	83		-	0
IgG com in running buffer	226	194.5	790	13	503	642	507	96	408	345	651	13
	163		163	45	781		854	81	282		894	12
HSA com in running buffer	152	169.5	109	97	62	64	60	100	88	80.5	105	55
	187		132	43	66		65	54	73		91	73
IgG com in PBS	210	183	269	19	101	90.5	72	99	224	174.5	4169	4
	156		333	22	80		70	100	125		2234	2
Albumin com in PBS	212	194	647	11	72	70.5	57	100	67	67	207	13
	176		325	7	69		63	100	67		80	98
Fibrinogen com In PBS	238	206.5	509	24	189	158	219	35	182	152.5	228	46
	175		196	54	127		184	45	123		141	81

DLS soft corona analysis with duplicates of all particles without pre-coating.

7.2.3 OVERVIEW OF HARD PROTEIN CORONA ANALYSIS CHAPTER 6.3.1

Description	average %			
	Human Plasma	PS	PS-Lut-COOH	PS-Lut-NH2
Ceruloplasmin	0,34	0,00	0,00	0,00
Haptoglobin	1,70	0,00	0,00	0,00
Haptoglobin-related protein	0,07	0,09	0,00	0,08
Alpha-1-antitrypsin	1,57	0,25	0,00	0,38
Alpha-1-antichymotrypsin	0,35	0,00	0,00	0,00
Alpha-2-macroglobulin	0,89	0,00	0,00	0,00
Serum amyloid P-component	0,06	0,00	0,00	0,00
Fibronectin	0,29	0,12	0,00	0,00
Alpha-1-acid glycoprotein 1	0,05	0,00	0,00	0,00
Serum amyloid A-1 protein	0,00	0,00	0,22	0,09
Lipopolysaccharide-binding protein	0,00	0,00	0,53	0,05
Alpha-1-acid glycoprotein 2	0,02	0,00	0,00	0,00
Alpha-2-antiplasmin	0,07	0,00	0,00	0,00
Antithrombin-III	0,16	0,00	0,00	0,05
Coagulation factor V	0,00	0,00	0,37	0,00
Coagulation factor XI	0,00	0,00	0,36	0,00
Fibrinogen alpha chain	0,85	0,28	7,85	0,32
Fibrinogen beta chain	1,00	0,51	6,23	0,42
Fibrinogen gamma chain	1,46	0,57	6,05	0,54
Heparin cofactor 2	0,37	0,00	0,00	0,00

Histidine-rich glycoprotein	0,08	0,00	5,82	0,00
Hyaluronan-binding protein 2	0,00	0,00	0,21	0,00
Kininogen-1	1,20	0,00	4,99	0,00
Plasma kallikrein	0,04	0,00	0,29	0,00
Plasminogen	0,16	0,00	0,00	0,00
Prothrombin	0,21	0,00	0,00	0,00
C4b-binding protein alpha chain	0,15	0,11	0,00	0,00
Complement C1q subcomponent subunit A	0,02	0,00	0,00	0,00
Complement C1q subcomponent subunit B	0,11	0,00	0,00	0,00
Complement C1q subcomponent subunit C	0,07	0,00	0,00	0,00
Complement C1r subcomponent	0,01	0,25	0,00	0,33
Complement C1s subcomponent	0,06	0,18	0,00	0,32
Complement C3	0,72	0,73	0,00	1,45
Complement C4-A	0,07	0,29	0,00	0,12
Complement C4-B	0,12	0,20	0,00	0,10
Complement component C8 alpha chain	0,03	0,00	0,00	0,00
Complement component C8 gamma chain	0,02	0,00	0,00	0,00
Complement component C9	0,05	0,00	0,00	0,00
Complement factor B	0,18	0,00	0,00	0,00
Complement factor H	0,27	0,00	0,20	0,00
Complement factor H-related protein 1	0,00	0,00	0,21	0,00
Plasma protease C1 inhibitor	0,15	0,28	0,08	0,37
Immunoglobulin lambda-like polypeptide 5	1,19	0,00	0,00	0,00
Immunoglobulin J chain	0,12	0,00	0,00	0,00
Ig kappa chain V-I region AG	0,32	0,00	0,00	0,00
Ig kappa chain V-I region EU	0,18	0,00	0,00	0,00

Ig kappa chain V-I region HK102 (Fragment)	0,02	0,00	0,00	0,00
Ig kappa chain V-I region Lay	0,11	0,00	0,00	0,00
Ig kappa chain V-II region TEW	0,27	0,00	0,00	0,00
Ig kappa chain V-III region SIE	0,58	0,00	0,00	0,00
Ig kappa chain V-IV region Len	0,28	0,00	0,00	0,00
Ig heavy chain V-I region HG3	0,13	0,00	0,00	0,00
Ig heavy chain V-III region WEA	0,04	0,00	0,00	0,00
Ig heavy chain V-III region VH26	0,16	0,00	0,00	0,00
Ig heavy chain V-III region TIL	0,13	0,00	0,00	0,00
Ig heavy chain V-III region BRO	0,54	0,00	0,00	0,00
Ig heavy chain V-III region GAL	0,12	0,00	0,00	0,00
Ig kappa chain C region	8,63	1,08	0,13	0,47
Ig gamma-1 chain C region	8,30	0,00	0,00	0,26
Ig gamma-2 chain C region	2,69	0,00	0,00	0,00
Ig gamma-2 chain C region	0,00	0,12	0,00	0,13
Ig gamma-3 chain C region	0,38	0,00	0,00	0,00
Ig gamma-4 chain C region	0,14	0,00	0,00	0,00
Ig mu chain C region	2,45	0,00	0,00	0,00
Ig mu chain C region	0,00	1,15	0,00	0,31
Ig alpha-1 chain C region	1,11	0,00	0,00	0,00
Ig alpha-1 chain C region	0,00	0,25	0,00	0,20
Ig alpha-2 chain C region	0,11	0,00	0,00	0,00
Ig delta chain C region	0,01	0,00	0,00	0,00
Ig mu heavy chain disease protein	0,03	0,00	0,00	0,00
Ig kappa chain V-III region VG (Fragment)	0,15	0,00	0,00	0,00
Ig heavy chain V-II region ARH-77	0,11	0,00	0,00	0,00

Ig lambda-6 chain C region	0,00	0,00	0,00	0,18
Ig lambda-2 chain C regions	2,52	0,00	0,00	0,00
Ig heavy chain V-I region V35	0,03	0,00	0,00	0,00
Ig lambda chain V-III region LOI	0,11	0,00	0,00	0,00
Bcl-2-related protein A1	0,11	0,00	0,00	0,00
Apolipoprotein A-I	1,23	16,69	5,22	14,83
Apolipoprotein A-II	0,00	0,00	0,00	0,25
Apolipoprotein A-IV	0,13	11,54	0,10	15,03
Apolipoprotein B-100	0,17	0,66	0,00	0,65
Apolipoprotein C-III	0,00	3,06	1,64	9,24
Apolipoprotein D	0,00	0,23	0,00	0,89
Apolipoprotein E	0,03	3,77	2,25	3,15
Beta-2-glycoprotein 1	1,45	0,00	9,68	0,00
Clusterin	0,34	51,81	14,44	42,80
Ig alpha-1 chain C region	0,00	0,25	0,00	0,20
Phospholipid transfer protein	0,00	0,16	0,00	0,65
Serum paraoxonase/arylesterase 1	0,06	0,37	0,00	0,49
Afamin	0,15	0,00	0,00	0,00
Alpha-1B-glycoprotein	0,13	0,00	0,00	0,00
Alpha-2-HS-glycoprotein	0,33	0,00	0,00	0,00
Angiotensinogen	0,27	0,00	0,00	0,00
Hemoglobin subunit alpha	0,01	0,00	0,00	0,00
Hemoglobin subunit beta	0,03	0,00	0,00	0,00
Hemopexin	0,82	0,00	0,00	0,00
Ig lambda-3 chain C regions	0,00	0,31	0,00	0,00
Inter-alpha-trypsin inhibitor heavy chain H1	0,18	0,00	0,00	0,00

Inter-alpha-trypsin inhibitor heavy chain H2	0,17	0,07	0,00	0,08
Inter-alpha-trypsin inhibitor heavy chain H4	0,10	0,00	5,98	0,00
Leucine-rich alpha-2-glycoprotein	0,02	0,00	0,00	0,00
Pregnancy zone protein	0,08	0,00	0,00	0,00
Probable ATP-dependent RNA helicase DDX46	0,00	0,00	0,00	0,06
Protein AMBP	0,11	0,00	0,00	0,00
Protein Njmu-R1	0,05	0,00	0,00	0,00
Putative protein ZNF815	0,00	0,00	0,00	0,11
Selenoprotein P	0,00	0,00	0,18	0,00
Serotransferrin	2,18	0,00	0,00	0,00
Serum albumin	45,59	0,89	0,47	0,80
Synaptosomal-associated protein 23	0,15	0,00	0,00	0,00
Transthyretin	0,39	0,40	0,48	0,51
UBX domain-containing protein 4	0,07	0,00	0,00	0,00
Vitamin D-binding protein	0,35	0,00	0,00	0,00
Zinc-alpha-2-glycoprotein	0,09	0,00	0,00	0,00
A-kinase anchor protein 8	0,00	0,17	0,00	0,00
CD5 antigen-like	0,13	0,07	0,00	0,00
Corticosteroid-binding globulin	0,04	0,00	0,00	0,00
Cysteine protease ATG4C	0,70	0,00	0,00	0,00
Cytoplasmic protein NCK2	0,08	0,00	0,00	0,00
Gelsolin	0,12	0,00	0,00	0,00
Ig gamma-1 chain C region	0,00	0,28	0,00	0,00
N-acetylmuramoyl-L-alanine amidase	0,03	0,00	0,00	0,00
Vitronectin	0,16	2,81	26,01	4,05

7.2.4 CHARACTERIZATION OF INDIVIDUAL AND POOLED HUMAN SERUM

	P2	P4	P5	P6	P7	P9	Pool
Rh1/nm	5	3	3	5	2	6	5
Rh2/nm	30	52	20	30	14	18	40
Rh3/nm	152	211	125	175	116	83	147
$\langle 1/Rh \rangle_z^{-1}/nm$	63	66	20	33	44	21	33

Determined hydrodynamic radii of individual as well as pooled human serum via DLS.

8 ZUSAMMENFASSUNG

Die Entwicklung von Nanomaterialien für die biomedizinische Anwendung hat in den letzten Jahren an enormer Bedeutung gewonnen. Besonders in der Therapie von Krebserkrankungen bietet das Verpacken von Wirkstoffen in einem Träger viele Vorteile gegenüber der Administration des Wirkstoffes alleine. Nanomaterialien sind aufgrund ihrer speziellen Eigenschaften dazu geschaffen, den Wirkstoff gezielt an den Wirkort zu transportieren. Auf diese Weise können die zytotoxischen Nebenwirkungen, die während einer Chemotherapie auftreten, reduziert werden. Darüber hinaus wird durch das Verpacken auch der Wirkstoff an sich vor Abbau geschützt.

Nichts desto trotz ist die Anwendung von Nanomaterialien in der Krebstherapie limitiert, da die physiologischen Prozesse, die ein Nanotransporter nach Administration hervorruft, nur schwer prognostiziert werden können. Bisher werden Nanotransporter üblicherweise intravenös verabreicht. Das bedeutet, dass diese sofort mit dem menschlichen Blut und den darin befindlichen Proteinen in Berührung kommen. Dies führt zur raschen Ausbildung einer Proteinhülle auf der Oberfläche der Nanomaterialien, welche deren chemischen und physikalischen Eigenschaften stark verändert.

Diese Studie untersucht den Einfluss einzelner Proteine sowie Proteinmischungen auf die physikochemischen Eigenschaften von Polystyrol-Partikeln als Modellsystem. Die Einzelproteine sowie Proteinmischungen, die Albumin- bzw. IgG-frei sind, wurden durch die Fraktionierung von menschlichem Blutplasma gewonnen. Die Inkubation der genannten Partikel in klar definierten Proteinmischungen wurde genutzt, um eine vorherbestimmte Proteinhülle auf der Partikeloberfläche auszubilden. Diese „künstliche“ Proteinhülle wurde im Anschluss untersucht im Hinblick auf stabilisierende bzw. destabilisierende Wirkung auf die Nanopartikel unter *in vivo*-Bedingungen mittels dynamischer Lichtstreuung. Zusätzlich wurde der Effekt der gegebenen Proteinhülle auf die Zellaufnahme in Makrophagen überprüft. Es konnte gezeigt werden, dass eine Stabilisierung von Partikeln im Hinblick auf das Aggregationsverhalten möglich ist, indem man Partikel mit bestimmten Proteinen vorbeschichtet.

Das Konzept der Partikelbeschichtung zur Stabilisierung gegenüber Aggregation wurde ausgedehnt, um die Schwierigkeiten zu überwinden, die die unterschiedliche Blutserumzusammensetzung von verschiedenen Individuen birgt.

Ein nächster Fokus wurde auf die Übertragbarkeit verschiedener *in vivo*-Modelle auf den Menschen gelegt. Es zeigte sich, dass sowohl das Aggregationsverhalten von Polystyrolpartikeln, als auch jenes von Dextran- und Stärke-umhüllten Partikeln sehr stark von der Proteinquelle abhängt.

Nachdem einzelne Aspekte, die Einfluss auf die Proteinadsorption auf Partikeln ausüben, untersucht wurden, wurde das Modellsystem ausgetauscht gegen liposomale Systeme, die dem siRNA-Transport dienen. Das Aggregationsverhalten der Liposomen bzw. Lipoplexe wurde mittels dynamischer Lichtstreuung untersucht und optimiert.

Zusammenfassend kann festgehalten werden, dass verschiedene Einflussfaktoren für die physikochemischen Eigenschaften von Nanomaterialien nach Exposition ins menschliche Blut gezielt untersucht wurden. So wurden viele Möglichkeiten aufgezeigt, welche zur Evaluation eines Nanomaterials vor *in vivo*-Versuchen herangezogen werden können. Zusätzlich wurden Optionen aufgezeigt, wie die Wechselwirkung von Proteinen mit Nanomaterialien gezielt zur Stabilisierung genutzt werden kann.